

**Auroral Ion Upflows in the F-region and
Topside Ionosphere**

Thesis submitted for the degree of
Doctor of Philosophy
at the University of Leicester

by

Craig Foster
Department of Physics and Astronomy
University of Leicester

September 1997

UMI Number: U103777

All rights reserved

INFORMATION TO ALL USERS

The quality of this reproduction is dependent upon the quality of the copy submitted.

In the unlikely event that the author did not send a complete manuscript and there are missing pages, these will be noted. Also, if material had to be removed, a note will indicate the deletion.



UMI U103777

Published by ProQuest LLC 2013. Copyright in the Dissertation held by the Author.
Microform Edition © ProQuest LLC.

All rights reserved. This work is protected against
unauthorized copying under Title 17, United States Code.



ProQuest LLC
789 East Eisenhower Parkway
P.O. Box 1346
Ann Arbor, MI 48106-1346

Auroral Ion Upflows in the F-Region and Topside Ionosphere

Craig Foster

Abstract

Ion flow along geomagnetic field lines is an important mechanism in the coupling of the magnetosphere-ionosphere system. Over the last 25 years or so, a wealth of satellite and radar observations has revealed the ionosphere as a steady and significant source of magnetospheric plasma. In the auroral ionosphere, field-aligned O^+ upflows are often detected with fluxes exceeding those observed at higher altitudes, indicating that the ionosphere actively supplies ions to the magnetosphere. A number of mechanisms, principally associated with disturbed ionospheric conditions, have been proposed to account for ion upflows. This thesis documents a study of ion upflows observed in the auroral F-region and topside ionosphere. The work is based almost exclusively on incoherent scatter measurements from the EISCAT facility. More than 12 years' UHF Common Programme observations were employed in a study of the variation of upflow characteristics as a function of time, altitude, season and solar and geomagnetic activity. The study was extended in altitude with the inclusion of 5 years' vertical measurement from the EISCAT VHF radar. A quantitative comparison between upflow occurrence and plasma heating events was also performed. In addition, a case study is presented, examining three intervals of transient ion upflow detected during a run of the UK EISCAT Special Programme UFIS. The three events highlight some of the energization processes that can occur at different altitudes to generate field-aligned flow. Finally, a more detailed numerical investigation examined a day-side upflow observed by EISCAT in March, 1992. The event was modelled employing a simple 1-D approximation to the ion momentum-balance equation. The model explored the relative effects of plasma pressure, gravity and neutral wind on the field-parallel ion velocity; it was found that knowledge of the ion composition was necessary for accurate modelling of the observations.

CONTENTS

CHAPTER 1

Introduction: The Solar-Terrestrial Environment and the Earth's Ionosphere

1.1 The Sun and the Solar Wind	1
1.2 The Terrestrial Environment	1
1.2.1 The Magnetosphere	1
1.2.2 The Ionosphere	2
1.2.3 The High-Latitude Ionosphere	4
1.4 Radar Measurements of the Ionosphere	5
1.5 Aims of the Present Study	6

CHAPTER 2

Ion Upflows in the High-Latitude F-region and Topside Ionosphere: Review and Theory

2.1 Introduction	7
2.2 Observations of Heavy Ions in the Magnetosphere	7
2.2.1 The Polar Wind	8
2.2.2 The Cleft Ion Fountain	8
2.2.3 Polar Cap Outflows	9
2.2.4 Auroral Zone Outflows	9
2.3 F-region Observations of Auroral Ion Upflows	12
2.4 Acceleration Mechanisms in the F-region and Topside Auroral Ionosphere	15
2.4.1 Thermal Diffusion	16
2.4.2 Field-aligned Component of Neutral Wind	17
2.4.3 Ion-neutral Frictional Heating	17
2.4.4 Ion Temperature Anisotropy and the Magnetic Mirror Force	20
2.4.5 Electron Heating	21
2.4.6 Transverse Ion Heating	23
2.4.7 Joule Heating of the Neutral Atmosphere	24
2.4.8 Auroral Plasma Cavity	25
2.5 Summary	25

CHAPTER 3

Incoherent Scatter and the EISCAT Facility

3.1 Introduction	27
3.2 Incoherent Scatter Theory	27
3.2.1 Determination of Ionospheric Parameters from an IS Spectrum	29
3.2.2 Measurement Techniques	32
3.3 The European Incoherent Scatter Facility	34

3.3.1 EISCAT Programmes	36
3.3.2 Analysis of EISCAT Data	37
3.3.3 Uncertainties in Derived Parameters	38
3.4 Summary	40

CHAPTER 4

EISCAT Observations of Nightside Auroral Plasma Upflows in the F-region and Topside Ionosphere

4.1 Introduction	42
4.2 Experimental Configuration	42
4.3 Observations: Introduction	43
4.4 Event 1: Upflow at 2200 UT	45
4.4.1 Event 1: Observations	45
4.4.2 Event 1: Discussion	46
4.5 Event 2: Upflow at 0030 UT	50
4.5.1 Event 2: Observations	50
4.5.2 Event 2: Discussion	50
4.6 Event 3: Upflow at 0045 UT	52
4.6.1 Event 3: Observations	52
4.6.2 Event 3: Discussion	52
4.7 Summary and Conclusions	53

CHAPTER 5

A Statistical Study of F-region and Topside Upflows using EISCAT Data from 1984 to 1996

5.1 Introduction	55
5.2 Data Sets and Selection Criteria	55
5.3 Results and Discussion	57
5.3.1 Diurnal Variation of Upflows: 200 to 500 km	58
5.3.2 Seasonal Variation of Upflows: 200 to 500 km	59
5.3.3 Diurnal Variation of Upflows: 300 to 800 km.	60
5.3.4 Examination of Ambient Field-aligned Flow	63
5.3.5 Variation of Upflows over a Solar Cycle	64
5.3.6 Upflow Occurrence as a Function of Kp	66
5.3.7 Upflow Occurrence and Ion Frictional Heating.	67
5.3.8 Upflows and Electron Temperature.	69
5.4 Summary and Conclusions	71

CHAPTER 6

An Investigation of a Simple Model and its Application to a Dayside Ion Upflow Event Observed by EISCAT

6.1 Introduction	73
6.2 Motivation for Present Study	73
6.3 Observations	74
6.4 The Model	75
6.5 Method and Results	76
6.5.1. Modelling of Observed Velocity Profiles	76
6.5.2. A Comparison of Force Terms	78
6.5.3 Consideration of the Magnetic Mirror Force	78
6.6 Assessment of the Model	79
6.6.1 Errors Arising from an Incorrect Ion Composition Model	79
6.6.2 Consideration of a Modified Ion Composition Model	81
6.6.3 The Effect of a Modified Ion Composition Model	82
6.7 Summary and Conclusions	84

CHAPTER 7

Summary

7.1 Introduction	85
7.2 Summary of Chapter 4	85
7.3 Summary of Chapter 5	86
7.4 Summary of Chapter 6	87

REFERENCES

ACKNOWLEDGEMENTS

Special thanks go to my supervisor, Dr Mark Lester, and to Dr Jackie Davies, for their advice, assistance and encouragement.

I am also grateful to all in Radio and Space Plasma Physics, both past and present, for their many and varied contributions.

Additional thanks go to the EISCAT group at the Daresbury and Rutherford Appleton Laboratory, in particular Dr Ian McCrea.

I would also like to acknowledge the support of the following:

The Director and staff of the EISCAT scientific association. EISCAT is an international facility supported by the national science councils of Finland, France, Germany, Japan, Norway, Sweden and the United Kingdom.

Dr Hermann Lühr for provision of EISCAT magnetometer cross data.

The Particle Physics and Astronomy Research Council for funding me through my study.

The staff of the World Data Centre, for supplying geomagnetic index data.

CHAPTER 1

Introduction: The Solar-Terrestrial Environment and the Earth's Ionosphere

1.1 The Sun and the Solar Wind

The thermal expansion of the Sun's upper atmosphere, the corona, generates an outward flux of particles into interplanetary space, a phenomenon termed the solar wind. The solar wind is a fully ionized plasma, predominantly comprised of protons and electrons. At a distance of 1 astronomical unit (AU), solar wind particles typically attain velocities of between 300 and 600 km s⁻¹. In general, the solar wind particle density lies between 1×10^6 and 1×10^7 m⁻³. The Sun's magnetic field is carried into interplanetary space by the highly conducting solar wind plasma, constituting the so-called interplanetary magnetic field (IMF). As the Sun rotates with a 27 day period, the IMF acquires a spiral form, as illustrated in Figure 1.1. Close to the Earth, interplanetary magnetic field lines make an angle of about 45° with the radial direction in the ecliptic plane. In the solar meridional plane, a neutral current sheet separates regions of sunward and anti-sunward directed magnetic field. The neutral sheet is often shaped such that some regions lie above and others below the ecliptic plane. As this pattern rotates with the Sun, the IMF in the vicinity of the Earth exhibits adjacent regions of sunward and anti-sunward directed field, schematically illustrated in Figure 1.1. There are typically two or four sectors, although at solar maximum the configuration can become more unstructured. The position of the neutral sheet with respect to the ecliptic plane is important since it determines the direction and magnitude the component of the IMF perpendicular to the ecliptic (the z-component). The z-component of the IMF greatly influences the degree of coupling between the solar wind and the terrestrial magnetosphere-ionosphere.

Solar electromagnetic radiation at X-ray and extreme ultraviolet (EUV) energies is the dominant factor in the ionization of the Earth's upper atmosphere. Fluxes at these wavelengths exhibit a strong dependence on the 11 year solar cycle; at solar maximum, the power of EUV and X-radiation can be enhanced by factors of about two and five, respectively, compared with solar minimum conditions.

1.2 The Terrestrial Environment

1.2.1 The Magnetosphere

As the solar wind particles travel Earthward, they are deflected by the geomagnetic field. The cavity thus formed in the solar wind is termed the magnetosphere. Figure 1.2 illustrates the principal regions of the terrestrial magnetosphere. The boundary of the magnetosphere is marked by the magnetopause, within which the energy density of the geomagnetic field exceeds that of the solar wind plasma. Deflected solar wind particles travel around the magnetopause current sheet in a region known as the magnetosheath. Sunward of

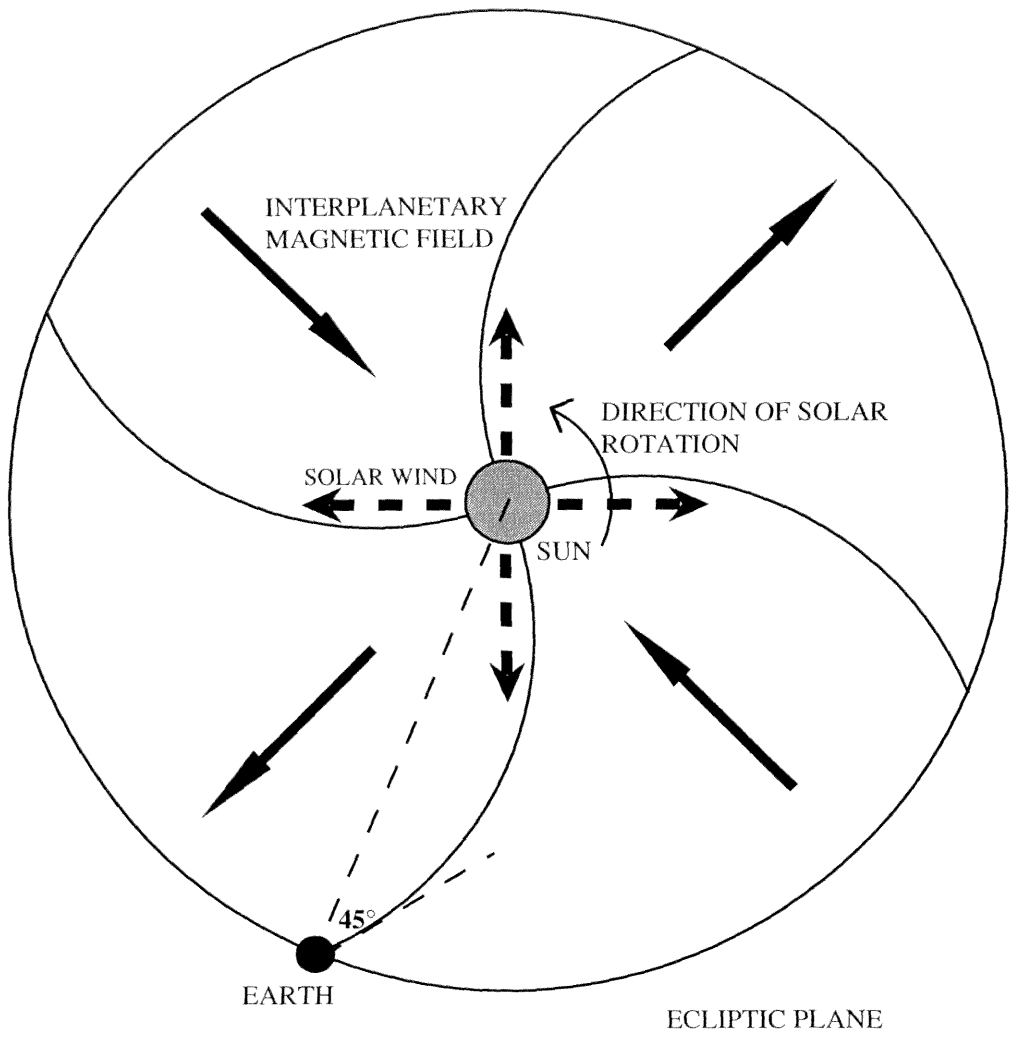


Figure 1.1 Schematic representation of the spiral structure of the interplanetary magnetic field, indicating also adjacent regions of sunward and anti-sunward directed field.

the magnetopause, a bow shock is formed where the supersonic solar wind particles encounter the hotter, denser magnetospheric plasma. On the day side, the bow shock typically lies up to 13.6 \times from the Earth in the same direction. Although the geomagnetic field effectively shields the near-Earth environment from the solar wind, the magnetosphere contains plasma

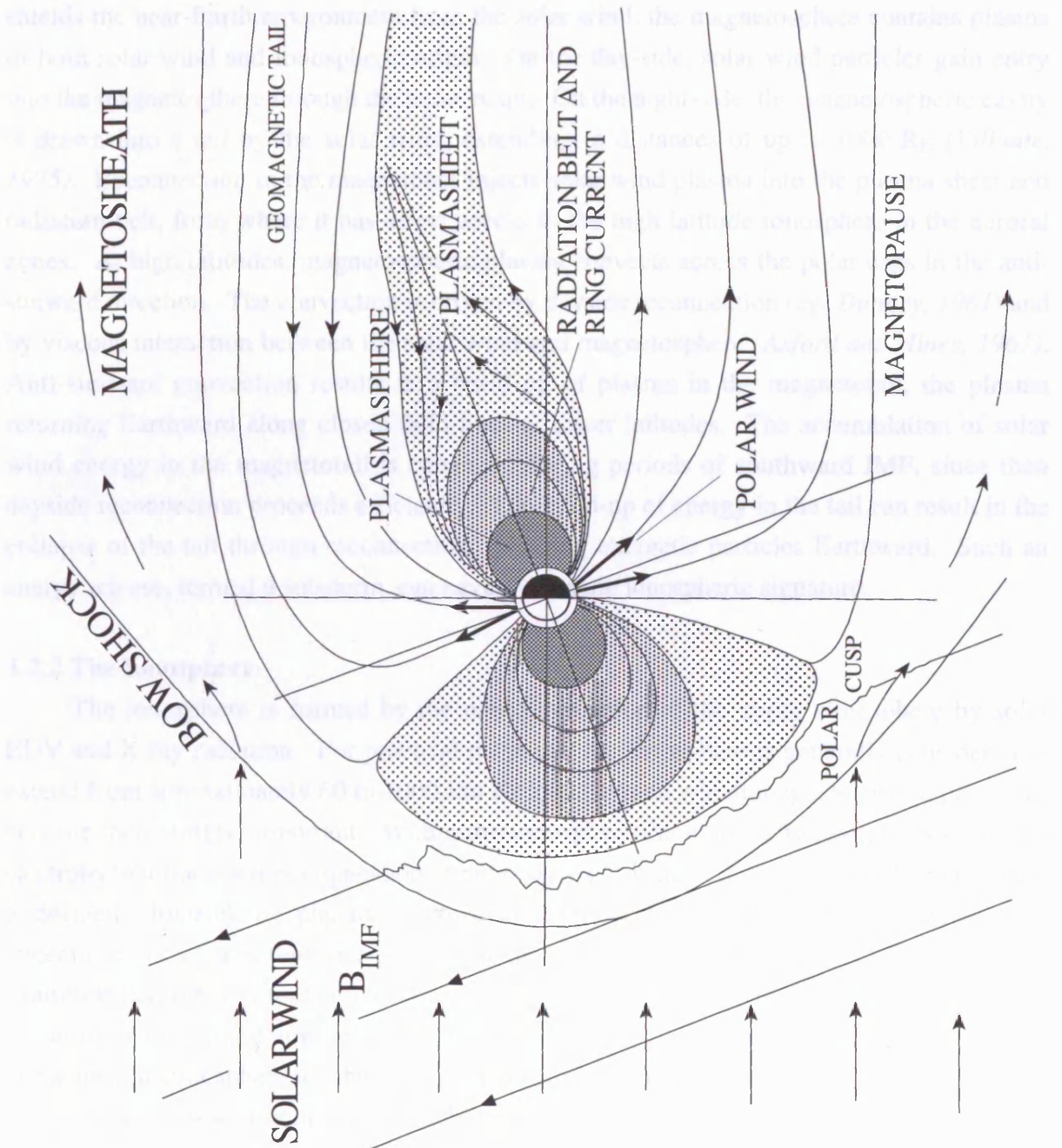


Figure 1.2 The interaction between the solar wind and the Earth's magnetic field, illustrating the principle regions of the magnetosphere.

the magnetopause, a bow shock is formed where the supersonic solar wind particles encounter the hotter, denser magnetosheath plasma. On the day-side, the bow shock typically lies up to $13 R_E$ from the Earth in the noon meridian. Although the geomagnetic field effectively shields the near-Earth environment from the solar wind, the magnetosphere contains plasma of both solar wind and ionospheric origin. On the day-side, solar wind particles gain entry into the magnetosphere through the polar cusps. On the night-side, the magnetospheric cavity is drawn into a tail by the solar wind, extending to distances of up to $1000 R_E$ (Villante, 1975). Reconnection in the magnetotail injects solar wind plasma into the plasma sheet and radiation belt, from where it has direct access to the high latitude ionosphere in the auroral zones. At high latitudes, magnetospheric plasma convects across the polar caps in the anti-sunward direction. The convection is driven by dayside reconnection (eg. Dungey, 1961) and by viscous interaction between the solar wind and magnetosphere (Axford and Hines, 1961). Anti-sunward convection results in a build up of plasma in the magnetotail, the plasma returning Earthward along closed field lines at lower latitudes. The accumulation of solar wind energy in the magnetotail is enhanced during periods of southward IMF, since then dayside reconnection proceeds efficiently. The build-up of energy in the tail can result in the collapse of the tail through reconnection, releasing energetic particles Earthward. Such an energy release, termed a substorm, can have a dramatic ionospheric signature.

1.2.2 The Ionosphere

The ionosphere is formed by the photo-ionization of the upper atmosphere by solar EUV and X-ray radiation. For practical purposes, the ionosphere is generally considered to extend from approximately 60 to 1000-km altitude, beyond which magnetospheric processes become increasingly important. Within the ionosphere there are sufficient numbers of free electrons to influence the propagation of radio waves; it is that effect by which the ionosphere is defined. Ionospheric plasma is, however, very weakly ionized, with charged particle concentrations of less than one percent of the neutral atmosphere density at all altitudes. Consequently, the structure and behaviour of the ionosphere is dependent to a large extent on the surrounding neutral atmosphere. It is, therefore, necessary to understand the composition of the neutral atmosphere in which the ionospheric plasma exists.

The regions of the upper atmosphere, illustrated in Figure 1.3, are generally defined according to the neutral temperature. Above approximately 100-km altitude, within the thermosphere, the neutral temperature increases steadily with altitude due to photodissociation of atomic oxygen by UV solar radiation. The neutral temperature reaches a limiting value at the thermopause, above which it stabilizes. The height of the thermopause and the maximum temperature of the thermosphere exhibit seasonal, diurnal and solar cycle variations.

The atmospheric density and pressure also diminish rapidly with increasing altitude, such that at 50 km they are approximately 0.1% of their sea-level values. The region of

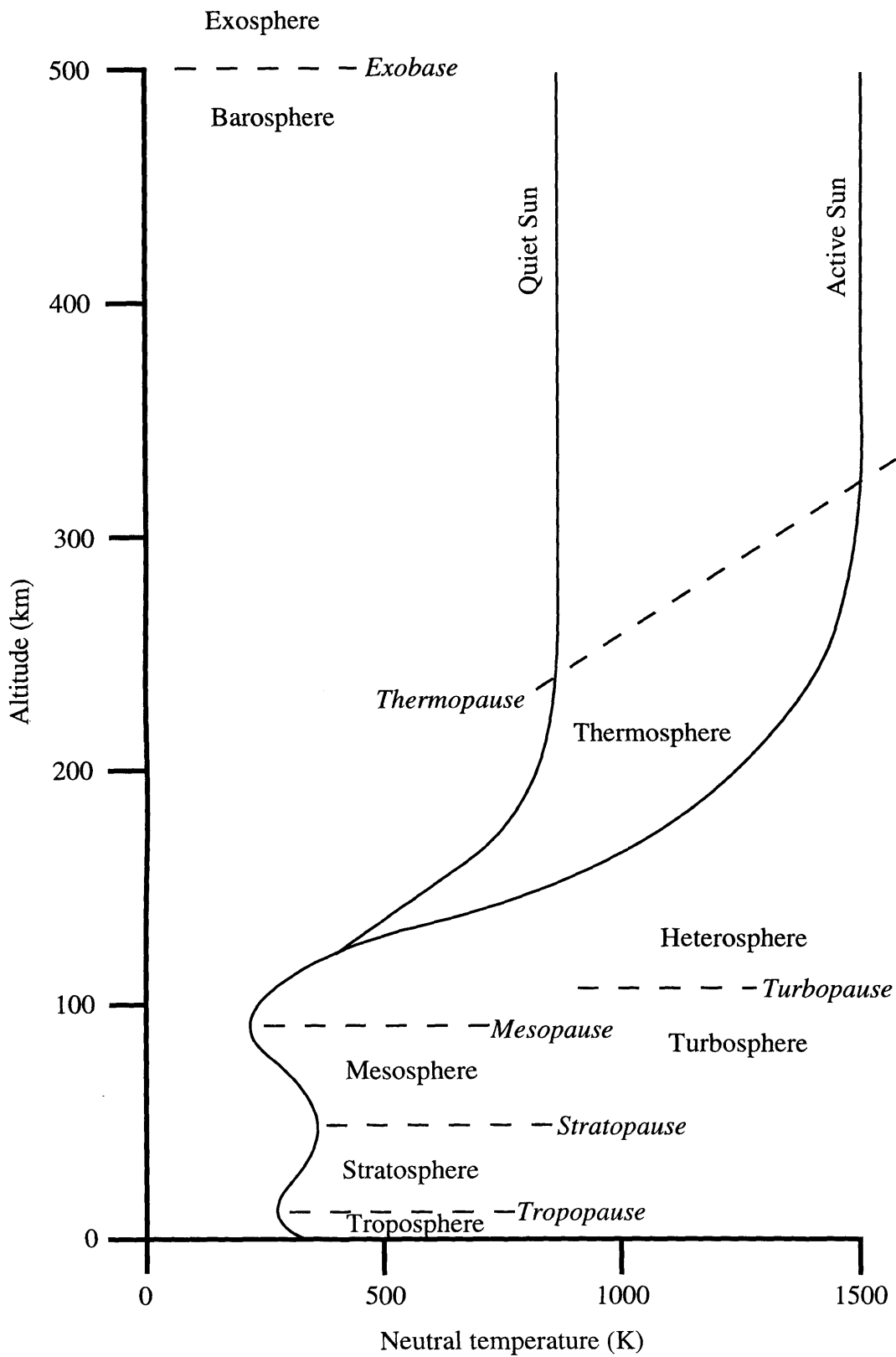


Figure 1.3 Altitude profile of the neutral atmospheric temperature for high and low solar activity.

atmosphere below about 500-km altitude is termed the barosphere, above which lies the exosphere, as illustrated in Figure 1.3. Within the barosphere, the atmospheric density is sufficiently large such that collisions prevent the escape of neutral gases. Beyond the exobase, however, the lighter species such as H and He can escape the Earth's gravitational field.

The composition of the neutral atmosphere also exhibits altitudinal variations. Below about 110-km altitude, turbulent mixing of the atmosphere means that the relative concentrations of the neutral species, principally O₂ and N₂, remain constant with height. The upper boundary of this region is termed the turbopause. Above the turbopause, the different masses of the neutrals leads to stratification of the atmosphere under the influence of gravity. Lighter species such as O, He and H become predominant with increasing altitude, each layer exhibiting a scale height dependent on the neutral particle mass and temperature.

The depth to which solar radiation can penetrate into the atmosphere is dependent on both the photon energy and the gases it is able to ionize. Thus the ionosphere is stratified into distinct layers, each characterized by its predominant ion species and peak electron density value. Figure 1.4 illustrates typical altitude profiles of electron density for the night-time and day-time ionosphere at mid-latitudes for moderate solar activity. Between solar maximum and minimum, the peak electron density can vary by a factor of two. The principal ionospheric layers are termed the D, E and F-regions, the latter comprising two distinct layers by day, the F1 and F2 regions. The D-region is produced by hard X-rays and cosmic rays, whilst softer X-ray and EUV radiation generates the E-region. The majority of EUV radiation is absorbed between about 150 and 180-km altitude, forming the daytime F1 layer. The E- and F1-regions are populated mainly by O⁺ and NO⁺ ions, the latter produced through chemical reactions. There is no strong absorption peak above the F1 region. The presence of the F2 layer, and its relatively high electron density, is accounted for by the ion loss rate decreasing faster than the ion production rate with increasing altitude. The electron densities in the D, E and F1 regions are determined largely by the balance between solar production and loss due to recombination, with transport effects being of lesser importance. Therefore, the peak electron densities in these regions exhibit a dependence both on the ion species present and their interactions with the surrounding neutral gas, as well as a dependence on diurnal, seasonal and solar cycle variations due to changing solar fluxes. In the F2 region, O⁺ is the dominant ion and transport processes such as diffusion become increasingly important as the neutral density decreases with altitude. Since there is no production peak corresponding to the F2 layer, the altitude of the electron density maximum is more variable than in the other regions, generally lying between 200 and 500-km altitude. Above the F2 peak, in the topside ionosphere, ion transport becomes the dominant loss process. At altitudes beyond about 700 km, O⁺ is gradually replaced by the H⁺ and He⁺ ions of the protonosphere. He⁺ ions are produced by photo-ionization of neutral He, whilst the H⁺ ions of the protonosphere are largely supplied by the ionosphere. By day, charge exchange between

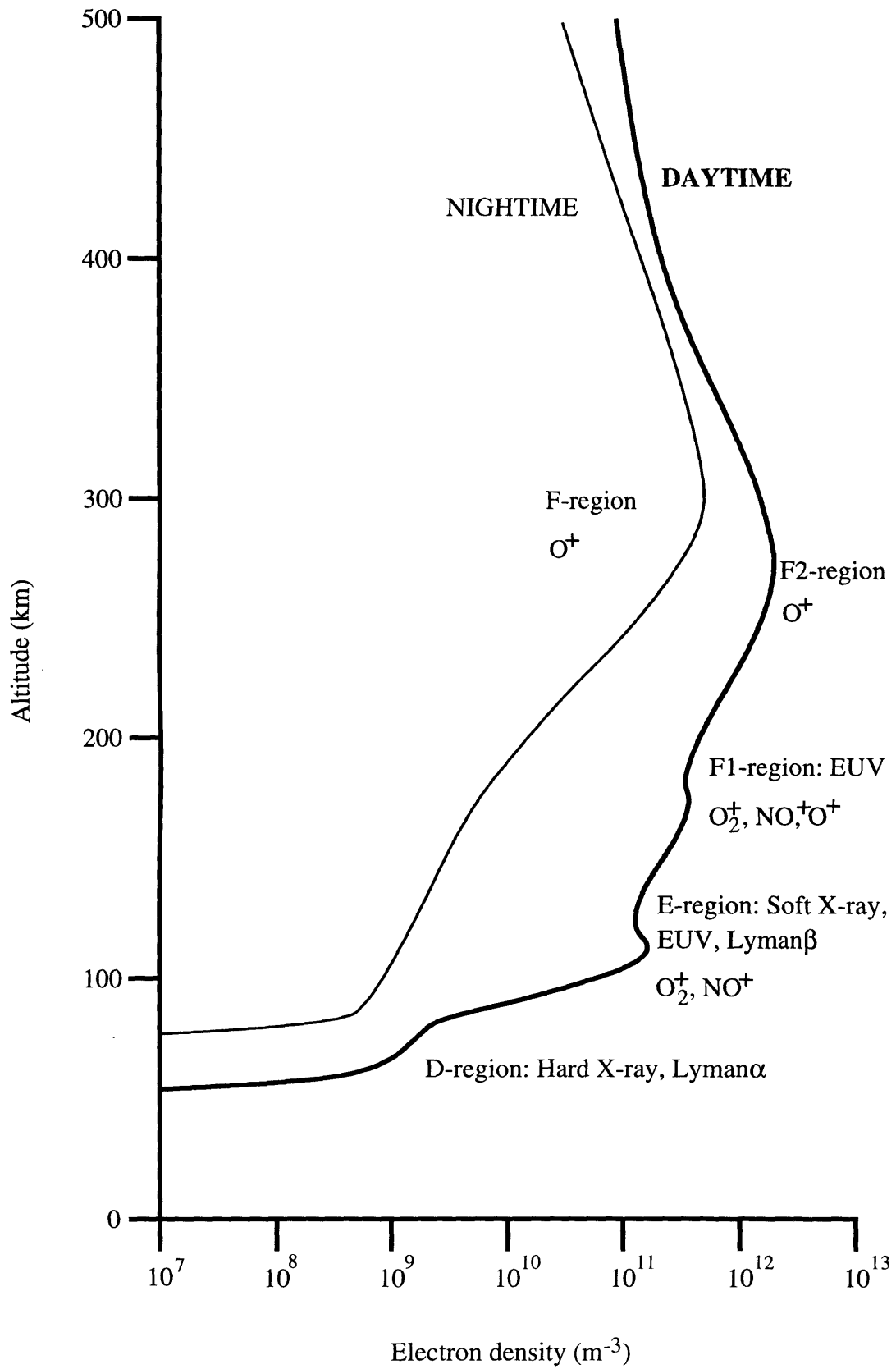


Figure 1.4 Typical mid-latitude ionospheric electron density profiles for moderate solar activity.

ionospheric O^+ and H produces H^+ ions that diffuse upward to the protonosphere. Return flow of H^+ on the night-side supplies the F2 ionosphere with O^+ ions via the reverse reaction. Hence, the topside F2 layer and protonosphere are coupled via ion flow along geomagnetic field lines.

1.2.3 The High-Latitude Ionosphere

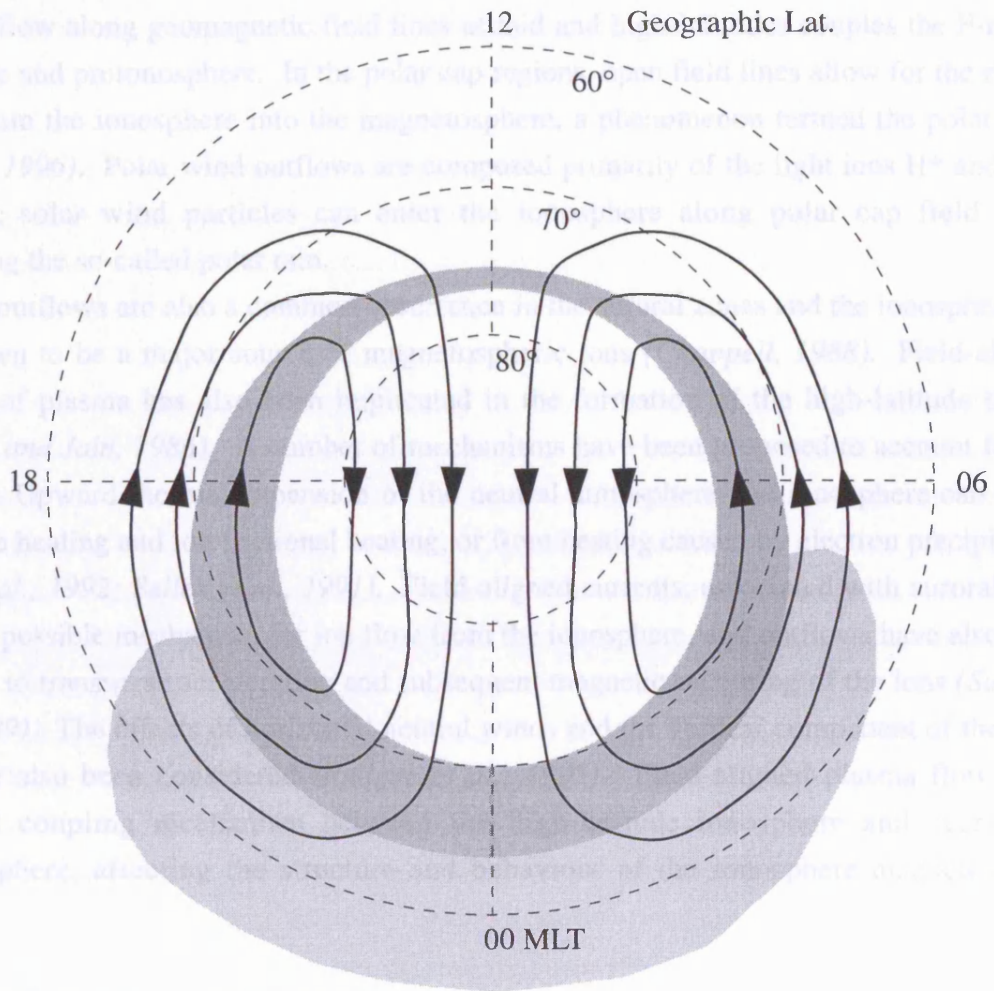
At latitudes greater than about 60° , the behaviour and structure of the ionosphere is principally governed by magnetospheric processes. Convection electric fields in the magnetosphere are mapped along geomagnetic field lines into the high-latitude ionosphere. The effects of electric fields in the ionosphere depend largely on altitude. At all ionospheric altitudes, the gyrofrequencies of the electrons are far greater than their collision frequencies. Consequently, the electrons are free to move with the $\mathbf{E} \times \mathbf{B}$ drift, where \mathbf{E} represents the external electric field and \mathbf{B} the geomagnetic flux density. Below about 150-km altitude, however, ion-neutral collision frequencies are large enough such that the geomagnetic field has no discernible effect on ion motions, hence the ions are driven in the direction of the external electric field. The differential ion-electron motion constitutes the electrojet current, which is coupled to the magnetosphere through geomagnetic field-aligned currents. Beyond about 150-km altitude, decreasing ion-neutral collision frequencies allow ions to flow with the $\mathbf{E} \times \mathbf{B}$ drift. Thus at F-region heights and above the ionospheric plasma experiences bulk motion driven by electric potentials that originate in the magnetosphere. In general, the ionospheric plasma moves antisunward over the poles and returns at lower geographic latitudes. The resulting twin-cell convection pattern is schematically illustrated in Figure 1.5. Electric potential differences in the high-latitude, F-region ionosphere can exceed 100 mV m^{-1} , sufficient to generate ion-neutral relative velocities in excess of 1 km s^{-1} . Ion-neutral relative motion results in frictional heating of the ions, leading to modification of the chemical composition of the ionosphere through increased recombination of O^+ (*Rees and Walker, 1968; St.-Maurice and Torr, 1978*). The formation of the main ionospheric trough, a region of depleted density in the nightside high-latitude ionosphere, is in part attributed to chemical modification due to ion frictional heating. The approximate location of the high-latitude trough is illustrated in Figure 1.5. Large electric fields can also heat the neutral atmosphere, predominantly at E-region altitudes, through Joule heating.

Heating of the ionized and neutral atmospheres through the action of electric fields is an important mechanism of energy exchange between the magnetosphere and high latitude ionosphere. The magnetosphere-ionosphere system is also coupled through the exchange of charged particles, which flow readily along geomagnetic field lines. Energetic electron precipitation into the high-latitude ionosphere is a common occurrence, giving rise to the visible aurora. Auroral electrons originate in the plasma sheet (see Figure 1.2) and are accelerated along field lines, to energies of between approximately 100 eV and 10 keV, into the latitudinally confined auroral ovals. The northern hemisphere auroral region, illustrated in

Figure 1.5, is centered on the geomagnetic poles and typically extends to around 65° latitude on the nightside, penetrating further equatorward with increasing geomagnetic activity (Feldstein and Galperin, 1985). Auroral precipitation leads to increased ionization, heating both the ionosphere and neutral atmosphere, and can also enhance the effect of ionic heating in the E-region through increased conductivities.

Ion flow along geomagnetic field lines into and out of the H-region ionosphere and protonosphere. In the polar cap region, the field lines allow for the escape of ions from the ionosphere into the magnetosphere, a phenomenon termed the polar wind (Ganguli, 1996). Polar wind outflows are composed primarily of the light ions H^+ and He^+ . Similarly, solar wind particles can enter the ionosphere along polar cap field lines, constituting the so-called polar cusp.

Ion outflows are also associated with the formation of the ionospheric lens often shown to be a ring-shaped structure in the ionosphere (Stern, 1988). Field-aligned transport of plasma from the ionosphere into the magnetosphere through high-latitude trough (Williams and Lee, 1991) and low-latitude trough (Stern and Lee, 1991) can account for ion outflows. Ionospheric convection patterns are also associated with auroral precipitation (Jones et al., 1992). The auroral precipitation is associated with neutral atoms, provide a possible mechanism for the formation of the ionospheric lens. The ionospheric lens has also been attributed to transient ionospheric modifications (Stern et al., 1989). The ionospheric lens is a ring-shaped structure in the ionosphere. The ionospheric lens is an important coupling mechanism between the ionosphere and the magnetosphere, affecting the ionospheric convection pattern.



-  Main Trough
-  Auroral Oval
-  Ionospheric Convection

Figure 1.5 Schematic representation of the ionospheric twin-cell convection pattern. The typical positions of the main ionospheric trough and auroral oval are also illustrated.

Figure 1.5, is centred on the geomagnetic poles and typically extends to around 65° latitude on the nightside, penetrating further equatorward with increasing geomagnetic activity (*Feldstein and Galperin, 1985*). Auroral precipitation leads to increased ionization, heating both the ionosphere and neutral atmosphere, and can also enhance the effect of Joule heating in the E-region through increased conductivities.

Ion flow along geomagnetic field lines at mid and high-latitudes couples the F-region ionosphere and protonosphere. In the polar cap regions, open field lines allow for the escape of ions from the ionosphere into the magnetosphere, a phenomenon termed the polar wind (*Ganguli, 1996*). Polar wind outflows are composed primarily of the light ions H^+ and He^+ . Similarly, solar wind particles can enter the ionosphere along polar cap field lines, constituting the so-called polar rain.

Ion outflows are also a common occurrence in the auroral zones and the ionosphere has been shown to be a major source of magnetospheric ions (*Chappell, 1988*). Field-aligned transport of plasma has also been implicated in the formation of the high-latitude trough (*Williams and Jain, 1986*). A number of mechanisms have been proposed to account for ion outflows. Upward thermal expansion of the neutral atmosphere and ionosphere can result from Joule heating and ion frictional heating, or from heating caused by electron precipitation (*Jones et al., 1992; Sellek et al., 1991*). Field-aligned currents, associated with auroral arcs, provide a possible mechanism for ion flow from the ionosphere, and outflows have also been attributed to transverse acceleration and subsequent magnetic mirroring of the ions (*Suvanto et al., 1989*). The effects of horizontal neutral winds and the vertical component of the \mathbf{ExB} drift have also been considered (*Rodger et al., 1992*). Field-aligned plasma flow is an important coupling mechanism between the high-latitude ionosphere and near-Earth magnetosphere, affecting the structure and behaviour of the ionosphere-magnetosphere system.

1.4 Radar Measurements of the Ionosphere

One of the most widely employed methods of ground-based remote sensing of the ionosphere is that of incoherent scatter (IS) (*Beynon and Williams, 1978*). Incoherent scatter radars, operating at VHF and UHF, rely on the quasi-coherent scatter of radiation by acoustic waves in the ionosphere. Analysis of IS allows for the derivation of ionospheric electron density, ion and electron temperatures and ion velocity along the line-of-sight of the radar. In addition, a number of other parameters may be obtained from IS measurements when suitable assumptions are made.

The present thesis is based primarily on observations obtained by the European Incoherent Scatter (EISCAT) facility (*Rishbeth and Williams, 1985*). The EISCAT system, located in northern Scandinavia, comprises a monostatic VHF radar and a tristatic UHF system. The latter allows for measurement of vector velocities in the volume of intersection of the three receiver beams. The different operating frequencies of the two systems allows for

observations within different altitude regions in the ionosphere. The theory of incoherent scatter, with particular reference to the EISCAT facility, is discussed in more detail in *Chapter 3*.

1.5 Aims of the Present Study

Ionospheric ion upflows are an important mechanism in the coupling of the ionosphere-magnetosphere system. Satellite and radar observations of the high-altitude, high-latitude ionosphere have revealed the presence of a wide variety of outflowing ion species. Measurements at lower altitudes have demonstrated that upflowing ion fluxes can exceed those observed in the magnetosphere, indicating that the ionosphere actively supplies ions to the magnetosphere. Furthermore, it has been suggested that the ionosphere alone might be a sufficient source of plasma for the magnetosphere, without the need for a solar wind contribution.

This thesis presents three complementary studies of ion upflows in the high-latitude, F-region ionosphere. The work is based upon observations from the EISCAT facility. A case study of three upflow events is presented in *Chapter 4*, highlighting some of the energization processes that can occur at different altitudes to generate field-aligned ion flow. A synoptic study of upflows based upon several years' worth of observations is documented in *Chapter 5*. The study illustrates the variation in upflow characteristics as a function of universal time (UT), altitude, season and solar and geomagnetic activity. The relationship between upflows and ion frictional heating in the high-latitude F-region is also quantitatively examined. Finally, *Chapter 6* presents a more detailed investigation of an upflow event, employing a simple one-dimensional approximation to the ion momentum balance equation. The study examines the ability of the model to account for the observed ion velocities, exploring the relative importance of plasma pressure, gravity, neutral wind, magnetic mirror force and thermal diffusion on the field-aligned ion momentum. It is also demonstrated that the ion composition is a vital factor if the observations are to be accurately modelled.

These studies shed further light on the nature of upflows in the high-latitude ionosphere. In particular, the results of the statistical study clearly indicate that the occurrence frequencies, velocities and fluxes of upflows are strongly dependent not only on UT and season, as has been demonstrated previously, but also on solar cycle. The modelling study, in addition to examining the relative importance of various acceleration mechanisms in a particular event, also questions the validity of such simple models.

CHAPTER 2

Ion Upflows in the High-Latitude F-region and Topside Ionosphere: Review and Theory

2.1 Introduction

Since the time of the earliest observations of heavy ions in the magnetosphere, numerous spacecraft and radar data have demonstrated that the ionosphere is an important source of magnetospheric plasma. Ion outflow along open geomagnetic field-lines in the polar caps, termed the polar wind, is a well documented phenomenon. Outflows are also commonly detected in the auroral regions. In recent years, radar and spacecraft observations of the high-latitude, F-region and topside ionosphere have revealed that heavy ion upflows are not simply a response to a magnetospheric requirement; rather, the ionosphere actively supplies the magnetosphere with plasma. This chapter describes the physical processes that can generate ion upflows in the high-latitude F-region and topside ionosphere. The discussion considers the theory, modelling and observations of these phenomena. Particular reference is made to radar observations in the northern hemisphere auroral region.

2.2 Observations of Heavy Ions in the Magnetosphere

Until the early 1970's, the Sun, solar wind and cosmic rays were thought to be the dominant source of magnetospheric plasma. Magnetospheric particles were observed to possess energies of order keV, whilst the energies of ionospheric particles were much less, of order eV. Hence it was generally believed that the dominant sources of magnetospheric plasma were extraterrestrial (*Chappell 1988*). Recognition of the ionosphere as a source of magnetospheric ions came with observations of the heavy ions He^+ and O^+ in the auroral zone with energies in excess of 1 keV (*Shelley et al., 1972*), and the discovery of heavy ions at magnetospheric altitudes (*Sharp et al. 1974, Johnson et al., 1974*). Over recent years, numerous satellite and rocket observations have demonstrated that the ionosphere is an important source of magnetospheric ions (eg. *Young et al., 1977; Ungstrup et al., 1979; Ghielmetti et al., 1978; Lockwood, 1982; Heelis et al., 1984; Lu et al., 1992; Arnoldy et al., 1992*). *Chappell (1988)* presented a comprehensive study of the importance of the terrestrial plasma source, based largely on data from the Dynamics Explorer 1 (DE-1) satellite. The author concluded that ion outflows can consist of particles with masses ranging from 1 to 32 amu, with energies between 1 eV and 10 keV. The total strength of the ionospheric source of magnetospheric ions was estimated by Chappell to be around $3.5 \times 10^{26} \text{ s}^{-1}$, primarily comprising H^+ , He^+ and O^+ ions. Chappell compared this figure with the estimated maximum solar wind input available from sub-solar reconnection, some $1.4 \times 10^{27} \text{ s}^{-1}$ (*Cowley, 1980*), and the solar wind flux of approximately $7 \times 10^{26} \text{ s}^{-1}$ that may enter through the flanks of the magnetotail (*Eastman et al., 1985*), arguing that the ionospheric input is at least comparable with these other sources. *Chappell et al. (1987)* even suggested that the

ionosphere alone is an adequate source of plasma for the magnetosphere, although *Chappell (1988)* stated a belief that plasma of both ionospheric and solar wind origin contribute to the magnetospheric plasma.

Ionospheric outflows are generally categorized according to one of four sources, these being the polar wind, the cleft ion fountain, the polar cap and the auroral zone (*Chappell, 1988*). The characteristics of these sources will be briefly discussed in the following section. Particular attention will be paid to auroral zone outflows and upflows, as these phenomena constitute the subject of this thesis.

2.2.1 The Polar Wind

The polar wind describes the escape of light ions, mainly H^+ and He^+ , along the open geomagnetic field-lines of the polar caps. The outflow is driven primarily by diffusion. The polar wind was first studied by *Banks and Holzer (1968)* and *Axford (1968)*. *Hoffman (1970)* presented the first observational evidence of the polar wind, detected as He^+ fluxes of order $1 \times 10^{12} \text{ m}^{-2} \text{ s}^{-1}$ above 250-km altitude. DE-1 observations of both H^+ and He^+ in the polar wind, between 65° and 81° ILAT (invariant latitude) at magnetospheric altitudes of order $2 R_E$, were reported by *Nagai et al. (1984)*. Heavy ions (O^+) with energies of less than 10 eV have also been detected in the polar wind by the S3-3 satellite near the auroral oval (*Shelley et al., 1976; Ghielmetti et al., 1978*).

The polar wind has been extensively modelled over the years, formerly using steady state approximations (eg. *Banks and Holzer, 1969a, b*). More recently, a number of time-dependent models have more accurately described the polar wind behaviour, including the presence of heavy ion outflows (*Gombosi et al., 1985; Gombosi and Killeen, 1987; Schunk and Sojka, 1989; Gombosi and Nagy, 1989; Ho et al., 1991*). *Abe et al. (1993)* presented a statistical study of polar wind outflows based on Akebono satellite observations. Figure 2.1, taken from *Abe et al. (1993)*, illustrates averaged parallel velocity distributions for H^+ , He^+ and O^+ as a function of magnetic local time and invariant latitude between 60° and 88° . The figure shows that, in general, stronger outflows are present at high latitudes and parallel velocities tend to decrease with increased ion mass. It is also noted that enhanced flows are evident within the auroral region, at around 68° ILAT on the night-side and 74° ILAT on the day-side as a result of auroral zone energization (see section 2.2.4).

In summary, the polar wind is typically characterized by light ion outflow, with H^+ fluxes of order $1 \times 10^{12} \text{ m}^{-2} \text{ s}^{-1}$ at energies of 1-2 eV and an He^+ content of between 1 and 10% at a few eV (*Chappell, 1988*). A comprehensive review of polar wind observations and theories has been presented by *Ganguli (1996)*.

2.2.2 The Cleft Ion Fountain

In addition to the light ions of the classical polar wind, heavy ion (O^+) outflows are also observed along polar cap field lines. Among the first such measurements were made by the

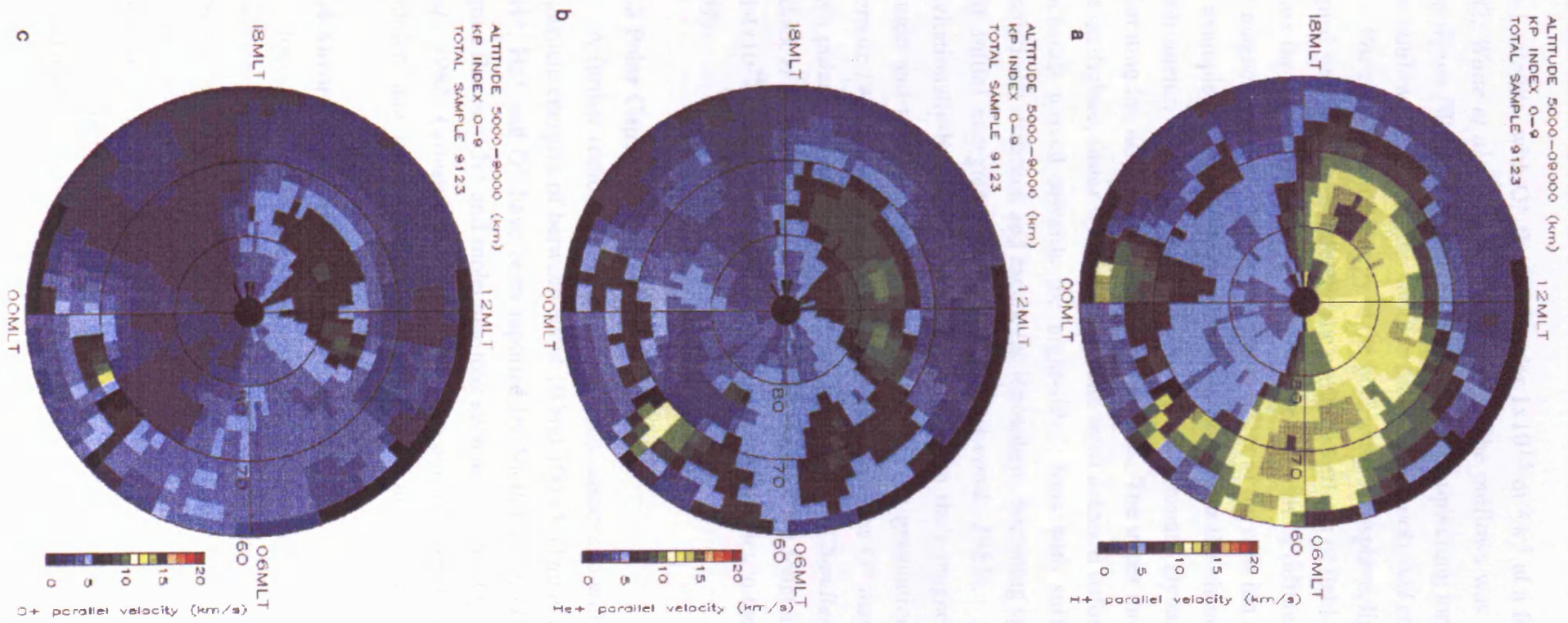


Figure 2.1 Polar plots of averaged parallel ion velocity as a function of invariant latitude and magnetic local time for (a) H⁺, (b) He⁺ and (c) O⁺. Derived from EXOS D satellite observations between February and September, 1990 and between March and August, 1991 (Abe *et al.*, 1993).

DE-1 satellite, with O^+ fluxes of order $1 \times 10^{13} \text{ m}^{-2} \text{ s}^{-1}$ at a few eV reported (*Shelley et al., 1982; Waite et al., 1985*). The source for the outflows was identified as the dayside polar cusp region (*Waite et al., 1985*), from where the upwelling ions convected into the polar cap. This outflow was termed the cleft ion fountain by *Lockwood et al., (1985a, c)*.

For a given initial energy in the polar cusp ionosphere, lighter ions attain a greater field-aligned velocity. Consequently, the combined effects of field-aligned motion and convection across the polar cap result in the dispersion of ions of different masses across the polar cap and magnetosphere. This characteristic effect of the cleft ion fountain has been observed by, for example, *Lockwood et al. (1985b)*, who termed the phenomenon the geomagnetic mass spectrometer. Figure 2.2 (*Chappell, 1988*) presents Dynamics Explorer 1 observations illustrating ion dispersion across the polar cap. The upper three panels of the figure indicate that the lighter, faster upflowing H^+ ions were detected before the He^+ and O^+ ions, as the spacecraft moved towards the night-side. Ions with sufficient energy will overcome gravitational attraction and escape the ionosphere, becoming spatially dispersed depending on their initial energies (*Horwitz and Lockwood, 1985*). Alternatively, lower energy, gravitationally-bound ions may “hop” between their magnetic mirror points at the lower altitude and the limit of their trajectories in the gravitational field at the upper altitude (*Horwitz 1984; Delcourt et al., 1988*). Thus at times O^+ may be seen to move both up and down polar cap field lines (*Chandler et al., 1991; Chandler 1995*). *Chappell (1988)* and *Pollock et al. (1990)* have estimated that the cleft ion fountain supplies between about 10^{25} and 4×10^{25} ions s^{-1} to the magnetosphere, with energies in the range 1 to 20 eV (*Giles et al., 1994*).

2.2.3 Polar Cap Outflows

A further source of ionospheric outflow associated with the polar cap is characterized by particle energies of between about 10 and 100 eV (*Yau et al., 1985*). Polar cap outflows of H^+ , He^+ and O^+ have been reported by *Shelley et al. (1982)*. In addition, lesser field-aligned fluxes of N^+ and molecular ions such as N_2^+ and O_2^+ have been observed (*Chappell et al., 1982; Craven et al., 1985*). These outflows tend to occur during more disturbed conditions and may be associated with the cleft ion fountain (*Chappell, 1988*).

2.2.4 Auroral Zone Outflows

Ionospheric ions with energies of order keV were first detected within the auroral zone (*Shelley et al., 1972*). Subsequently, a number of satellite observations have indicated the presence of ionospheric ions within this region at energies of order 10 eV to 10 keV, at altitudes between about 1000 km and several Earth radii. Auroral zone ion outflows are generally characterized according to the ion pitch angle, being described as either field-aligned “ion beams” or confined pitch-angle “ion conics” (eg. *Shelley et al., 1976; Lockwood, 1982; Lu et al., 1992*). For example, *Ungstrup et al. (1979)* reported ISIS-2 observations of

DE 1-RIMS:

U.T.	09:45	10:00	10:15	10:30	10:45	hrs:mns.
r	3.85	4.08	4.27	4.42	4.54	R _E
MLT	9.9	10.0	10.2	10.4	10.6	hrs.
λ	71.1	74.0	76.7	79.1	81.3	deg.

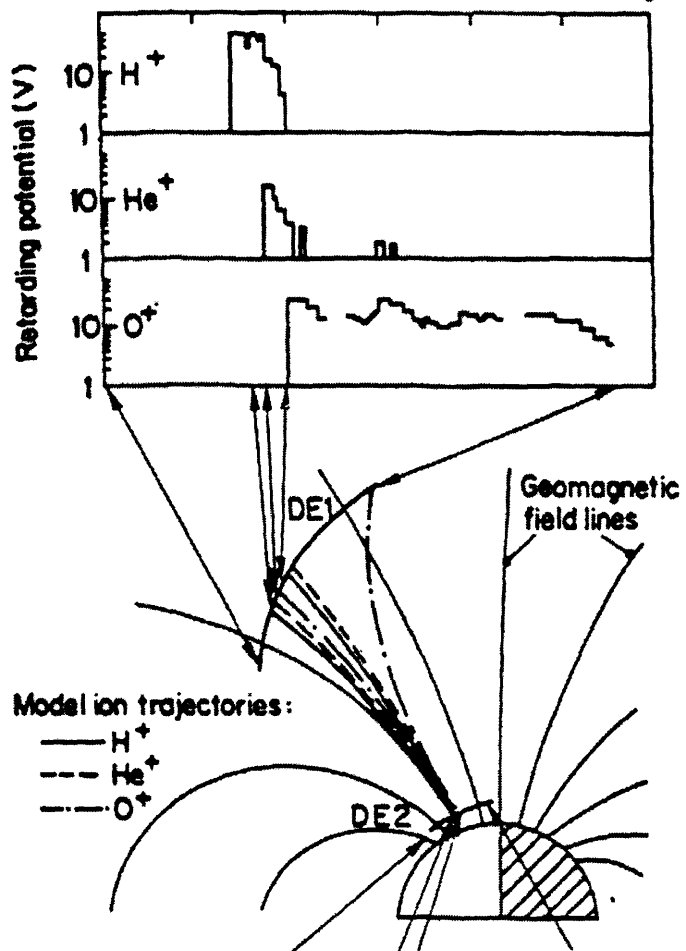


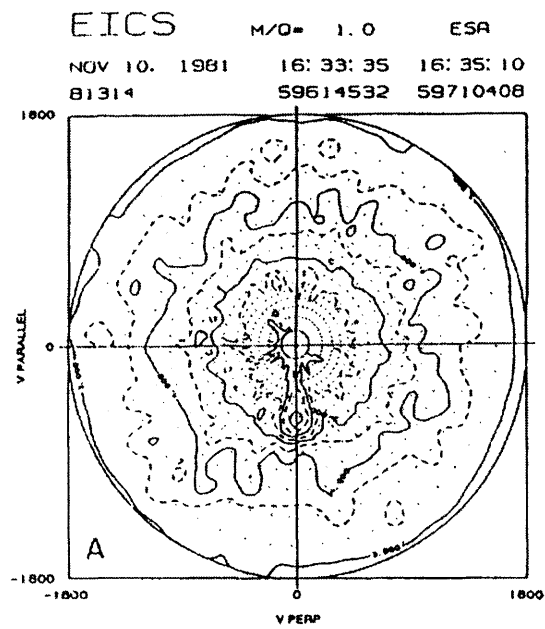
Figure 2.2 An illustration of mass dispersion across the polar cap, the geomagnetic mass spectrometer. The upper three panels show the sequential encounter of H⁺, He⁺ and O⁺ by DE-1 as it moved toward the night-side polar cap (*Chappell, 1988*).

ion conics at 1400-km altitude with pitch angles between 90° and 135° . Ungstrup and co-authors indicated that these ion conics were usually detected near the boundaries of the auroral oval. *Lu et al. (1992)* presented near-simultaneous DE-1 and DE-2 observations, from about 700 and 12000-km respectively, of low energy (< 5 eV) O^+ ion conics at the lower altitude and high energy (~ 100 eV) ion beams at the higher altitude. A number of studies (eg. *Yau et al., 1984; Heelis et al., 1984; Lockwood et al., 1985c*) have demonstrated that ion conics are initiated at lower altitudes, around 1000 km, than ion beams, and the ions are accelerated upwards by the magnetic mirror force to altitudes where parallel acceleration occurs, at perhaps $1 R_E$ and above.

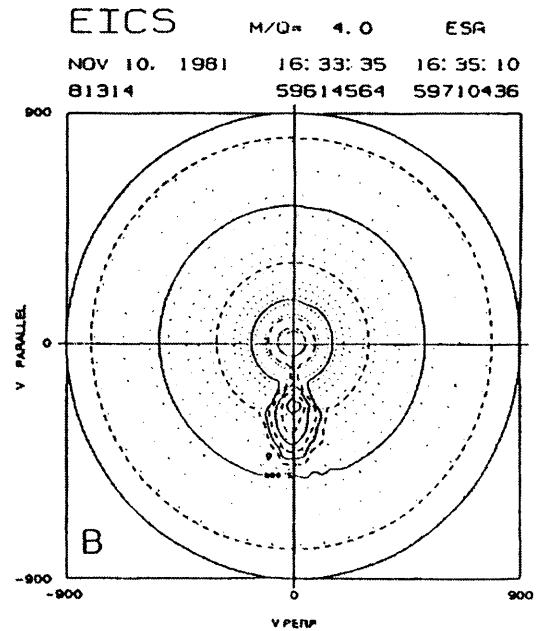
The sources of parallel electric fields along auroral field-lines and their role in the generation of ion beams has been addressed by a number of authors, as summarized by *Horwitz (1982)*. Parallel electric fields of the order 1 V m^{-1} near $1 R_E$ have been reported by, for example, *Mozer et al. (1977)*. Parallel electric fields are associated with field-aligned auroral electron beams. It was argued by *Horwitz (1982)* that the same fields could accelerate ions out of the ionosphere. This scenario is consistent with numerous observations of ion beams at auroral latitudes (eg. *Ghielmetti et al., 1978; Lu et al., 1992*). For example, Figure 2.3 illustrates velocity-space contours for H^+ , He^+ and O^+ measured by DE-1 at approximately 700-km altitude (*Lu et al., 1992*). The beam-like distributions, most clearly seen for He^+ and O^+ , indicate acceleration through an upward electric field at auroral latitudes. Statistical analyses suggest that ion beams are observed predominantly over the auroral zone (*Ghielmetti et al., 1978*).

The presence of outflows with constrained pitch angle distributions (ion conics) indicates transverse heating of the ions, that in turn points to the existence of perpendicular electric fields (*Sharp et al., 1977*). Energization can result from resonant interaction of the ions with electrostatic ion acoustic and ion cyclotron waves (*Ungstrup et al., 1979; Norqvist et al., 1996*) or with lower hybrid waves (*Chang and Coppi, 1981; Retterer et al., 1994*). The waves may be generated by local plasma instabilities; for example, ion cyclotron waves are unstable to field-aligned current strengths that are often detected at auroral latitudes (*Kindel and Kennel, 1971; Forme et al., 1993*). These and a number of other transverse acceleration mechanisms, and the processes believed to produce them, are addressed by *Crew et al. (1990)* and *Moore et al. (1996)*. *Gorney et al. (1981)* found that the occurrence of ion conic distributions was less dependent on altitude than that of ion beams, and that during quiet periods conics were formed mainly at altitudes between 1000 and 2000-km altitude, below where ion beams are typically observed. These findings are again consistent with observations of, for example, *Klumpar (1979), Heelis et al. (1984), Yau et al. (1984)* and *Lu et al. (1992)*.

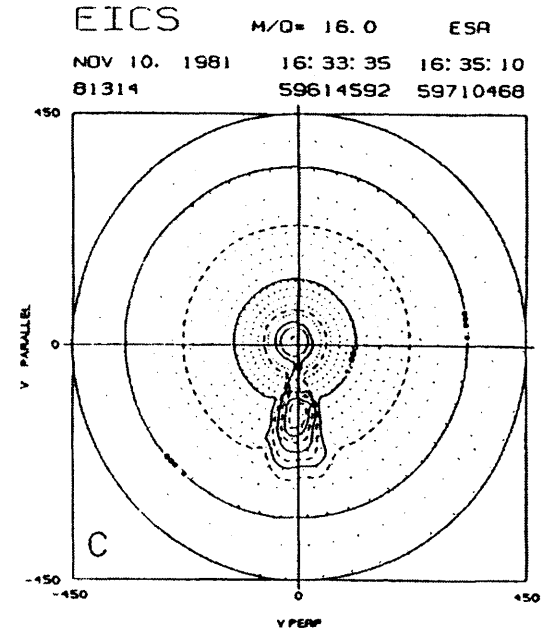
A statistical analysis of S3-3 satellite observations (*Ghielmetti et al., 1978*) indicated that keV O^+ and H^+ outflows occurred approximately 60% of the time within a region corresponding to the statistical auroral oval. Similarly, *Klumpar (1979)* studied ISIS 1



(a)



(b)



(c)

Figure 2.3 Velocity-space contours for (a) H^+ , (b) He^+ and (c) O^+ at approximately 700-km altitude, measured by DE-1 (*Lu et al., 1992*).

and 2 data, concluding that transverse ion acceleration and subsequent outflow was predominantly a winter, night-side, auroral zone phenomenon, with an occurrence probability of over 50% at certain times at 1400-km altitude (Figure 2.4). During Summer and at altitudes above 2750 km, Klumpar found a preponderance of transverse ion acceleration events within the dayside cleft region. *Lockwood et al. (1985c)* and *Pollock et al. (1990)* have arrived at similar conclusions. *Yau et al. (1984)* examined outflow characteristics derived from DE-1 data acquired between 8000 and 23000-km altitude. These authors found that the distribution for H^+ and O^+ outflows was auroral-oval-like, and that conic distributions for both ion species exhibited a dawn-dusk asymmetry in favour of the dusk sector. These findings were comparable with those of *Ghielmetti et al. (1978)*. Moreover, Yau and co-workers indicated that the occurrence frequency of O^+ conics was dependent on magnetic activity. In summary, there is ample evidence of both transverse and parallel acceleration of cold ionospheric ions within the auroral zone, resulting in outflow to magnetospheric altitudes.

A number of sounding rocket observations of auroral ion outflows appear in the literature, for example *Kintner et al. (1986)* and *Retterer et al. (1994)*. *Arnoldy et al. (1992)* presented TOPAZ 3 observations from 1100-km altitude of heating of O^+ and H^+ to energies of order 10 eV, which they attributed to transverse heating by lower hybrid waves in the region above an aurora. These authors further concluded that transverse acceleration of ions is a common occurrence above aurorae. Notably, *Whalen et al. (1978)* reported low energy O^+ fluxes with near-90° pitch angle at altitudes of around 500 km, indicating that transverse acceleration mechanisms may operate at relatively low altitudes.

In summary, satellite and rocket observations of ion outflow from the auroral ionosphere have steadily increased in number since the early 1970s. In particular, data from the Dynamics Explorer satellites have indicated several source regions, capable of populating the magnetosphere with a significant proportion of ionospheric ions. A number of different acceleration processes appear to operate at different points along geomagnetic field-lines (*Sagawa et al., 1991*), from topside ionospheric altitudes out to several Earth radii. Particle energies ranging from a few eV to several keV are observed, and an extensive data base has allowed for evaluation of outflow occurrence probabilities. Satellites and rockets have mapped large areas of the high-latitude topside ionosphere and magnetosphere, but generally do not observe down to F-region heights. Thus the low-altitude response to topside outflows was uncertain until the advent of ground-based radar observations in the auroral F-region ionosphere.

In order to distinguish between flows which exceed the gravitational escape energy, which for O^+ is approximately 10 eV, with those less energetic field-parallel flows that might not escape the ionosphere, the term “upflows” will be used from hereon to refer to the latter, regardless of energy or velocity (*Loranc and St.-Maurice, 1994*). These upflows consist primarily of O^+ , since that is generally the dominant ion in the ionosphere above about

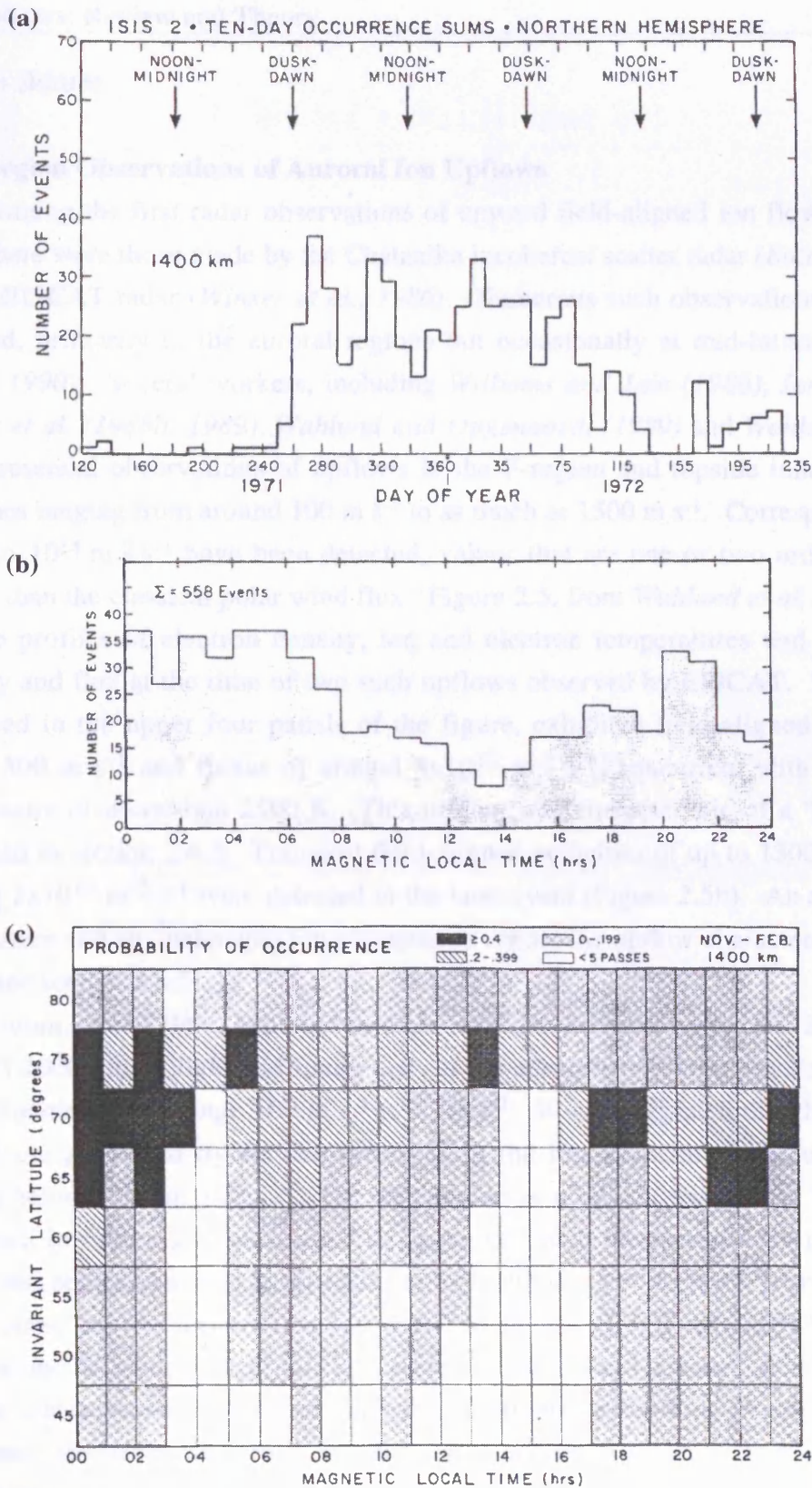


Figure 2.4 (a) Ten-day occurrences for transversely accelerated ion (TAI) events in the northern hemisphere between day 120 of 1971 and day 255 of 1972, derived from ISIS 2 measurements at 1400-km altitude. A total of 558 events were detected, most of which occurred during the winter months. (b) One-hour occurrence sums of TAI's at 1400-km altitude in the northern hemisphere, derived from the same measurements as panel (a). TAI's favour the 12 hours centred on magnetic midnight. (c) Occurrence probability of TAI's at 1400-km between November 1971 and February 1972 as a function of invariant latitude and magnetic local time (*Klumpar, 1979*).

150-km altitude.

2.3 F-region Observations of Auroral Ion Upflows

Among the first radar observations of upward field-aligned ion flows in the F-region ionosphere were those made by the Chatanika incoherent scatter radar (*Bates, 1974*) and later by the EISCAT radar (*Winser et al., 1986*). Numerous such observations have since been reported, primarily in the auroral regions but occasionally at mid-latitudes (eg. *Yeh and Foster 1990*). Several workers, including *Williams and Jain (1986)*, *Jones et al. (1988)*, *Winser et al. (1988b, 1989)*, *Wahlund and Opgenoorth (1989)* and *Wahlund et al. (1992)*, have presented observations of upflows in the F-region and topside ionosphere, with ion velocities ranging from around 100 m s^{-1} to as much as 1500 m s^{-1} . Corresponding ion fluxes of up to $10^{14} \text{ m}^{-2} \text{ s}^{-1}$ have been detected, values that are one or two orders of magnitude greater than the classical polar wind flux. Figure 2.5, from *Wahlund et al. (1992)*, illustrates altitude profiles of electron density, ion and electron temperatures and field-aligned ion velocity and flux at the time of two such upflows observed by EISCAT. The earlier event, displayed in the upper four panels of the figure, exhibited field-aligned ion velocities of nearly 500 m s^{-1} and fluxes of around $8 \times 10^{13} \text{ m}^{-2} \text{ s}^{-1}$, concurrent with an enhanced ion temperature of more than 2500 K. This upflow was characteristic of a “type 1” event, as discussed in section 2.4.3. Transient field-aligned velocities of up to 1300 m s^{-1} and fluxes nearing $2 \times 10^{14} \text{ m}^{-2} \text{ s}^{-1}$ were detected in the later event (Figure 2.5b). An enhanced electron temperature and an unchanged ion temperature render the upflow characteristic of a “type 2” event (see section 2.4.5).

Loranc et al. (1991) analysed vertical ion drifts detected by the DE-2 satellite between 200 and 1000-km altitude and found that, in the auroral zone, flows tended to be upwards, with velocities in the range 100 m s^{-1} to 3 km s^{-1} . It was suggested that these large upward flows were generated by sudden increases in the ion temperature through ion frictional heating below 500-km altitude. The distribution of upward flows below 1000-km altitude, illustrated in Figure 2.6, was found to agree well with the morphology of outflowing ion beams and conics observed by satellites at high altitudes, most clearly seen in panels (a) and (b). Loranc and co-authors concluded that there is a close connection between F-region upflows and magnetospheric outflow events in the auroral ionosphere. In addition, large vertical velocities were observed more frequently above 600-km altitude than below. The occurrence frequency of vertical ion drifts with speeds exceeding 100 m s^{-1} was seen to be dependent on magnetic activity. Furthermore, the peak occurrence frequency on the night-side was generally smaller than on the day-side. Loranc and co-workers argued that the very large observed drifts were the vertical component of bulk field-aligned flow, and *not* attributable to the vertical component of the \mathbf{ExB} convection. Notably, the upward field-aligned fluxes observed at low-altitudes often *exceeded* those detected in the magnetosphere, implying that ionospheric upflows are not simply a response to higher altitude loss processes;

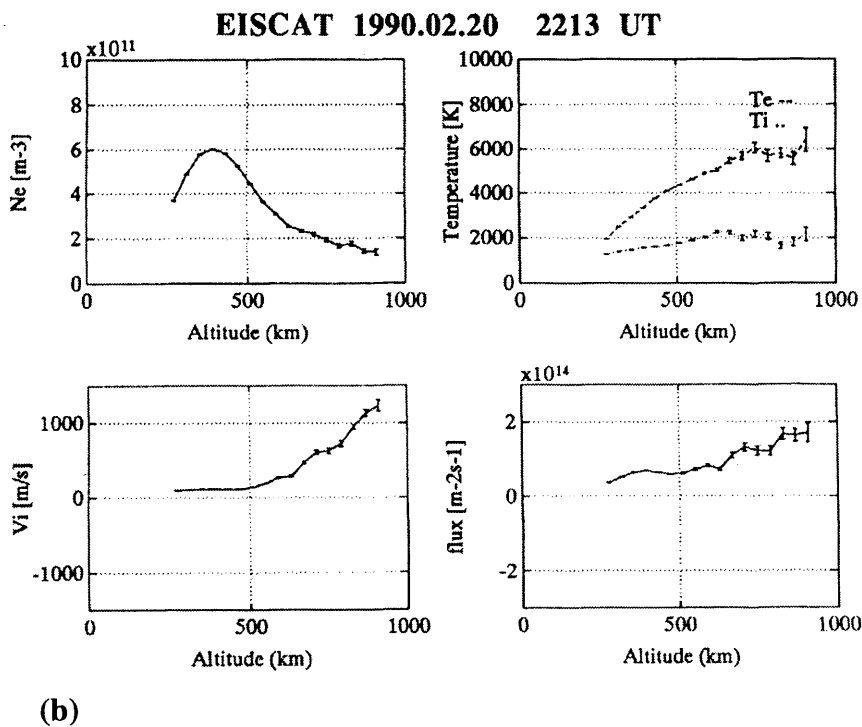
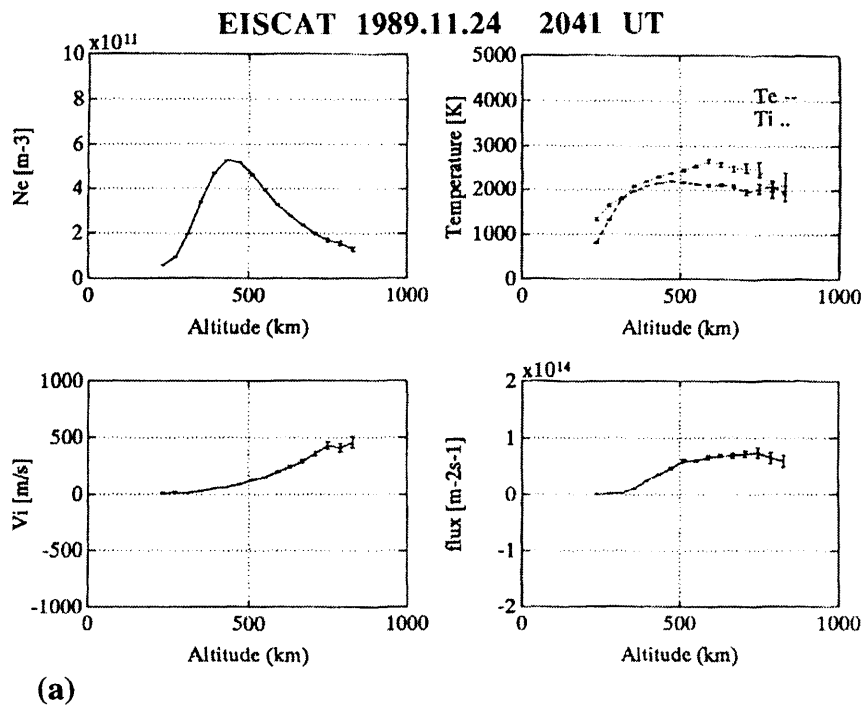


Figure 2.5 Altitude profiles of electron density, electron and ion temperatures, field-aligned ion velocities and field-aligned ion fluxes (positive outward) at the time of (a) a type 1 and (b) a type 2 ion upflow (*Wahlund et al., 1992*).

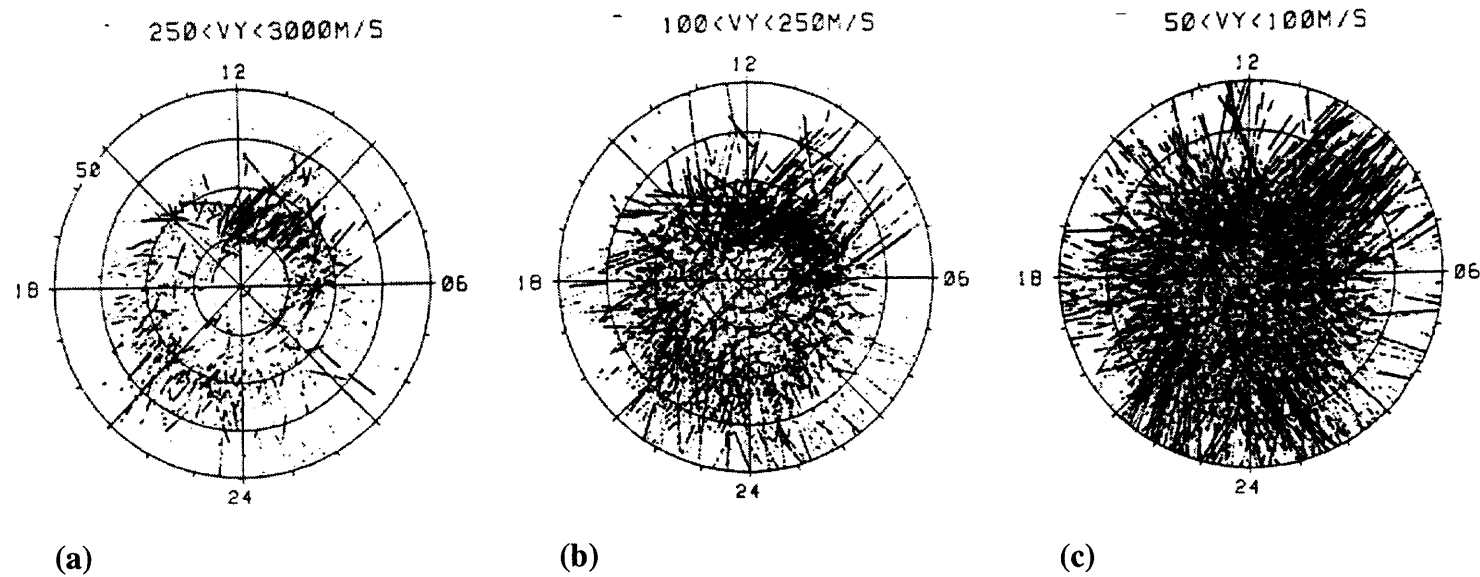


Figure 2.6 Scatter plot of the location of vertical ion drift observations in invariant latitude-magnetic local time coordinates. The lowest latitude shown is 50° . The panels show upward ion drifts with magnitudes in the ranges (a) $250\text{-}3000\text{ m s}^{-1}$, (b) $100\text{-}250\text{ m s}^{-1}$ and (c) $50\text{-}100\text{ m s}^{-1}$ (Loranc *et al.*, 1991).

rather, the F-region and topside actively supply ions to higher altitudes.

A statistical study of large F-region field-parallel flows was presented by *Keating et al. (1990)*. These authors analysed EISCAT Common Programme 1 data collected between 1985 and 1987 and derived seasonal and diurnal distributions of upflow occurrence frequencies for a range of altitudes between 200 and 500 km. An upflow (or downflow) “event” was deemed to have occurred if either the field-aligned ion velocity exceeded 100 m s^{-1} or the flux was greater than $10^{13} \text{ m}^{-2} \text{ s}^{-1}$. These criteria, discussed in more detail in *Chapter 5*, were based on previous observations of field-aligned flows (*Winser et al. 1989*) and theoretical analyses, and are similar to the criteria adopted by *Loranc et al. (1991)*. The diurnal and seasonal upflow occurrence distributions derived by *Keating et al. (1990)* are included as *Figure 2.7*. Keating and co-authors observed that upflows were most frequent during winter and on the night-side at the latitude of EISCAT, with a maximum occurrence at around 2100 UT and above 400-km altitude. Fewer upflows were observed on the day-side, possibly because the auroral oval is then typically at a higher latitude than the EISCAT radar. Keating and co-workers also examined the correlation between the observed flux magnitudes and ion and electron temperatures. *Figure 2.8* illustrates the relationship between upward ion flux at 400-km altitude and ion temperature at 200 km for three ranges of electron temperature at the lower altitude. The vertical line in each panel represents the mean ion temperature at 200-km altitude and 2100 UT wintertime for the period covered by the study. The figure indicates that the number of upflows at 400 km tends to be greater during periods of enhanced ion temperature, exhibiting also a dependence on electron temperature at lower altitudes. Keating and co-authors remarked that more and larger upflows were observed when both ion and electron temperatures were enhanced.

Satellite observations of outflowing O^+ beams and conics, at altitudes in excess of around 1000 km, have been interpreted in terms of parallel and transverse acceleration of the ions. Such acceleration mechanisms are generally considered to be effective at altitudes above about 1000 km, often above auroral arcs. At lower ionospheric altitudes, other acceleration mechanisms become important. For example, *Winser et al. (1988b)* interpreted field-aligned F-region plasma flows of order 100 m s^{-1} in terms of an equatorward neutral wind, thermal expansion of the neutral atmosphere as a result of Joule heating, and enhanced ion diffusion. These processes have been quantitatively considered in numerical models of ion upflow events. The models employed range from single-ion, one-dimensional, steady-state approximations (eg. *Jones et al., 1988*) to multi-ion time dependent approaches (eg. *Bailey and Sellek, 1990; Loranc and St.-Maurice, 1994; Wilson, 1994; Robineau et al., 1996*).

The Sheffield University plasmasphere and ionosphere model (SUPIM) is a typical example of the latter (*Bailey and Sellek, 1990*). The model solves the time-dependent equations of continuity, momentum and energy for a multi-ion plasma in one dimension, that is, along the geomagnetic field direction. SUPIM has been employed by *Sellek et al. (1991)*

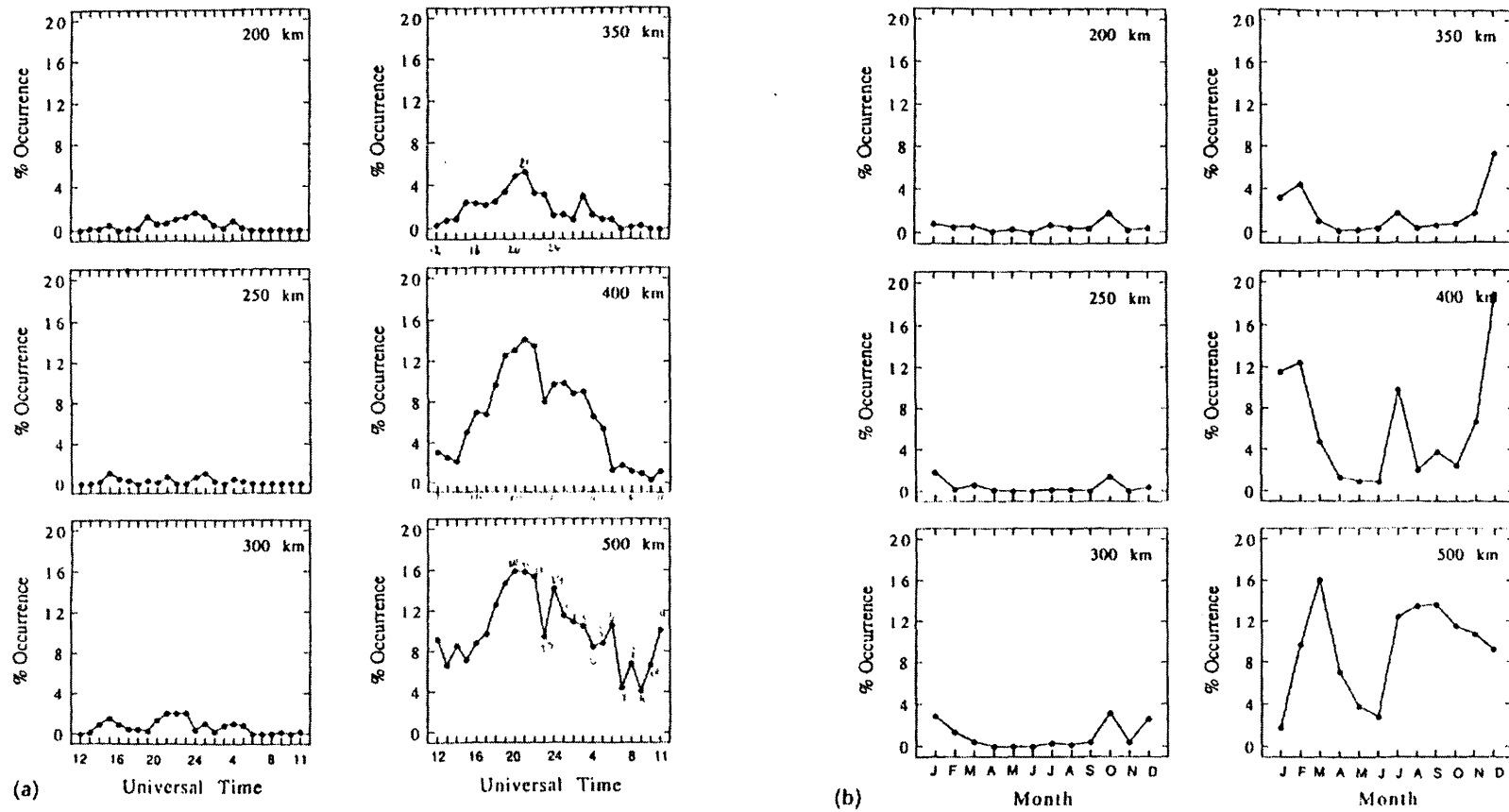


Figure 2.7 (a) Diurnal variation (in hourly bins) of upflow frequency occurrence for six altitude levels between 200 and 500 km. (b) Annual variation (in monthly bins) of upflow frequency occurrence at the same altitudes (*Keating et al., 1991*).

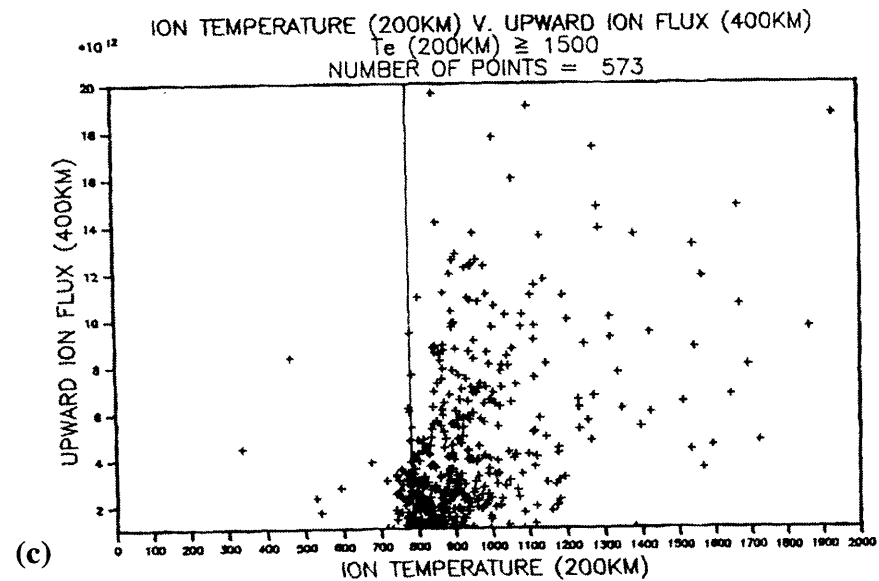
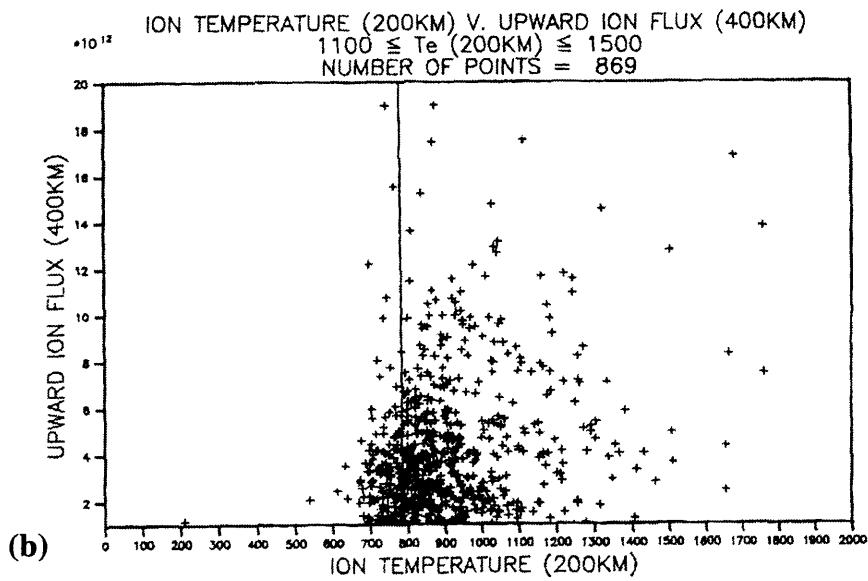
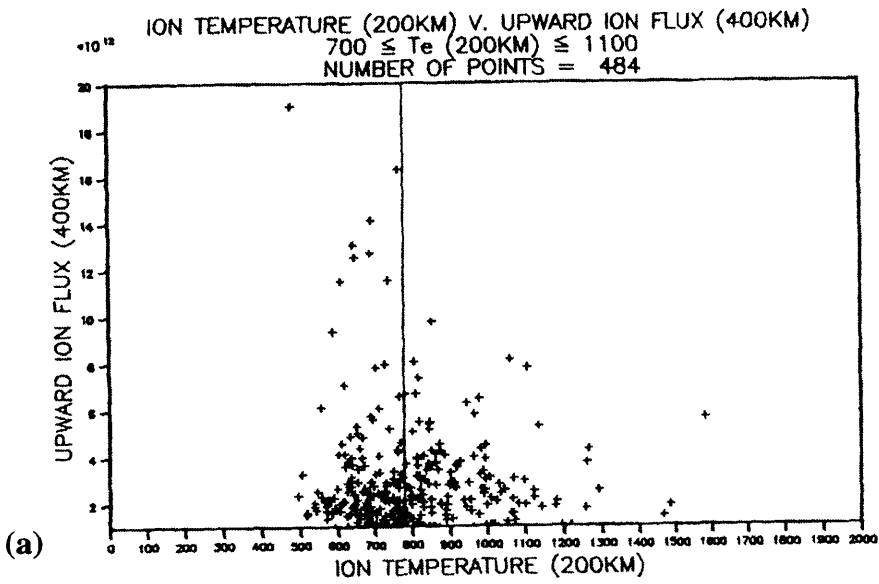


Figure 2.8 Relationship between upward ion flux ($>10^{12} \text{ m}^{-2} \text{ s}^{-1}$) at 400 km with ion temperature for electron temperatures in the range (a) 700-1100 K, (b) 1100-1500 K and (c) > 1500 K (*Keating et al., 1990*).

and *Heelis et al. (1993)* in investigations of field-aligned plasma flows generated by large convection electric fields. These studies are addressed in more detail in section 2.4.3. A similar approach is adopted by the Field Line Interhemispheric Plasma (FLIP) model (*Torr et al., 1990*). The FLIP model has been adapted by *Liu et al. (1995)* in order to simulate satellite observations of topside ion upflows, and by *Caton et al. (1996)* to explain EISCAT observations of F-region ion upflows.

A comparison of two time-dependent fluid models was presented by *Robineau et al. (1996)*. These codes were employed by *Blclly et al. (1996)*, initially in an investigation of the relative importance of ion-frictional heating, heat flux perturbations and upward field-aligned currents in the generation of upflows. The numerical models simulated well the overall characteristics of an ion outflow event observed by the EISCAT VHF radar (*Blclly and Alcaydé, 1994*). *Robineau et al. (1996)* concluded that both models were at least valid between 300 and 1500 km, and provided suitable boundary conditions for kinetic approximations which are required to model processes such as wave-particle interaction and non-Maxwellian velocity distributions at topside and magnetospheric altitudes.

Kinetic models have been described by, for example, *Wilson (1994)* and *Loranc and St.-Maurice (1994)*. The former simulated O⁺ upflows resulting from ion frictional heating in the high-latitude F-region. The results compared favourably with some topside satellite and radar data.

Much simpler models have been employed by some workers to investigate specific upflow events (eg. *Jones et al., 1988*). These approximations generally consider the one-dimensional momentum balance equation along the geomagnetic field direction, for a single ion under steady-state conditions. Using such an approach, *Jones et al. (1988)* reproduced remarkably well the observed velocity profiles during two F-region ion upflow events observed by the EISCAT radar, as illustrated in Figure 2.9. In the figure, the observed velocity values are shown as dots with error bars. The solid line in each panel represents the modelled field-parallel ion velocity, determined from estimates of pressure gradients, frictional drag, the magnetic mirror force and gravity, assuming steady-state flow. *Wahlund et al. (1992)* attempted to interpret EISCAT observations of upflows in a similar manner. These authors compared the magnitude of the available momentum terms, namely pressure gradients, the mirror force and gravity, with the momentum required to produce the observed field-aligned ion velocity and altitudinal acceleration. For some of the events the available momentum was sufficient to generate the upward flows only above 600-km altitude. *Wahlund* and co-workers suggested that the discrepancy below that height could be accounted for by neutral winds, which drive the plasma to field-aligned velocities of a few tens of m s⁻¹ (eg. *Rodger et al., 1992*). The work of *Jones et al. (1988)* and *Wahlund et al. (1992)* is discussed in more detail in the modelling study presented in *Chapter 6*.

Some of the above processes for the generation of upward plasma flow in the high-latitude ionosphere have been reviewed by *Rodger et al. (1992)*. The principal factors

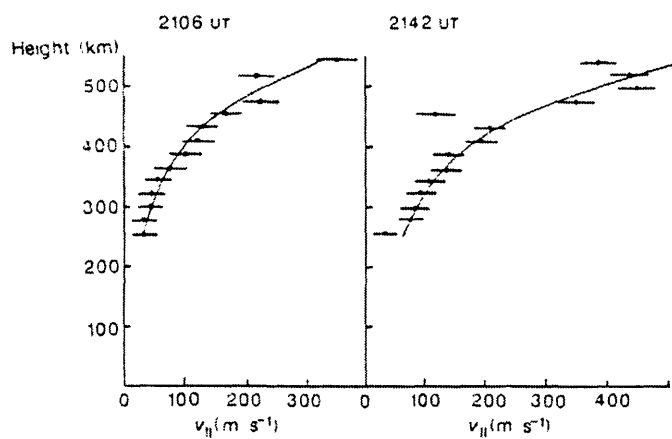


Figure 2.9 Height profiles of the observed and model values of plasma velocity parallel to the magnetic field-line at 2106 and 2142 UT on 6 May 1987. Observed values are dots with error bars, and predicted values are solid curves (*Jones et al., 1988*).

influencing field-aligned plasma flow between 100 and 1000-km altitude are illustrated schematically in Figure 2.10. These mechanisms will be discussed in detail in the following section, from both an observational and theoretical perspective. Particular reference will be made to EISCAT observations of upward ion flows in the auroral F-region ionosphere.

2.4 Acceleration Mechanisms in the F-region and Topside Auroral Ionosphere

The momentum equation describing geomagnetic field-aligned motion for a single ion may be expressed as

$$N_i m_i \frac{dv_{\parallel}}{dt} = -(\nabla \cdot \underline{\mathbf{p}})_{\parallel} + N_i z \mathbf{E}_{\parallel} - N_i m_i v_{in} (\mathbf{v}_{\parallel} - \mathbf{u}_{n\parallel}) - N_i k_B \beta_i \partial_{\parallel} T_{i\parallel} - N_i m_i \mathbf{g}_{\parallel} \quad (2.1)$$

where

m_i	= ion mass	z	= ion charge
t	= time	$T_{i\parallel}$	= field-parallel ion temperature
v_{\parallel}	= field-parallel ion velocity	v_{in}	= ion-neutral collision frequency
k_B	= Boltzmann's constant	\mathbf{E}_{\parallel}	= field-parallel polarization electric field
N_i	= ion number density	β_i	= thermal diffusion coefficient
$\underline{\mathbf{p}}$	= pressure tensor		
∂_{\parallel}	= spatial gradient along geomagnetic field direction		
$\mathbf{u}_{n\parallel}$	= field-aligned component of neutral wind		
\mathbf{g}_{\parallel}	= field-parallel component of gravitational acceleration		

The assumption of a single ion is normally appropriate for the F-region ionosphere, where O^+ dominates. Also, electron-neutral collisions have been disregarded. The terms on the right-hand side of equation 2.1 represent, briefly, pressure-driven diffusion, acceleration by an electric field, ion-neutral frictional drag, thermal diffusion due to an ion temperature gradient and gravity. Positive terms indicate upward ion acceleration.

For gyrotropic ion motion, the pressure tensor takes the form (eg. *Suvanto et al., 1989*)

$$p_{ij} = p_{\parallel} b_i b_j - p_{\perp} (\delta_{ij} - b_i b_j) \quad (2.2)$$

where δ_{ij} is the Kronecker delta, $\hat{\mathbf{b}}$ is the unit vector parallel to the geomagnetic field and p_{\parallel} and p_{\perp} are, respectively, the pressures parallel and perpendicular to $\hat{\mathbf{b}}$. The pressure force per unit volume can be found by evaluating the divergence of p_{ij} . Then, for a curl-free geomagnetic field,

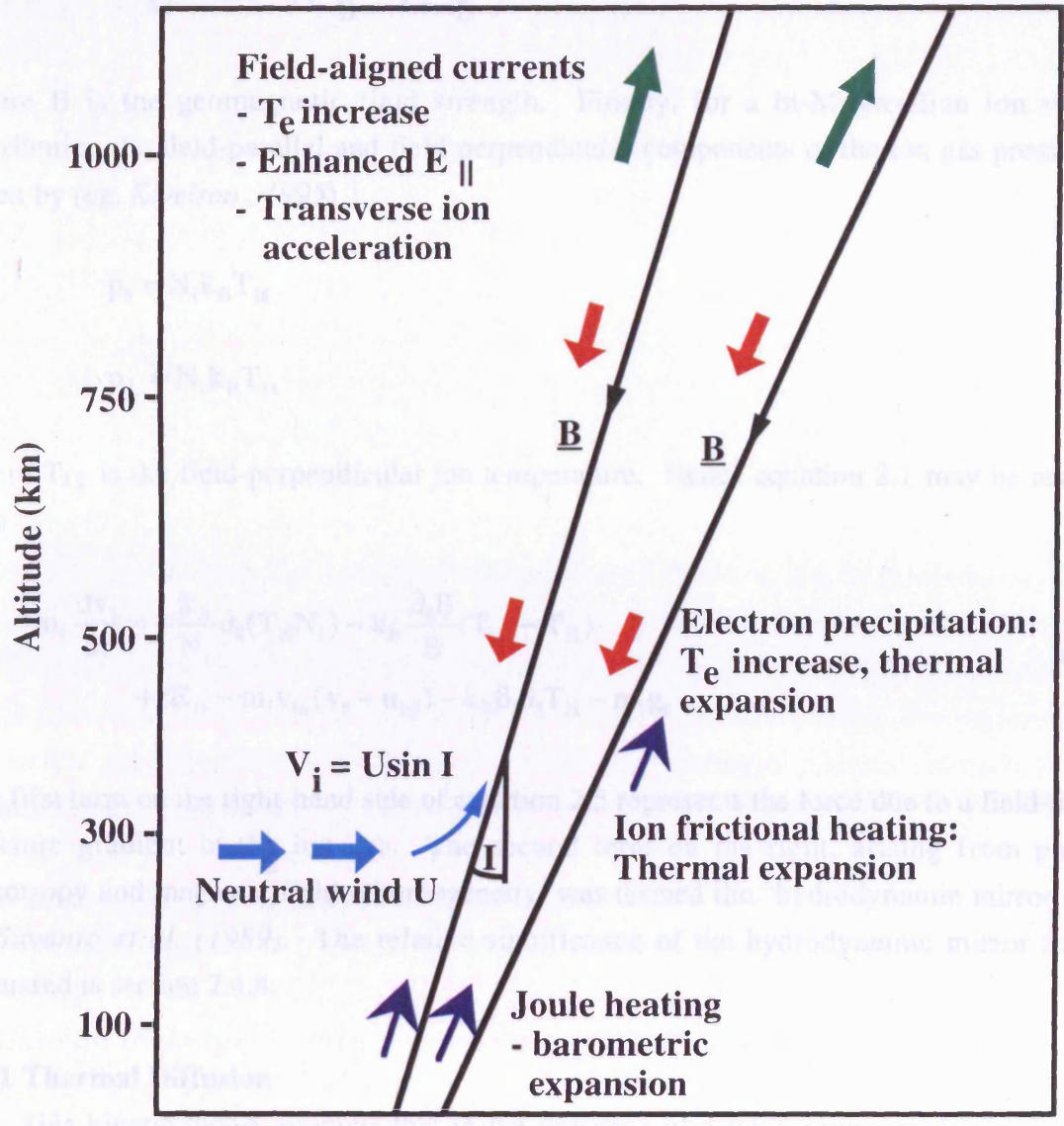


Figure 2.10 Schematic diagram illustrating the principal factors affecting field-aligned ion acceleration (adapted from *Rodger et al., 1992*).

$$\nabla \cdot \underline{\mathbf{p}}_{\parallel} = \partial_{\parallel} p_{\parallel} - p_{\parallel} \frac{\partial_{\parallel} B}{B} + p_{\perp} \frac{\partial_{\parallel} B}{B} \quad (2.3)$$

where B is the geomagnetic field strength. Finally, for a bi-Maxwellian ion velocity distribution the field-parallel and field-perpendicular components of the ion gas pressure are given by (eg. *Kivelson*, 1995)

$$p_{\parallel} = N_i k_B T_{i\parallel} \quad (2.4a)$$

and

$$p_{\perp} = N_i k_B T_{i\perp} \quad (2.4b)$$

where $T_{i\perp}$ is the field-perpendicular ion temperature. Hence equation 2.1 may be rewritten thus

$$\begin{aligned} m_i \frac{d\mathbf{v}_{\parallel}}{dt} = & -\frac{k_B}{N_i} \partial_{\parallel} (T_{i\parallel} N_i) - k_B \frac{\partial_{\parallel} B}{B} (T_{i\perp} - T_{i\parallel}) \\ & + z\mathbf{E}_{\parallel} - m_i \mathbf{v}_{in} (\mathbf{v}_{\parallel} - \mathbf{u}_{n\parallel}) - k_B \beta_i \partial_{\parallel} T_{i\parallel} - m_i \mathbf{g}_{\parallel} \end{aligned} \quad (2.5)$$

The first term on the right-hand side of equation 2.5 represents the force due to a field-parallel pressure gradient in the ion gas. The second term on the right, arising from pressure anisotropy and magnetic field inhomogeneity, was termed the ‘‘hydrodynamic mirror force’’ by *Suvanto et al.* (1989). The relative significance of the hydrodynamic mirror force is discussed in section 2.4.4.

2.4.1 Thermal Diffusion

Gas kinetic theory predicts that in the presence of a temperature gradient gases will diffuse, even in the absence of a density gradient and other external forces (eg. *Richmond*, 1983). The penultimate term of equation 2.5 represents diffusion of the ion gas resulting from a gradient in the field-parallel ion temperature, where β_i is the thermal diffusion coefficient. In general, a temperature gradient in either the neutral or ion gas causes thermal diffusion. *Conrad and Schunk* (1979) showed that, for an O^+ - O mixture under F-region conditions, the thermal diffusion coefficient associated with a gradient in the ion temperature is small if the ion-neutral temperature ratio is less than four. Similarly, the ordinary diffusion correction factor, which acts to reduce the ambipolar thermal diffusion coefficient, is important only when the ratio of ion to neutral temperature is greater than four. Furthermore, the neutral temperature gradient, ∇T_n , is generally so small that thermal ambipolar diffusion due to ∇T_n is also negligible. Hence thermal diffusion may reasonably be neglected from the momentum equation.

Now, assuming ambipolar flow (eg. *Robineau et al., 1996*) for a singly-charged ion the third term on the right-hand side of equation 2.5 equates to

$$z\mathbf{E}_{\parallel} = -\frac{1}{N_e} \partial_{\parallel} (N_e k_B T_e) \quad (2.6)$$

where N_e is the electron number density and T_e the electron temperature. Hence, for a quasi-neutral plasma

$$\begin{aligned} N_e m_i \frac{d\mathbf{v}_{\parallel}}{dt} = & -\partial_{\parallel} [N_e k_B (T_{i\parallel} + T_e)] \\ & -N_e k_B \frac{\partial_{\parallel} \mathbf{B}}{B} (T_{i\perp} - T_{i\parallel}) - N_e m_i v_{in} (\mathbf{v}_{\parallel} - \mathbf{u}_{n\parallel}) - N_e m_i \mathbf{g}_{\parallel} \end{aligned} \quad (2.7)$$

where the first term on the right-hand side represents diffusion due to gradients in electron density, ion temperature or electron temperature. Equation 2.7 therefore represents the field-parallel ion acceleration as a function of the pressure gradient, hydrodynamic mirror force, ion-neutral frictional drag and gravity. Although a simplification, the expression is instructive when considering mechanisms capable of generating substantial ion upflows in the auroral F-region ionosphere.

2.4.2 Field-aligned Component of Neutral Wind

The field-aligned ion flow may be modulated by the field-parallel component of neutral wind, $\mathbf{u}_{n\parallel}$. In the evening sector, the meridional neutral wind tends to be directed equatorward (*Rees et al., 1984a*), so that plasma is driven upwards along the magnetic field direction. Using EISCAT radar observations, *Williams and Jain (1986)* and *Winser et al. (1986)* examined the role of field-aligned upflows in the formation of the high-latitude trough. Both groups of authors estimated that the parallel ion velocity induced by the neutral wind was approximately 30 m s^{-1} , or about 30% to 50% of the total observed field-aligned velocity. Horizontal neutral winds at high latitudes can attain speeds of hundreds of m s^{-1} . Therefore, at the latitude of the EISCAT radar (69.6° N) field-aligned ion motion of 100 m s^{-1} could conceivably be generated by neutral winds (*Wahlund et al., 1992*).

2.4.3 Ion-neutral Frictional Heating

The ion temperature can become significantly enhanced through ion frictional heating, as described by, for example, *Rees and Walker (1968)* and *St.-Maurice and Schunk (1979)* and reviewed in detail by *Davies (1996)*. Ion frictional heating is typically most effective at F-region altitudes. Hence the plasma pressure gradient is modified by ion temperature enhancements, resulting in field-aligned ion acceleration.

In the high-latitude F-region ionosphere, plasma flows in the direction of the $\mathbf{E} \times \mathbf{B}$ drift.

Enhanced convection electric fields, which often exceed 100 mV m^{-1} , can drive the ions at large velocities relative to the neutral atmosphere, resulting in heating of the ions through frictional contact with the neutrals. The response of the ion temperature is almost instantaneous. The neutral particles are heated at a similar rate, but exhibit little increase in temperature due to their far greater number density. Below about 130-km altitude, increased ion-neutral coupling tends to inhibit large ion-neutral relative velocities and consequently the degree of heating is less.

An important consequence of an ion-neutral relative velocity is the deviation of the ion thermal velocity distribution from the Maxwellian form. This in turn results in anisotropy of the ion temperature, the ions being heated preferentially in the direction perpendicular to the geomagnetic field. These phenomena have been addressed extensively by, for example, *Schunk and Walker (1972)*, *St.-Maurice and Schunk (1979)* and *Hubert and Kinzelin (1992)*. The effect of ion temperature anisotropy on the ion parallel velocity is discussed in section 2.4.4.

In addition, the relative concentration of molecular ions in the F-region can become enhanced as a result of increased reaction rates during periods of enhanced ion temperature (*St.-Maurice and Torr, 1978*). The influence of ion composition on the analysis and interpretation of incoherent scatter will be discussed in *Chapter 3*, and addressed in more detail in *Chapter 6*.

Ion frictional heating can have a dramatic effect on the F-region ion temperature. *McCrea et al. (1991)* indicated that a relative velocity of about 1 km s^{-1} was sufficient to double an ion temperature of about 900 K at 300-km altitude. F-region ion upflows are often observed during intervals of enhanced perpendicular electric fields and ion frictional heating (*Bates, 1974; Winser et al., 1988b, c, 1989; Wahlund et al., 1992*). *Jones et al. (1988)* attributed EISCAT observations of F-region upflows to upward ambipolar diffusion resulting from an elevated ion temperature. By assuming steady state conditions, Jones and co-authors successfully modelled the field-aligned velocities in two events in terms of the modified parallel pressure gradient, as illustrated in Figure 2.9. *Jones et al. (1992)* also noted that stronger heating did not necessarily result in greater upward fluxes, since the rate of recombination increases with ion temperature (*St.-Maurice and Torr, 1978*). *Wahlund et al. (1992)* also reported EISCAT observations of upflows during intervals of enhanced ion temperature. One such event is shown in Figure 2.5(a). As is common with this type of event, the measured velocities increased with altitude, reaching 500 m s^{-1} at 800 km, with corresponding fluxes of around $8 \times 10^{13} \text{ m}^{-2} \text{ s}^{-1}$. However, Wahlund and co-authors concluded that thermal diffusion could account for the upflow only above about 600-km altitude. It was proposed that neutral wind drag could account for the field-aligned velocities observed at the lower altitudes (see section 2.4.2).

There is ample evidence that ion frictional heating is a contributing factor in the generation of high-latitude field-aligned upflows. The statistical study of *Keating et al.*

(1990) indicated that perhaps 50% of auroral upflows are associated with ion frictional heating. In turn, ion frictional heating is generated by ionospheric electric fields.

Electric fields in the high-latitude ionosphere arise as a direct consequence of magnetospheric convection. Thus, enhancements in magnetospheric electric fields result in increased perpendicular electric fields in the ionosphere. Large ionospheric electric fields are also associated with the electrodynamics of auroral precipitation, as discussed by, for example, *de la Beaujardière et al. (1977)*, *Marklund (1984)*, *Opgenoorth et al. (1990)*, *Aikio et al. (1993)* and *Lewis et al. (1994)*. Observations have often revealed the presence of enhanced electric fields on one edge of auroral arcs. *McCrea et al. (1991)* noted a number of such features in EISCAT observations, where regions of elevated ion temperature were seen adjacent to E-region electron density enhancements, as illustrated in Figure 2.11. These observations correspond to the “asymmetric” auroral arcs described by *Marklund (1984)*. *Opgenoorth et al. (1990)* proposed that the enhanced electric field is necessary to maintain current continuity between the upward field-aligned current out of the precipitation region and a downward directed current at either the poleward or equatorward edge of the arc. These authors further concluded that the direction of the enhanced field tends to be in the direction of the background convection field, and on the equatorward side of the arc in the pre-midnight sector and poleward of it post-midnight. *Opgenoorth* and co-authors indicated that arc-associated electric fields may exceed 100 mV m^{-1} within a narrow region that is typically not wider than the arc itself.

Ionospheric electric fields may also be modified by geomagnetic micropulsations. Geomagnetic field oscillations, with periods between a few seconds and several minutes, are manifest in the F-region as fluctuations in the field-perpendicular ion velocity. Observations of ion frictional heating, induced by a Pc5 micropulsation, have been presented by *Crowley et al. (1985)*.

The response of the field-aligned velocity to an enhanced perpendicular electric field has been investigated by, for example, *Sellek et al. (1991)*, *Heelis et al. (1993)* and *Moffett et al. (1993)* using the Sheffield University ionosphere and plasmasphere model (SUPIM). The study of *Heelis et al. (1993)* examined the time-dependent response of a magnetic flux tube to an imposed convection velocity of 2 km s^{-1} , a so-called sub-auroral ion drift (SAID) event. It was found that the resulting upward velocity, which could exceed 1 km s^{-1} at 1000-km altitude, was dependent on the rise-time of the SAID velocity. For the fastest onset time of 15 seconds, the maximum field-aligned temperature gradient, and hence pressure gradient, was attained almost immediately, and the field-aligned ion flow reached its maximum value before the pressure gradient was diminished. These results are illustrated in Figure 2.12. The figure also shows the evolution of the O^+ temperature and field-aligned velocity up to 20 minutes into the SAID event. When the SAID was imposed on longer time scales of 10 to 20 minutes, diffusion occurred as the SAID velocity increased to its maximum value, resulting in smaller pressure gradients and, therefore, lesser field-aligned velocities. The above studies all

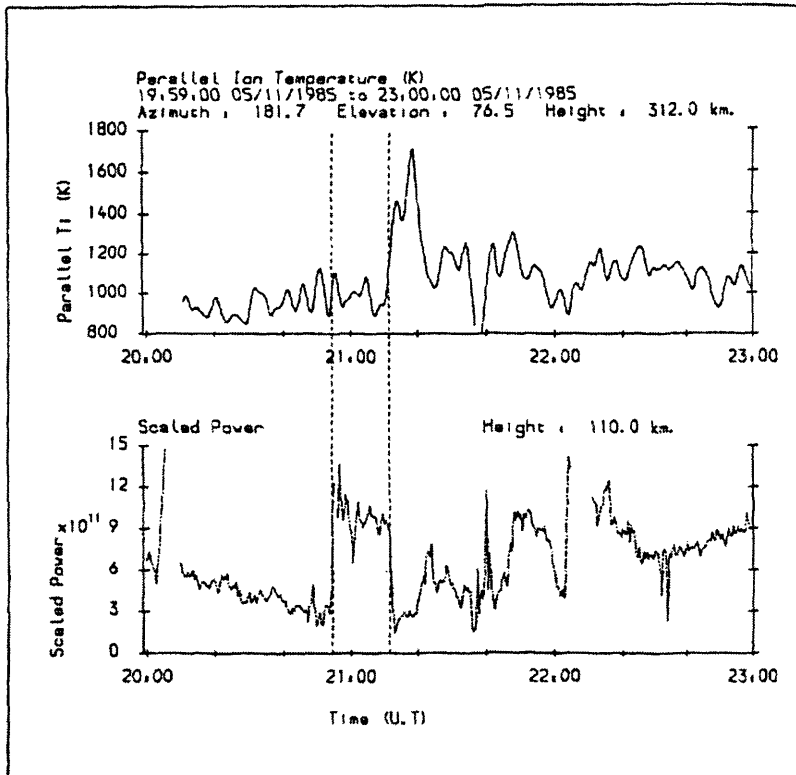


Figure 2.11 Simultaneous F-region field-parallel ion temperature and E-region electron density during auroral precipitation events on 5 November, 1985. One of the auroral events (2100 UT) was associated with a substantial increase in the ion temperature; the temperature increase was observed adjacent to the auroral arc (*McCrea et al., 1991*).

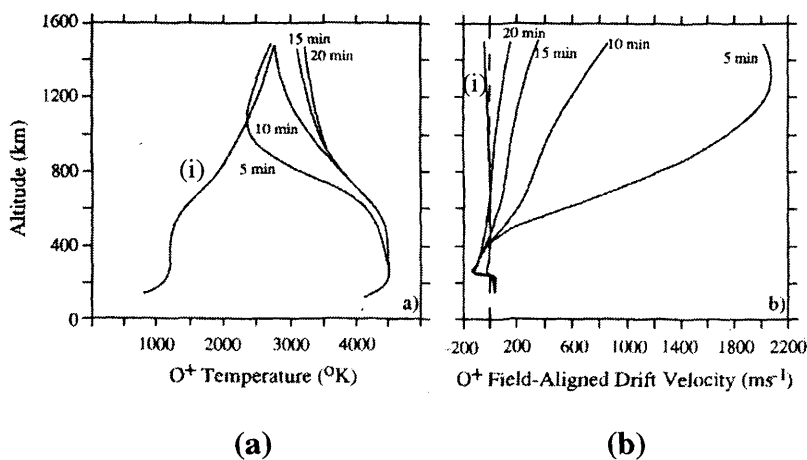


Figure 2.12 Altitude profiles of (a) the O^+ temperature and (b) the O^+ field-aligned velocity at 5-minute intervals during a SAID event with velocity 2 km s^{-1} reached in 15 seconds. (i) indicates the initial ion temperature and velocity in a stationary flux tube (*Heelis et al., 1993*).

predicted downward plasma flow at 300-km altitude and upward flow above about 400 km, the pressure peak being somewhere between those heights. Upward flows are, however, often observed below 250-km altitude (*Jones et al., 1988; Wahlund et al., 1992*). *Sellek et al. (1991)* suggested that the discrepancy between model and observations might be resolved by considering neutral atmospheric upwelling due to E-region Joule heating, which was not accounted for in the model. Nevertheless, such studies clearly demonstrate the coupling between enhanced perpendicular electric fields and auroral ion upflows.

Other workers have modelled the effect of ion frictional heating on field-aligned plasma flow. A semikinetic model by *Wilson (1994)* imposed perpendicular electric fields of up to 200 mV m^{-1} , generating parallel drift speeds of up to 2 km s^{-1} below 1000-km altitude, corresponding to O^+ fluxes of order $1 \times 10^{13} \text{ m}^{-2} \text{ s}^{-1}$. As with the models of SAID events, *Wilson (1994)* also noted that the magnitude of the upflows depended on the rate of ion heating. Other modelling analyses have indicated that ion frictional heating is at least partially responsible for generating field-aligned upflows (*Loranc and St.-Maurice 1994, Liu et al. 1995, Blelly et al. 1996, Caton et al. 1996*).

In summary, ion upflows can be generated through modification of the parallel plasma pressure resulting from ion frictional heating. Field-aligned plasma flow acts to attain a new equilibrium scale height. This type of upflow, a thermal upwelling of the plasma in response to strong perpendicular electric fields and ion frictional heating, was labelled a “type 1” event by *Wahlund et al. (1992)*. Type 1 upflows have been shown to be a major factor in the formation of the high latitude trough (*Winser et al., 1986; Williams and Jain, 1986*).

2.4.4 Ion Temperature Anisotropy and the Magnetic Mirror Force

It was noted in section 2.4.3 how ion-neutral relative flow results in anisotropy of the ion temperature, the component of ion temperature perpendicular to the geomagnetic field being greater than the parallel component. Under such conditions and in the presence of the divergent geomagnetic field, the ions will experience an upward force. This force, termed the “hydrodynamic mirror force” by *Suvanto et al. (1989)*, is represented by the second term on the right-hand side of equation 2.7. *Suvanto* and co-authors estimated that, between about 200 and 500-km altitude at auroral latitudes, the magnitude of the mirror force could be between 1 and 10% of the opposing gravitational downforce on O^+ . Similar conclusions have been reached by *Körösmezey et al. (1992)*. It was found by *Sellek et al. (1991)* in a study of SAID events that a 10% reduction in the gravitational acceleration, to simulate the effects of the mirror force, had little effect on the resulting ion velocities. *Jones et al. (1988, 1992)* also included the effect of the mirror force to account for their observations of upflows associated with ion frictional heating. These authors suggested, though, that thermal diffusion was the most important factor in producing the upflow.

2.4.5 Electron Heating

In addition to ion heating, enhancements in electron temperature can also modify the plasma pressure gradient, leading to bulk field-aligned plasma flow through an increased polarisation electric field (*Rodger et al., 1992; Blelly et al. 1996*). A number of mechanisms capable of electron energization have been proposed. Primarily, the electron temperature is influenced by the solar EUV flux. EUV radiation creates energetic photoelectrons, which transfer heat to the ambient electrons through collisions (*Schunk and Nagy, 1978*).

In the E-region, below about 120-km altitude, the electron population can be heated by interactions with plasma instabilities. At such low altitudes, the ions are largely collisionally constrained by the neutral atmosphere, whilst the electrons move under the influence of the \mathbf{ExB} convection drift. Hence net currents exist in the E-region, driven by the same electric fields that lead to frictional heating in the F-region. If these currents exceed a certain threshold, related to the ion acoustic speed, Farley-Buneman instabilities are generated (*Farley, 1963; Buneman, 1963*), and the electrons are heated by a process analogous to frictional heating between particles. This process is known as electron turbulent heating (*Schlegel and St.-Maurice, 1981; Robinson, 1992*).

At higher altitudes, secondary electrons produced by particle precipitation are an important heat source in the high-latitude ionosphere. The heating effect of electron precipitation through secondary electron production has been addressed by, for example, *Walker and Rees (1968)* and *Whittaker (1977)*. *Wahlund and Opgenoorth (1989)* and *Wahlund et al. (1992)* reported observations of ion upflows, with velocities in excess of 400 m s^{-1} , associated with significantly enhanced electron temperatures in the upper F-region, but with no evidence of elevated ion temperatures. The upflows were observed above auroral arcs and occurred more frequently, and were often stronger, than the “type 1” upflows. *Wahlund et al. (1992)* labelled these features “type 2” ion upflows, as described in section 2.3; an example of such is illustrated in Figure 2.5(b). *Caton et al. (1996)* investigated EISCAT observations of type 2 F-region upflows, considering separately the effects of soft ($< 1 \text{ keV}$) electron precipitation, convection-driven ion frictional heating and downward electron heat fluxes from the magnetosphere, using the Field Line Interhemispheric Plasma (FLIP) model (*Liu et al., 1995*). Caton and co-authors concluded that soft electron precipitation and downward heat flux, affecting mainly the electron temperature, were the primary driving mechanisms of the upflows, with ion frictional heating of lesser importance. Earlier work by *Liu et al. (1995)* compared the FLIP model (*Torr et al., 1990*) with HILAT and DE-2 satellite observations of topside upflows associated with soft electron precipitation and ion frictional heating. Liu and co-authors indicated that precipitation-induced ionization and electron heating, together with ion frictional heating, were the principal drivers of the upflows. Recently, *Blelly et al. (1996)* separately modelled the effects of \mathbf{ExB} -induced ion frictional heating, downward electron heat flow from the magnetosphere and upward field-aligned current densities of a few tens of $\mu\text{A m}^{-2}$. The response of the ion temperature and velocity to

ion frictional heating was observed to be similar to that in the SAID studies of, for example, *Heelis et al. (1993)*. For instance, maximum upward velocities of 500 m s^{-1} were induced by an ExB drift of 50 mV m^{-1} . Furthermore, *Blelly and co-authors* found that the effects of the field-aligned current and the downward electron heat flux were very similar, inducing field-aligned velocities of 500 m s^{-1} at 1600-km altitude.

The above are examples of ion upflows related to enhanced F-region and topside electron temperatures occurring in the vicinity of auroral precipitation. As such, they resemble the type 2 events described by *Wahlund et al. (1992)*. However, the modelling studies of *Liu et al. (1995)* and *Blelly et al. (1996)* have indicated that ion frictional heating can also be an important factor in these type of events.

Recently, the effects of current-driven instabilities on the electron temperature at topside altitudes of 1000 km and greater have been investigated (*Forme et al., 1993; Wahlund et al., 1993*). Electrostatic ion-acoustic and ion-cyclotron waves have been shown to become unstable to field-aligned current densities of a few $\mu\text{A m}^{-2}$ (*Kindel and Kennel, 1971*), as does the Buneman instability (*Forme et al., 1993*). *Forme and co-authors* conducted a theoretical study of the effects on topside ion and electron temperatures of these current-driven instabilities. It was found that the instabilities were initiated by current densities of a few tens of $\mu\text{A m}^{-2}$ and normally appeared at altitudes above about 2000 km, although the ion-cyclotron instability was triggered as low as 1200 km. Upward field-aligned currents of such magnitude are well documented (*Wahlund et al., 1992*). Such low-frequency turbulence is able greatly to enhance the electron temperature, through increased “anomalous” resistivity (*Swift, 1965; Papadopoulos, 1977*) that arises from the increased scattering of electrons by the turbulent electric field. A further consequence of increased resistivity is the enhancement of any parallel electric field which might exist.

The type 2 upflows described by *Wahlund et al. (1992)* were described briefly in section 2.3 (see Figure 2.5b). Significantly, *Wahlund and co-authors* found that type 2 upflows could not be explained *solely* in terms of thermal upwelling resulting from an enhanced electron temperature, although this was a contributing factor. *Wahlund and co-workers* also noted enhanced ion-line spectra during a number of type 2 upflows, an example of which is illustrated in Figure 2.13. The naturally enhanced spectral shoulders are indicative of acoustic turbulence and, therefore, possibly enhanced field-aligned electric fields. Consequently, it was concluded that the type 2 upflows were probably generated by enhanced field-aligned electric fields caused by anomalous resistivity in the presence of plasma turbulence. *Wahlund et al. (1992)* also considered the possibility that the upflowing ions might carry a significant portion of the field-aligned current, as argued by *Block and Fälthammar (1968)*. *Wahlund and co-authors* estimated that the observed flux would correspond to a current density of about $10 \mu\text{A m}^{-2}$, a value consistent with that considered in the modelling study of *Blelly et al. (1996)*.

In a companion paper to *Forme et al. (1993)*, *Wahlund et al. (1993)* presented EISCAT

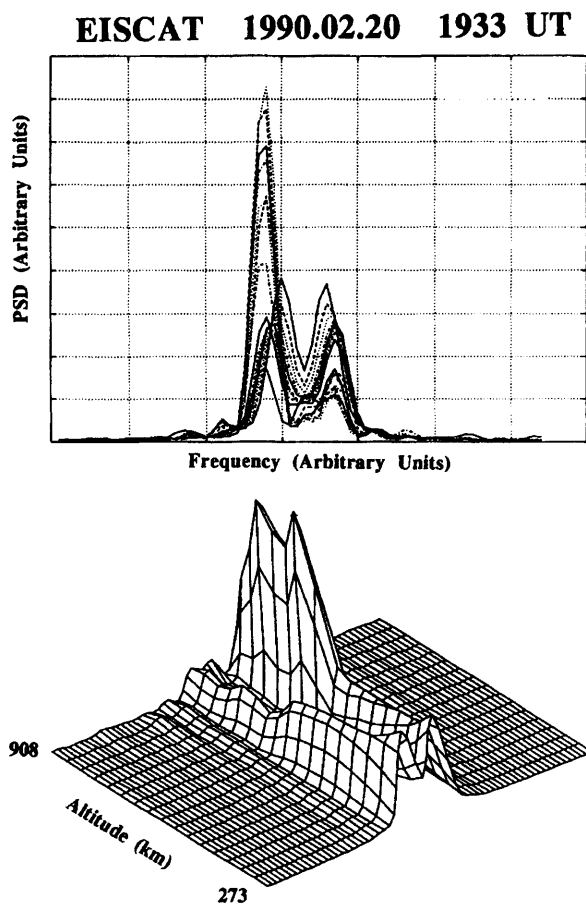


Figure 2.13 Incoherent scatter ion-line spectrum during a type 2 ion upflow observed by the EISCAT facility on February 20, 1990. The upper panel shows superposed normalized spectra from all long-pulse range gates. The lower panel shows the same spectra as a function of altitude. The spectra exhibit naturally enhanced ion-acoustic “shoulders”, indicating the sporadic existence of ion-acoustic turbulence (*Wahlund et al., 1992*).

observations of enhanced electron temperatures of up to 8000 K near 1500-km altitude. The electron heating was correlated with ion-acoustic turbulence and electron precipitation between 170 and 230-km altitude, corresponding to electron energies between 100 and 500 eV. The presence of ion-acoustic turbulence was inferred from naturally enhanced ion-line spectral shoulders, as noted previously by *Foster et al. (1988)*, *Rietveld et al. (1991)* and *Wahlund et al. (1992)*. *Wahlund et al. (1993)* suggested that an H^+/O^+ two-stream instability was the cause of the observed ion-acoustic turbulence. The calculations of *Forme et al. (1993)* indicated that electron heating resulting from anomalous resistivity caused by low-frequency turbulence is of major importance in the topside ionosphere, acting in addition to classical collisional heating. Such instabilities might also generate Alfvén waves, which can cause upward ion flow through ponderomotive acceleration (*Li and Temerin, 1993; Lee and Parks, 1996*). Finally, it is noted that transverse ion heating is also associated with low-frequency plasma turbulence (*Ungstrup et al., 1979*), leading to upward ion acceleration via the hydrodynamic magnetic mirror force, as discussed in section 2.4.4. Transverse ion heating is discussed briefly in the following section.

Electrons are an important link in the transfer of energy between the magnetosphere and ionosphere. Electron energization can occur via a range of processes, *viz.* E-region turbulent heating, particle precipitation, field-aligned currents and, at topside altitudes, increased resistivity induced by plasma instabilities. Electron heating can modify the electron pressure gradient and, therefore, the ambipolar electric field, resulting in upward ion acceleration. Enhanced parallel electric fields in regions of increased resistivity might also aid upward ion acceleration. In addition, transverse ion heating by current-driven instabilities can generate outward acceleration. These processes are symptomatic of disturbed auroral conditions.

2.4.6 Transverse Ion Heating

It was discussed in section 2.4.4 how DC perpendicular electric fields can lead to ion temperature anisotropy and subsequent ion upflow via the magnetic mirror force (*Suvanto et al., 1989*). In general, the presence of conical ion velocity distributions implies transverse heating of the ions. In turn, transverse ion heating indicates that energization results from perpendicular electric fields which come in a number of guises, a variety of which have been summarized by *Moore et al. (1996)*. Heating by ion cyclotron waves (*Ungstrup et al., 1979; Norqvist et al., 1996*) and lower hybrid waves (*Chang and Coppi, 1981; Retterer et al., 1994*) was referred to in section 2.2.4. Transverse ion acceleration is also induced by impulsive electric fields, when the field fluctuates at frequencies in excess of the ion cyclotron frequency (*Hultqvist et al., 1988; Newman, 1990*).

A number of possible energy sources have been proposed to generate such instabilities, as summarized by *Moore et al. (1996)*. Low frequency turbulence is unstable to field-aligned currents and, therefore, current-driven low-frequency turbulence is a likely mechanism for the production of ion conics, as observed by rockets and satellites in the topside (*Lu et al., 1992*),

often above auroral arcs (*Arnoldy et al., 1992*). Transverse ion acceleration has been detected at altitudes as low as 500 km (*Whalen et al., 1978, 1991*).

Recently, *Ganguli et al. (1994)* proposed a mechanism capable of generating low frequency plasma waves in regions of strongly sheared convection velocity, potentially leading to transverse ion heating. *Tsunoda et al. (1989)* presented HILAT satellite observations that indicated a strong correlation between ion heating and convection velocity shears in the dayside auroral oval at 800-km altitude. Ganguli and co-workers found a similar correlation in the nightside auroral zone. These authors argued that the observed ion temperatures could not be explained in terms of classical frictional heating in the light of the small convection speeds observed. Rather, it was proposed that sheared flows could excite low-frequency plasma waves, such as the Kelvin-Helmholtz instability, leading to the formation of strongly-sheared flows. The sheared flows may seed ion-cyclotron and lower-hybrid waves, potentially leading to ion heating.

2.4.7 Joule Heating of the Neutral Atmosphere

It has been described how E-region currents can lead to turbulent heating of the electrons at low altitudes (see section 2.4.5). In addition, the auroral electrojet current can cause Joule heating of the neutral atmosphere (*Cole, 1962*). This has the effect of lifting the neutral atmosphere through thermal expansion of the gas, resulting in a lifted F-region and field-aligned plasma flow (*Raitt et al., 1975*). *Bates (1973)* reported Chatanika observations of field-aligned velocities as high as 100 m s^{-1} resulting from enhanced Joule heating. More typically, parallel ion flows associated with Joule heating exhibit velocities of a few tens of m s^{-1} . In their study of the high-latitude trough, *Winser et al. (1986)* approximated upward field-parallel velocities resulting from Joule heating, arriving at values of between 10 and 25 m s^{-1} . *Rees et al. (1984b, 1984c)* reported upward velocities of similar magnitude on the night-side during auroral disturbances. Theoretical estimates of neutral wind velocities resulting from Joule heating of the atmosphere have also been made by *Hays et al. (1973)* and *Fuller-Rowell (1984, 1985)*. The latter author concluded that vertical velocities of up to 40 m s^{-1} could result from Joule heating induced by an electric field of 100 mV m^{-1} .

A number of workers, including *Williams and Jain (1986)*, *Winser et al. (1988b, c)* and *Jones et al. (1988)* have concluded that Joule heating and subsequent upward expansion of the neutral atmosphere is an important factor in the generation those upflows associated with enhanced perpendicular electric fields, the “type 1” events described by *Wahlund et al. (1992)* and illustrated in Figure 2.6(a). *Jones et al. (1988)* suggested that Joule heating of the neutral atmosphere may be important in lifting the ions to altitudes where the ion-neutral collision frequency is small enough such that other mechanisms, for example the magnetic mirror force, can further accelerate the plasma with decreasing resistance.

2.4.8 Auroral Plasma Cavity

The presence of regions of depleted plasma density in the high-altitude auroral ionosphere have been reported by *Calvert (1981)* and *Persoon et al. (1988)*. *Calvert (1981)* described an “auroral plasma cavity” centred at 70° invariant latitude and approximately 6° wide, penetrating down to $1.8 R_E$, although *Hultqvist (1991)* reported that cavities sometimes extend as low as 1000-km altitude. *Singh et al. (1989)*, employing a fluid model of the plasma, investigated the effects of such a cavity on auroral ionospheric O^+ flows. Singh and co-authors concluded that a cavity maintained at $1 R_E$ could draw a steady-state O^+ flux of order $1 \times 10^{12} \text{ m}^{-2} \text{ s}^{-1}$, whilst, for a cavity at 3000-km altitude, fluxes of $1 \times 10^{13} \text{ m}^{-2} \text{ s}^{-1}$ could be generated. The upward flux from the ionosphere was observed first near the cavity, the flux front moving downward at the ion-acoustic speed. This process can draw a large O^+ flux from the ionosphere without the need for low-altitude heating of the plasma. *Persoon et al. (1988)* reported that the auroral plasma cavity is highly correlated with field-aligned distributions of upflowing ions. High-altitude plasma cavities have been considered as a possible source of O^+ upflows by *Lu et al. (1992)* and *Wahlund et al. (1992)*. However, as noted by *Wahlund* and co-authors, an auroral plasma cavity requires perhaps 1 hour to reach a steady state (*Singh et al., 1989*), and does not require a low-altitude driving force. These features are not consistent with the transient F-region upflows reported by, among others, *Wahlund et al. (1992)*.

2.5 Summary

Over the last 25 years or so, it has become increasingly apparent that the ionosphere is a major source of magnetospheric plasma. Indeed, it has been suggested that ionospheric plasma alone could populate the magnetosphere, without the need for extraterrestrial sources. Satellite observations in the high-altitude, high-latitude ionosphere altitude have revealed a veritable zoo of outflowing energetic ions, dominated by H^+ , He^+ and O^+ outflows.

The polar cap is a consistent source of light ions escaping along open field lines as the polar wind. The polar wind consists largely of H^+ and He^+ ions with energies of order 1 eV and with fluxes of order $1 \times 10^{12} \text{ m}^{-2} \text{ s}^{-1}$. On occasion, O^+ fluxes of order $1 \times 10^{13} \text{ m}^{-2} \text{ s}^{-1}$ are observed on polar cap field-lines, contradictory to classical polar wind theory. The dayside cleft region was identified as the source region for these upwelling ions, which convect anti-sunward across the polar cap in the cleft ion fountain.

At lower latitudes, the auroral oval is a steady source of H^+ ions and, in the dusk sector, of He^+ . In addition, during disturbed auroral conditions large upflowing fluxes of energetic O^+ are commonly observed. Satellite measurements have revealed transient O^+ fluxes of order $1 \times 10^{14} \text{ m}^{-2} \text{ s}^{-1}$, with energies ranging from a few eV to several keV. High-altitude outflows are typically characterized as either ion beams or conics, defined according to the velocity pitch-angle distribution. Conics tend to exhibit lower energies, of perhaps 5 to 100 eV, than keV ion beams, and conics are often observed at lower altitudes than beams.

Rocket and satellite measurements indicate that there must be upward ion acceleration at F-region altitudes to account for the fluxes, energies and compositions of outflows observed at high altitudes. Radar measurements in the auroral ionosphere have revealed transient ion upflows with fluxes of order $1 \times 10^{14} \text{ m}^{-2} \text{ s}^{-1}$ and velocities of up to several km s^{-1} . Hence, ionospheric upflows seem a likely source for higher altitude outflows. Statistical analyses of F-region ionospheric upflows have demonstrated that these phenomena are common near the cusp and throughout the auroral oval, consistent with high altitude observations of outflows.

Ionospheric fluxes in excess of those observed in the magnetosphere are sometimes observed, indicating that the ionosphere is not simply responding to a magnetospheric requirement, but is actively providing upward fluxes. A number of acceleration mechanisms have been described which operate in the auroral ionosphere. These processes generally pertain to heating of the plasma, and subsequent thermal expansion, during active auroral conditions. Large perpendicular electric fields can lead to Joule heating of the ions and neutrals, as well as turbulent electron heating in the E-region. Bulk electron heating may also result from particle precipitation, through both collisions and enhanced “anomalous” resistivity in the presence of field-aligned-current-induced instabilities. Low-frequency plasma instabilities can be generated by a number of other processes, including sheared convection flows, and may heat the ions transverse to the geomagnetic field direction, leading to outward acceleration by the magnetic mirror force.

In summary, the auroral ionosphere is a consistent and significant source of ions for the magnetosphere. Field-aligned ion upflows, consisting primarily of O^+ , are commonly detected, with fluxes of order 1×10^{13} to $1 \times 10^{14} \text{ m}^{-2} \text{ s}^{-1}$ and velocities ranging between tens of m s^{-1} to a few km s^{-1} . The energies and velocity distributions of these upflows indicate a variety of acceleration processes which are primarily associated with disturbed auroral conditions.

The following chapters include case studies of ion upflows associated with enhanced perpendicular electric fields, particle precipitation and enhanced electron temperatures. In addition, a statistical analysis of F-region and topside upflows observed by the EISCAT radar is presented, examining diurnal, seasonal and solar cycle upflow variations and dependencies on ion and electron temperatures. Finally, some of the acceleration mechanisms discussed in the present chapter are investigated in a simple model of an F-region upflow event.

CHAPTER 3

Incoherent Scatter and the EISCAT Facility

3.1 Introduction

The combined effects of pressure gradients and electrostatic forces in the ionosphere generates acoustic waves. The scatter of electromagnetic radiation at radio frequencies by such waves can yield information on a number of plasma parameters, such as electron density and ion temperature. This process is known as incoherent scatter and is employed by ground based radars for studies of the Earth's plasma atmosphere. The theory of incoherent scatter is reviewed in this chapter, including a brief discussion of how the scattered signal relates to some ionospheric parameters. Measurement techniques are then addressed, with particular reference to the European Incoherent Scatter (EISCAT) system, followed by a description of the analysis process and the uncertainties inherent in the derived parameters.

3.2 Incoherent Scatter Theory

Incoherent scatter (IS) considers the ionospheric scatter of electromagnetic radiation of wavelengths much shorter than the smallest scale irregularities in the ionosphere. The earliest considerations of incoherent scatter therefore treated electrons as free particles. Theory predicted a return power proportional to the electron density (*Fabry, 1928*), and a frequency spectrum Doppler-broadened over a bandwidth of several hundred kHz by the random thermal motions of the electrons (*Gordon, 1958*). Initial experiments indicated that the returned power was as predicted, but with a spectrum corresponding to the thermal motion of the ions, giving far greater power per unit bandwidth (*Bowles, 1958*). The problem was tackled independently by several workers, including *Fejer (1960)*, *Dougherty and Farley (1960)* and *Hagfors (1961)*, who concluded that the signal resulted from scattering off acoustic waves in the plasma.

Electrostatic attraction causes ions to form a shielding layer around each electron. The radius of this layer is termed the Debye length, D , and is determined by the balance between electric potential and the thermal motion of the ions, such that

$$D = \left(\frac{\epsilon_0 k_B T_e}{e^2 N_e} \right)^{\frac{1}{2}} \cong 69 \left(\frac{T_e}{N_e} \right)^{\frac{1}{2}} \quad (3.1)$$

where e represents the electron charge, N_e and T_e the electron density and temperature, respectively, k_B is Boltzmann's constant and ϵ_0 the permittivity of free space. The Debye length is dependent upon a variety of factors, including altitude, time of day, season and degree of solar activity, ranging from a few mm at the F-region peak to tens of cm in the E-region and topside ionosphere. On scales shorter than the Debye length, electrons can be

considered as free particles, and true incoherent scatter would occur for electromagnetic radiation at such wavelengths. However, on scales much greater than D , the electrons cannot be considered as independent since they are coupled to the ions. A combination of thermal electron motion and electrostatic coupling generates ion-acoustic and electron-acoustic waves in the plasma. These waves propagate in all directions over a continuous spectrum of frequencies. Electromagnetic radiation with a wavelength greater than D will scatter off those acoustic plasma waves for which the Bragg criterion is satisfied; it is this *quasi-coherent* scatter that produces the observed IS spectrum. This process is not, therefore, true Thomson, or incoherent, scatter, but is generally referred to as such in the absence of a more appropriate term.

The incoherent scatter spectrum comprises four parts, due to scatter from both ion and electron acoustic waves propagating toward and away from the radar. An idealized incoherent scatter spectrum is illustrated in Figure 3.1. For a transmitted signal of wavelength λ , the Doppler shift arising from scatter off ion and electron acoustic waves, respectively, is given by

$$F_i(\lambda) = \pm \frac{2}{\lambda} \left[\left(\frac{k_B T_i}{m_i} \right) \left(1 + \frac{T_e}{T_i} \right) \right]^{\frac{1}{2}} \quad (3.2)$$

$$F_e(\lambda) = \pm f_p \left(1 + \frac{12\pi^2 D^2}{\lambda^2} \right)^{\frac{1}{2}} \quad (3.3)$$

where T_i and m_i represent the ion temperature and mass. The plasma frequency, f_p , is given by

$$f_p = \left(\frac{e^2 N_e}{4\pi^2 \epsilon_0 m_e} \right)^{\frac{1}{2}} \quad (3.4)$$

in which m_e is the electron mass. The ion-lines in the spectrum, arising from scatter by ion-acoustic waves, typically exhibit a Doppler shift of a few kHz, whilst the greater velocity of the electron-acoustic waves results in a shift of a few MHz in the electron lines. Broadening of the ion lines occurs as a result of Landau damping. The ion-acoustic wave velocity is well within the Maxwell distribution of ion thermal velocity, as illustrated in Figure 3.2. Hence there are always more ions travelling at lesser rather than greater speeds than the acoustic wave, resulting in attenuation of the wave. This gives rise to broadening of the two ion spectral lines, which merge and produce the double humped ion spectrum characteristic of incoherent scatter. In the E-region, the bandwidth of the ion-line is typically of the order 10

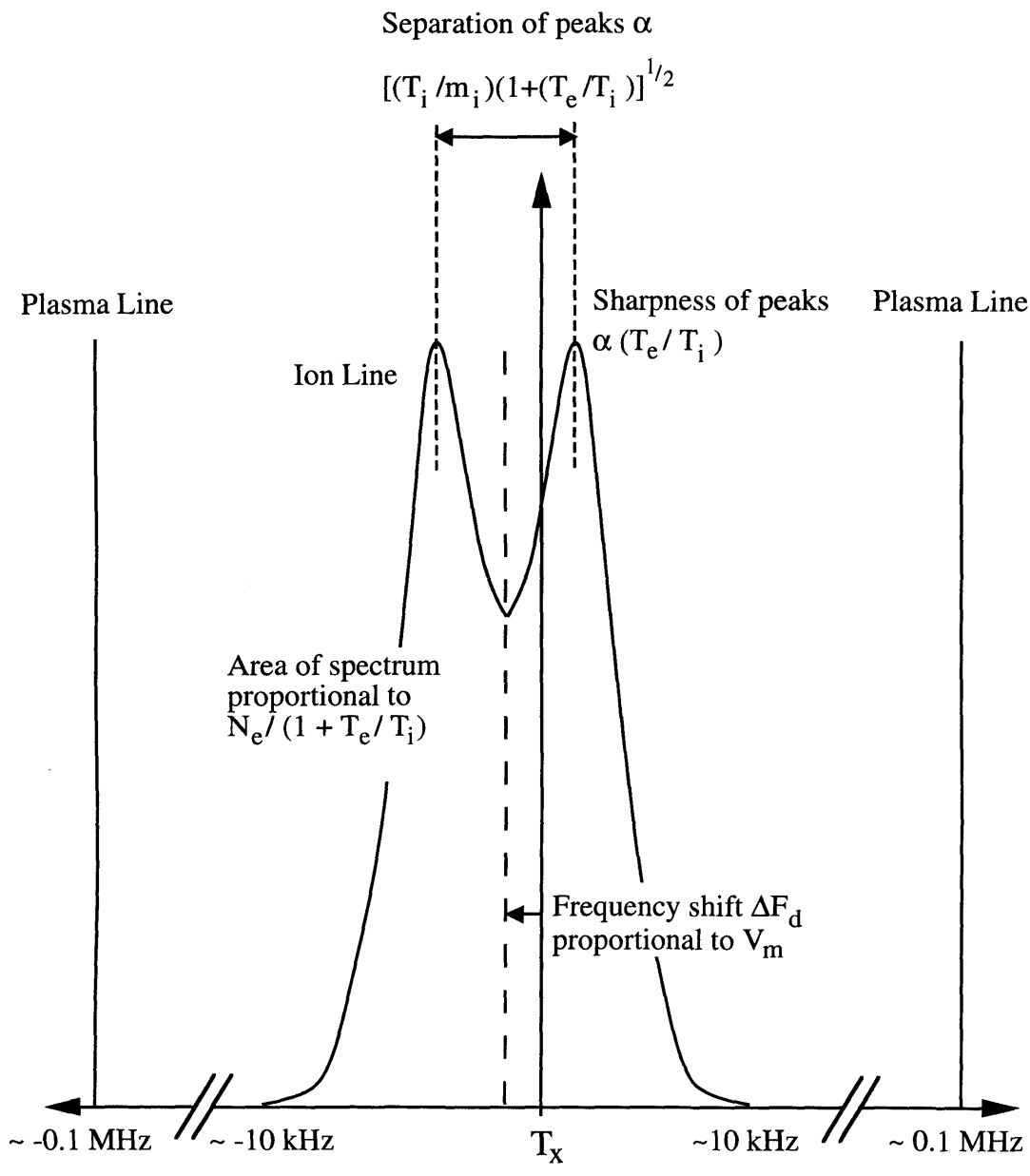


Figure 3.1 An idealized incoherent scatter spectrum, illustrating the effects of various parameters on the shape of the spectrum.

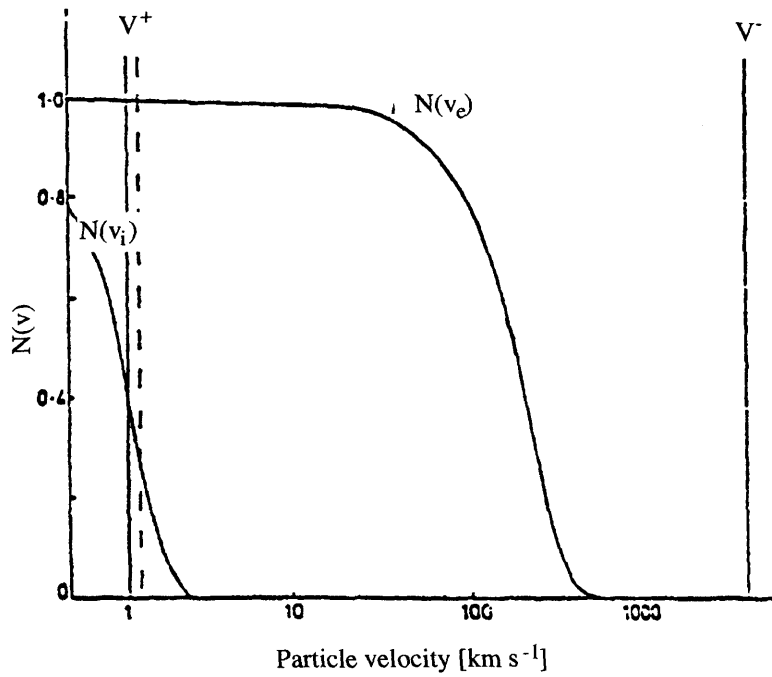


Figure 3.2 Maxwellian velocity distributions of thermal electrons $N(v_e)$ and thermal ions $N(v_i)$, and phase velocities of electron-acoustic (V^-) and ion-acoustic (V^+) waves, for $N_e=10^{12} \text{ m}^{-3}$, $m_i=16$ and $T_i=T_e=1000 \text{ K}$ (Beynon and Williams, 1978).

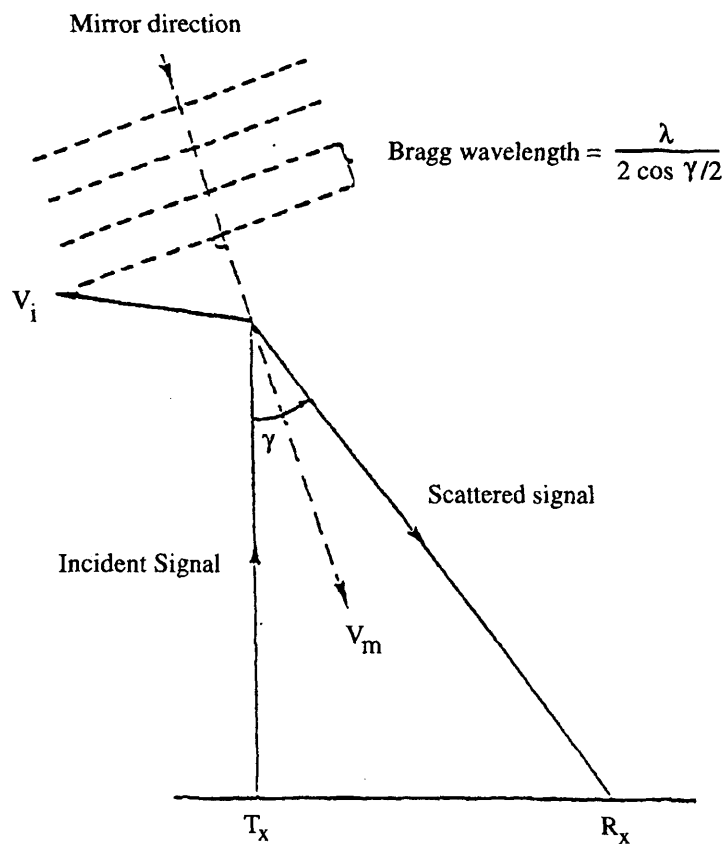


Figure 3.3 Scattering geometry for a bistatic incoherent scatter radar (Rishbeth and Williams, 1985).

kHz, increasing to around 50 kHz in the F-region and some 100 kHz in the topside. The electron-acoustic lines (plasma lines) are attenuated very little, since electron acoustic waves travel at a velocity much greater than the bulk of the thermal electron population. Hence, the plasma lines remain sharp.

In addition to the frequency shifts of its components, the spectrum as a whole may be Doppler-shifted due to bulk motion of the plasma. Figure 3.1 indicates this and some of the other factors that define the shape of the spectrum. The spectral shape is also dependent on the frequency of the transmitted pulse, particularly for wavelengths not greatly exceeding D . For a given ratio of electron temperature to ion temperature, the spectral minimum becomes more distinct for longer wavelengths. The following section describes how the electron-ion temperature ratio and other ionospheric parameters can be determined from the incoherent scatter spectrum.

3.2.1 Determination of Ionospheric Parameters from an IS Spectrum

The process of incoherent scatter and the derivation of ionospheric parameters therefrom are reviewed by, for example, *Evans (1969)* and *Beynon and Williams (1978)*. The following section summarises the effects of various plasma parameters on the form of the backscattered spectrum and how these parameters can therefore be derived from analysis of the spectrum.

Electron density. The total power, P_s , scattered from a height h and received at the antenna may be expressed as

$$P_s(h) = \frac{K\sigma N_e(h)}{h^2} \quad (3.5)$$

in which K is a constant proportional to the transmitted power and the effective collecting area of the antenna. Under normal ionospheric conditions the bulk of the backscattered power is within the ion spectrum, and for radar wavelengths much greater than D , the scattering cross section, σ , is given by

$$\sigma = \sigma_e (1 + T_e/T_i)^{-1} \quad (3.6)$$

where σ_e is the cross section for direct backscatter from a single electron, approximately equal to 10^{-28} m^2 . The ionospheric electron density can therefore be determined from measurements of received power, given that the temperature ratio can be obtained from the shape of the spectrum and the constant K from measurements of electron density by an independent diagnostic instrument.

Alternatively, the electron density may be determined by measurement of the Faraday

rotation of a polarized signal, or by measurement of the frequency offset of the plasma lines. The difficulties associated with these more complex techniques are addressed by *Beynon and Williams (1978)*.

Ion temperature, electron temperature and ion mass. As discussed, the resolution of the ion-line spectral peaks is dependent on the degree of Landau damping experienced by the ion-acoustic waves. The amount of attenuation is governed by the gradient of the ion velocity distribution at the ion-acoustic speed (see Figure 3.2), and this speed is proportional to the ratio of electron to ion temperature. For larger values of the temperature ratio, the gradient of the ion velocity distribution becomes shallower and so the degree of attenuation less, resulting in sharper spectral peaks. Thus the temperature ratio can be determined from the ratio of the peak power of the spectrum to the depth of the central minimum.

Having established the temperature ratio, the ratio of ion temperature to ion mass can be calculated. This is achieved by measuring the separation of the ion lines, which is approximately equal to twice the ion acoustic frequency, ΔF_i (equation 3.2). An absolute value of ion temperature, and hence electron temperature, can then be obtained if the ion mass is known. For the majority of incoherent scatter analyses, values of ion mass are obtained from standard composition models, the relative concentrations of ions being well known within certain regions of the ionosphere. Between these regions, however, a mixture of several ion species may be present. For example, below about 150 km altitude molecular NO^+ and O_2^+ ions dominate, but these are progressively replaced by atomic O^+ with increasing altitude. Within such transition regions the relative proportions of each species are generally not well known and changes in composition can be difficult to differentiate from variations in temperature. Similar problems can arise when the plasma composition is modified under disturbed conditions. It is illustrated in *Chapter 6* how the adoption of different ion composition models can affect the values of parameters obtained from IS analysis.

When two ion species of substantially different mass are present their masses may be directly determined from the shape of the spectrum; in particular, from the slope of the spectrum at the half power points. This method has been employed to derive ion masses in the transition region between molecular and atomic species (*Lathuillère et al., 1983*) and between O^+ and the light ions of the topside ionosphere (*Moorcroft, 1964*). Alternatively, the ion composition in these transition regions may be deduced by interpolating the ion temperature profile from altitudes where the ion composition is well known (*Evans, 1969*).

Plasma velocity. The entire incoherent scatter spectrum may be Doppler shifted as a result of bulk plasma motion. The measured Doppler shift corresponds to the component of the mirror velocity along the radar line-of-sight. For a monostatic radar, the mirror direction is along the beam, and for a bistatic system is along the bisector of the beams; the latter situation is

illustrated in Figure 3.3. The mean Doppler shift, ΔF_d , due to a velocity v_m along the mirror direction is given by

$$\Delta F_d = \frac{2v_m}{\lambda} \cos\left(\frac{\gamma}{2}\right) \quad (3.7)$$

where γ is the angle between the transmitter and receiver beams. The Doppler shift, ΔF_d , is typically small (of order 100 Hz) compared with the width of the spectrum, necessitating an accurate measurement of the spectrum for determination of the velocity.

Other measurable parameters. Density, temperatures and drift velocity are typically obtained routinely from incoherent scatter spectra for most ionospheric conditions. Within certain altitude regimes or when conditions allow, three other parameters may also be determined directly from the spectrum.

At heights below about 140 km, where the ion-neutral collision frequency greatly exceeds the ion-acoustic frequency, ion-acoustic waves cease to propagate and the ion spectrum narrows into a single hump. Assuming equal ion and electron temperatures allows the ion-neutral collision frequency to be determined from the spectral shape. The assumption of equal temperatures restricts this technique to altitudes below about 120 km.

Additionally, the plasma lines can become enhanced by precipitating suprathermal electrons, and measurement of these lines can provide information on the spectrum of the precipitating particles. Finally, it is possible that an electric current density could be directly determined from measurements of any difference between the Doppler shifts of the ion and electron lines of the spectrum.

A number of other ionospheric and neutral atmosphere parameters can be determined from those directly obtained from the incoherent scatter spectrum. Typically, the electric field and the Hall and Pedersen conductivities are derived. Table 3.1 lists these and some other parameters that can be determined from incoherent scatter.

Table 3.1 Parameters obtained from incoherent scatter measurements

Directly Measurable	Indirectly Derived
Electron Density, N_e	Neutral Density, N_n
Electron Temperature, T_e	Neutral Temperature, T_n
Ion Temperature, T_i	Electric Field, E
Ion Drift Velocity, v_i	Neutral Velocity, U
Ion Mass, m_i	Ionospheric Conductivities, Σ_P, Σ_H
Ion-Neutral Collision Frequency, ν_{in}	Current Density, j
Photoelectron Flux	Heat Flux, Φ

3.2.2 Measurement Techniques

In practice, incoherent scatter radars generate autocorrelation functions (ACF's) from the received signals, from which plasma parameters are recovered. The ACF and the incoherent scatter spectrum constitute a Fourier pair.

The received pulse is sampled at discrete intervals and, in the simplest case, the samples are "gated" over a time τ . Cross products are formed from samples within a gate to produce *lags* of different intervals. Multiple estimates of each lag are combined to form the measured ACF. Figure 3.4 illustrates ACF formation for a single pulse of length τ , where the receiver is gated such that the signal is scattered from a mean range R . It is apparent that there are fewer estimates of the longer lags, greatly reducing the signal to noise ratio (SNR) for these longer lags. Also, the range of heights which the different lags cover decreases with lag number, introducing an uneven spatial distribution for different lags within the ACF. These problems can be overcome by gating after the evaluation of cross-products, which allows greater flexibility in the formation of the ACF's.

Considering the simple case of a single pulse monostatic system, there are a number of constraints on the form of the transmitted pulse, arising primarily from the need for good SNR and adequate height resolution. If the receiver is gated over a time τ then there are contributions to the returned signal from a height range $c\tau$, yielding a height resolution of $c\tau/2$, where c is the speed of light in free space (see Figure 3.4). This range must be less than the ionospheric scale height (H) in order that altitude variations are adequately described. For vertical transmission the pulse length should therefore be shorter than $2H/c$, although higher spatial resolution and hence shorter pulse lengths are often required for the study of small scale features such as sporadic E-layers. In addition, the pulse length and the receiver recovery time set a minimum range from which echoes can be received, the height of which is increased if several pulse schemes are transmitted within the pulse repetition period (prp). Furthermore, sampling is continued after the last signal gate to obtain background noise from altitudes where the signal component is negligible, in order that the background can be subtracted during analysis. The maximum range from which the signal is received sets a lower limit on the prp.

The above criteria mean that short pulse-lengths are desirable, but conflicting requirements place lower limits on the pulse length. The signal to noise ratio is directly proportional to the pulse length, τ . In the particular case of the EISCAT radar, for example, the SNR from a mean range R over the bandwidth of the ion line spectrum is given by (*Rishbeth and Williams, 1985*)

$$\text{SNR} = \frac{P_s}{P_n} \propto \frac{\hat{P}\tau N_e}{R^2 [1 + (T_e/T_i)]} \quad (3.8)$$

where P_s is the signal power, P_n is the noise power and \hat{P} represents the peak transmitter

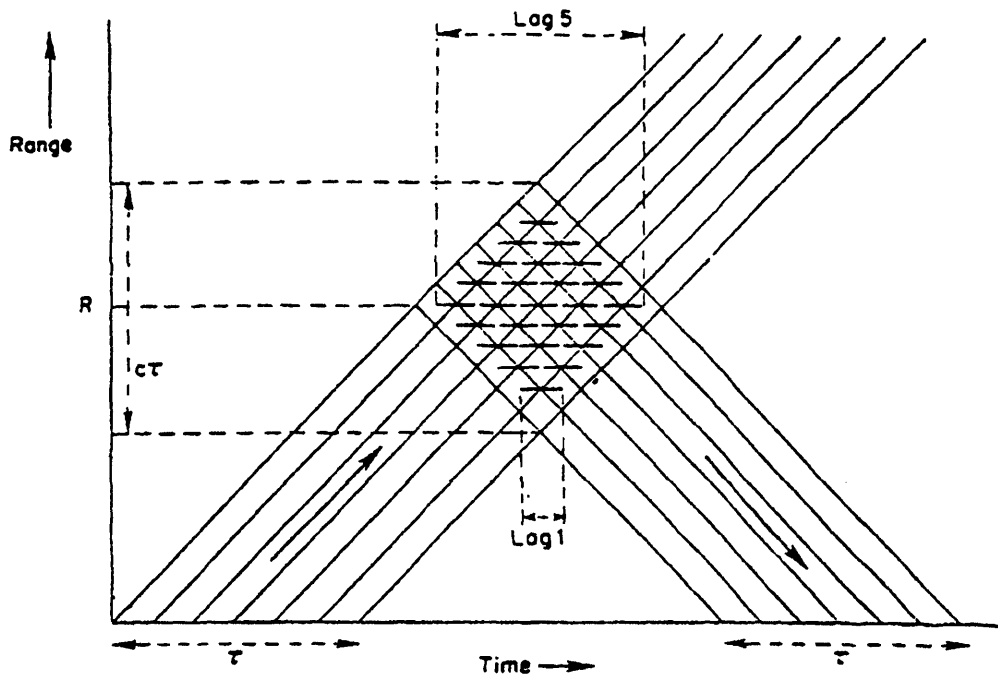


Figure 3.4 Range-time diagram illustrating ACF lag formation for a single pulse; as described in section 3.2.2 (*Rishbeth and Williams, 1985*).

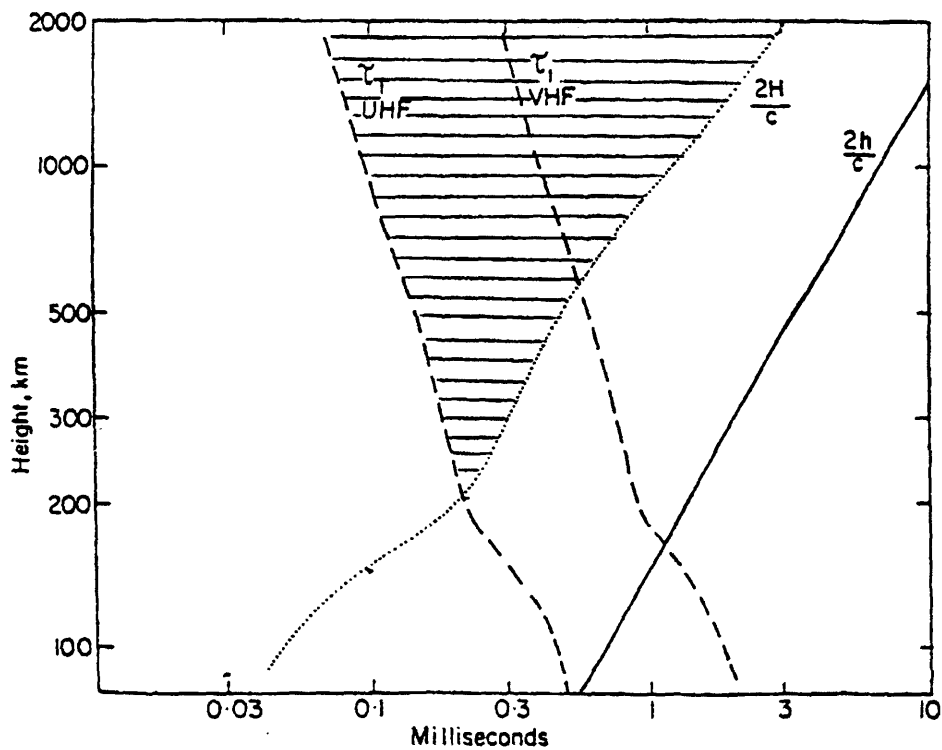


Figure 3.5 Constraints on allowed pulse lengths for EISCAT experiments. Pulse time-of-flight = $2h/c$; pulse length giving resolution equal to scale height (ie. minimum useful height resolution) = $2H/c$; ionospheric correlation times for UHF and VHF radars = τ_1 . Pulse lengths for UHF experiments must be greater than $\tau_1(\text{UHF})$ and less than $2H/c$ (*Rishbeth and Williams, 1985*).

power. For a pulsed radar, the accuracy of the returned power is related to τ by the following expression

$$\frac{\Delta P_s}{P_s} = \frac{1 + \text{SNR}^{-1}}{(b\tau N)^{\frac{1}{2}}} \quad (3.9)$$

where b represents the filter bandwidth and N the total number of pulses integrated. The uncertainties in the other derived parameters are also inversely proportional to τ , as indicated by equation 3.10 (see section 3.3.3). The fundamental need to maximise the SNR therefore makes longer pulses desirable. Furthermore, to obtain maximum spectral resolution the pulse length, τ , must be greater than the correlation time of the ionosphere, which is equivalent to the reciprocal of the ion-line bandwidth. Figure 3.5 illustrates how, for a vertically transmitted pulse, the conflicting requirements of adequate spectral resolution and height resolution constrain the pulse length for the EISCAT UHF and VHF radars. For multistatic observations the constraints tend to be less severe. The intersection of the beams provides a spatial resolution which is usually less than the scale height, allowing a long pulse to be transmitted, thus affording adequate spectral resolution.

Where single pulse schemes are unsuitable, a variety of multiple-pulse or alternating code pulse schemes may be employed. Multi-pulse schemes consist of a series of short subpulses, which provide the required height resolution, transmitted at variable intervals within an envelope of sufficient duration to provide the necessary spectral resolution (*Farley, 1972*). Figure 3.6 illustrates the nature of a simple multi-pulse scheme. Four subpulses are transmitted at times 0 , τ' , $4\tau'$ and $6\tau'$ within an envelope of duration τ . Thus lags of τ' to $6\tau'$ can be calculated, affording a height resolution corresponding to τ' , but with the spectral resolution of a pulse of length τ . Multi-pulse schemes suffer from relatively poor SNR, caused primarily by clutter of the signal due to scatter from ranges other than R , as illustrated in Figure 3.6. If the lag interval is at least $2\tau'$ then this self-clutter is uncorrelated and does not contribute to the ACF. Another disadvantage of multi-pulse schemes is the lack of a true zero lag, although sometimes this can be provided by transmitting a single pulse of length τ at another frequency.

Further improvements in height resolution may be achieved by reversing the phase of the transmitted signal for some of the subpulses, according to a series of Barker codes (*Barker, 1958; La Hoz, 1982*). Similar phase changes in the receiver have the effect of concentrating most of the power of the pulse group into the height range corresponding to one element.

Extremely high spatial resolution in conjunction with good spectral resolution and signal to noise ratio can be achieved with alternating codes (specific to the EISCAT system), whereby continuous sequences of subpulses of length τ' are phased such that a full ACF can

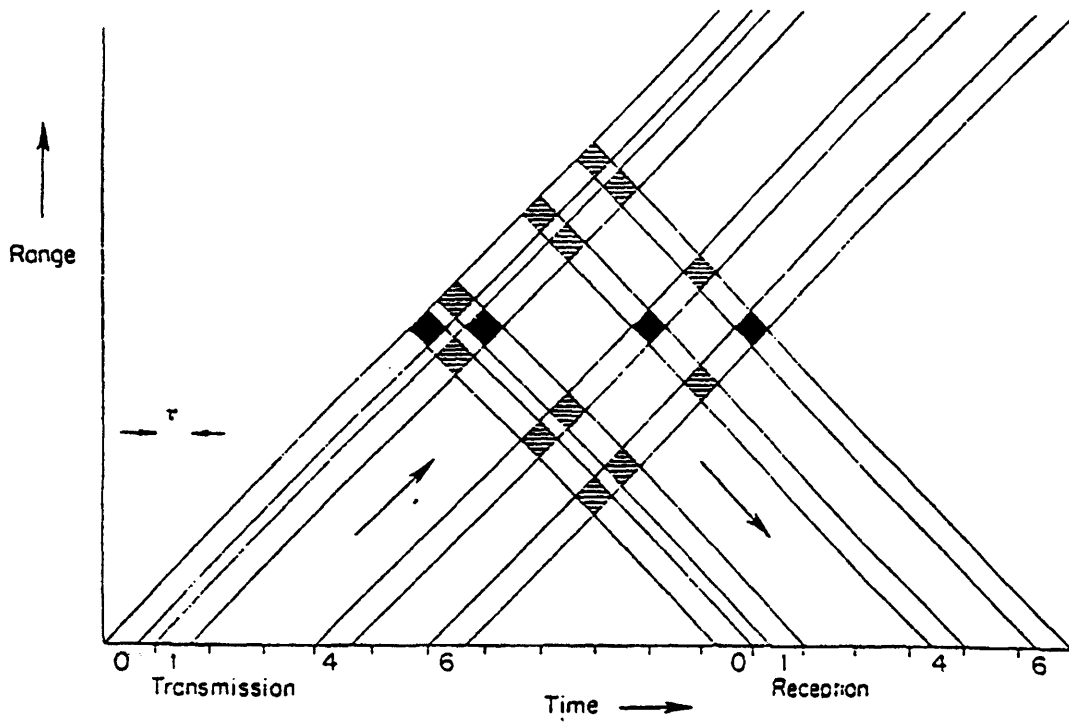


Figure 3.6 Range-time diagram for a simple 4-pulse multi-pulse scheme; as described in section 3.2.2 (*Rishbeth and Williams, 1985*).

be obtained from a range with an altitude resolution corresponding to a single sample interval (*Lehtinen and Haggstrom, 1987*).

3.3 The European Incoherent Scatter Facility

The European Incoherent Scatter (EISCAT) facility consists of three radars, a tristatic UHF system, a monostatic VHF system and a monostatic UHF radar. In addition, the EISCAT Association runs a dynasonde and HF heater. The tristatic UHF radar commenced full operation in 1982, whilst VHF radar observations are available from 1985 to the present. Operation of the new monostatic UHF system, situated on the Svalbard archipelago, has recently commenced. As yet, little data are available from this radar, and further discussion will be limited to the established systems; the UHF tristatic radar will henceforth be referred to simply as the UHF radar. Figure 3.7 illustrates the geographic locations of the EISCAT antennas. The VHF system has both transmitter and receiver co-located in Tromsø, Norway. The UHF radar also transmits from and receives at Tromsø, with receivers also sited in Kiruna, Sweden and Sodankylä, Finland. There follows a brief description of the general characteristics of these radars, and how the received signals are processed to generate the measured autocorrelation functions. More detailed descriptions are available in, for example, *Hagfors et al. (1982)*, *Folkestad et al. (1983)* and *Rishbeth and Williams (1985)*.

The UHF tristatic system. Each of the UHF antennas is a 32m diameter paraboloid with an effective collecting area of 570 m² and a half-power beam width of 0.6°. The antennas are fully and independently steerable in both azimuth and elevation, although the minimum elevation of the Tromsø antenna is limited to 2° above the horizon. The transmitter, powered by a single klystron, is capable of a peak power of about 2 MW on a maximum duty cycle of 12.5%, providing an average power of about 250 kW. The transmitter can operate on any one of 16 frequencies, spaced at 0.5 MHz intervals around the central frequency of 933.5 MHz. The frequency can be changed on timescales of order microseconds, although only eight separate channels are available for reception.

The system noise temperature is around 90-110 K at Tromsø and 30-35 K at Kiruna and Sodankylä. The remote sites receive elliptically polarized signals, corresponding to the transmission of circular polarization at Tromsø. The received signal is mixed down to 120 MHz, then attenuated and divided between the 8 channels. The signal in each channel is mixed down to 30 MHz and bandpass filtered. After further mixing and baseband filtering the signal is amplified; finally, sine and cosine inputs are fed into the analogue-to-digital converter (ADC). The signal is then sampled; to obtain the maximum amount of information, the sampling rate should be equivalent to twice the signal bandwidth (*Shannon, 1948*). The maximum sampling rate is 500 kHz, although sampling up to 10 MHz is possible in specific channels. The output from the ADC is then delivered to the correlator.

The UHF radar wavelength of approximately 30 cm is suitable for incoherent scatter

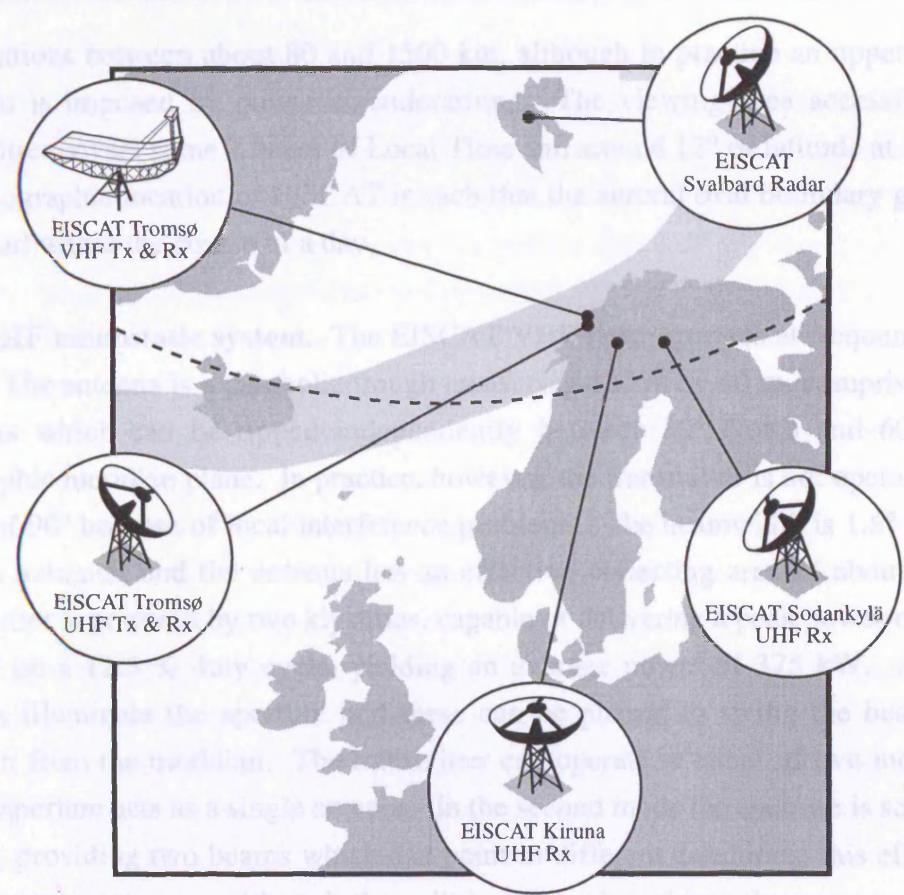


Figure 3.7 Illustration of the location of the EISCAT UHF and VHF antennae. The shaded region indicates the approximate location of the auroral region under quiet geomagnetic conditions at 0000 UT.

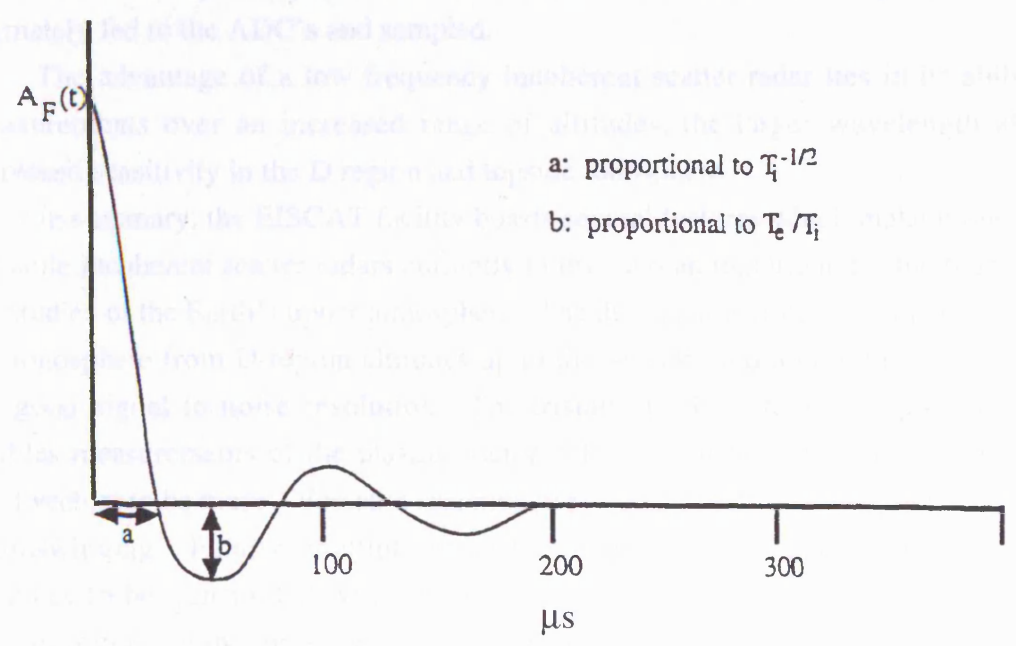


Figure 3.8 Schematic illustration of an ACF, indicating how initial quick-fit parameters are obtained.

observations between about 80 and 1500 km, although in practice an upper limit of around 600 km is imposed by power considerations. The viewing area accessible to the UHF transmitter covers some 2 hours of Local Time and around 12° of latitude at 300-km altitude. The geographic location of EISCAT is such that the auroral oval boundary generally sweeps overhead within the course of a day.

The VHF monostatic system. The EISCAT VHF radar operates at frequencies around 224 MHz. The antenna is a parabolic trough measuring 120 m by 40 m, comprised of four equal sections which can be tipped independently between 30° North and 60° South in the geographic meridian plane. In practice, however, the transmitter is not operated at elevations south of 90° because of local interference problems. The beamwidth is 1.8° in elevation and 0.6° in azimuth, and the antenna has an effective collecting area of about 3100 m^2 . The transmitter is powered by two klystrons, capable of delivering a peak power of approximately 3 MW on a 12.5 % duty cycle, yielding an average power of 375 kW. An array of 128 dipoles illuminate the aperture and these can be phased to swing the beam up to 21° in azimuth from the meridian. The transmitter can operate in either of two modes; in one, the whole aperture acts as a single antenna. In the second mode the aperture is separated into two halves, providing two beams which can point in different directions; this effectively creates two separate antennas, although the split beam mode reduces the power received by each antenna by a factor of four.

Reception in the VHF radar is analogous to that in the UHF. The system noise temperature of the VHF system is around 250-300 K, which is adequate considering the higher level of sky noise at VHF. As with the UHF receivers, the processed signals are ultimately fed to the ADC's and sampled.

The advantage of a low frequency incoherent scatter radar lies in its ability to make measurements over an increased range of altitudes, the larger wavelength allowing for increased sensitivity in the D region and topside ionosphere.

In summary, the EISCAT facility boasts several features which make it one of the most versatile incoherent scatter radars currently in use, and an important ground based instrument for studies of the Earth's upper atmosphere. The dual nature of the system enables probing of the ionosphere from D-region altitudes up to the topside, and high transmitter power allows for good signal to noise resolution. The tristatic UHF system is at present unique, and enables measurements of the plasma vector velocity, temperature anisotropies and electric field vectors to be made. Versatile scanning experiments are possible with the option of rapid beamswinging. Finally, multiple frequency operation allows for combinations of pulse schemes to be transmitted within a single prp, allowing for simultaneous probing of the various regions of the ionosphere at high time resolutions. The development of the EISCAT facility and some of its scientific achievements are reviewed by *Rishbeth and Van Eyken (1993)*.

3.3.1 EISCAT Programmes

EISCAT time is apportioned equally between the operation of Special Programmes, designed and run by scientists from individual associate member countries, and Common Programmes, which are run routinely by EISCAT staff. The purpose of Common Programmes is to provide a long-term and consistent data base of general use to all associates. Over the years, new Common Programmes have been introduced and all have undergone refinement. At present there are seven Common Programmes, four for the UHF system (CP-1, 2, 3 and 5) and three for the VHF radar (CP-4, 6 and 7). There follows a brief description of those Common Programmes from which data presented in this thesis were obtained.

Common Programme 1, as with its forerunners CP-0 and CP-M1, is a fixed pointing-direction experiment in which the transmitter beam is approximately aligned along the geomagnetic field direction. The experiment was designed to provide high time resolution observations of dynamic phenomena such as auroral arcs. In its present incarnation, CP-1-K, the remote site antenna beams intersect the Tromsø beam at 278-km altitude; previous versions also incorporated four pointings in the E region. CP-1 takes full advantage of the frequency agility of EISCAT, transmitting long-pulse, power profile and alternating code pulse schemes. CP-1-type experiments have been operated regularly since about 1982, providing a large and consistent data base of measurements. CP-1 observations provided the majority of the data employed in the statistical analysis described in *Chapter 5*, and were also used for the modelling study of *Chapter 6* of the present thesis.

Common Programme 2 performs a rapid four position scan of the transmitter, including one field-aligned and one vertical position, the remaining two to the south and south-east of the vertical. In the present version of the experiment, the remote antennas follow the scan, observing the transmitter beam at 278-km altitude. The dwell time is 1.5 minutes at each position. CP-2 transmits the same pulse schemes as CP-1. Common Programme 2 and its earlier versions, including CP-M2, were designed to resolve spatial and temporal variations in wave-like phenomena, hence the short cycle time of 6 minutes. Both vertical and field-aligned observations from CP-2 were employed in the statistical study (*Chapter 5*).

Common Programme 7 is a VHF experiment designed to make high altitude observations, facilitating, for example, studies of plasma outflows in the topside ionosphere. The transmitter points at 90° elevation, and under favourable conditions can receive signal from around 300 km to beyond 1500-km altitude. CP-7 transmits long-pulse and power profile schemes. Data from this experiment were used to provide high-altitude observations for the statistical study of *Chapter 5*.

Of the other Common Programmes, CP-3 performs a 26 minute, sixteen position latitude scan in the meridian plane, with the remote site antennas following the scan as in CP-

2. CP-5, a little run experiment, is similar to CP-3 but with fewer positions in the scan and an extended dwell time in the field-aligned position. The two remaining experiments, CP-4 and CP-6, are VHF programmes. CP-4 is a split-beam experiment based on the old UK Special Programme POLA, whilst CP-6 was designed for mesospheric and D-region studies, employing Barker coding to obtain an altitude resolution of order 1 km. On occasion, UHF and VHF programmes are run simultaneously, such as CP-1 with CP-7.

In addition to the seven Common Programmes, there are three Unusual Programmes. These are designed for the study of specific ionospheric phenomena such as sporadic E-layers, and can be run at very short notice when appropriate conditions arise.

3.3.2 Analysis of EISCAT Data

Thus far, the theory of incoherent scatter has been outlined, highlighting the dependence of the incoherent scatter spectrum upon various ionospheric parameters. The practical application of the technique has been discussed, with particular reference to the EISCAT radar. The final stage of the process is the retrieval of ionospheric parameters from the spectrum or, equivalently, the ACF. Autocorrelation functions are formed in the correlator. The correlator is a dedicated computer system that takes the samples output by the ADC (see section 3.3) and computes autocorrelations, cross-correlations or pulse profiles, depending on the pulse pattern. At this stage, identical measurements from different channels may be added together to reduce the level of uncorrelated noise. Similarly, successive correlator dumps are integrated, typically over 5 to 10 seconds; this pre-integration period sets the maximum temporal resolution for the experiment. A zero lag might be inserted into the ACF for multi-pulse or alternating code measurements, and other corrections such as the removal of satellite echoes may be necessary. Finally, the ACF's are written to a permanent storage medium.

A number of instrumental effects influence the form of the measured ACF, which must therefore be corrected prior to parameter fitting. The three main effects arise from the form of the transmitted pulse, the weighting of the lags during correlation and the receiver response. The ACF of the scattered pulse is the product of the ACF of the transmitted pulse and the incoherent scatter ACF. Further modification of the function occurs in the receiver, the output of which is equal to the convolution of the received ACF and that of the baseband filter. Finally, the correlator will introduce effects due to weighting of the lags caused by gating of the samples prior to cross-correlation. This latter effect has been much alleviated since the introduction, in 1984, of the GEN system of correlator programs, which allow gating after the evaluation of cross products (*Turunen, 1986*). The effects of the instrument on the measured ACF are addressed in some detail by *Rishbeth and Williams (1985)*.

Each of these known instrumental effects can be removed, after which the background noise is subtracted from each signal gate. An estimate of the background level is obtained from samples taken beyond the farthest signal gate. The resulting signal ACF's are then suitable for derivation of ionospheric parameters.

Initially, a crude estimate of the electron density is made, based on the backscattered power (equation 3.5), where the system constant is neglected and the ion and electron temperatures are assumed to be equal. Subsequently, the ion velocity may be determined. Bulk plasma motion introduces a Doppler shift to the entire spectrum, which results in an ACF with both real and imaginary components. Using a matched filter procedure, the ion drift velocity may be deduced and its effect removed from the ACF. The resultant real ACF can then be used to determine other ionospheric parameters.

Deduction of parameters proceeds by means of fitting the measured ACF to a theoretical function, corresponding to known plasma parameters. Initially, 'quick-fit' approximations of ion and electron temperatures are assumed, based on the time to the first cross-over and the amplitude of the first minimum in the ACF, as depicted in Figure 3.8. These approximations are used to correct the initial electron density value. A theoretical spectrum is then derived, based on the quick-fit estimates of plasma temperature and electron density. Alternatively, the parameters from a previous fit, or from an adjacent signal gate, may act as initial estimates. The empirical function is compared with the measured function in the time domain and the former iteratively corrected until the variance between the two is less than a specified threshold. If no acceptable fit is achieved within a given number of iterations, as defined by the analyst, the process is terminated and no parameters are returned.

Generally, estimates of four parameters are obtained on a routine basis: electron density, ion and electron temperatures and ion drift velocity. Other parameters, such as ion-neutral collision frequency and ion composition, may be determined, although, as described earlier, this is possible only under favourable conditions.

3.3.3 Uncertainties in Derived Parameters

For a quantitative interpretation of incoherent scatter measurements, it is necessary to appreciate the uncertainties in the derived parameters. This requires an awareness of the possible sources of error, the most significant of which are addressed below.

Random error. A variety of empirical relationships have been established which relate the random error in a given plasma parameter to the received signal to noise ratio. *Du Castel and Vasseur (1972)* concluded that random uncertainties in plasma temperature measurements and electron density values were related to the error in signal power by

$$\frac{\Delta P_s}{P_s} \approx \frac{\Delta N_e}{N_e} \approx \frac{\Delta T_e}{2T_e} \approx \frac{\Delta T_i}{2T_i} \quad (3.10)$$

where $\Delta P_s/P_s$ is defined in equation 3.9. The error in the line of sight ion velocity, v_i , is expressed as

$$\Delta v_i = (0.5 + \text{snr}^{-1}) \frac{\lambda}{2} \frac{\Delta F_i}{(b\tau N)^{\frac{1}{2}}} \quad (3.11)$$

ΔF_i is the ion line half-width, which is approximately equal to twice the ion-acoustic frequency (equation 3.2). *Murdin (1979)* derived similar relationships, based on a simulated data set, with the exception of the electron density error which was found to be twice that given by *Du Castel and Vasseur (1972)*. An experimental determination of random uncertainties in electron density, plasma temperatures and ion velocity was undertaken by *McCrea (1989)*, and the results found to be in reasonable agreement with those of other workers (eg. *Williams et al., 1984; Jones et al., 1986*). Although there is some variation between all the estimates, each agrees that the random error is inversely proportional to a factor $(\text{SNR} \cdot \sqrt{N})^{-1}$. Random errors presented in this thesis are based on the relationships of *Du Castel and Vasseur (1972)*.

Fit error. As described previously, parameters are retrieved from analysis of EISCAT data by minimising the variance between the measured ACF and a theoretical function. In the case of the analysis program employed in the present study, the sum of the residuals between the two functions is used to calculate an uncertainty in each derived parameter. This uncertainty is referred to as the fit error; it is typically less than the random error, but the two may be combined to give an overall error estimate.

Error due to non-Maxwellian velocity distribution. Standard EISCAT analysis assumes Maxwellian velocity distributions for ions and electrons along the radar line-of-sight. The presence of a relative velocity between the ions and neutrals may cause the line-of-sight ion velocity distribution to depart from the Maxwellian (eg. *Cole, 1971; St. Maurice and Schunk, 1979; Hubert and Kinzelin, 1992*). The effect is particularly pronounced for high ion-neutral relative velocities and large aspect angles (*Lockwood et al., 1987*). During such intervals, the form of the ion velocity distribution is generally not well known, depending largely on the species and type of collision involved. A non-Maxwellian velocity distribution tends to distort the IS spectrum, producing a maximum, or at least a reduced minimum, about the central frequency (*Raman et al., 1981*), and increasing the backscattered power (*Lockwood et al., 1988*). Analysis of such a spectrum, assuming a Maxwellian thermal velocity distribution, tends to overestimate the line-of-sight ion temperature and underestimate the electron temperature (eg. *Lockwood et al, 1988; Moorcroft and Schlegel, 1989; McCrea, 1989*). A number of workers have successfully retrieved reasonable parameters from such spectra by assuming non-Maxwellian velocity distributions based on simple collision models (eg. *Winser et al., 1987*). Further errors may arise if, as suggested by *Maehlum et al. (1984)*, the thermal electron distribution does not remain isotropic within regions of field-aligned currents.

Error due to ion composition. Standard analysis of EISCAT data generally adopts a model for ion composition in order to retrieve the ion temperature. The model specifies a time-invariant profile of the relative concentrations of ions as a function of altitude, as illustrated in Figure 3.9. The actual composition profile is sensitive to diurnal and seasonal variations. Nevertheless, for undisturbed conditions, the adopted model is largely representative of the true ion composition profile. However, the ion composition can become significantly modified during active conditions, for example through increased reaction rates during intervals of ion frictional heating and as a result of transport processes (eg. *St.-Maurice and Torr, 1978; Raitt et al., 1975*). These effects are generally most marked between 150 and 300-km altitude, where enhanced temperature may increase the relative proportion of molecular ions through recombination (eg. *Lathuillère, 1987*). An underestimate of the fractional content of molecular ions results in underestimates of ion and electron temperatures, by a fraction approximately equal to the ratio between the real and assumed ion masses (*Lockwood et al., 1993*). Since disturbed conditions are often the subject of detailed quantitative analysis, the possible errors inherent in the assumption of a composition profile must be considered. The effects of ion composition modification on parameters derived from IS analysis is addressed in more depth in *Chapter 6* of this thesis. It should be noted that the adoption of a model is not the sole method of obtaining ion mass. A number of workers (eg. *Lathuillère et al., 1983*) have deduced the composition profile directly from EISCAT measurements, as described in section 3.2.1.

Error due to single temperature analysis. Under conditions of relative ion-neutral flow, the different ion-neutral collision frequencies of each species in a multi-ion plasma results in the divergence of their respective temperatures (*Hubert and Lathuillère, 1989*). The temperature difference is greatest in the direction of the magnetic field line (*Lathuillère and Hubert, 1989*). Moreover, the measured line-of-sight ion temperature is not simply a weighted mean of the temperature of each species. However, standard EISCAT analysis assumes that the line-of-sight temperatures of all species are equal. Ion temperature measurements derived from such a single temperature analysis may therefore be inaccurate during intervals of relative ion-neutral flow, particularly when significant proportions of more than one ion are present. The limitations of EISCAT analysis during intervals of high ion-neutral relative velocity are addressed in more detail by *McCrea (1989)* and *McCrea et al. (1995)*.

3.4 Summary

In this chapter, the process of incoherent scatter of radio waves by acoustic waves in the ionosphere has been outlined. The application of this phenomenon to ground based investigations of the Earth's upper atmosphere has been described, with particular reference to the EISCAT radar, detailing how a number of atmospheric parameters may be obtained

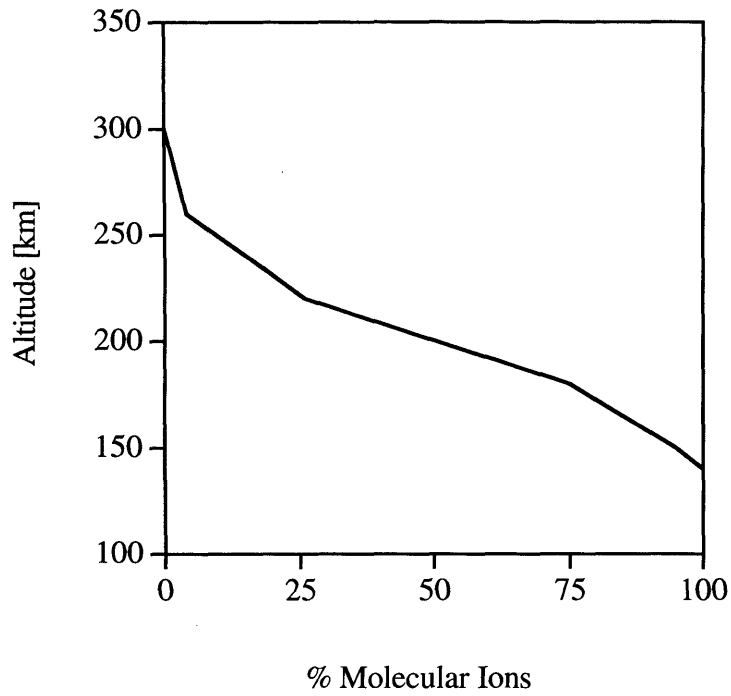


Figure 3.9 Illustration of the ion composition model adopted for standard EISCAT analysis, showing how the proportion of molecular ions varies as a function of altitude. The molecular species assumed present are NO^+ and O_2^+ in the ratio 3:1, with the atomic population consisting of O^+

using the technique. The general characteristics of the EISCAT UHF and VHF systems have been summarized, and the processes of data retrieval and analysis outlined. The uncertainties inherent in incoherent scatter data have been addressed, arising from both the measurement and analysis of the received spectra. A brief description of EISCAT Common Programmes has also been presented.

CHAPTER 4

EISCAT Observations of Nightside Auroral Plasma Upflows in the F-region and Topside Ionosphere

4.1 Introduction

This chapter presents EISCAT observations of three events of ion upflow detected during a six hour run of the UK special programme UFIS. The UFIS programme provided vertical observations through the E-region to the topside ionosphere. In addition, tristatic UHF measurements were made at 315-km altitude. A more detailed description of the UFIS programme is given in the following section.

Three intervals of transient ion upflow were observed during a six hour interval from 2100 UT on 17 January, 1990. One event was clearly associated with electron precipitation. F-region observations of an enhanced perpendicular electric field and ion heating are consistent with upward acceleration resulting from thermal plasma expansion; at higher altitudes the upflow is thought to have resulted from electron heating and field-aligned currents. A later event exhibited vertical ion velocities of similar magnitude, again associated with an elevated electron temperature, but in this case there was no evidence of significant ion heating. A third event observed above about 600-km altitude was apparently unaccompanied by lower altitude upflows, although the vertical field-of-view could not provide simultaneous measurements along the same field-line at lower altitudes, rendering the experiment insensitive to possible temporal variations within a field-aligned structure.

These observations illustrate some of the ion energization processes which can occur at different altitudes within the structure of an auroral arc, and are consistent with the measurements reported by *Wahlund et al. (1992, 1993)* and with the theoretical work of *Blelly et al. (1996)*.

4.2 Experimental Configuration

The UK EISCAT Special Programme UFIS was designed to provide observations of upward flowing ions in the F-region and topside ionosphere, with both the EISCAT UHF and VHF radars taking simultaneous measurements of the high latitude ionosphere. By necessity, the VHF radar operates at 90° elevation, and in this experiment the UHF radar also points vertically to allow for a continuous range of observations from the E-region into the topside ionosphere. A schematic of the experimental configuration is presented in Figure 4.1.

In the UHF experiment, long-pulses of 350 μ s are transmitted on four channels for F-region observations extending between 150 and 500-km altitude (LP in Figure 4.1). Twelve signal gates are formed using GEN-type weighting (*Turunen, 1986*), resulting in a range increment of approximately 31 km and a range resolution of 84 km. In addition to the long-pulse, a 30 μ s power profile scheme is transmitted for measurements of returned power between 90 and 150 km altitude (PP in Figure 4.1). The remote UHF receiver beams from

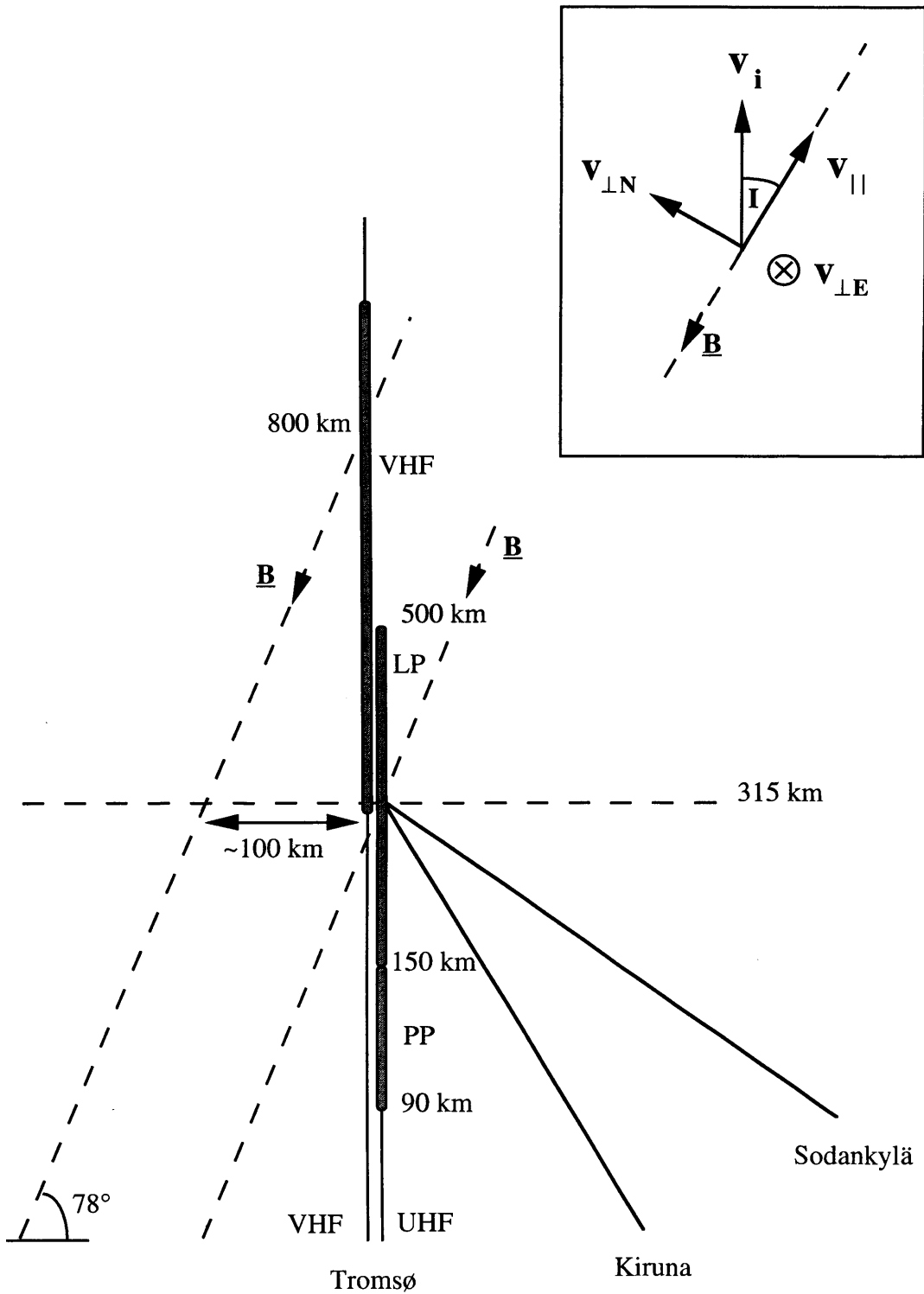


Figure 4.1 Schematic showing the configuration of Special UK EISCAT Programme UFIS. Shaded areas indicate the altitude ranges of observations of the UHF and VHF radars (LP = Long-pulse, PP = Power profile). Inset shows the parallel, perpendicular and vertical components of velocity with respect to the geomagnetic field.

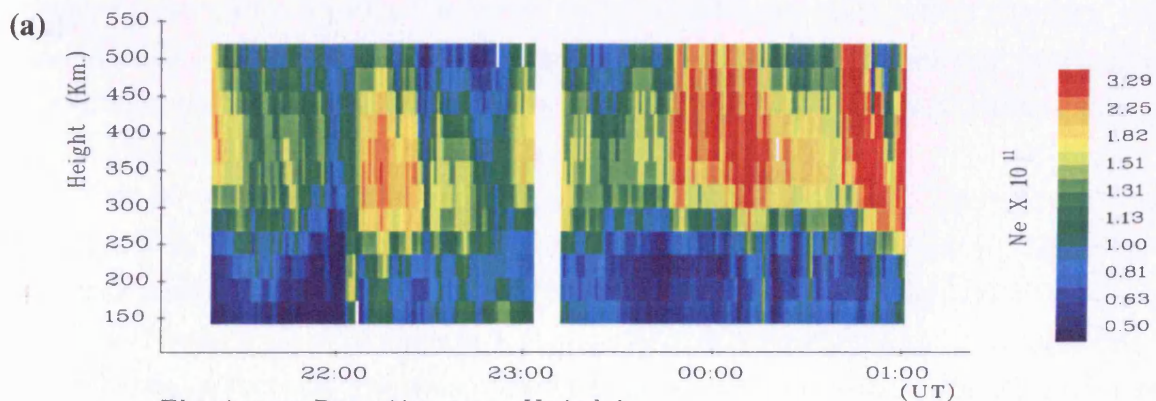
Kiruna and Sodankylä intersect the Tromsø beam at an altitude of 315 km, enabling the full ion vector velocity to be calculated at this height. The VHF system transmits 750 μs pulses on two channels for observations between 315 and 1260 km (VHF in Figure 4.1). A total of 15 signal gates are formed at increments of 67.5 km, each with a range resolution of approximately 180 km.

4.3 Observations: Introduction

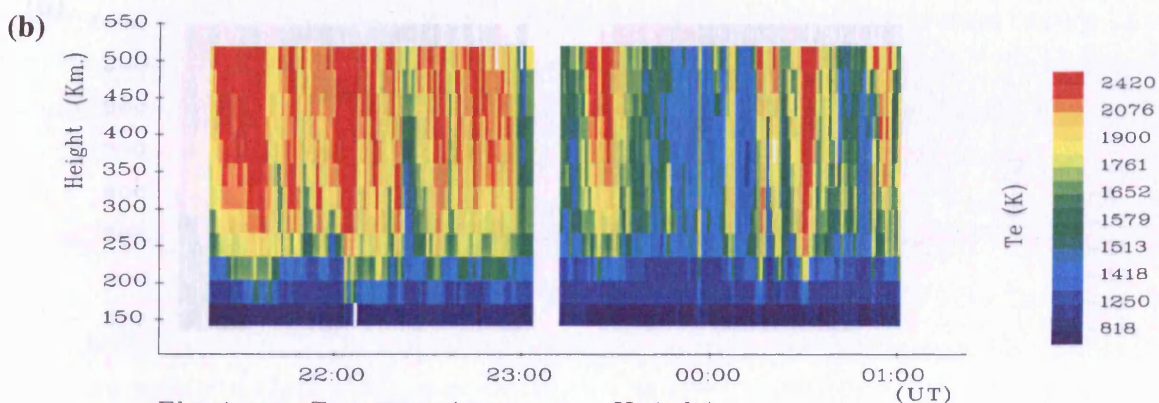
The data discussed here were obtained from a run of UFIS that commenced at 2100 UT on 17 January 1990 and finished at 0250 UT on the following day. The remote site UHF data and the Tromsø VHF data were post-integrated at a resolution of two minutes, whilst the better signal to noise ratio of the Tromsø UHF data permitted analysis at one minute resolution. Where present in figures, uncertainties in the parameters are derived from the formulae of *Du Castel and Vasseur (1972)*, (see section 3.3.3).

Panels (a) to (c) in Figure 4.2 present UHF long-pulse measurements of, respectively, electron density, electron temperature and ion temperature, as observed vertically between 2100 and 0100 UT. UHF and VHF long-pulse observations of vertical ion velocity for the same interval are illustrated in panels (a) and (b), respectively, of Figure 4.3. Positive values of velocity represent flow towards the receiver (ie. vertically downward). A number of intervals of upward vertical ion flow are evident in Figure 4.3, most obviously between 0000 and 0100 UT. However, the scales on these figures do not indicate clearly the magnitudes of the flows. More detailed investigation reveals that large upward velocities (greater than about 100 m s^{-1}) occurred on three occasions, at 2200 UT, 0030 UT and around 0040 UT. These intervals will be discussed in detail in the following sections.

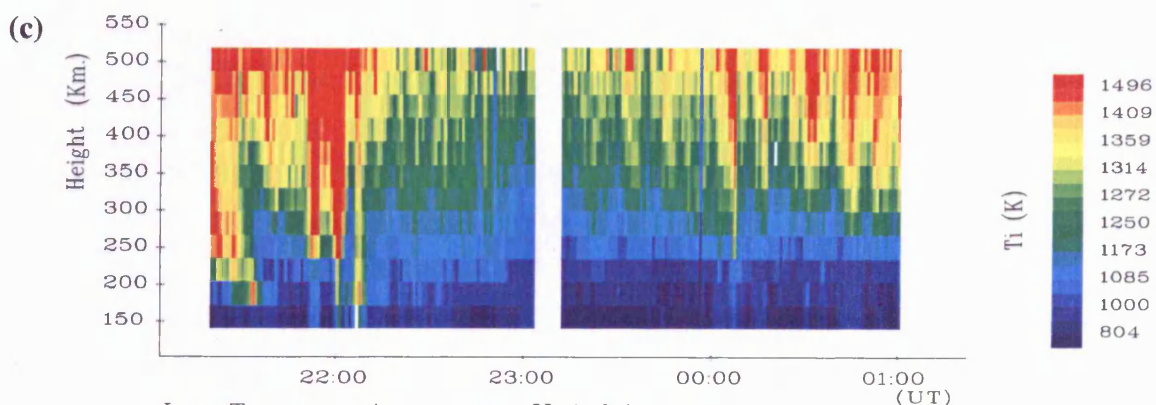
It should be emphasized that the measured velocities were vertical, and not field-aligned. The full ion vector velocity can only be calculated at an altitude of 315 km, where the remote receiver beams intersect the Tromsø UHF beam. However, consideration of the geometry of the system (Figure 4.1 inset) reveals that the zonal component of field-perpendicular velocity, $\mathbf{v}_{\perp E}$, can contribute only up to a few m s^{-1} to the observed vertical velocity, \mathbf{v}_i . The meridional velocity, $\mathbf{v}_{\perp N}$, makes a greater contribution to \mathbf{v}_i . The magnitude of the vertical component of $\mathbf{v}_{\perp N}$ is equal to $\mathbf{v}_{\perp N} \sin I$, or approximately $0.2 \mathbf{v}_{\perp N}$, given that the geomagnetic dip angle, I , is around 12° at the latitude of Tromsø. However, the field-parallel component of velocity makes the greatest contribution to \mathbf{v}_i , the vertical component of \mathbf{v}_{\parallel} being equal to $\mathbf{v}_{\parallel} \cos I$, or approximately $0.98 \mathbf{v}_{\parallel}$. Thus, if the measured value of $\mathbf{v}_{\perp N}$ is small relative to the observed vertical velocity, the latter can be interpreted as an indicator of the magnitude of the field-parallel velocity. Furthermore, if the meridional flow were southward then this would contribute to a downward vertical velocity. Thus the vertical velocities presented in the figures can be considered as *representative* of field-parallel velocities. However, if \mathbf{v}_{\perp} varies with latitude, and since the perpendicular drift-velocities map along



Electron Density vs. Height
 From Tromso 17/01/1990
 az., el. = 182.0 89.9



Electron Temperature vs. Height
 From Tromso 17/01/1990
 az., el. = 182.0 89.9



Ion Temperature vs. Height
 From Tromso 17/01/1990
 az., el. = 182.0 89.9

Figure 4.2 EISCAT SP-UK-UFIS long-pulse observations, 17-18 January 1990; (a) electron density, (b) electron temperature and (c) vertical ion temperature from UHF observations.

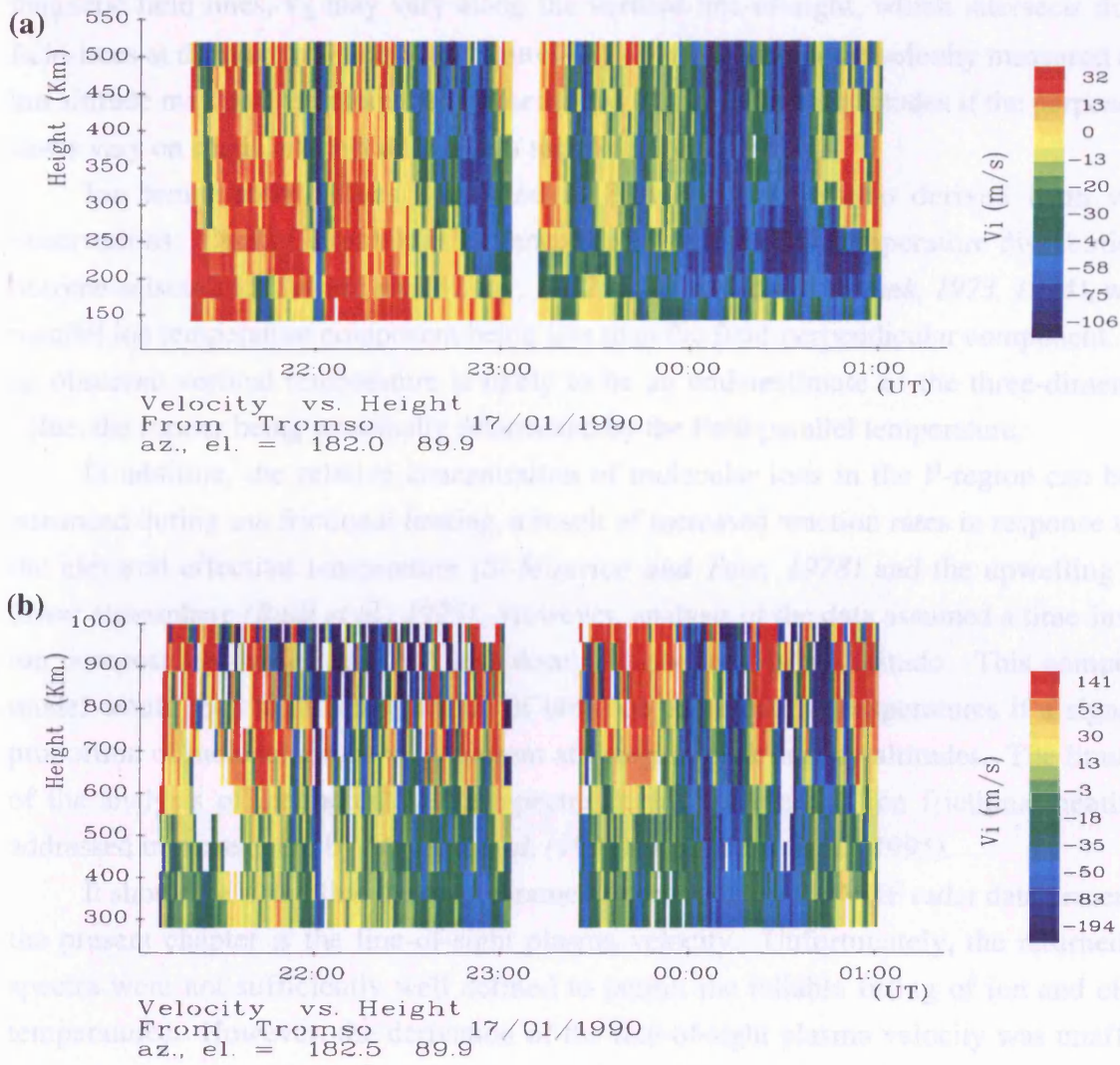


Figure 4.3 Vertical ion velocity from (a) UHF and (b) VHF UFIS long-pulse observations for the same interval as Figure 4.2.

magnetic field lines, v_{\perp} may vary along the vertical line-of-sight, which intersects different field-lines at different altitudes (see Figure 4.1). The perpendicular velocity measured at 315-km altitude may not, therefore, be representative of that at higher altitudes if the perpendicular flows vary on spatial extents of less than approximately 100 km.

Ion temperature values illustrated in Figure 4.2 were also derived from vertical observations. During intervals of enhanced ion flow, the ion temperature distribution can become anisotropic (*Schunk and Walker, 1972; St-Maurice and Schunk, 1973, 1974*), with the parallel ion temperature component being less than the field-perpendicular component. Then, an observed vertical temperature is likely to be an underestimate of the three-dimensional value, the former being principally determined by the field-parallel temperature.

In addition, the relative concentration of molecular ions in the F-region can become enhanced during ion frictional heating, a result of increased reaction rates in response to both the elevated effective temperature (*St-Maurice and Torr, 1978*) and the upwelling of the lower atmosphere (*Raitt et al., 1975*). However, analysis of the data assumed a time-invariant ion composition model, with O^+ ions dominant above 250-km altitude. This composition model would lead to underestimation of both ion and electron temperatures if a significant proportion of molecular ions were present at F-region peak density altitudes. The limitations of the analysis of incoherent scatter spectra during intervals of ion frictional heating are addressed in more detail by *McCrea et al. (1995)* and *Davies et al. (1995)*.

It should be noted that the only parameter derived from the VHF radar data presented in the present chapter is the line-of-sight plasma velocity. Unfortunately, the returned VHF spectra were not sufficiently well defined to permit the reliable fitting of ion and electron temperatures. However, the derivation of the line-of-sight plasma velocity was unaffected. To validate the velocities derived from the VHF radar data, they were compared with those measured by the UHF radar, over the altitude range where both radars observed simultaneously, approximately 315 to 500 km (see Figure 4.1). Figure 4.4 presents time series of velocity as measured by both radars at 300, 400 and 500-km altitude between 2100 and 0100 UT. It is noted that these VHF gates do not give totally independent measurements since the range resolution for the VHF experiment is approximately 180 km. The red lines indicate UHF observations, with associated uncertainties. For clarity, errors in the VHF observations (blue lines) are not marked but are in general greater than those for the UHF measurements. The figure illustrates that, within the uncertainties, the measured velocities are in agreement. Hence it is believed that the VHF line-of-sight velocity measurements are reliable, up to at least 800-km altitude.

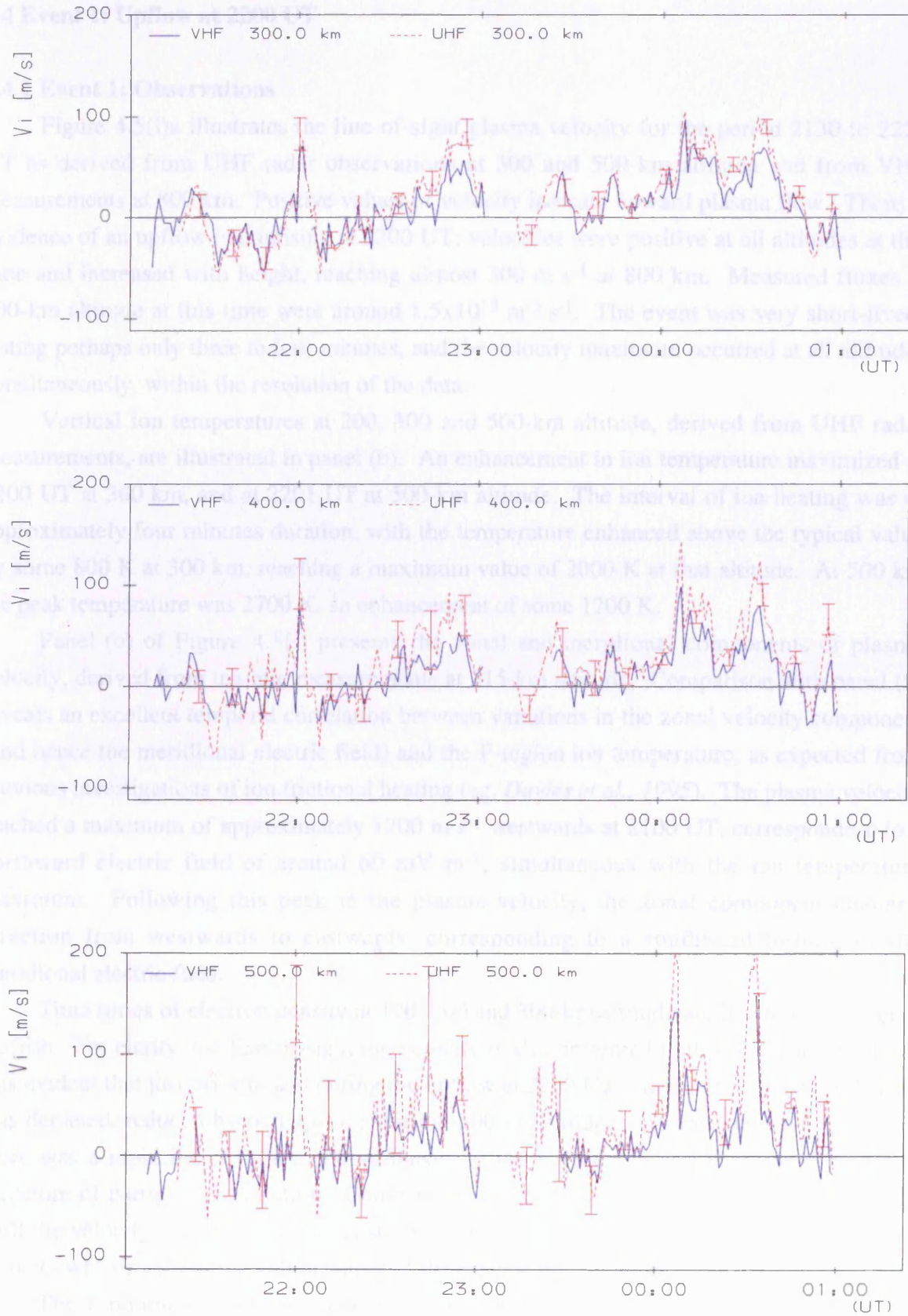


Figure 4.4 Comparison of vertical ion velocity derived from UHF (red) and VHF (blue) UFIS observations at 300, 400 and 500 km altitude.

4.4 Event 1: Upflow at 2200 UT

4.4.1 Event 1: Observations

Figure 4.5(i)a illustrates the line-of-sight plasma velocity for the period 2130 to 2220 UT as derived from UHF radar observations at 300 and 500-km altitude and from VHF measurements at 800 km. Positive values of velocity indicate upward plasma flow. There is evidence of an upflow maximising at 2200 UT; velocities were positive at all altitudes at this time and increased with height, reaching almost 300 m s^{-1} at 800 km. Measured fluxes at 500-km altitude at this time were around $1.5 \times 10^{13} \text{ m}^{-2} \text{ s}^{-1}$. The event was very short-lived, lasting perhaps only three to four minutes, and the velocity maximum occurred at all altitudes simultaneously, within the resolution of the data.

Vertical ion temperatures at 200, 300 and 500-km altitude, derived from UHF radar measurements, are illustrated in panel (b). An enhancement in ion temperature maximized at 2200 UT at 300 km, and at 2201 UT at 500-km altitude. The interval of ion heating was of approximately four minutes duration, with the temperature enhanced above the typical value by some 800 K at 300 km, reaching a maximum value of 2000 K at that altitude. At 500 km the peak temperature was 2700 K, an enhancement of some 1200 K.

Panel (c) of Figure 4.5(i) presents the zonal and meridional components of plasma velocity, derived from tristatic measurements at 315-km altitude. Comparison with panel (b) reveals an excellent temporal correlation between variations in the zonal velocity component (and hence the meridional electric field) and the F-region ion temperature, as expected from previous investigations of ion frictional heating (eg. *Davies et al., 1995*). The plasma velocity reached a maximum of approximately 1200 m s^{-1} westwards at 2100 UT, corresponding to a northward electric field of around 60 mV m^{-1} , simultaneous with the ion temperature maximum. Following this peak in the plasma velocity, the zonal component changed direction from westwards to eastwards, corresponding to a southward turning of the meridional electric field.

Time series of electron density at 120, 200 and 300-km altitude are illustrated in Figure 4.5(ii)b. For clarity, the line-of-sight ion velocity is also presented in this figure as panel (a). It is evident that just prior to and during the upflow at 2200 UT, the F-region electron density was depleted, reduced by perhaps one third at 300-km altitude. At approximately 2205 UT there was a rapid increase in electron density at lower F-region and E-region altitudes, a signature of particle precipitation. Comparison of the electron density at 200 km (panel b) with the velocity components (Figure 4.5(i)c) reveals that the eastward turning of the zonal velocity was simultaneous with the onset of the particle precipitation.

The F-region electron temperature at 200, 300 and 500-km altitude is illustrated in Figure 4.5(ii)c. A substantial increase in electron temperature of some 2000 K was observed at 500 km, with smaller enhancements at 200 and 300 km, concurrent with the reduction in ion velocity and cessation of ion frictional heating, and coincident with the enhancement in

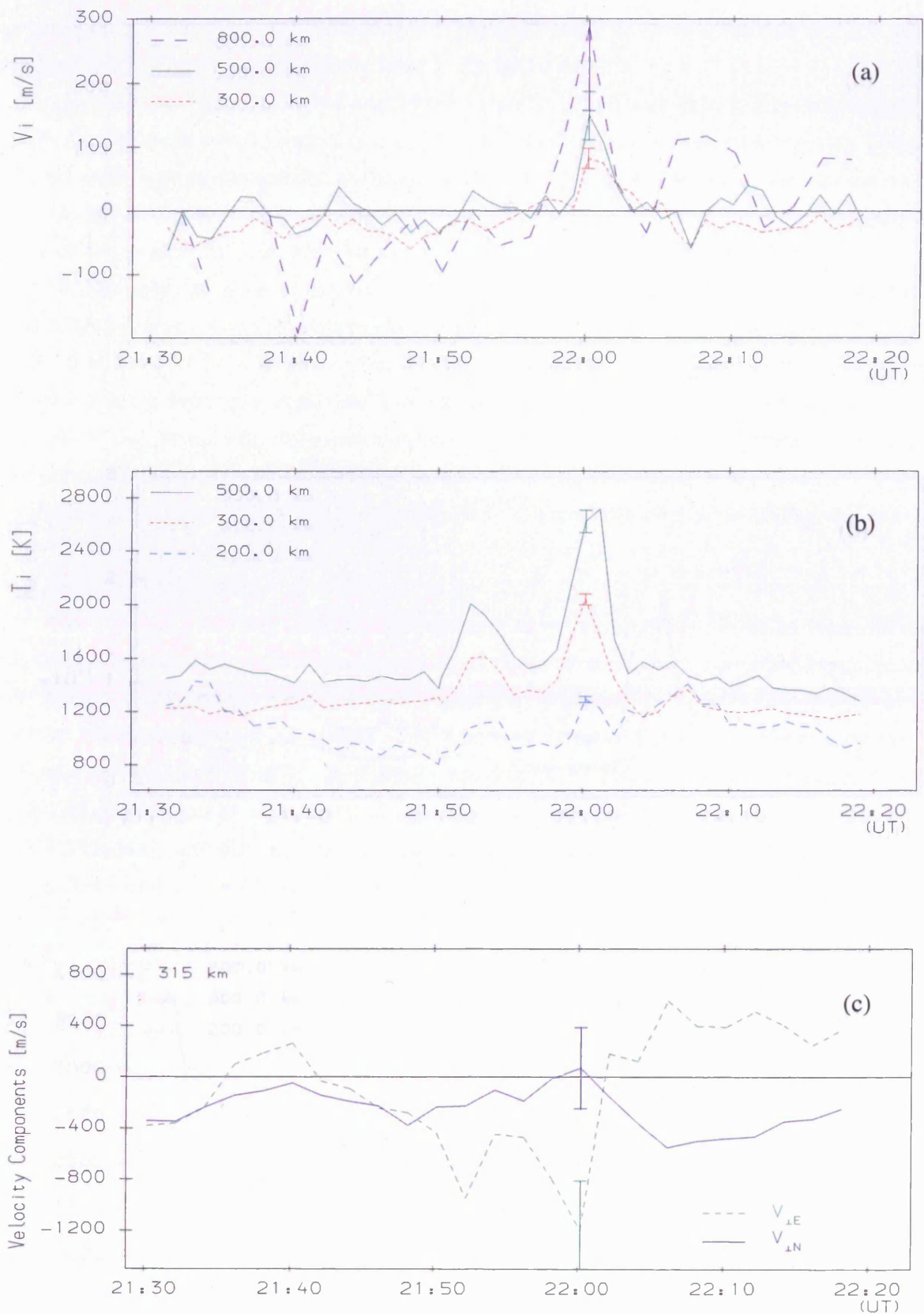


Figure 4.5(i) (a) UFIS UHF (300 and 500 km) and VHF (800 km) measurements of the vertical ion velocity on 17 January 1990. Positive values indicate upward ion flow. (b) UHF measurements of the vertical ion temperature at 200, 300 and 500 km. (c) Zonal and meridional components of ion velocity, calculated from UHF tristatic observations at 315 km altitude.

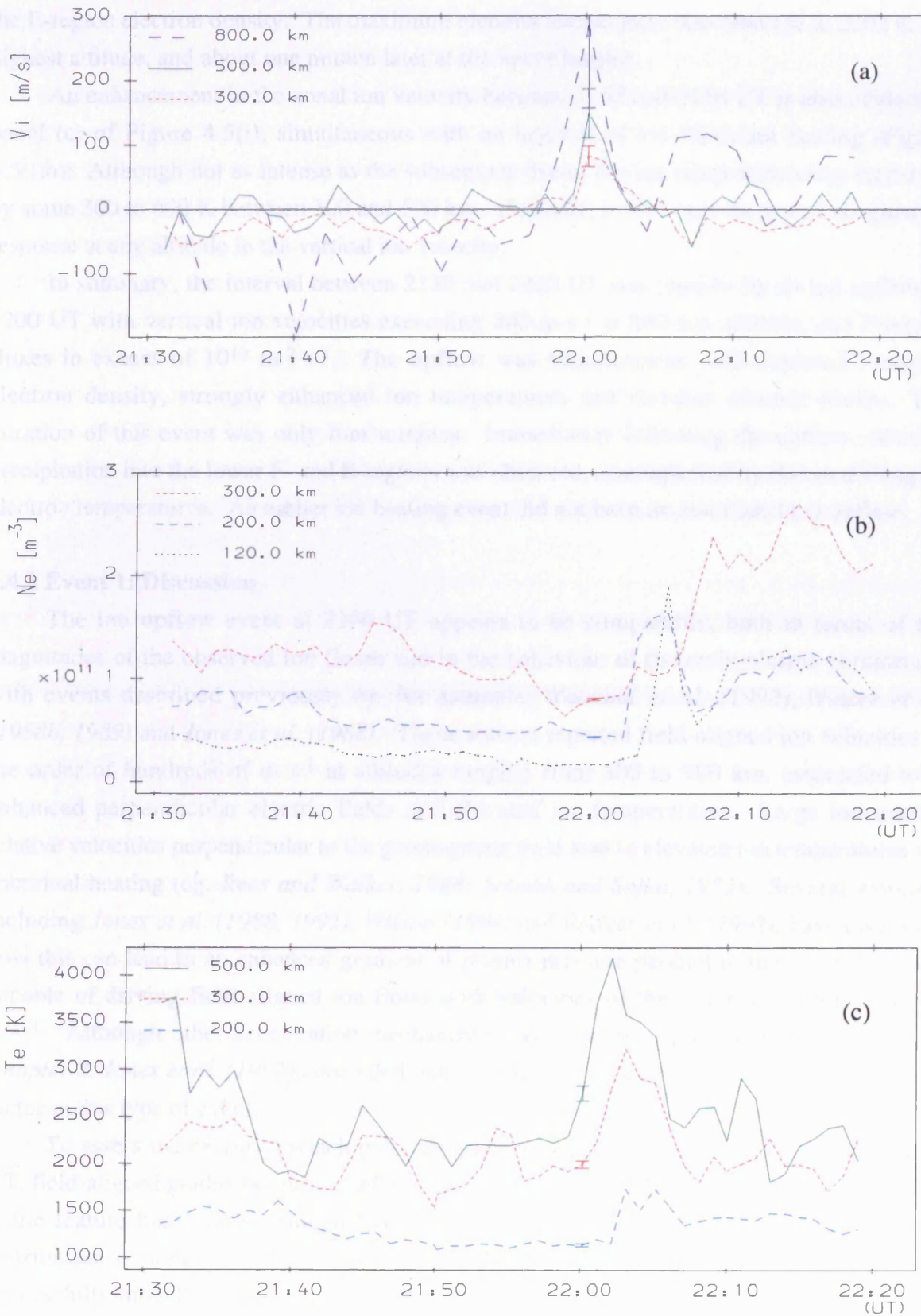


Figure 4.5(ii) (a) Same as Figure 4.5(i)a. (b) UHF long-pulse (200 and 300 km) and power-profile (120 km) measurements of electron density. (c) UHF observations of electron temperature at 200, 300 and 500 km.

the E-region electron density. The maximum electron temperature was detected at 2202 at the highest altitude, and about one minute later at the lower heights.

An enhancement in the zonal ion velocity between 2150 and 2156 UT is also evident in panel (c) of Figure 4.5(i), simultaneous with an interval of ion frictional heating (Figure 4.5(i)b). Although not as intense as the subsequent event, the ion temperature was increased by some 300 to 600 K between 300 and 500 km. However, in this case there was no apparent response at any altitude in the vertical ion velocity.

In summary, the interval between 2130 and 2220 UT was marked by an ion upflow at 2200 UT with vertical ion velocities exceeding 300 m s^{-1} at 800-km altitude, and F-region fluxes in excess of $10^{13} \text{ m}^{-2} \text{ s}^{-1}$. The upflow was simultaneous with depleted F-region electron density, strongly enhanced ion temperatures and elevated electric fields. The duration of this event was only four minutes. Immediately following the upflow, electron precipitation into the lower F- and E-regions was observed, accompanied by elevated F-region electron temperatures. An earlier ion heating event did not have an associated ion upflow.

4.4.2 Event 1: Discussion

The ion upflow event at 2200 UT appears to be comparable, both in terms of the magnitudes of the observed ion fluxes and in the behaviour of the main plasma parameters, with events described previously by, for example, *Wahlund et al. (1992)*, *Winser et al. (1988b, 1989)* and *Jones et al. (1988)*. These authors reported field-aligned ion velocities of the order of hundreds of m s^{-1} at altitudes ranging from 300 to 900 km, associated with enhanced perpendicular electric fields and elevated ion temperatures. Large ion-neutral relative velocities perpendicular to the geomagnetic field lead to elevated ion temperatures via frictional heating (eg. *Rees and Walker, 1968*; *Schunk and Sojka, 1982*). Several workers, including *Jones et al. (1988, 1992)*, *Wilson (1994)* and *Rodger et al. (1992)*, have discussed how this can lead to an enhanced gradient of plasma pressure parallel to the magnetic field, capable of driving field-aligned ion flows with velocities of the order of several hundred m s^{-1} . Although other acceleration mechanisms have also been proposed, as discussed in *Chapter 2*, *Jones et al. (1992)* concluded that the plasma pressure gradient was the dominant factor in this type of event.

To assess the extent to which pressure gradients might account for the upflow at 2200 UT, field-aligned gradients must be inferred from vertical ones. This assumption is applicable if the feature has a large enough latitudinal extent such that the horizontal temperature distribution is homogeneous, as discussed by *Blelly et al. (1996)*. Blelly and co-authors successfully modelled EISCAT-VHF observations of vertical upflows associated with wide scale phenomena, which corresponded to events of more than one hour duration. Although the upflow at 2200 UT was only a transient feature, the occurrence of maximum ion temperatures and maximum vertical ion velocities at all altitudes simultaneously suggests a feature that “switched on” near 2200 UT, having a latitudinal extent of at least 100 km (see

Figure 4.1), rather than a small scale, field-aligned feature that moved through the radar field-of-view. Hence field-parallel gradients might be assumed from vertical observations. With this assumption in mind, the vertical diffusion velocity, resulting solely from plasma pressure gradients, was modelled. Although a simple approach, *Jones et al. (1988, 1992)* successfully explained similar observations of field-aligned upflows associated with enhanced plasma temperature in terms of pressure gradients alone; the event at 2200 UT was modelled in the same way to provide a more quantitative comparison with the observations of Jones and co-authors. However, at altitudes above 250 km the pressure gradient at 2200 UT was consistent with *downward* plasma flow, whereas the observations indicated upward flow at all heights between 150 and 800 km. As discussed in *Chapter 6*, though, such a model is greatly influenced by the ionospheric composition model adopted both for the analysis of the data and in the model itself. The true composition is often not well known, particularly during disturbed conditions, hence the results of this simple model may not be reliable. Therefore, it should not be inferred that the observed upflow was not driven, at least in part, by field-aligned pressure gradients.

As previously stated, the field-perpendicular plasma velocities have components in the vertical direction, and it is possible that the large vertical flows seen at high altitudes could be the result of enhanced \mathbf{ExB} drift speeds. Assuming a moderate parallel velocity, say 50 m s^{-1} , at 800-km altitude, and neglecting the vertical component of $\mathbf{v}_{\perp E}$, a northward meridional velocity in excess of 1200 m s^{-1} would be required to produce the observed vertical velocities of nearly 300 m s^{-1} . Such values are unlikely and were never observed at 315-km altitude in these data.

It seems most likely that the transient event observed at 2200 UT was associated with an auroral arc. Numerous observations have indicated the occurrence of ion upflows in the vicinity of arcs (eg. *Wahlund et al. 1992; Lu et al. 1992*), the upflows being attributed to a variety of acceleration mechanisms. At F-region altitudes, heating of the electron gas by soft particle precipitation can lead to upward diffusion via thermal plasma expansion (*Rodger et al., 1992; Wahlund et al., 1993; Liu et al., 1995*). Large convection electric fields are often observed in the vicinity of auroral arcs (*Marklund, 1984; Opgenoorth et al., 1990; Lewis et al., 1994*). As discussed in *Chapter 2*, enhanced electric fields can result in enhanced pressure gradients through ion frictional heating. Satellite and rocket observations of higher energy outflows, occurring above auroral arcs, have been attributed to transverse ion acceleration by low frequency waves, such as ion cyclotron waves (*Ungstrup et al., 1979; Klumpar, 1979; Heelis et al., 1984; Retterer et al., 1994*). Ion conics are generally observed at altitudes above 1000 km, although *Whalen et al. (1978)* reported such heating at altitudes between 400 and 500 km. Ion-acoustic instabilities that are unstable to field-aligned currents can also lead to enhanced (anomalous) resistivity and significant Joule heating of the electrons (*Swift, 1965; Wahlund et al., 1993; Forme et al., 1993*). Forme and co-authors demonstrated that these instabilities were initiated at altitudes above 1000 km, but conduction could lead to heating at

lower altitudes, where classical collisional heating also becomes important. Upward ion fluxes could be generated both by the modification of the electron pressure gradient and by enhanced field-parallel electric fields, the latter resulting from the increased resistivity in the presence of field-aligned currents (*Wahlund et al., 1992, 1993*).

There was indeed evidence of auroral precipitation between 2200 and 2205 UT (Figure 4.5(ii)b), both in the enhanced topside and F-region electron temperature, and in the increased electron density at 120 and 200-km altitude. The interval of F-region frictional heating was associated with an elevated perpendicular electric field, which was observed approximately three minutes prior to the density enhancement and, therefore, apparently situated on the leading edge of the arc. There is no indication of any latitudinal drift of the feature at 2200 UT; the enhancement in ion temperature was observed at all heights simultaneously, consistent with the small meridional velocity measured at the time. Between 2200 and 2202 UT there was a reversal in the zonal velocity from 1200 m s^{-1} westwards to around 200 m s^{-1} eastwards, corresponding to a change from a region of large northward electric field to a moderate southward field of approximately 10 mV m^{-1} . This feature is characteristic of a convection shear, as discussed by *Ganguli et al. (1994)*. These authors described how strongly sheared flows in the topside ionosphere could generate low frequency plasma waves, potentially leading to ion heating and thermal ion upflows. However, here the electric field reversal was concomitant with a *reduction* in the ion temperature, hence it is unlikely that the convection shear was the cause of the observed ion heating. The southward turning of the electric field was coincident with the enhancement in F-region electron temperature. In contrast with the ion heating event, the electron temperature enhancement was detected first at the higher altitudes, indicating an equatorward drift of perhaps 600 m s^{-1} ; this is greater than the meridional velocity measured at 2200 UT at 315 km, but is similar to velocities measured between 2205 and 2210 UT. The increased ionization was also observed first at 200 km, with higher energy precipitation evident later at 120-km altitude. This again is consistent with an equatorward drifting field-aligned arc. However, these observations are at variance with the earlier conjecture, based on the ion temperature data, that a large-scale feature “switched-on” at approximately 2200 UT. It is possible, of course, that a field-aligned feature moving meridionally through the radar field-of-view within one post-integration period could show signatures in all range gates simultaneously, as with the ion temperature in Figure 4.5(i)b. However, it is estimated that the drift velocity of the feature would need to have been approximately 1 km s^{-1} in this case, whereas the meridional velocity measured at 315 km altitude did not exceed 200 m s^{-1} at that time. It is suggested that the observed time-series of vertical ion velocity, ion temperature, electron density and electron temperature may have been produced by an auroral arc which first drifted eastward into the radar field-of-view and then again southward.

Therefore, it seems probable that the upflow observed at 2200 UT resulted from a combination of processes related to the passage of an auroral arc through the radar beam. The

observations indicate that the electron temperature increased with altitude, and that the temperature maximum was evident first at the higher altitudes. Although reliable electron temperature measurements are not available beyond 500 km, it might be inferred that the electron temperature maximum at 800 km occurred between 2200 and 2202 UT at the geographic latitude of EISCAT; that is, at the time of the observed upflow at that altitude. This is in accordance with observations reported by *Wahlund et al. (1993)*, who associated topside ion upflows with transient, high altitude electron heating resulting from the simultaneous presence of field-aligned currents and ion-acoustic turbulence. These authors also showed that such heating was correlated with electron precipitation in the 100-500 eV energy range, indicated by increased ionization between altitudes of 170 and 230 km. This is also consistent with the observations of elevated topside electron temperature followed by enhanced electron density at 200-km altitude. It is surmised that the upflow observed at 800 km was related to electron heating above a field-aligned auroral arc, which at 2200 UT was poleward of EISCAT, whilst the upward velocities observed at lower altitudes were probably induced by ion heating, resulting from the velocity shear and enhanced convection electric field on the equatorward edge of the arc. The geometry of the system is such that the plasma flows along different geomagnetic field-lines were detected simultaneously in the vertical line-of-sight. The acceleration regions then moved out of the field-of-view as the arc drifted equatorward, indicated by subsequent F-region electron heating and enhanced ionization.

Blilly et al. (1996) modelled EISCAT-VHF observations of a large-scale ion upflow by imposing a combination of an enhanced convection electric field and an upward field-aligned current, successfully reproducing the general features of the event. Although this was a long-lived feature (lasting more than an hour) where ion and electron heating were observed simultaneously, the model does not preclude the possibility that transient upflows related to auroral arcs can be generated by the same mechanisms. Indeed, it is possible that the event presented here was long-lived, but only observed for a few minutes as it passed through the EISCAT beam.

Finally, it is noted that the zonal drift velocity turned eastward just prior to 2140 UT. However, between 2142 and 2202 UT, westward flow was then observed. This pattern of flow is put into a wider spatial context by observations during this interval from the EISCAT magnetometer cross. An eastward electrojet was apparent between about 2140 and 2200 UT, consistent with the westward flow measured by the EISCAT radars. At 2200 UT a substorm-enhanced westward electrojet was detected in the magnetometer data. These observations are also consistent with the eastward flow and electron precipitation detected by the EISCAT radars from 2200 UT.

In summary, this event exhibits characteristics common to both the type 1 and type 2 upflows described by *Wahlund et al. (1992)*, with the presence of F-region upflows related to enhanced electric fields and ion frictional heating, and higher altitude, greater magnitude upward velocities associated with enhanced electron temperatures. The F-region and topside

upflows observed here are probably not directly related to one another, since the acceleration occurs along different geomagnetic field-lines.

4.5 Event 2: Upflow at 0030 UT

4.5.1 Event 2: Observations

Figures 4.6(i) and (ii) display data from SP-UK-UFIS for the interval between 0020 and 0100 UT on 18 January 1990. The vertical ion velocity measured at 350, 500 and 800-km altitude is illustrated in panel (a) of each figure. An upflow was observed between 0028 and 0034 UT, the vertical ion velocity increasing with altitude from less than 100 m s^{-1} at 350 km to some 300 m s^{-1} at 800 km. Vertical ion fluxes were somewhat greater than in the previous event, reaching some $5 \times 10^{13} \text{ m}^{-2} \text{ s}^{-1}$ at 500-km altitude. Figure 4.6(i)c reveals zonal and meridional flow magnitudes equivalent to perpendicular electric fields of only 30 mV m^{-1} or less. The southward to northward turning of the meridional velocity is equivalent to a change in electric field of only approximately 10 mV m^{-1} . There is correspondingly little indication of frictional heating of the ion population (panel b); no enhancements in ion temperature were detected at 350 km, although at 200 and 500 km there were peak increases of perhaps 300 K, separated by two minutes, with that at 500 km simultaneous with the maximum ion velocity at that altitude. There is a good correlation between the vertical ion velocity and an enhancement in the F-region electron temperature, at least at 500 km, where a temperature increase of some 1500 K was observed, as illustrated by panel (c) of 4.6(ii). The electron density (Figure 4.6(ii)b) was relatively high throughout the entire period from 0020 to 0100 UT; comparison with electron densities at 120 km between 2140 and 2200 UT (Figure 4.5(ii)b) reveals around a four-fold increase during the later period. This high level of ionization is indicative of production by electron precipitation.

In contrast to the earlier event, the upflow at 0030 UT was observed simultaneously with an interval of enhanced F-region electron temperature, with only moderate perpendicular electric fields and little ion heating. Although the maximum observed vertical velocities were similar in each event, that at 0030 UT exhibited larger upward fluxes.

4.5.2 Event 2: Discussion

In terms of the magnitude of the maximum vertical ion velocity and the duration of the event, the upflow observed around 0030 UT is comparable with the earlier feature. However, in the later event only modest increases in the vertical ion temperature were detected during the upflow, consistent with the moderate measured convection velocities. Furthermore, in the earlier event the electron temperature at the lower altitudes was seen to increase subsequent to the upflow, whereas here there appears to be a direct correlation between the enhanced electron temperature and the vertical ion velocity at 500-km altitude. The observed electron heating might be due to a downward heatflux of magnetospheric origin, or the result of

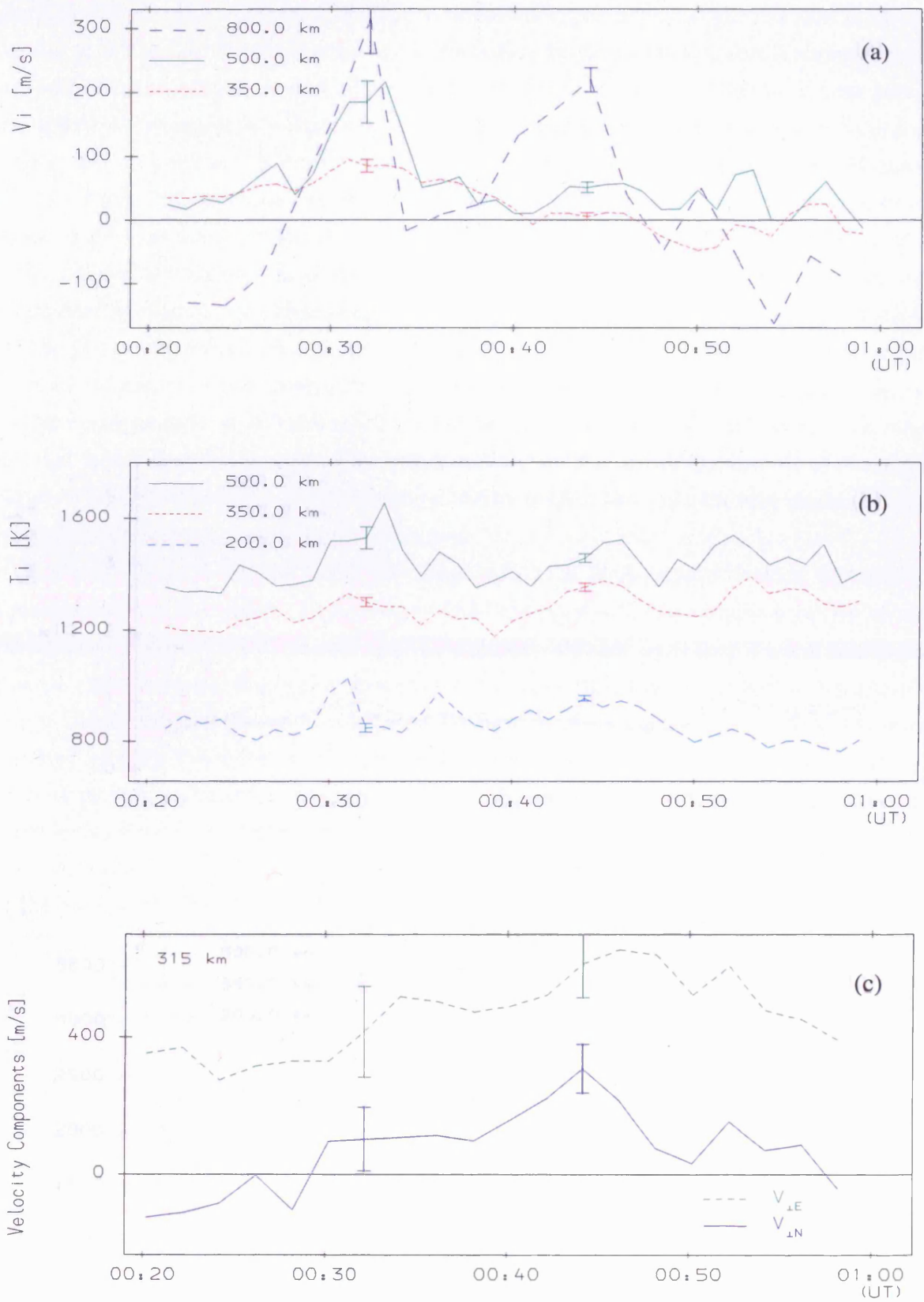


Figure 4.6(i) Same as Figure 4.5(i) but for 0020 - 0100 UT on 18 January 1990.

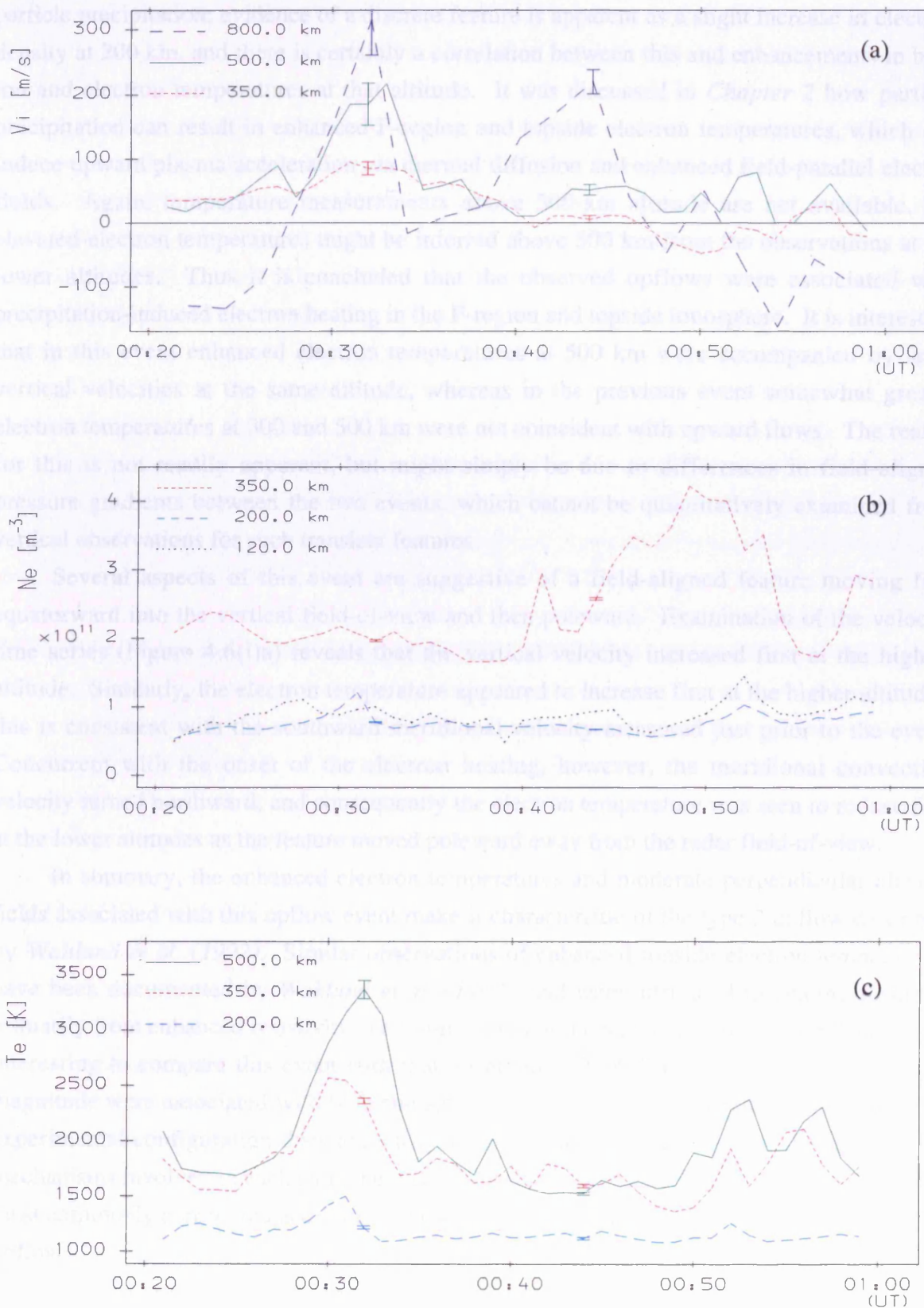


Figure 4.6(ii) Same as Figure 4.5(ii) but for 0020 - 0100 UT on 18 January 1990.

particle precipitation; evidence of a discrete feature is apparent as a slight increase in electron density at 200 km, and there is certainly a correlation between this and enhancements in both ion and electron temperatures at that altitude. It was discussed in *Chapter 2* how particle precipitation can result in enhanced F-region and topside electron temperatures, which can induce upward plasma acceleration via thermal diffusion and enhanced field-parallel electric fields. Again, temperature measurements above 500-km altitude are not available, but elevated electron temperatures might be inferred above 500 km from the observations at the lower altitudes. Thus it is concluded that the observed upflows were associated with precipitation-induced electron heating in the F-region and topside ionosphere. It is interesting that in this event enhanced electron temperatures at 500 km were accompanied by large vertical velocities at the same altitude, whereas in the previous event somewhat greater electron temperatures at 300 and 500 km were not coincident with upward flows. The reason for this is not readily apparent, but might simply be due to differences in field-aligned pressure gradients between the two events, which cannot be quantitatively examined from vertical observations for such transient features.

Several aspects of this event are suggestive of a field-aligned feature moving first equatorward into the vertical field-of-view and then poleward. Examination of the velocity time series (Figure 4.6(i)a) reveals that the vertical velocity increased first at the highest altitude. Similarly, the electron temperature appeared to increase first at the higher altitudes; this is consistent with the southward meridional velocity measured just prior to the event. Concurrent with the onset of the electron heating, however, the meridional convection velocity turned northward, and consequently the electron temperature was seen to reduce first at the lower altitudes as the feature moved poleward away from the radar field-of-view.

In summary, the enhanced electron temperatures and moderate perpendicular electric fields associated with this upflow event make it characteristic of the type 2 upflow described by *Wahlund et al. (1992)*. Similar observations of enhanced topside electron temperatures have been documented by *Wahlund et al. (1993)*, and were attributed to heating resulting primarily from enhanced resistivity due to precipitation-induced ion-acoustic turbulence. It is interesting to compare this event with that observed at 2200 UT, when upflows of similar magnitude were associated with both enhanced ion and electron temperatures. Although the experimental configuration does not allow for a quantitative assessment of the acceleration mechanisms involved in each case, these two events exhibit characteristics consistent with the most commonly considered acceleration processes which can lead to F-region and topside ion upflows.

4.6 Event 3: Upflow at 0045 UT

4.6.1 Event 3: Observations

A third ion upflow was detected between 0038 and 0046 UT (Figure 4.6(i)a). This event was markedly different from the previous two, in that large upward velocities were seen only in data from the VHF radar. Moderate vertical ion velocities, of less than 50 m s^{-1} , were observed up to 500-km altitude by both UHF and VHF radars. Enhanced upward flows were evident from 600-km altitude, exceeding 200 m s^{-1} at 0044 UT at an altitude of 800 km. There was no evidence of ion heating at F-region altitudes during the upflow (Figure 4.6(i)b). Slight increases in the zonal and meridional ion velocities were evident (panel c), although the perpendicular electric field attained a maximum of perhaps only 35 mV m^{-1} . The F-region electron temperature exhibited no response at the time of the upflow (Figure 4.6(ii)c). However, a transient increase in the electron density at 350-km altitude was evident during the event, with a more sustained and substantial enhancement following the upflow (Figure 4.6(ii)b). As noted previously, there is evidence of precipitation into the lower F and E-regions throughout the entire period from 0020 to 0100 UT.

In summary, the third upflow observed in this data set differs from the previous two in that it occurred beyond the observing range of the UHF radar, and was detected only by the VHF radar at altitudes above 600 km. Furthermore, the maximum observed velocities were of the order of 200 m s^{-1} , some 100 m s^{-1} less than was seen in the other events at the same altitude. Of the earlier two ion upflows, one was associated with enhanced ion and electron temperatures, the other with elevated electron temperatures alone; however, the upflow at 0044 UT was apparently uncorrelated with any temperature variations at lower altitudes.

4.6.2 Event 3: Discussion

The moderate vertical velocities near the F-region peak measured during this event are consistent with the undisturbed ion and electron temperatures at these altitudes. It is possible that the upflow detected at 600-km altitude is the result of downward heatflow into the topside ionosphere, leaving the electron temperature unaffected at lower heights. The heating could also be related to soft particle precipitation; just prior to the maximum observed velocity, an ionization peak was apparent at 350 km. However, this was not detected below about 300-km altitude, which is suggestive of precipitation with a maximum energy below the range associated with bulk electron heating at high altitudes (*Wahlund et al., 1993*).

A further possibility is that the upflow was associated with a field-aligned feature present at higher latitudes than the radar field-of-view. Enhanced field-aligned plasma flows, translated into large vertical velocities, might then be detected only at high altitudes within the VHF radar field-of-view (see Figure 4.1). Such an interpretation must remain purely speculative, since, without observations away from the radar field-of-view, the effects of spatial and temporal variations cannot be fully resolved. This highlights one of the limitations

of single pointing direction experiments such as UFIS which, although offering measurements at high temporal resolution, yield relatively little spatial information.

4.7 Summary and Conclusions

Observations from a six hour run of the special UK EISCAT programme UFIS have been presented, detailing three distinct intervals of upward ion flow from the F-region ionosphere. Table 4.1 summarises the primary characteristics of the events in terms of the observed ionospheric parameters.

Table 4.1

Time	V_i (800 km)	Flux (500 km)	ΔT_i (500 km)	ΔT_e (500 km)	$E_{\perp N}$ (315 km)
2200 UT	280 m s ⁻¹	$1.5 \times 10^{13} \text{ m}^{-2} \text{ s}^{-1}$	1100 K	500 K	60 mV m ⁻¹
0030 UT	300 m s ⁻¹	$5 \times 10^{13} \text{ m}^{-2} \text{ s}^{-1}$	< 200 K	1500 K	- 30 mV m ⁻¹
0040 UT	200 m s ⁻¹	$1 \times 10^{13} \text{ m}^{-2} \text{ s}^{-1}$	~ 0 K	~ 0 K	- 35 mV m ⁻¹

At 2200 UT, simultaneous UHF and VHF measurements indicated that the vertical ion velocity increased steadily with altitude from the F-region into the topside ionosphere, attaining flow speeds of nearly 300 m s⁻¹, with fluxes of order $10^{13} \text{ m}^{-2} \text{ s}^{-1}$. The F-region upflow was simultaneous with a period of ion frictional heating, the result of an enhanced and sheared convection electric field on the edge of an auroral arc. At higher altitudes, the upward flow was thought to be related to elevated electron temperatures and field-aligned currents. Thus the event was reminiscent of both the type 1 and type 2 upflows described by *Wahlund et al. (1992)*, and perhaps also of the large-scale features modelled by *Blally et al. (1996)*. These observations demonstrate some of the features that can exist within the structure of an auroral arc and which can induce upward plasma flow in the F-region and topside ionosphere.

Similar upward ion fluxes were observed at 0030 UT. In this case, the upflow was associated with enhanced electron temperatures, moderate convection flows and F-region particle precipitation. These features are characteristic of the type 2 upflow described by *Wahlund et al. (1992, 1993)*, in which topside electron heating is attributed to enhanced resistivity due to low-frequency turbulence induced by field-aligned currents. Upward ion acceleration can result from both increased pressure gradients and enhanced field-aligned electric fields.

Finally, an upflow was detected at altitudes above the observing range of the UHF radar, but which was evident in the VHF data from 600 km upwards. Smaller vertical velocities were observed in this event, which was apparently uncorrelated with any features observed at lower altitudes. Limitations imposed by the experimental conditions inhibit the interpretation this event, although the upflow was again likely related to topside plasma

heating.

This data set gives an indication of the variety of characteristics of ion upflow events, and the diversity of accelerating mechanisms involved. Three distinct events from this single six hour run of SP-UK-UFIS were presented. The simultaneous operation of the UHF-tristatic and VHF radars, with both transmitters observing along a vertical line of sight, allowed for the direct comparison of observations from E-region altitudes up into the topside ionosphere. However, there are spatial and temporal ambiguities inherent in any single pointing experiment such as UFIS. The interpretation of line-of-sight measurements in terms of field-parallel features is hindered when transient, field-aligned features are observed in the vertical field-of-view necessary for the VHF radar. Also, although good temporal resolution is achieved, no direct measurements are obtained from regions beyond the field-of-view of the radar, thus limiting the information available concerning the spatial evolution of features associated with the ion upflows. In the future, velocity observations from the Superdarn CUTLASS radar (*Greenwald et al., 1995*) may enable these single-point observations to be placed in a wider spatial context.

CHAPTER 5

A Statistical Study of F-region and Topside Upflows using EISCAT Data from 1984 to 1996

5.1 Introduction

The case study presented in *Chapter 4* demonstrated some features which are common to upflows in the F-region auroral ionosphere. However, single events do not provide information about the occurrence frequency of upflows, nor do they give a view of the general conditions prevalent during these events. Such information can be obtained from studies of large numbers of observations covering an extended period of time. This chapter presents a statistical study of F-region and topside ion upflow events observed with the EISCAT radar. The study employs Common Programme data taken between 1984 and 1996. The occurrence frequency of upflowing ion events (UFIs) is studied over the altitude range 200 to 500 km, utilizing field-aligned observations from Common Programmes One and Two. The study is extended in altitude with measurements from Common Programme Seven obtained between 1990 and 1995.

Statistical studies based on observations from single instruments, such as the EISCAT radar, can suffer because of the limited latitudinal extent that may be covered. However, the large data bases that are accumulated and the excellent temporal resolution achieved do allow for informative studies of ion upflow events, such as that presented by *Keating et al. (1990)*. Since that particular survey, several more years' worth of EISCAT observations have become available, including topside data up to about 1000-km altitude. Thus it is pertinent to extend the work of Keating and co-authors, in terms of both time and altitude range covered, to document longer-term variations of ion upflow events. Furthermore, a larger data set should also provide more statistically dependable distributions, less affected by "anomalous" periods.

Initial results of the statistical study are discussed with respect to the findings of *Keating et al. (1990)*. Then, the high-altitude CP-7 observations are considered, followed by an investigation of the occurrence frequency of UFIs as a function of solar phase and geomagnetic activity. Finally, a quantitative study of the relationship between UFIs and enhanced ion and electron temperatures is presented.

5.2 Data Sets and Selection Criteria

For this study, data were collated from EISCAT Common Programmes One, Two and Seven (CP-1, CP-2 and CP-7). As described in *Chapter 3*, CP-1 is a fixed pointing-direction experiment in which the transmitter beam is aligned approximately along the geomagnetic field direction at Tromsø. Reliable data from this experiment cover the period from January 1984 to the present. For the investigation, data from a total of 94 CP-1 experiments, up to February 1996, were employed. Although this 12 year interval encompasses seven versions of the programme, the differences between each do not affect the study. In addition to CP-1

data, observations from the field-aligned position in CP-2 were included. Data from 47 runs of CP-2 were obtained, representing four versions of the experiment from May 1984 to March 1996. Although the transmitter beam points along the field direction for only 25% of the total observing time in this experiment, these data are a valuable addition to the analysis. It should be noted that, due to the curvature of the geomagnetic field-lines, a transmitter beam said to be “field-aligned” is only so over a limited altitude range. The transmitter elevation angles for Common Programmes One and Two are such that the beam is intended to be field-aligned at approximately 300-km altitude; with increasing distance away from this height, the angle between the transmitter beam and the field-line tangent may be up to 0.5° . Furthermore, it has recently been remarked that the elevation angles used for “field-aligned” pointing in both CP-1 and CP-2 since late 1986 have been about half a degree in error. However, these inaccuracies are unimportant with regard to the present study, which only requires measurements that are approximately field-aligned.

Finally, CP-7 data from April 1990 to September 1995 provided *vertical* measurements of the F-region and topside ionosphere. However, the limited size of this data set and the often poor signal quality at high altitudes detracts from the usefulness of these observations.

In order to facilitate an initial comparison with the diurnal and seasonal distributions presented by *Keating et al. (1990)*, identical criteria were adopted in the present study to identify “events” of ion upflow. Thus an upflow was defined as an upward field-aligned flux of greater than $10^{13} \text{ m}^{-2} \text{ s}^{-1}$ and/or a field-aligned velocity in excess of 100 m s^{-1} . Keating and co-workers based these threshold values on experience with EISCAT observations of field-aligned flows in the high-latitude ionosphere, which indicate that upflows normally only exceed these values during limited intervals. Keating and co-authors cited observations reported by *Jones et al. (1988)* and *Winser et al. (1989)* as examples of such events, since when other authors have presented observations that further justify these selection criteria (eg. *Wahlund et al., 1992*). The velocity threshold is greater than values that might be expected due to neutral winds and plasma pressure gradients under quiet conditions, typically a few tens of m s^{-1} (*Winser et al., 1986; Jones et al., 1988*), whilst the flux threshold is an order of magnitude greater than the typical polar wind outflow (see *Chapter 2, section 2.2.1*).

In order to compile upflow occurrence statistics, Keating and co-authors computed a “percentage frequency occurrence” of upflows within various altitude and time bins. This parameter expressed the number of “events” as a fraction of the total number of observations in that bin. An “observation” was defined as a single interval of data post-integrated at 5-minute resolution. Thus the percentage frequency occurrence represented the fraction of observing time that upflows occurred within a given bin.

The technique assumes that, within a given interval, the total number of observations is constant with altitude. This is obviously true for the above definition of an observation. However, it should be recalled that in standard analysis of EISCAT data the derived parameters (electron density, ion and electron temperatures) are returned by the analysis

program only if a fit to the measured spectrum is achieved. The poorer signal quality received from the farther range gates means that fewer spectra can be fitted with increasing altitude. Hence, the number of observations for which reliable parameters are obtained is generally *less* at the higher altitudes than the total number of data dumps. For this reason, in the present study an “observation” is defined as a single interval of post-integrated data for which fits were achieved for all parameters. In addition, the signal-to-noise ratio was required to be greater than 2%. Using this definition, the frequency occurrence of upflows was then defined as the number of upflows expressed as a percentage of the total number of observations within the same range *and* time bin.

An initial study investigated the difference in upflow distributions obtained using the two contrasting definitions of an “observation”. For the purposes of this comparison, CP-1 data from the three-year period considered by *Keating et al. (1990)* were employed. It was found that the adopted definition did not significantly affect the total number of observations below 400-km altitude, as indicated diagrammatically by the full lines in Figures 5.1 and 5.2. Such a result is expected, since for the lower range gates nearly all post-integration dumps contain reliable data. However, at and above this altitude the present definition leads to a reduction with altitude in the number of observations. Diurnal and seasonal upflow occurrence distributions, derived using the method described by Keating and co-authors, are presented as dotted lines in Figures 5.1 and 5.2. Note that the results of *Keating et al. (1990)* are not exactly reproduced since the data set employed here may differ slightly from that used in the former study. For comparison, the histograms of Figures 5.1 and 5.2 illustrate upflow distributions obtained using the present description of an observation. It is evident that, in general, the definition employed does not significantly affect the derived distributions. However, there are large differences in the calculated occurrence frequencies for intervals when the total number of observations is relatively low, for example in the winter months at 500-km altitude. This highlights the need for a larger data set in order to allow for a sound statistical analysis.

5.3 Results and Discussion

The initial study examined 12 years of EISCAT field-aligned measurements derived from Common Programmes One and Two. Observations from six altitude ranges were binned at hourly intervals. The range gates each covered 30 km, the approximate height resolution for these experiments, and were centred on 200, 250, 300, 350, 400 and 500-km altitude. These ranges match those employed by *Keating et al. (1990)*, and thus afford a direct comparison of results. For each time bin and range gate, the percentage occurrence frequency of upflows was computed using the method described in the previous section.

CP-1 field-aligned observations 850128 to 871117, SNR limit 2%

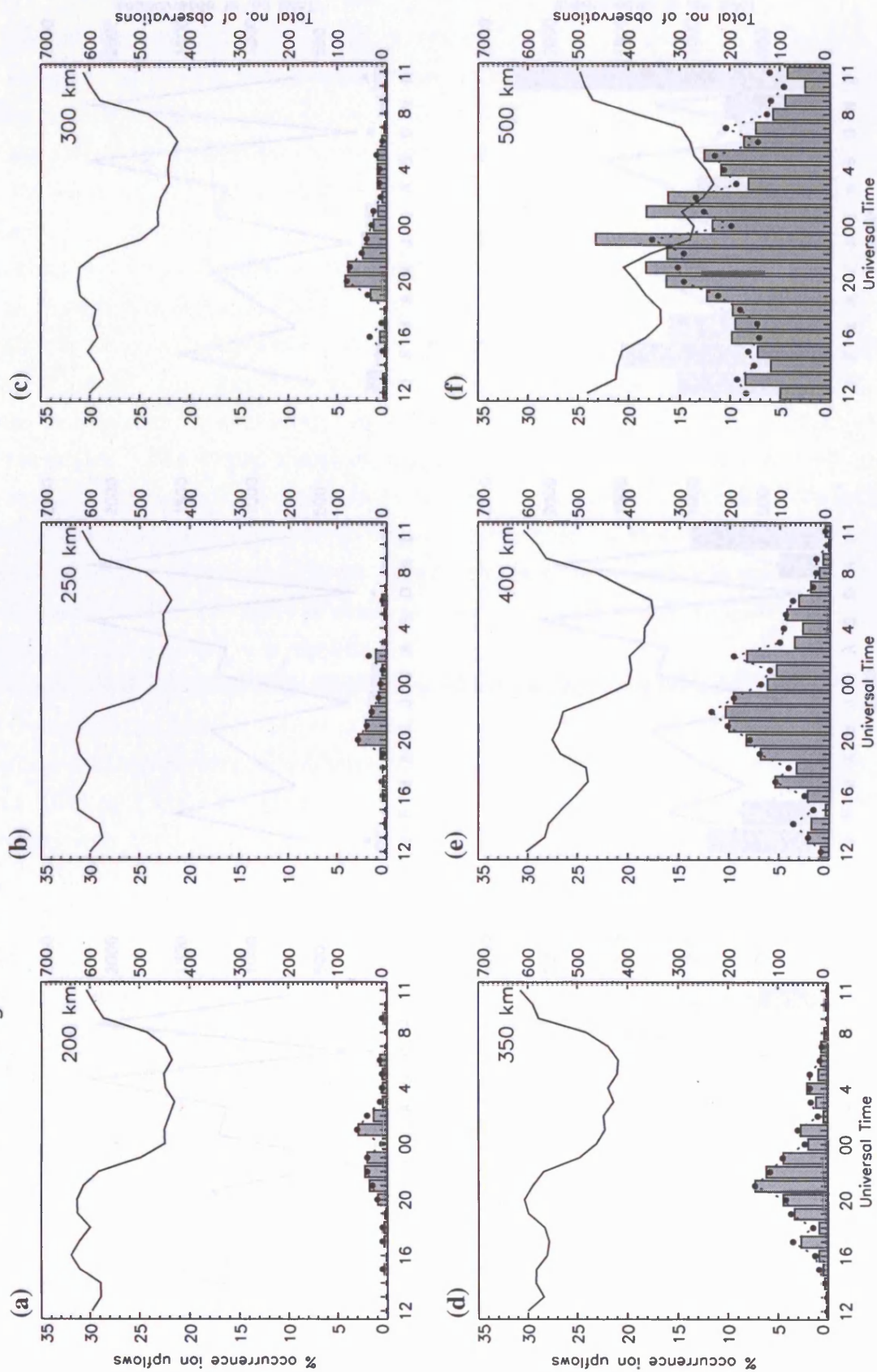


Figure 5.1 Histograms indicating the diurnal variation of the frequency occurrence of field-aligned upflows for six altitudes between 200 and 500 km during 1985 - 1987. The equivalent distributions derived using the method of *Keating et al. (1990)* are shown as the dotted line. The full line indicates the total number of observations within each bin at each height.

CP-1 field-aligned observations 850128 to 871117, SNR limit 2%

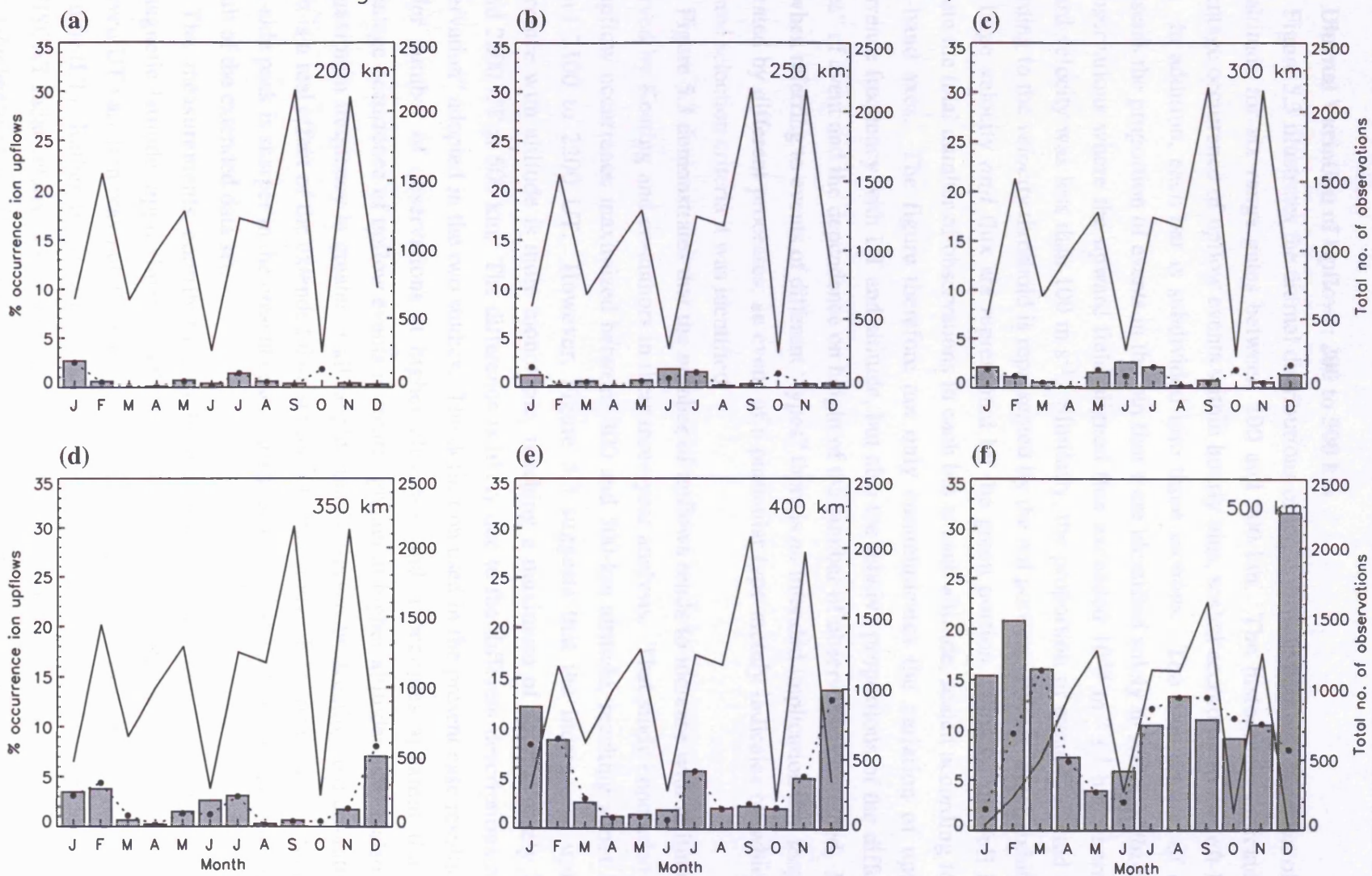


Figure 5.2 Same as Figure 5.1 but showing annual variations with data binned according to month.

5.3.1 Diurnal Variation of Upflows: 200 to 500 km

Figure 5.3 illustrates the diurnal distributions of ion upflow events as a function of UT and altitude for six range gates between 200 and 500 km. The histograms indicate the percentage occurrence of upflow events within hourly bins, scaled according to the left-hand axes. In addition, each bar is subdivided into three sections. The blue portion of each represents the proportion of events in the bin that were identified solely in terms of *flux*; that is, observations where the upward field-aligned flux exceeded $10^{13} \text{ m}^{-2} \text{ s}^{-1}$ but where the upward velocity was less than 100 m s^{-1} . Similarly, the proportion of events selected only according to the *velocity* threshold is represented by the red portion. Events which exhibited both large velocity *and* flux are represented by the green portion. Finally, the full lines indicate the total number of observations in each bin at each altitude, scaled according to the right-hand axes. The figure therefore not only communicates the variation of upflow occurrence frequency with UT and altitude, but also the relative proportions of the different “types” of event and the dependence on height of the number of observations obtained. Note that when referring to events of different “types” there is *no* intended implication that they are generated by different processes; an event of a particular type merely indicates by which of the three selection criteria it was identified.

Figure 5.3 demonstrates that the number of upflows tends to increase with altitude, as observed by Keating and co-authors in their three-year analysis. That study concluded that the upflow occurrence maximized between 400 and 500-km altitude, reaching about 16% around 2100 to 2200 UT. However, Figure 5.3 suggests that the increase in upflow occurrence with altitude is more monotonic, reaching a maximum of approximately 23% around 2200 UT at 500 km. The difference is likely due to the different descriptions of an “observation” adopted in the two studies. The definition used in the present case results in a smaller number of observations at higher altitudes, and it becomes apparent that the percentage occurrence of upflow events is clearly greater at higher altitudes. Note also that the maximum frequency is greater at all heights than observed by Keating and co-authors, which is a real effect of the extended data set used in this study. It is apparent, too, that the night-side peak is sharper in the present case, particularly above the 300-km range gate, again a result of the extended data set.

The measurements contributing to Figure 5.3 were all obtained from a single geomagnetic latitude, approximately 69° N , the latitude of the EISCAT transmitter. The observed UT variation may not, therefore, reflect a real dependence of upflow occurrence on local time (LT). Rather, the variation could be due to the change, with time, in the location of the EISCAT radar relative to the auroral zone. Previous statistical analyses (eg. *Klumpar, 1979; Ghielmetti et al., 1978; Yau et al., 1984; Loranc et al., 1991*) have revealed that the spatial distribution of upflows and outflows is auroral-oval-like. Hence, the variation evident in Figure 5.3 would be unexpected if the radar observed within the auroral oval at all times. However, on the day-side the auroral oval is typically positioned at higher geographical

CP-1 and CP-2 field-aligned observations 840124 to 960319, SNR limit 2%

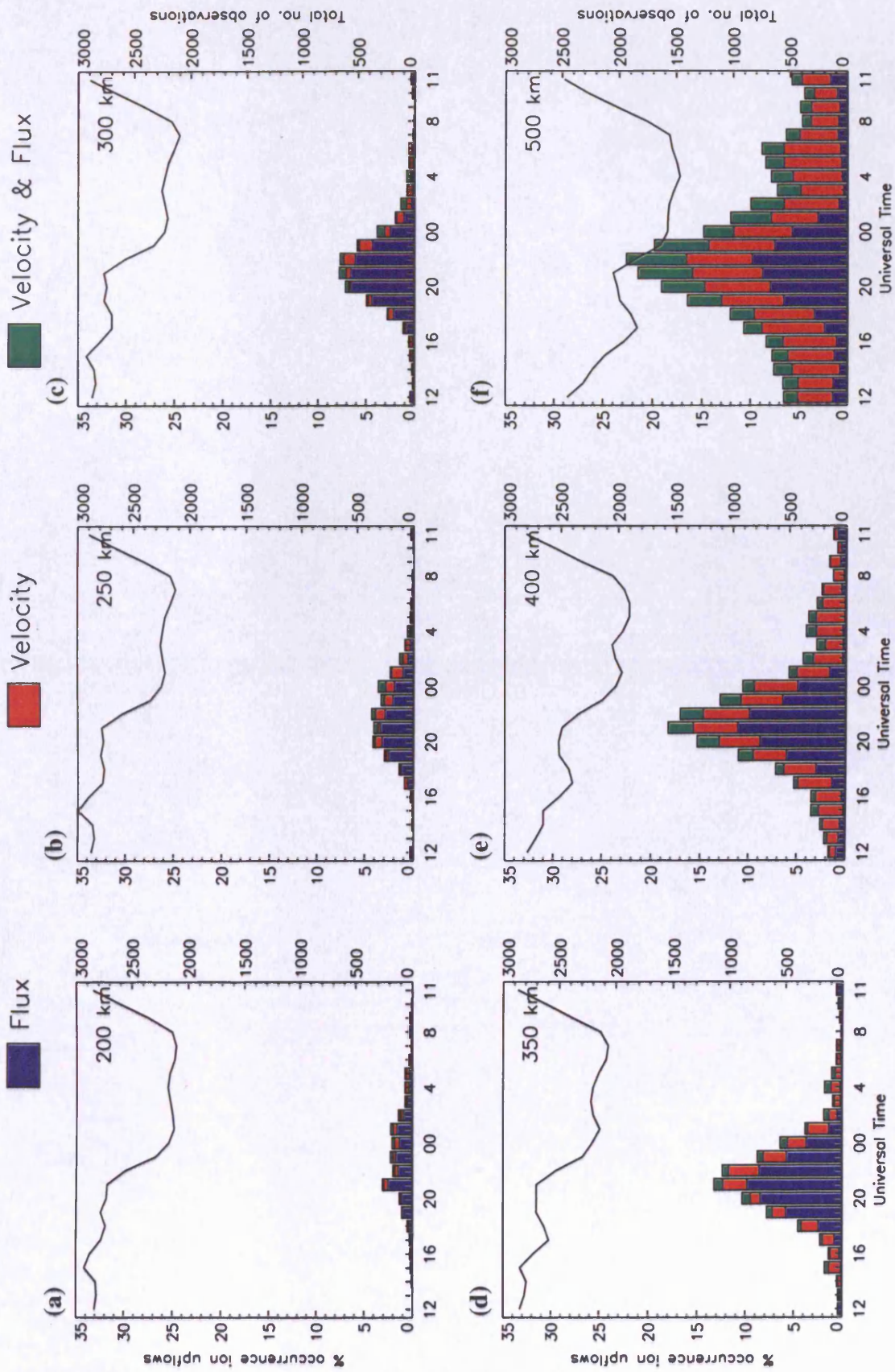


Figure 5.3 Diurnal variations of field-aligned upflow occurrence frequencies between 200 and 600 km, derived from EISCAT UHF observations from 1984 to 1996. The histogram bars are subdivided to illustrate the occurrence frequencies of events exceeding the flux threshold only, the velocity threshold only, and both. The full line indicates the total number of observations within each hourly bin.

latitudes than the EISCAT transmitter (beyond around 70° N between about 0600 to 1800 UT), so that at such times the radar observes *outside* a region where high upflow occurrence is expected. On the night-side, however, the auroral oval typically extends to below 69° N and the EISCAT facility is then within a region where higher upflow occurrence is expected. Thus it appears that the apparent LT variation could be a largely geographical effect. It should be noted, though, that *Klumpar (1979)* indicated that outflows were a predominantly night-side phenomenon at auroral zone latitudes. Although that study concentrated on altitudes of around 1400 km, it suggests that there may indeed be a dependence of upflow occurrence frequency on LT. There is probably both a local time and latitudinal variation in the distribution of upflows, both of which influence the distributions of Figure 5.3. As noted in *Chapter 4*, combined temporal and spatial effects are difficult to resolve from single-point measurements such as those derived from EISCAT radar observations. This point was also appreciated by Keating co-workers.

Finally, it is manifest from Figure 5.3 how the type of upflow event varies with height. Up to 300-km altitude, the majority of all events exhibit fluxes above the specified threshold value but with upward velocities of less than 100 m s^{-1} . However, beyond 350-km altitude the occurrence of large velocities increases steadily, indicated by the red portion of each bar. The percentage occurrence of flux events peaks around 2100 UT at 400 km and is then slightly reduced in the highest range gate. However, greater numbers of large fluxes *are* observed with increasing altitude and are accompanied by velocities above the threshold value, as revealed by the green portion of each bar.

In summary, then, upward velocities in excess of 100 m s^{-1} are uncommon below 350-km altitude, but become increasingly likely with increasing height; large field-aligned velocities are detected by the EISCAT radar up to approximately 12% of the time at 500-km altitude. Upward field-aligned fluxes of greater than $10^{13} \text{ m}^{-2} \text{ s}^{-1}$ occur less than 5% of the time below 250 km, but the occurrence frequency of such events increases monotonically with altitude, reaching a 15% maximum at 500 km. Finally, upflows are in general observed by EISCAT between 15% and 20% of the time in the pre-midnight sector between 400 and 500-km altitude.

5.3.2 Seasonal Variation of Upflows: 200 to 500 km

In keeping with the initial comparison with the paper of *Keating et al. (1990)*, seasonal distributions of ion upflow events in the same six range bins are presented in Figure 5.4. There is considerable variation over the year in the number of observations at each altitude, with up to 6000 measurements around March and September and fewer than 1000 in December at the highest altitude. The total number of observations in the 200-km range gate approached 60000, some four times that available for the study of Keating and co-workers.

With regard to the upflow occurrence statistics, Figure 5.4 exhibits distributions similar to those of Keating and co-authors up to the 300-km range gate. At 350 km, however, Figure

CP-1 and CP-2 field-aligned observations 840124 to 960319, SNR limit 2%

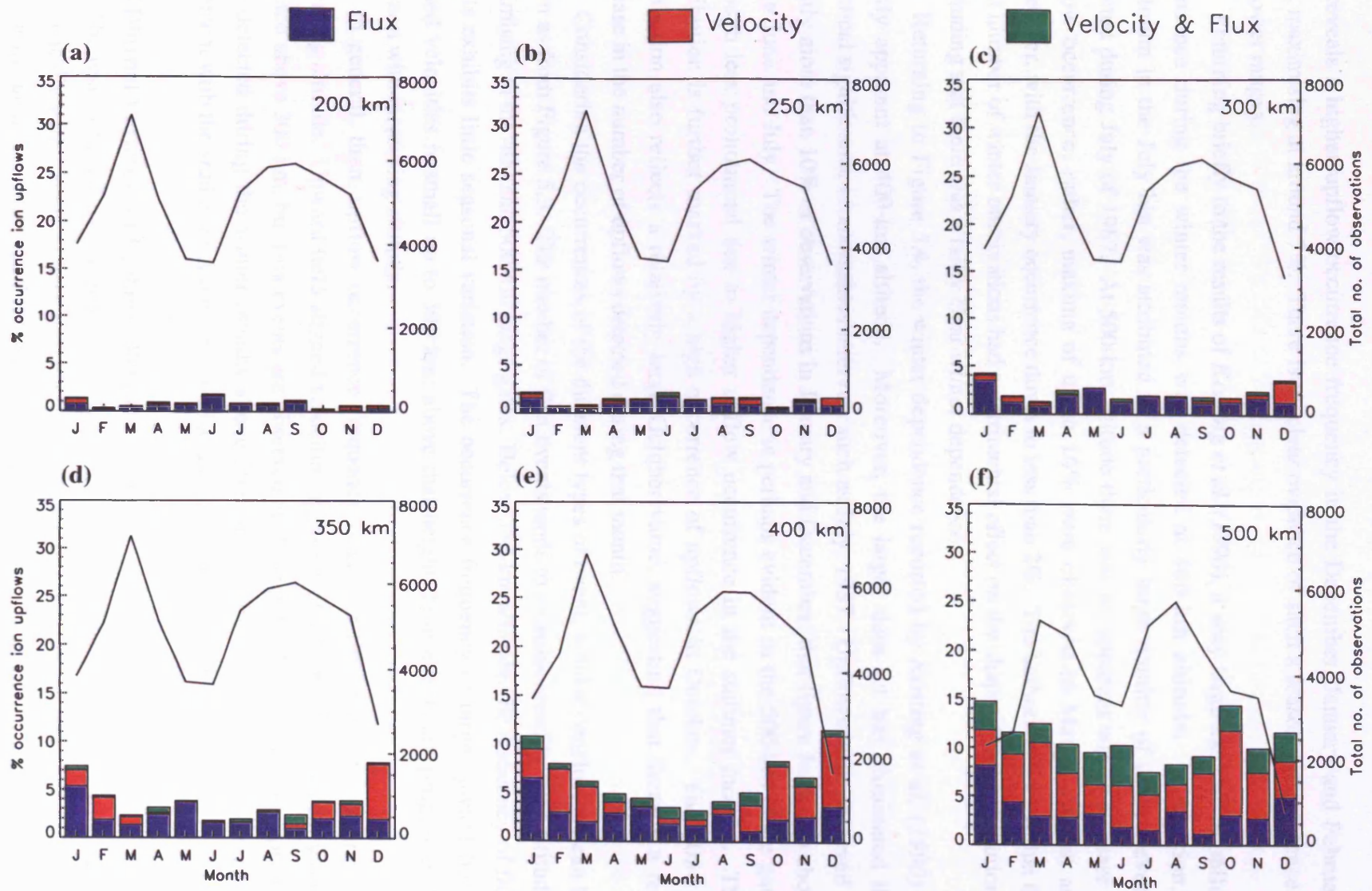


Figure 5.4 Same as Figure 5.3 but showing annual variations with data binned according to month.

5.4 reveals a higher upflow occurrence frequency in the December, January and February bins, maximising at around 7%. There is no clear evidence of such a seasonal dependence at the lower ranges.

Returning briefly to the results of *Keating et al. (1990)*, a very large increase in upflow occurrence during the winter months was detected at 400-km altitude. In addition, a maximum in the July bin was attributed to a particularly large number of upflow events detected during July of 1987. At 500-km altitude there was no apparent winter increase in upflow occurrence; rather, maxima of up to 16% were observed in March, August and September, with the January occurrence down to less than 2%. The authors indicated that the small number of winter observations had a detrimental effect on the shape of the distributions, concluding that there was a fairly clear winter dependence.

Returning to Figure 5.4, the winter dependence reported by *Keating et al. (1990)* is readily apparent at 400-km altitude. Moreover, the larger data set has eliminated the statistical significance of anomalous intervals such as July, 1987. Upflows were observed in slightly more than 10% of observations in January and December, that figure falling to about 3% in June and July. The winter dependence is perhaps evident in the 500-km range gate, although less pronounced due to higher upflow occurrence in the summer months. The distribution is further marked by a high occurrence of upflows in October. The 400-km distribution also reflects a relatively large October value, suggesting that there is a real increase in the number of upflows detected during that month.

Considering the occurrences of the different types of event, similar conclusions can be drawn as from Figure 5.3. The number of flux events tends to increase steadily with altitude, maximising in the 400 and 500-km range gates. Below 350-km altitude, the frequency of flux events exhibits little seasonal variation. The occurrence frequency of large upward field-aligned velocities is small up to 300 km; above that height these events are progressively common with increasing altitude.

In general, then, upflow occurrence frequency is greater throughout the year with increasing altitude. Upward field-aligned velocities in excess of 100 m s^{-1} are typically only detected above 300 km, but flux events are observed at all heights. Distinctly more upflows were detected during the winter months above 300 km, an observation which is in good agreement with the studies of *Klumpar (1979)* and *Keating et al. (1990)*.

5.3.3 Diurnal Variation of Upflows: 300 to 800 km.

The results thus far indicate that the frequency of ion upflow events tends to increase monotonically with height, at least up to 500 km. This altitude is effectively an upper range limit for the analysis, since the EISCAT radar experiments CP-1 and CP-2 seldom provide reliable field-aligned observations above this altitude. However, higher altitude *vertical* observations are available from the VHF radar experiment Common Programme Seven. Around five years of CP-7 data, obtained between April 1990 and September 1995, were

collated and analysed, as described in section 5.2, to generate occurrence distributions of upflows as a function of UT and altitude. In this case, six altitude gates spaced at 100-km intervals between 300 and 800 km were chosen. Each gate extended over a range of approximately 70 km, the altitude resolution of the experiment. The data were further partitioned into hourly bins. Again, the upflow occurrence frequency was deduced according to the total number of observations within the given time and altitude bin.

As before, an upflow event was defined as an upward velocity in excess of 100 m s^{-1} or an upward flux greater than $10^{13} \text{ m}^{-2} \text{ s}^{-1}$. However, it should be emphasized that parameters obtained from CP-7 are derived from vertical observations, not field-aligned. Hence the distributions illustrated in Figure 5.5 represent the frequency occurrence of *vertical* upflow events.

From the figure, it is immediately apparent that the distributions for 300, 400 and 500-km altitude differ from those for the same ranges derived from the CP-1 and CP-2 observations, illustrated in Figure 5.3. A greater occurrence of upflows is evident in the CP-7 data, which also exhibit more day-side events. Furthermore, the occurrence maxima lie between 0000 and 0200 UT, as opposed to the pre-midnight maxima noted previously.

To examine the extent to which the vertical pointing direction could account for these differences, the analysis was also performed on the *vertical* observations from the CP-2 experiment. Since CP-2 observations constitute a relatively small fraction of the combined CP-1 and CP-2 data set, it was first established that the CP-2 field-aligned measurements were indeed a representative subset of the data base. Subsequently, diurnal distributions of upflows were derived from CP-2 vertical observations. Figure 5.6 displays the distributions for 300, 400 and 500-km altitude. It is clear that these distributions are more akin to those derived from the CP-7 data (Figure 5.5) than from the field-aligned observations (Figure 5.3). Although the CP-2 vertical data produce lower occurrence frequencies, the maxima are detected around 0000 UT, as with the CP-7 observations, rather than pre-midnight as with the field-aligned observations. Therefore, it seems likely that the distributions derived from the CP-7 data are indeed characteristic of the vertical pointing direction employed in the experiment.

As discussed in *Chapter 4*, there are components of the zonal, meridional and field-aligned ion velocities in the vertical direction. The vertical component of $\mathbf{v}_{\perp E}$ is typically small, perhaps only a few m s^{-1} , so that the vertical velocity, \mathbf{v}_i , may be approximated by the expression

$$\mathbf{v}_i = \mathbf{v}_{\parallel} \cos I + \mathbf{v}_{\perp N} \sin I \cong 0.98 \mathbf{v}_{\parallel} + 0.2 \mathbf{v}_{\perp N} \quad (5.1)$$

where I , the magnetic dip angle at the altitude of the measurements, is approximately 12° . Hence if the meridional component of velocity, $\mathbf{v}_{\perp N}$, is small with respect to the field-aligned component, \mathbf{v}_{\parallel} , the measured vertical velocity is indeed representative of that in the field-

CP-7 vertical observations 900409 to 950927, SNR limit 2%

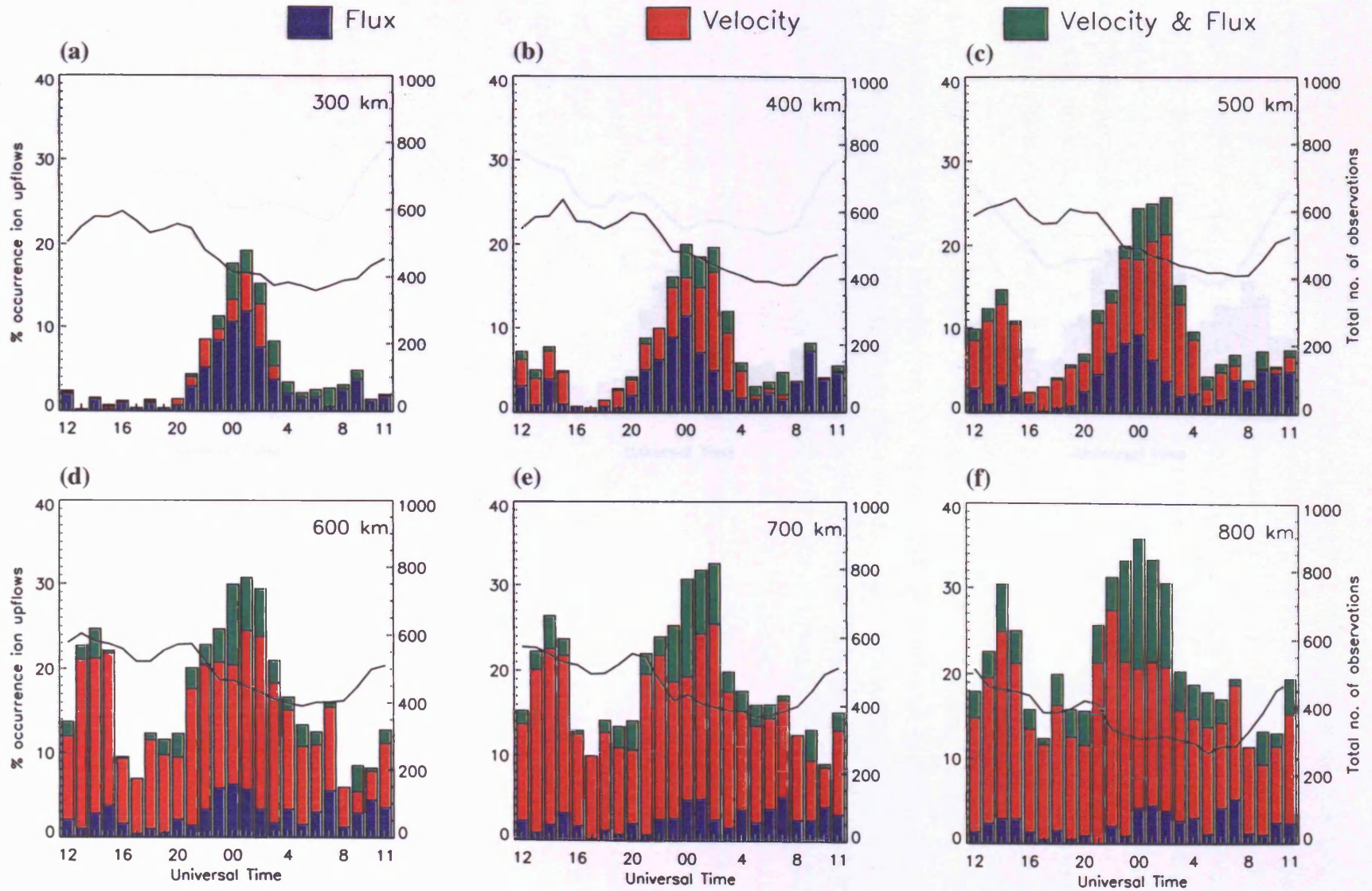


Figure 5.5 Diurnal variations of vertical upflow occurrence frequencies between 300 and 800 km, derived from EISCAT VHF observations from 1990 to 1995. Histogram bars are subdivided as for Figure 5.3.

CP-2 vertical observations 850410 to 960319, SNR limit 2%

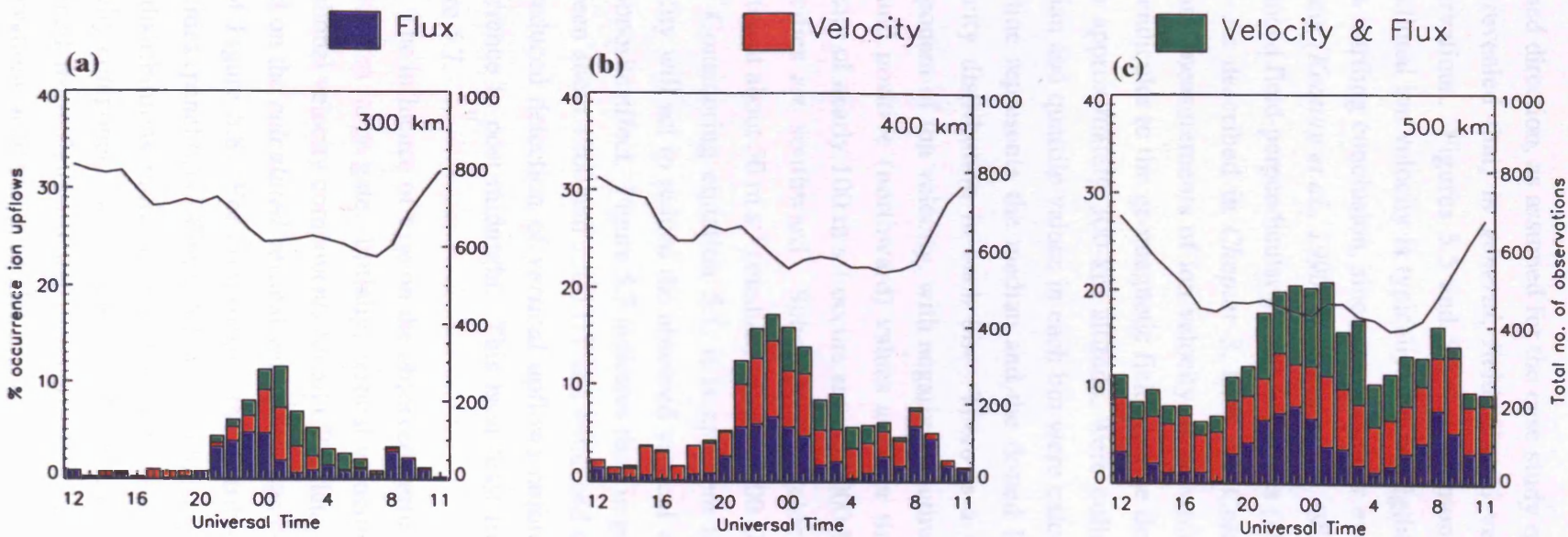


Figure 5.6 Diurnal variations of vertical upflow occurrence frequencies at 300, 400 and 500 km, derived from EISCAT UHF CP-2 observations from 1985 to 1996. Histogram bars are subdivided as for Figure 5.3.

aligned direction, as assumed for the case study of *Chapter 4*. However, the current analysis has revealed that, *in general*, field-aligned velocities cannot be inferred from vertical observations. Figures 5.5 and 5.6 have demonstrated that the vertical component of the meridional ion velocity is typically non-negligible during events of plasma upflow. This is not a startling conclusion, since many upflow events occur during intervals of ion frictional heating (*Keating et al., 1990; Wahlund et al., 1992; Chapter 4*) that are, in turn, the result of enhanced field-perpendicular plasma velocities (*Davies, 1996*).

As described in *Chapter 3*, EISCAT Common Programmes One and Two provide tristatic measurements of ion velocity, from which the components of velocity parallel and perpendicular to the geomagnetic field may be derived. All available measurements of $v_{\perp N}$, from approximately 300-km altitude, were collated and binned at hourly intervals. The median and quartile values in each bin were calculated and are illustrated in Figure 5.7; the full line represents the median and the dotted lines the upper and lower quartiles of the velocity distribution in each bin. There is a clear diurnal variation in the meridional component of ion velocity, with negative (southward) values between about 1200 and 2300 UT and positive (northward) values at other times. The maximum (median) southward velocity of nearly 100 m s^{-1} occurs around 2000 UT; at this time some 75% of all calculated velocities are southward. Subsequently, velocity values become increasingly positive, peaking at about 50 m s^{-1} (median) around 0200 UT.

Considering equation 5.1, it is apparent that a southward, or negative, meridional velocity will act to reduce the observed vertical velocity, whilst a northward flow will have the opposite effect. Figure 5.7 indicates that, in general, the vertical velocity will be reduced between about 1200 and 2300 UT and enhanced at other times. This effect may account for the reduced detection of *vertical* upflows before midnight and the shift of the maximum occurrence to post-midnight. This is at least true at 300 km, the altitude represented by Figure 5.7.

The influence of $v_{\perp N}$ on the observed vertical velocity was examined quantitatively for the 300-km range gate. Initially, vertical velocities were derived from the field-parallel and meridional velocity components for all CP-2 data. Then, a frequency distribution of upflows, based on the *calculated* vertical velocities, was derived as before, and is presented as panel (a) of Figure 5.8. For comparison, the distribution obtained from the *observed* vertical velocities (panel (a) of Figure 5.6) is included as panel (b). The close agreement between the two distributions indicates that the vertical observations are affected by the meridional velocity component, suggesting also that this is the only cause of the different distributions obtained from field-aligned and vertical observations. It is supposed that the vertical observations at higher altitudes are similarly affected, although this cannot be tested since measurements of the velocity components are not generally available above 300-km altitude. Hence the effect of $v_{\perp N}$ on the vertical observations accounts for the shift of the peak of the vertical upflow distribution to post-midnight. However, the distributions of Figures 5.5 and

CP-1 and CP-2 field-aligned observations, SNR limit 2%
840131 to 960213

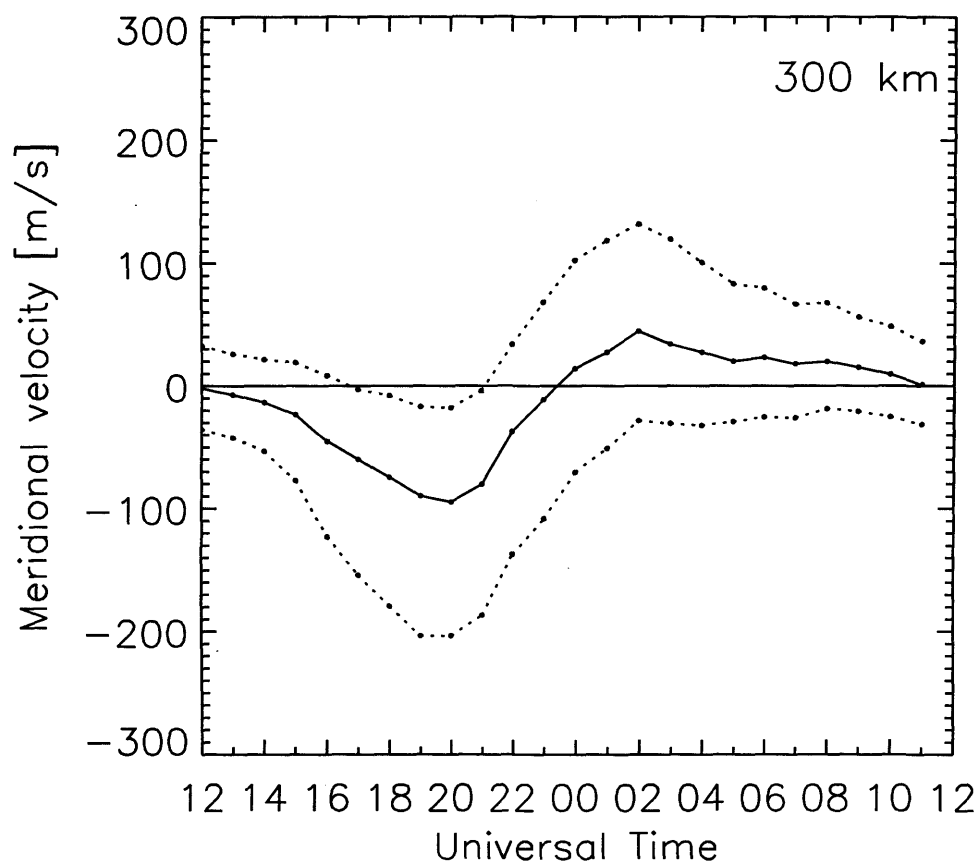


Figure 5.7 Median (full line) and quartile values of $v_{\perp N}$ in hourly bins as a function of UT at 300 km, derived from EISCAT measurements between 1984 and 1996.

CP-2 vertical observations, SNR limit 2%
850410 to 960319

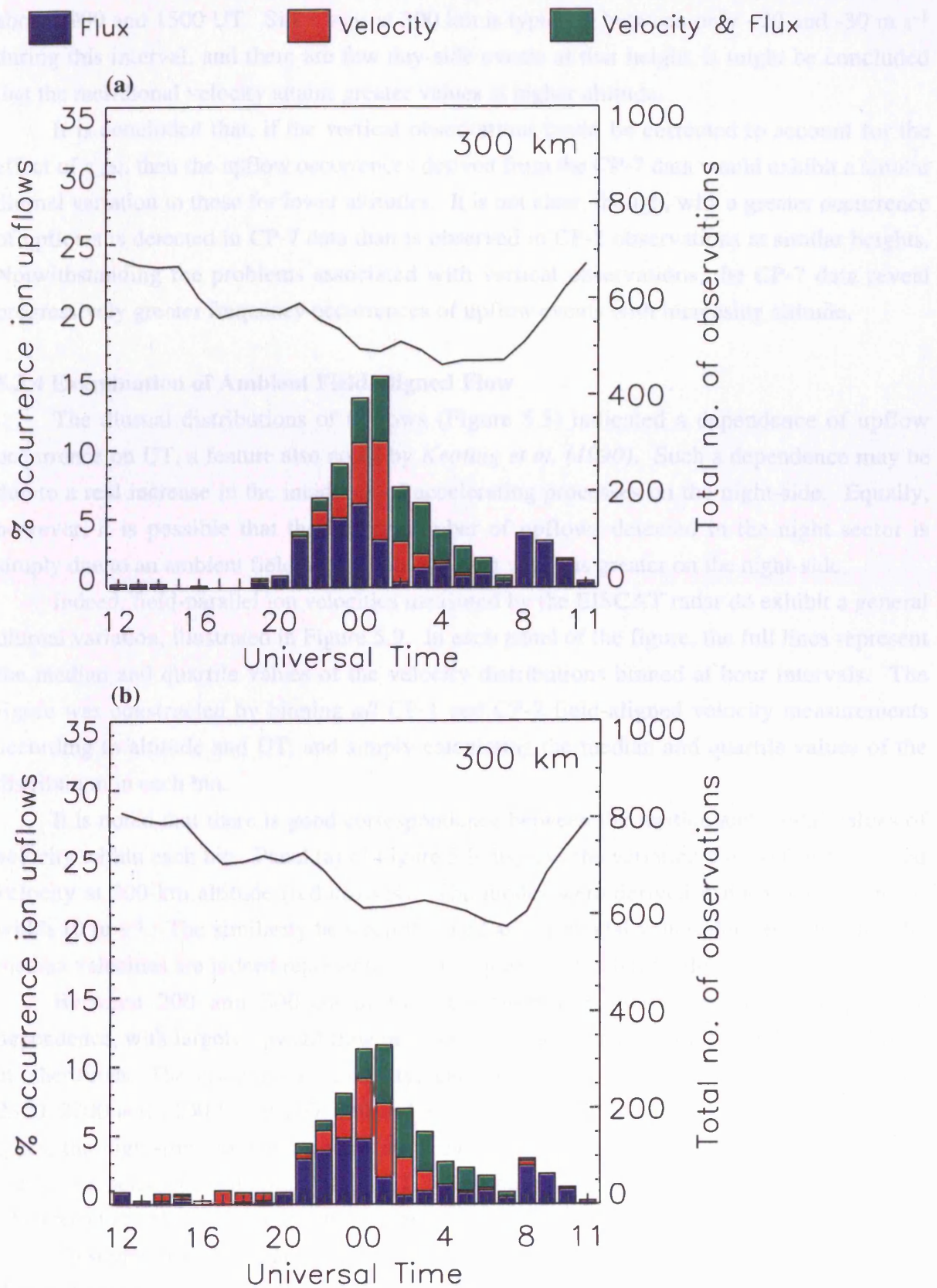


Figure 5.8 (a) Diurnal distribution of *vertical* upflows derived from vertical velocities calculated from CP-2 tristatic measurements of $v_{\perp N}$ and v_{\parallel} . (b) Same as Figure 5.6(a).

5.6 also indicate an increased occurrence of day-side events above 300-km altitude, between about 0900 and 1500 UT. Since $v_{\perp N}$ at 300 km is typically between only +20 and -30 m s⁻¹ during this interval, and there are few day-side events at that height, it might be concluded that the meridional velocity attains greater values at higher altitude.

It is concluded that, if the vertical observations could be corrected to account for the effect of $v_{\perp N}$, then the upflow occurrences derived from the CP-7 data would exhibit a similar diurnal variation to those for lower altitudes. It is not clear, though, why a greater occurrence of upflows is detected in CP-7 data than is observed in CP-2 observations at similar heights. Notwithstanding the problems associated with vertical observations, the CP-7 data reveal progressively greater frequency occurrences of upflow events with increasing altitude.

5.3.4 Examination of Ambient Field-aligned Flow

The diurnal distributions of upflows (Figure 5.3) indicated a dependence of upflow occurrence on UT, a feature also noted by *Keating et al. (1990)*. Such a dependence may be due to a real increase in the incidence of accelerating processes on the night-side. Equally, however, it is possible that the higher number of upflows detected in the night sector is simply due to an ambient field-aligned plasma drift which is greater on the night-side.

Indeed, field-parallel ion velocities measured by the EISCAT radar do exhibit a general diurnal variation, illustrated in Figure 5.9. In each panel of the figure, the full lines represent the median and quartile values of the velocity distributions binned at hour intervals. The figure was constructed by binning *all* CP-1 and CP-2 field-aligned velocity measurements according to altitude and UT, and simply calculating the median and quartile values of the distribution in each bin.

It is noted that there is good correspondence between the median and modal values of velocity within each bin. Panel (a) of Figure 5.9 displays the variation with UT of the modal velocity at 200-km altitude (red crosses). The modes were derived using velocity bins of width 10 m s⁻¹. The similarity between the median and modal values demonstrates that the median velocities are indeed representative of “typical” field-aligned flows.

Between 200 and 300-km altitude the median velocity exhibits a simple UT dependence, with largely upward flow between about 2000 and 0200 UT and downward flow at other times. The velocities are small, typically not exceeding 40 m s⁻¹, maximizing around 2300, 2200 and 2100 UT at 200, 250 and 300-km altitude, respectively. In the upper range gates, the night-time maximum remains at 2100 UT but there is an additional peak in the median velocity, centred around 0600 UT, which becomes positive in the 500-km range bin. The spread of velocities, greater at the higher altitudes, is still generally less than 50 m s⁻¹.

To summarise, the figure demonstrates that there is an ambient field-aligned flow that is directed upward between about 1800 and 0400 UT, maximizing near to local magnetic midnight (2200 UT), and downward at other times. This variation is probably a consequence of the neutral wind pattern. On the night-side, typically southward neutral winds tend to drive

CP-1 and CP-2 field-aligned observations 840124 to 960319, SNR limit 2%

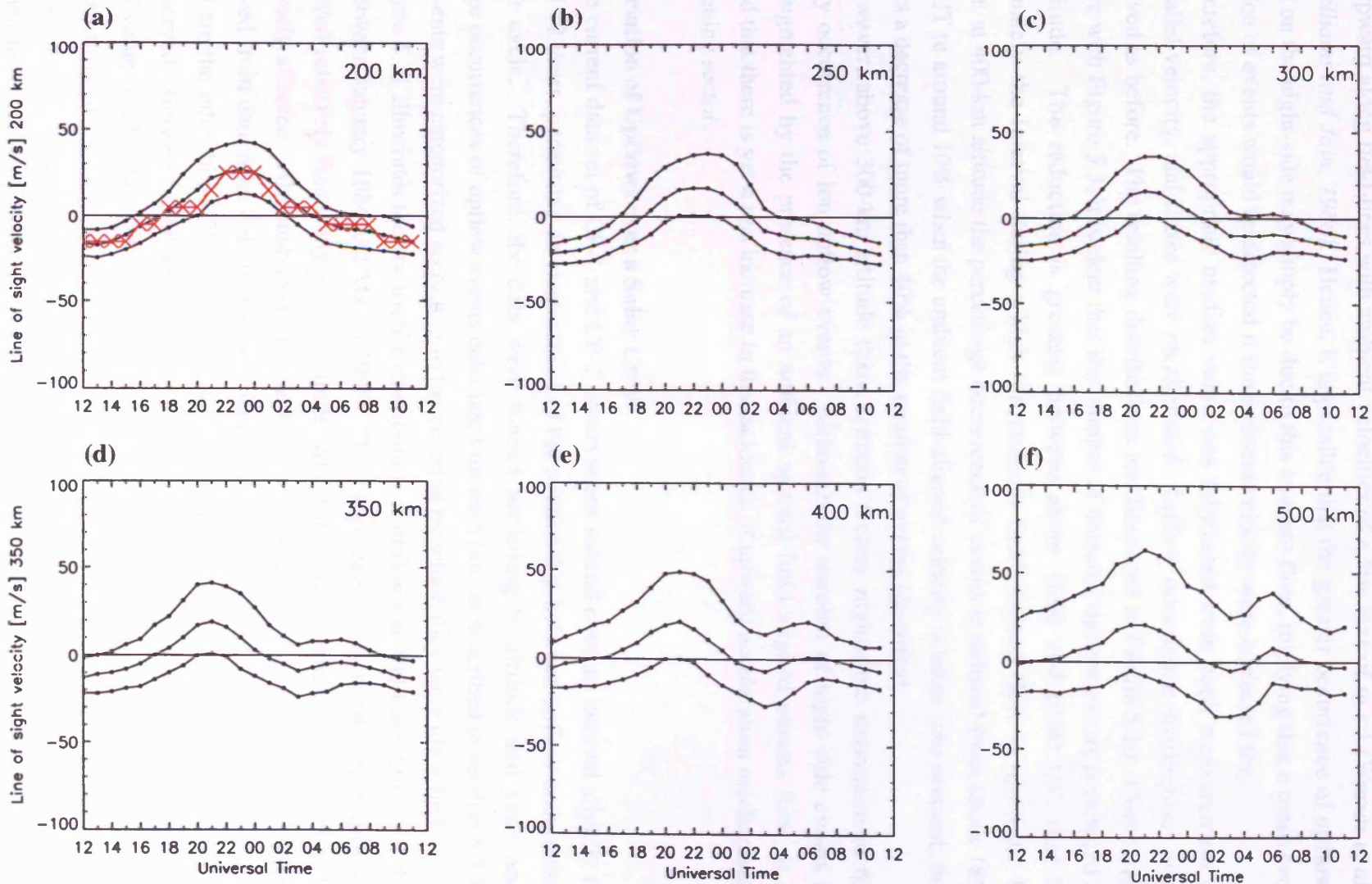


Figure 5.9 Variation of the field-parallel ion velocity as a function of UT and altitude. Velocity measurements at each altitude were binned at hourly intervals and median (full line) and quartile values derived for each bin. The red line in panel (a) indicates the modal value of $v_{||}$ in each bin at 200-km altitude (see text for details).

plasma upward along field-lines with ambient velocities of a few tens of m s^{-1} (Winser *et al.*, 1986; Williams and Jain, 1986). Hence, it is possible that the greater occurrence of upflows observed on the night-side may simply be due to this ambient flow, implying that a more even distribution of events would be detected if the ambient velocity were corrected for.

Therefore, the appropriate median value was subtracted from each measurement of field-parallel velocity, and fluxes were recalculated. Upflow occurrence distributions were then derived as before. The resulting distributions are illustrated in Figure 5.10. Comparing this figure with Figure 5.3, it is clear that the number of detected upflow events is reduced at each altitude. The reduction is greatest between about 1800 and 0100 UT, that is, approximately the interval during which the ambient field-aligned flow is upward. In particular, at 400-km altitude the percentage occurrence of events is reduced from about 18% at 2100 UT to around 10% when the ambient field-aligned velocity is taken into account; this represents a decrease of more than 40% in the number of events identified.

However, above 300-km altitude there remains a clear night-time maximum in the frequency occurrence of ion upflow events. Although the number of night-side events is clearly augmented by the presence of an ambient upward field-aligned plasma flow, it is concluded that there is yet a real increase in the incidence of upward acceleration mechanisms in the evening sector.

5.3.5 Variation of Upflows over a Solar Cycle

The current data set of CP-1 and CP-2 observations extend over an interval slightly in excess of 12 years, permitting an examination of the relationship between upflow occurrence and solar cycle. Therefore, the data were binned according to altitude and year, and percentage occurrences of upflow events calculated for each bin, as described in section 5.3.1. Again, events were categorized according to the criterion by which they were identified.

Figure 5.11 illustrates the occurrence distribution of upflows at 400-km altitude for the period between January 1984 and March 1996. This range-gate was selected since upflows are observed relatively frequently at this altitude, whilst the total number of observations is not adversely affected. Although thirteen year-bins are included in the figure, that for 1996 was derived from data from only two experiments and is therefore less representative of the year than are the other bins. The figure reveals a dependence on year of the type of upflow event observed. Between 1988 and 1992 the majority of events exhibited fluxes above the threshold value, whilst during this period there were very few velocity events, and only a small proportion of the upflows exhibited both large fluxes *and* velocities. However, the opposite situation is apparent for the remaining intervals, namely 1984 to 1987 and 1993 to 1996, when few events exhibited fluxes above the threshold value but which exceeded the velocity criterion. It was noted that a similar distribution (not illustrated), albeit with reduced upflow frequencies, was obtained when the flux and velocity threshold values were increased to $2 \times 10^{13} \text{ m}^{-2} \text{ s}^{-1}$ and 200 m s^{-1} , respectively, demonstrating that the clear variation in the

CP-1 and CP-2 field-aligned observations 840124 to 960319, SNR limit 2%

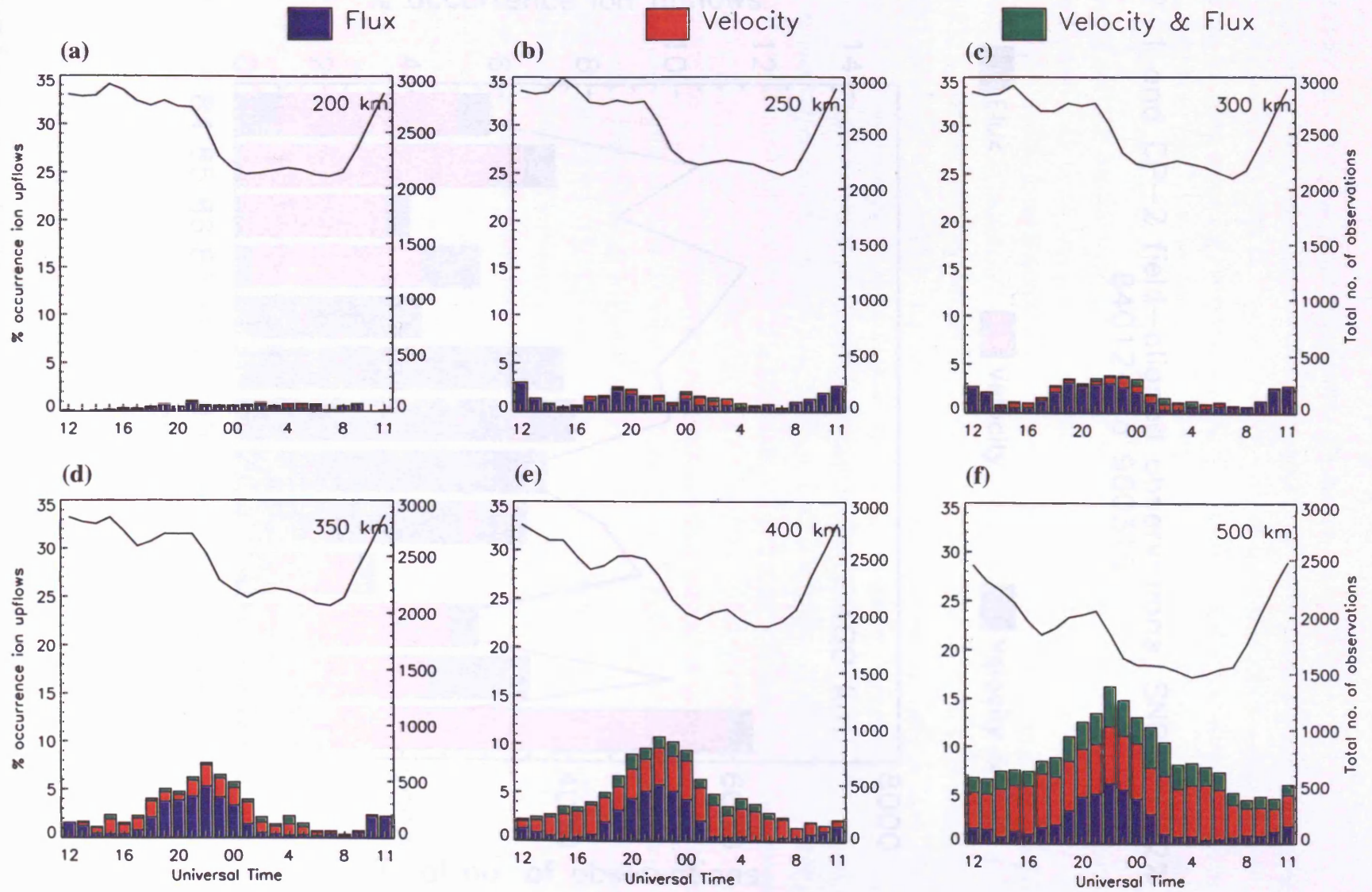


Figure 5.10 Same as Figure 5.3 but with the upflows measured against the median values of Figure 5.9.

type of event is not a consequence of the arbitrary selection criteria.

The period from around late 1987 to the middle of 1993 corresponded to the more active period of Solar Cycle 23, "active" here signifying a sunspot number (R_z) of greater than about 50. The remaining intervals covered by the present data set, however, fall within the less active periods of Solar Cycles 21 and 22 (Solar Cycle Catalog Data Set, 1981). The study examined the interval from September 1981 to May 1984, coincident with the descending phase of solar cycle 21. Yan and co-authors (1982) was a factor of two larger than the outflow rate between 1983 and 1984. It was also noted that various outflow rates were not statistically significant. Hence, the study was primarily greater than 10 eV ions, was observed.

Previous studies have demonstrated that the magnitude and composition of ionospheric outflow on solar cycle 23. The study examined the interval from September 1981 to May 1984, coincident with the descending phase of solar cycle 21. Yan and co-authors (1982) was a factor of two larger than the outflow rate between 1983 and 1984. It was also noted that various outflow rates were not statistically significant. Hence, the study was primarily greater than 10 eV ions, was observed.

CP-1 and CP-2 field-aligned observations, SNR limit 2%
840124 to 960319

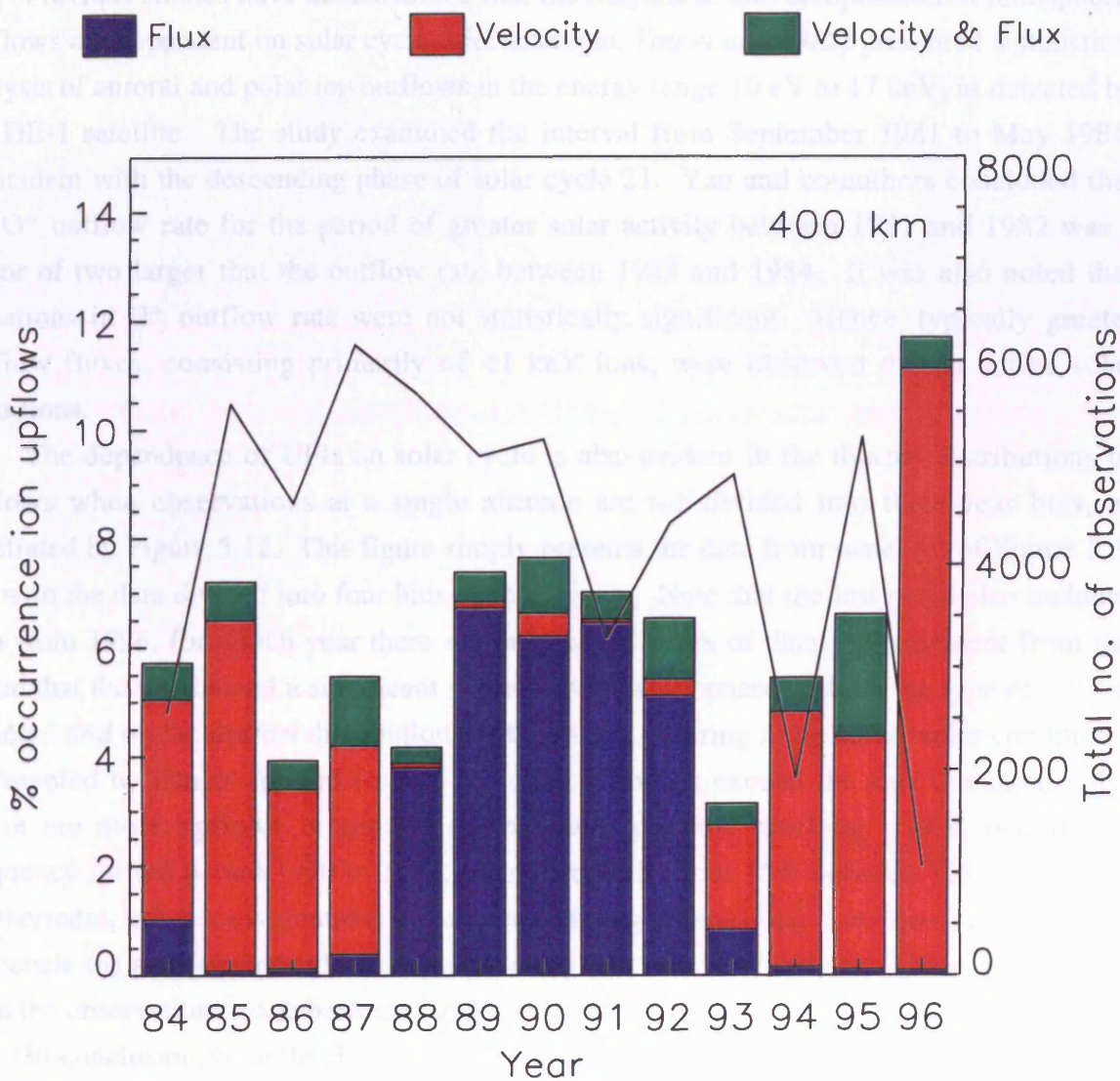


Figure 5.11 Frequency occurrence of upflows as a function of year between 1984 and 1986 at 400-km altitude. Histogram bars are subdivided as for Figure 5.3.

type of event is *not* a consequence of the arbitrary selection criteria.

The period from around late 1987 to the middle of 1993 corresponded to the more active period of Solar Cycle 22, “active” here signifying a sunspot number (R_z) of greater than about 50. The remaining intervals covered by the present data set, however, fell within the less active periods of Solar Cycles 21 and 22 (*Solar-Geophysical Data*, 27 Feb. 1996). These loosely-defined intervals of greater and lesser solar activity correspond well to the changes in upflow characteristics documented above, with flux events predominant during generally active solar conditions and velocity events prevalent at other times.

Previous studies have demonstrated that the magnitude and composition of ionospheric outflows are dependent on solar cycle. For example, *Yau et al. (1985)* presented a statistical analysis of auroral and polar ion outflows in the energy range 10 eV to 17 keV, as detected by the DE-1 satellite. The study examined the interval from September 1981 to May 1984, coincident with the descending phase of solar cycle 21. Yau and co-authors concluded that the O^+ outflow rate for the period of greater solar activity between 1981 and 1982 was a factor of two larger than the outflow rate between 1983 and 1984. It was also noted that variations in H^+ outflow rate were not statistically significant. Hence, typically greater outflow fluxes, consisting primarily of <1 keV ions, were observed during active solar conditions.

The dependence of UFIs on solar cycle is also evident in the diurnal distributions of upflows when observations at a single altitude are sub-divided into three-year bins, as illustrated by Figure 5.12. This figure simply presents the data from panel (e) of Figure 5.3, but with the data divided into four bins of three years. Note that the last panel also includes data from 1996, for which year there are only a few hours of data. It is evident from the figure that there is indeed a significant variation with solar phase on both the type of upflow detected *and* on the diurnal distributions of the events. During more active solar conditions, represented by panels (b) and (c), the majority of events exceed the flux threshold only. There are more upflows in general during these periods, reaching a 30% occurrence frequency for the period 1990 to 1992, compared with about 15% between 1984 and 1986. Furthermore, broader distributions are observed during quieter solar conditions, as illustrated by panels (a) and (d). Indeed, the familiar diurnal variation of upflows is scarcely evident from the observations made between 1993 and 1996.

In conclusion, both the distributions of upflows and the type of event exhibit a strong dependence on solar cycle. The diurnal distributions presented by *Keating et al. (1990)* were derived from observations taken between 1985 and 1987, and are therefore representative of the ascending phase of solar cycle 22. However, as indicated by Figure 5.12, markedly different distributions could have been obtained from a different sample data set.

Keating and co-authors suggested that many supposed upflow events detected at altitudes above 400 km were, in fact, due to large scatter in derived velocity and flux values, arising from reduced signal-to-noise ratios high altitudes. It is possible, then, that some of the

CP-1 and CP-2 field-aligned observations, SNR limit 2%

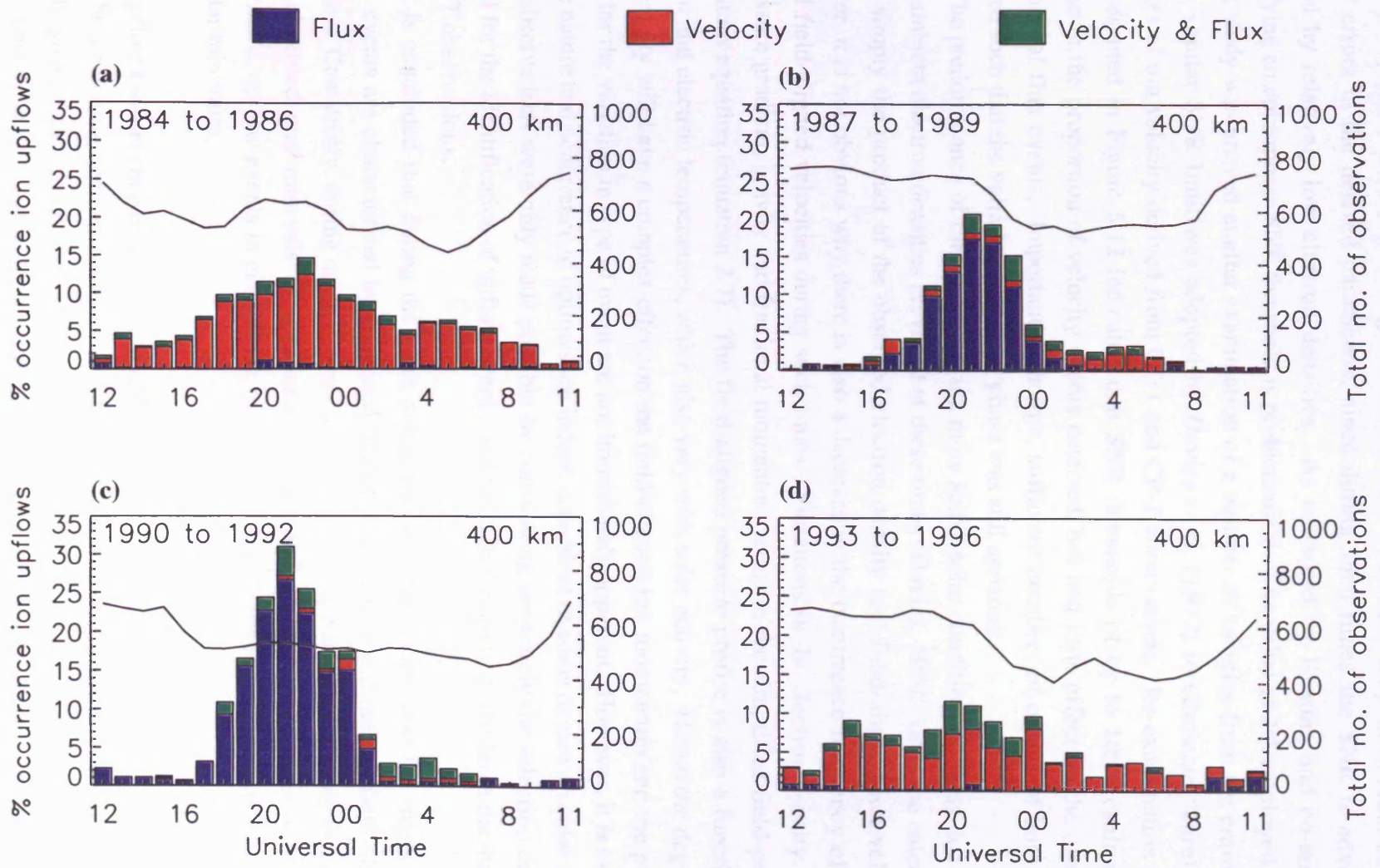


Figure 5.12 Same as panel (e) of Figure 5.3 but with observations further divided into four three-year bins, illustrating the variation in the diurnal upflow occurrence distribution over one solar cycle.

“velocity” upflows identified during less active solar conditions may have resulted from greater errors in the derived parameters, since during such times the SNR is adversely affected by relatively low electron densities. As remarked by Keating and co-authors, quantifying an appropriate SNR threshold is problematical. The value of 2% employed in the present study was arrived at after examination of a number of samples from the entire data set. A similar SNR limit was adopted by *Davies et al. (1997)* to eliminate “unreliable” estimates of ion velocity derived from CP-1 and CP-2 observations. Re-examination of the data presented in Figure 5.12 indicated that SNR thresholds of up to 10% resulted in a decrease in the proportion of velocity events detected, but had little effect on the observed frequency of flux events. Importantly, though, sufficient numbers of events of both types remained such that the variation with solar phase was still apparent.

The predominance of flux events during more active solar conditions is likely due to the higher ambient electron densities prevalent at these times (*Davies, 1990*), since the calculated flux is simply the product of the observed electron density and field-aligned ion velocity. However, it is not obvious why there is also a decrease in the occurrence frequency of large upward field-aligned velocities during such times. Variations in the electron density affect the pressure gradient, gravity and frictional momentum terms in the simplified field-parallel momentum equation (equation 2.7). The field-aligned pressure profile is also a function of both ion and electron temperatures, which also vary with solar activity. Hence the degree of solar activity will have a complex effect on the field-aligned ion momentum and the precise causes for the variation in type of event are not immediately apparent. However, it is evident that the nature and occurrence of upflows are indeed dependent to some degree on solar cycle. These observations were only made possible by considering separately the selection criteria adopted for the identification of upflow events, and through the study of the large database of EISCAT observations.

It is concluded that during the more active phase of the solar cycle the majority of upflow events are characterized by enhanced field-aligned fluxes and modest field-aligned velocities. Conversely, during quieter solar conditions, large upward field-aligned fluxes are rarely observed and intervals of enhanced field-aligned velocities are more common. Furthermore, upflow events in general are more frequently observed during solar maximum than solar minimum.

5.3.6 Upflow Occurrence as a Function of K_p

The preceding section demonstrated that the occurrence frequency of upflows was typically greater during solar maximum than that during solar minimum. Increased solar activity tends to enhance geomagnetic activity through the influence of disturbances such as solar flares. Magnetic activity on the Earth can be represented by the K_p index (*Bartels, 1949*). K_p values are derived at 3-hourly intervals, using measurements from 11 mid-latitude magnetometer stations situated around the globe. The K_p index ranges from 0 to -1, 1, +1, -2

etc. through to a maximum of 9; values of between 2 and 3 are characteristic of quiet to moderate geomagnetic activity.

The variation with geomagnetic activity of the diurnal distribution of upflow events is illustrated in Figure 5.13. Observations from 400-km altitude were categorized according to K_p value, with four ranges representing varying degrees of magnetic activity, namely, $0 \leq K_p \leq 1+$, $-2 \leq K_p \leq 2+$, $-3 \leq K_p \leq 3+$ and $K_p \geq 4$. It is evident that the number of upflow events increases with greater geomagnetic activity. This is attributable to the fact that features commonly associated with the generation of upflows, such as ion frictional heating and particle precipitation, occur more frequently during disturbed magnetic conditions. This observation is consistent with the study of *Yau et al. (1985)*. DE-1 measurements of high-latitude outflows revealed that the O^+ outflow rate was greater during active geomagnetic conditions ($3 \leq K_p \leq 5$) than at quiet times ($K_p \leq 2$). Yau and co-authors also noted that the outflow rate for $K_p \geq 6$ was a factor of 30 times greater than the value for $K_p = 0$.

5.3.7 Upflow Occurrence and Ion Frictional Heating.

It was discussed in *Chapter 2* how F-region ion frictional heating (IFH) may contribute to the production of upward plasma flows in the high-latitude ionosphere. A number of studies (eg. *Davies et al., 1997; McCrea, 1989; McCrea et al., 1991*) have presented occurrence distributions of high-latitude, F-region ion frictional heating events. *Davies et al. (1997)* employed EISCAT observations in an investigation of the diurnal distribution of IFH events under various geomagnetic and IMF conditions. In that study, ion frictional heating events were characterized by an increase in the measured ion temperature of more than 100 K above the unperturbed value for that altitude; the unperturbed value was defined as the modal value of ion temperature for *each* experiment run. Furthermore, only events that occurred in at least two consecutive post-integration periods were accepted, in order to eliminate uncorrelated “spikes” in the ion temperature data, thought to be caused by satellite echoes or system faults (*McCrea et al., 1991*). Using these criteria, Davies and co-authors derived diurnal occurrence distributions of ion frictional heating at 300-km altitude. The data from each experiment run were first partitioned into 30-minute bins. Then, for each half-hour bin, the number of intervals in which heating events were detected was expressed as a fraction of the total number of bins. The selection method was based upon that of *McCrea et al. (1991)* and *St.-Maurice and Hanson (1982)*, and is described in detail by *Davies et al. (1997)*.

A similar analysis was adopted in the present study, in order to derive diurnal distributions of ion frictional heating events suitable for comparison with the upflow distributions. For each experiment run in the CP-1 and CP-2 data set, modal ion temperatures were calculated for each of the six range gates between 200 and 500 km. Then, frictional heating events were identified as increases above the mode of more than 100 K. However, in order to remain consistent with the earlier analysis of ion upflows, events occurring in only one post-integration bin were accepted. Finally, the number of events within hourly bins

CP-1 and CP-2 field-aligned observations 840124 to 960319, SNR limit 2%

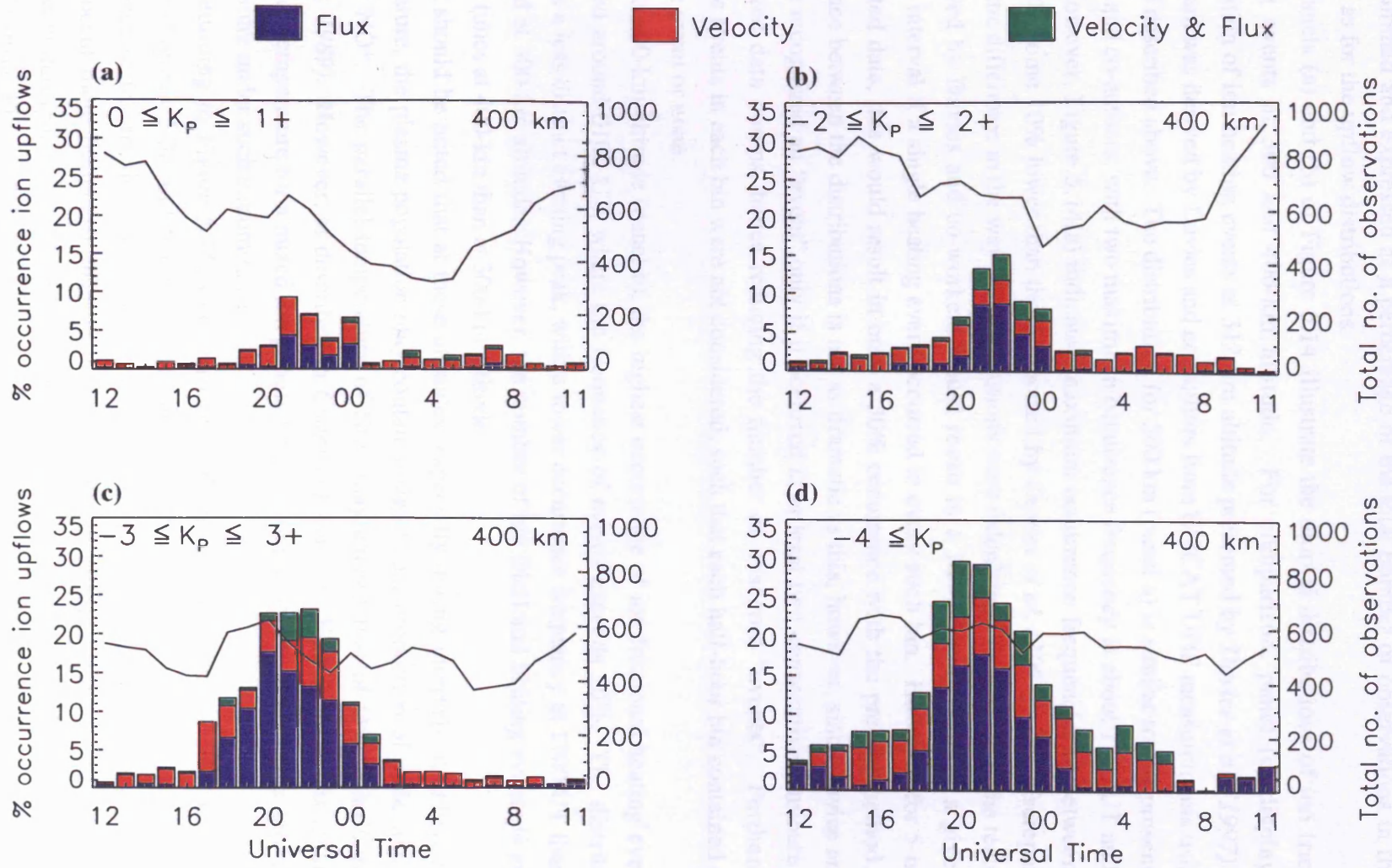


Figure 5.13 Same as panel (e) of Figure 5.3 but with observations further divided according to K_p value, illustrating the variation in the diurnal upflow occurrence distribution with geomagnetic activity.

were summed and expressed as a percentage of the total number of observations in the bin, exactly as for the upflow distributions.

Panels (a) and (b) of Figure 5.14 illustrate the diurnal distributions of ion frictional heating events at 300 and 400-km altitude. For comparison, panel (c) displays the distribution of ion heating events at 312-km altitude presented by *Davies et al. (1997)*. This histogram was derived by Davies and co-authors from EISCAT UHF measurements using the method described above. The distribution for 300 km (panel a) is similar to that presented by Davies and co-authors, with two maxima in occurrence frequency at about 1700 UT and 2300 UT. However, Figure 5.14(a) indicates maximum occurrence frequencies of between 30% and 40%, some 10% lower than those reported by *Davies et al. (1997)*. The discrepancy is due to the difference in the way the distributions were calculated. For example, the technique employed by Davies and co-workers would result in a 100% occurrence for a given 30-minute interval if a single heating event occurred in every such bin. However, for 5-minute integrated data, this would result in only a 30% occurrence with the present method. The difference between the distributions is not as dramatic as this, however, since Davies and co-authors recognized an “event” only if it occurred in at least two consecutive 5-minute post-integrated data dumps, hence reducing the number of observed “events”. Furthermore, multiple events in each bin were not considered, such that each half-hour bin contained either a single event or none.

At 400-km altitude (panel b), the highest occurrence of ion frictional heating events is observed around 0100 UT, where the frequency of events exceeds 50%. The distribution exhibits a less distinct evening peak, with a lower occurrence frequency at 1700 UT than was detected at 300-km altitude. However, the number of ion frictional heating events is greater at most times at 400-km than at 300-km altitude.

It should be noted that at these altitudes, especially during intervals of enhanced ion temperature, the plasma population may contain a significant proportion of molecular ions, namely NO^+ . The parallel temperature of NO^+ may exceed that of O^+ (*Lathuillere and Hubert, 1989*). However, as described in *Chapter 3*, standard EISCAT analysis assumes a single ion temperature for a mixed ion population, resulting in inaccuracies in the derived ion temperature under such circumstances.

Returning to Figure 5.14, a comparison with the upflow distributions for the same altitude (Figures 5.3c and 5.3e), there is no obvious correlation between the statistical occurrence of ion frictional heating and ion upflow events. In general, frictional heating events occur more frequently than upflows, such that it appears possible that *all* upflows could occur during intervals of enhanced ion temperature.

However, Figures 5.15(a) and (b) present distributions of intervals of *simultaneous* ion upflow and frictional heating events, at 300 and 400-km altitude, respectively. A crude comparison of these distributions with Figures 5.3(c) and 5.3(e), included as panels (c) and (d) in Figure 5.15, suggests that perhaps 50% of upflows occur during intervals of enhanced

CP-1 and CP-2 field-aligned observations, SNR limit 2%
840124 to 960319

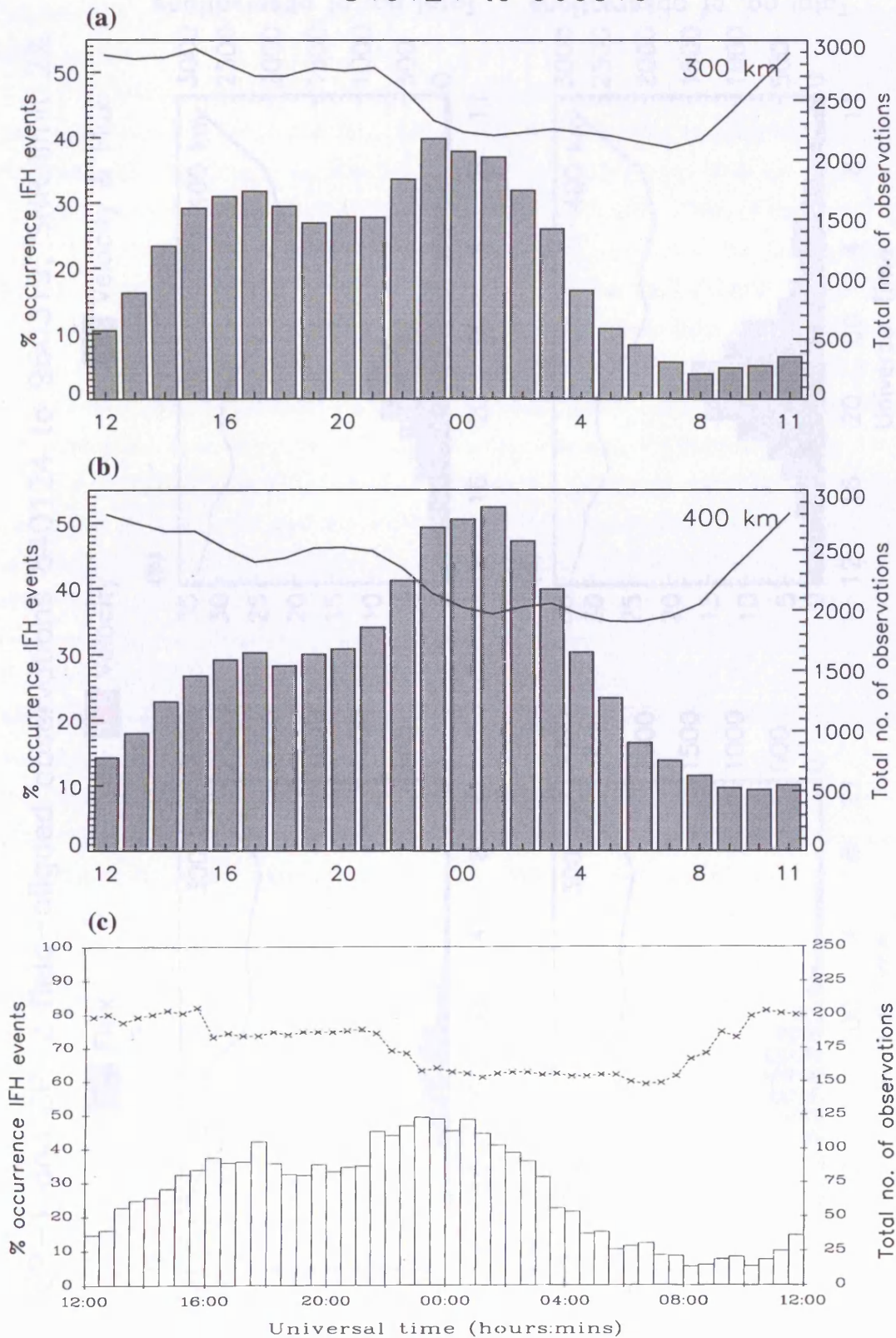


Figure 5.14 Diurnal distribution of ion frictional heating events at (a) 300 km and (b) 400 km derived from CP-1 and CP-2 field-aligned observations from 1984 to 1996. (c) Distribution of ion frictional heating at 312 km (from *Davies et al., 1997*).

CP-1 and CP-2 field-aligned observations 840124 to 960319, SNR limit 2%

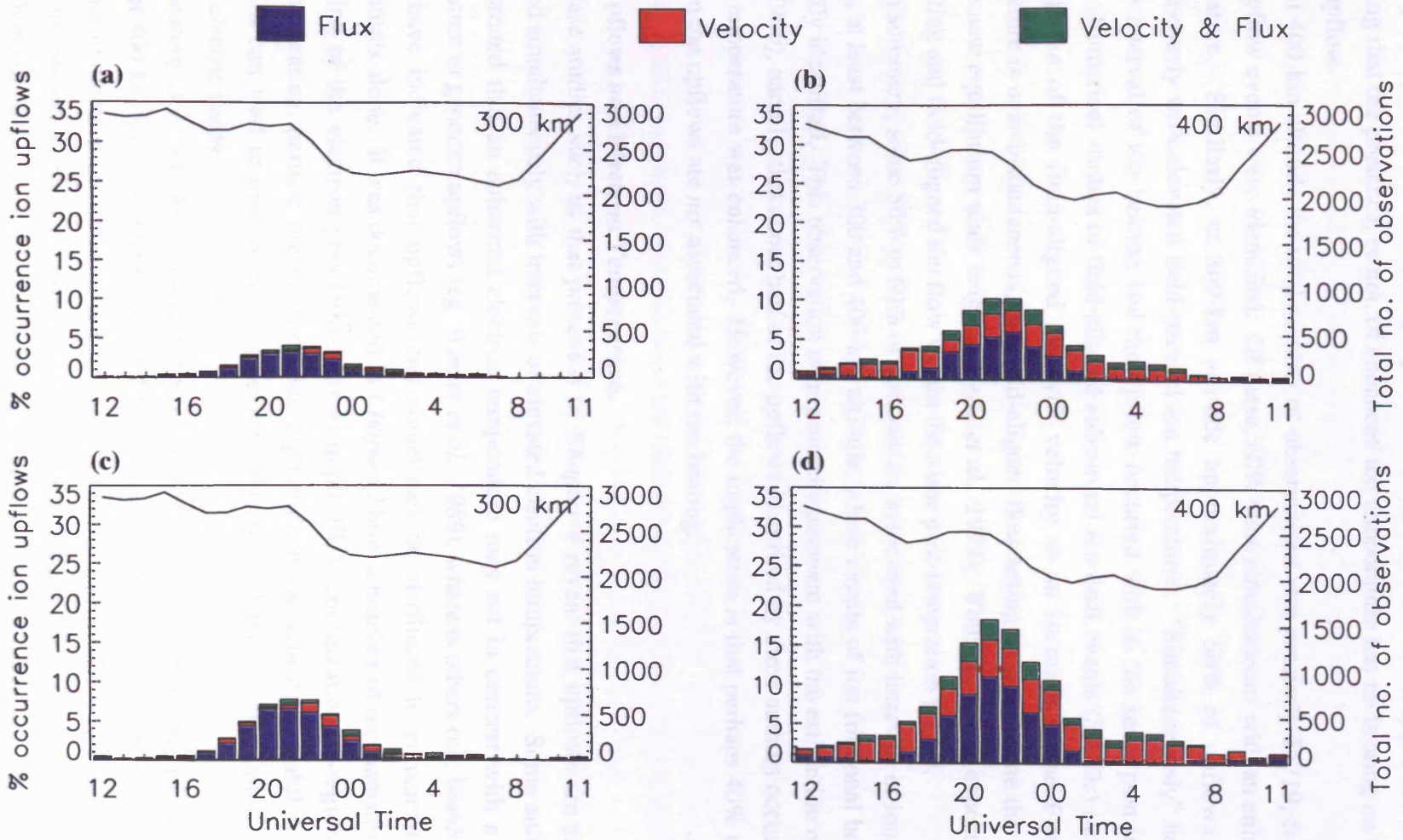


Figure 5.15 Diurnal distributions of simultaneous upflow and ion frictional heating events at (a) 300 and (b) 400 km. (c) Same as Figure 5.3(c). (d) Same as Figure 5.3(e).

ion temperature. Furthermore, the proportions of the different event types are unchanged, indicating that the presence, or not, of enhanced ion temperature has no bearing on the nature of the upflow.

At 400-km altitude the total number of observations was precisely 55719, from which 3322 upflow events were identified. Of these, 60% were simultaneous with an enhanced ion temperature. Similarly, at 300-km altitude approximately 50% of upflows occurred simultaneously with elevated field-parallel ion temperatures. "Simultaneously" here means that the interval of ion heating and the upflow occurred within the same post-integration period. Numerical studies of field-aligned subauroral ion drift events (SAIDs) indicate that the response of the field-aligned ion drift velocity to an increase in the F-region ion temperature is near-instantaneous, the field-aligned flow acting to redistribute the plasma to attain a new equilibrium scale height (*Heelis et al., 1993*). Thus we might expect to detect ion heating and field-aligned ion flow within the same post-integration period.

In summary, some 50% to 60% of upflows are associated with intervals of ion frictional heating, at least between 300 and 400-km altitude, where events of ion frictional heating can be readily identified. This observation is in general agreement with the estimation of *Keating et al. (1990)*, namely, that about half of the upflows identified by these authors occurred when the ion temperature was enhanced. However, the implication is that perhaps 40% to 50% of F-region ion upflows are *not* associated with ion heating.

5.3.8 Upflows and Electron Temperature.

Case studies such as that presented in *Chapter 4* reveal that upflows are sometimes observed simultaneously with intervals of elevated electron temperature. Some authors have demonstrated that an enhanced electron temperature may act in concert with a high ion temperature to generate upflows (eg. *Winser et al., 1989*), whereas others (eg. *Wahlund et al., 1992*) have indicated that upflows can sometimes be attributed to enhanced electron temperatures alone. It was documented in *Chapter 2* how a number of mechanisms can lead to heating of the electron population, for example EUV energization, E-region electron turbulent heating, particle precipitation and high-altitude ion-acoustic instabilities. These processes can lead to upward ion acceleration through enhanced polarization and field-aligned electric fields.

Keating et al. (1990) examined the relationship between large upward field-aligned fluxes at 400 km and ion temperature at 200 km, the observations being further categorized according to electron temperature at the lower altitude. These authors concluded that more upflow events occurred when both ion and electron temperatures at lower altitudes were higher than normally observed. Furthermore, measured upward fluxes were typically greater at such times. Inherent in these conclusions was the adoption of a mean ion temperature, representative of winter-time values at 2100 UT and 200-km altitude. The mean temperature was based upon all Common Programme observations made between 1985 and 1987 (*Farmer*

et al., 1990), the period of the study. The assumption of such a gross average is reasonable for the ion temperature. *Davies (1996)* derived ambient ion temperatures from EISCAT observations at 312-km altitude for the period 1985 to 1991. Between 1985 and 1987 relatively little variation in the modal value was detected, the temperature typically falling between 750 and 950 K. These figures compare favourably with the mean value of about 870 K employed by Keating and co-authors.

To examine the statistical relationship between enhanced *electron* temperatures and ion upflows, an appropriate base value against which to identify elevated temperatures is required. Since the ion temperature exhibits little diurnal variation, it is comparatively straightforward to derive meaningful diurnal averages, as described above (*McCrea et al.*, 1991; *Davies*, 1996). However, this approach is inappropriate for the electron temperature, which is primarily dependent on solar flux and hence exhibits large diurnal, seasonal and solar cycle fluctuations. Instead, median values of electron temperature, derived from distributions categorized according to altitude, UT, season and solar cycle, were calculated and used as a basis against which to measure electron temperature enhancements.

Having established base values by which to identify intervals of elevated electron temperature, a similar analysis to that described in section 5.3.7 was performed. That is, diurnal upflow distributions were derived for events where the electron temperature enhancement exceeded a specified threshold. An arbitrary value of 100 K was adopted; to a crude approximation, an electron temperature increase of 100 K would have a similar effect on the plasma pressure as an increase in ion temperature of the same magnitude.

Figure 5.16 illustrates the diurnal distribution of upflows at 400-km altitude which were concurrent with either an elevated ion or electron temperature, or both. The form of the distribution is clearly comparable with that of Figure 5.3(e), with similar proportions of the different event types evident. Hence the events represented in Figure 5.16 are a characteristic subset of *all* observed upflows. A quantitative examination of the data revealed that about 80% of all upflows detected at 400-km altitude occurred during intervals when either the ion or electron temperature was enhanced. It is noted that *Keating et al. (1990)* examined the relationship between upflows at 400-km altitude with heating events at 200 km. There was no suggestion, however, that upflows should not be associated with ion or electron heating at the same altitude. Indeed, case studies have revealed that upflows and enhanced plasma temperatures occur simultaneously at the same height (*Jones et al.*, 1988; *Wahlund et al.*, 1992; *Chapter 4*).

The limitations of the selection technique for identifying upflows and ion frictional heating events have already been addressed, *viz.* the problems associated with defining threshold parameters and of determining ambient values against which to measure changes. It has been shown that representative ambient ion temperatures can be obtained by calculating the modal value for a given experiment run (*McCrea*, 1989; *Davies*, 1996). In the present study, enhancements in electron temperature were measured according to differences between

observed and median values, the latter based on HISCAT CP-1 and CP-2 observations between 1984 and 1996. Therefore, local enhancements in electron temperature would not be detected if the current "ambient" temperature was sufficiently greater than the median value.

CP-1 and CP-2 field-aligned observations, SNR limit 2%
840124 to 960319

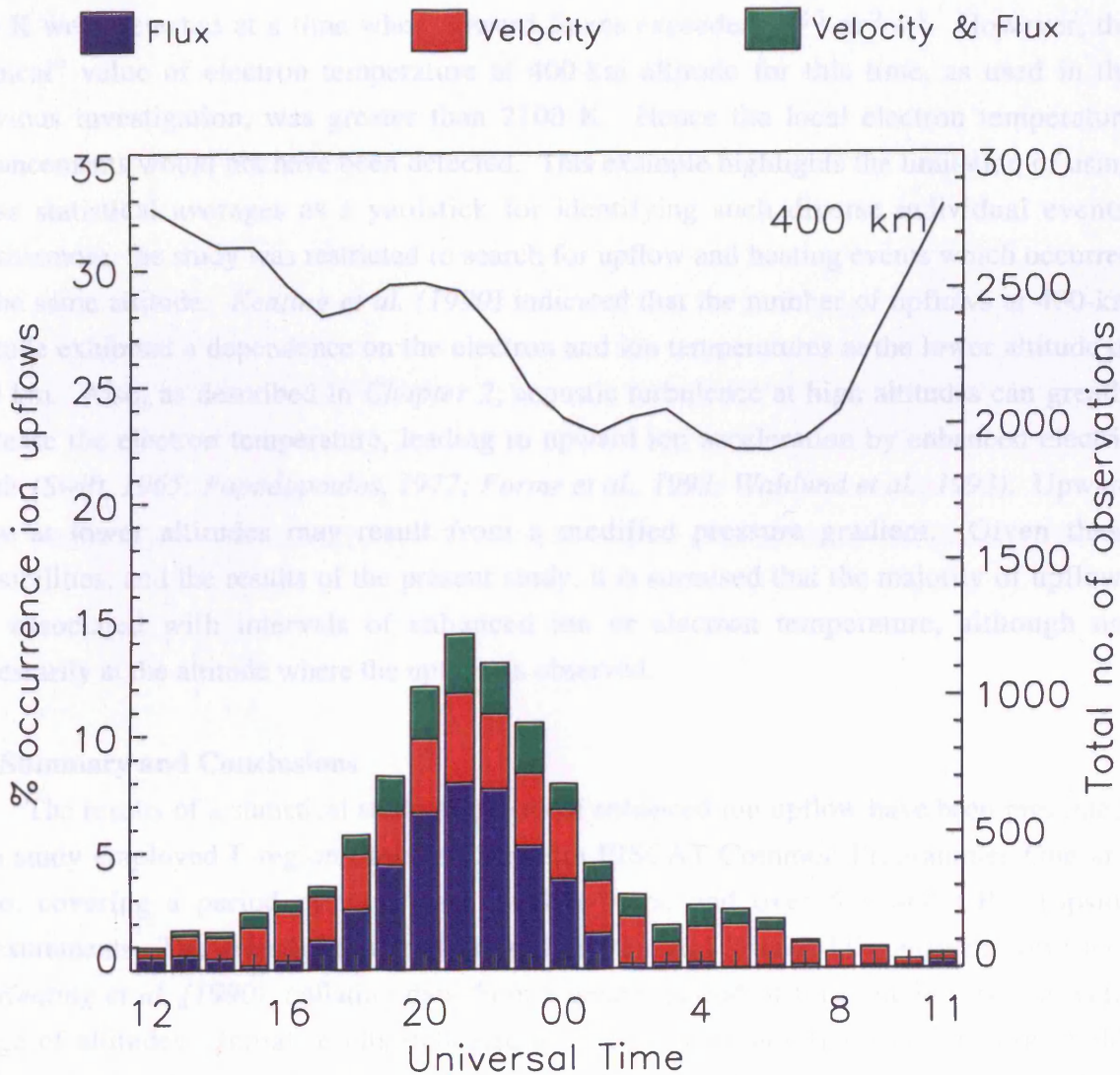


Figure 5.16 Diurnal distribution of upflows (400 km) simultaneous with either an enhanced ion or electron temperature.

observed and median values, the latter based on EISCAT CP-1 and CP-2 observations between 1984 and 1996. Therefore, local enhancements in electron temperature would not be detected if the current “ambient” temperature was sufficiently greater than the median value. An example of such is apparent in CP-1 observations from October 27, 1988, illustrated in Figure 5.17. The figure presents time-series of field-aligned ion flux, field-parallel ion temperature and electron temperature at 400-km altitude between 1600 and 2200 UT. Between about 1900 and 2000 UT, transient electron temperature enhancements of well over 100 K were detected at a time when upward fluxes exceeded $10^{13} \text{ m}^{-2} \text{ s}^{-1}$. However, the “typical” value of electron temperature at 400-km altitude for this time, as used in the previous investigation, was greater than 2100 K. Hence the local electron temperature enhancements would not have been detected. This example highlights the limitation of using gross statistical averages as a yardstick for identifying such diverse individual events. Furthermore, the study was restricted to search for upflow and heating events which occurred at the same altitude. *Keating et al. (1990)* indicated that the number of upflows at 400-km altitude exhibited a dependence on the electron and ion temperatures at the lower altitude of 200 km. Also, as described in *Chapter 2*, acoustic turbulence at high altitudes can greatly increase the electron temperature, leading to upward ion acceleration by enhanced electric fields (*Swift, 1965; Papadopoulos, 1977; Forme et al., 1993; Wahlund et al., 1993*). Upward flow at lower altitudes may result from a modified pressure gradient. Given these possibilities, and the results of the present study, it is surmised that the majority of upflows are associated with intervals of enhanced ion or electron temperature, although not necessarily at the altitude where the upflow is observed.

5.4 Summary and Conclusions

The results of a statistical study of events of enhanced ion upflow have been presented. The study employed F-region observations from EISCAT Common Programmes One and Two, covering a period of more than twelve years, and over 5 years’ CP-7 topside measurements. The investigation has followed on from and extended the analysis performed by *Keating et al. (1990)*, collating data from a greater period of time and covering a wider range of altitudes. Initial results indicated a higher occurrence frequency of large field-aligned plasma flows in the evening sector, in agreement with the work of Keating and co-authors. However, the inclusion of vertical observations up to 800-km altitude revealed that the frequency of upflows increases steadily with height, whereas the study of Keating and co-workers suggested that the peak occurrence maximized between 400 and 500-km altitude. The present analysis also established that vertical observations are, in general, affected by the meridional component of ion velocity, which itself exhibits a strong diurnal variation.

The current study also revealed a pronounced seasonal dependence of upflow occurrence, with a greater frequency of UFIs during the winter months at 350 and 400-km altitude. It was also remarked that the large data set employed in the present study reduced

the influence of 'anomalous' intervals such as the July 1987 period noted by Keating *et al.* (1990). The preponderance of events in the evening sector is partially attributable to an ambient upward

CP-1 Field-Aligned Observations, 27/10/1988

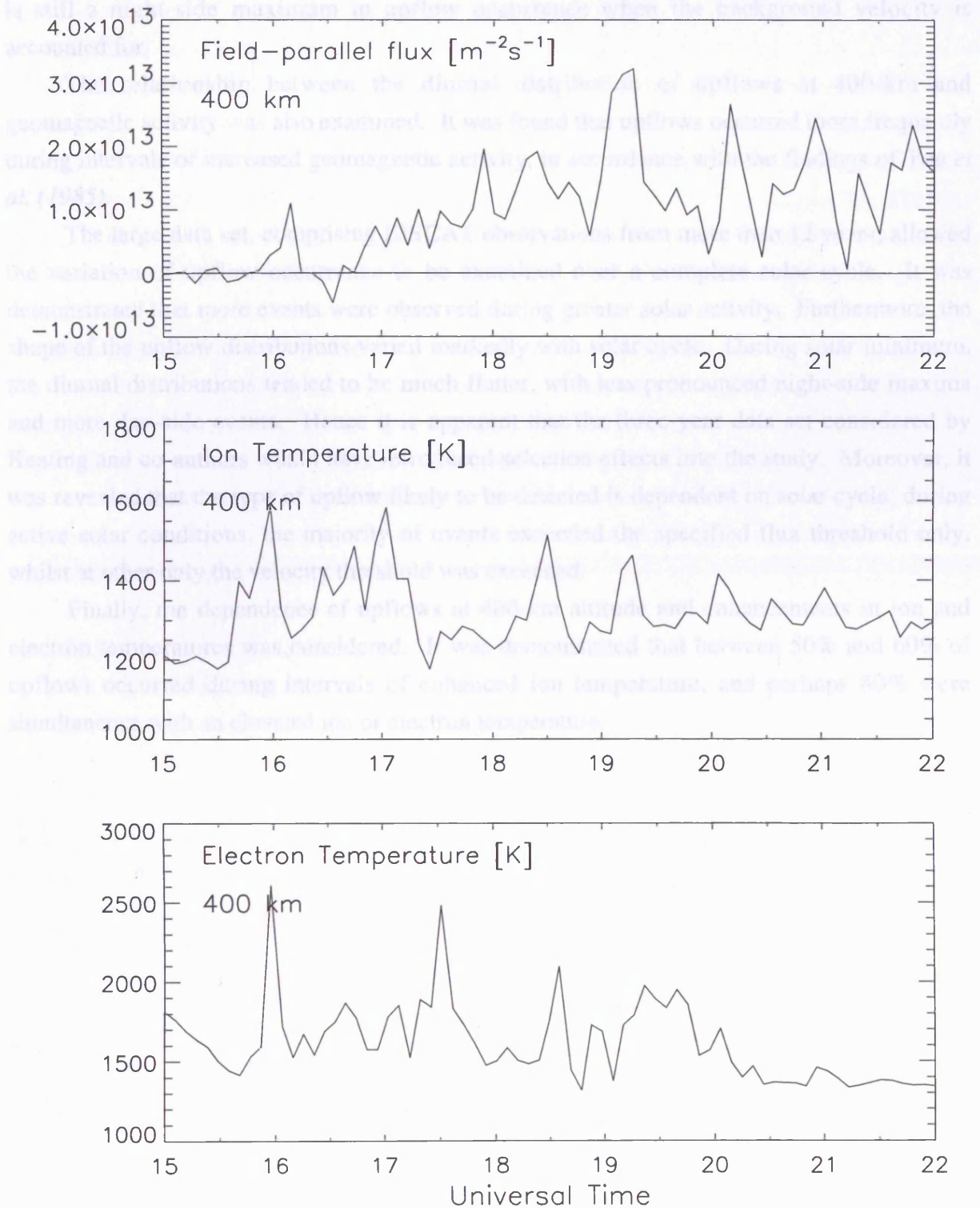


Figure 5.17 EISCAT CP-1 observations from 27 October 1988. Between 1900 and 2000 UT, transient electron temperature enhancements of up to 500 K occurred at a time when upward fluxes exceeded $10^{13} \text{ m}^{-2} \text{ s}^{-1}$.

the influence of “anomalous” intervals such as the July 1987 period noted by *Keating et al. (1990)*. The preponderance of events in the evening sector is partially attributable to an ambient upward field-aligned flow centred around local magnetic midnight. However, there is still a night-side maximum in upflow occurrence when the background velocity is accounted for.

The relationship between the diurnal distribution of upflows at 400-km and geomagnetic activity was also examined. It was found that upflows occurred more frequently during intervals of increased geomagnetic activity, in accordance with the findings of *Yau et al. (1985)*.

The large data set, comprising EISCAT observations from more than 12 years, allowed the variation of upflow occurrence to be examined over a complete solar cycle. It was demonstrated that more events were observed during greater solar activity. Furthermore, the shape of the upflow distributions varied markedly with solar cycle. During solar minimum, the diurnal distributions tended to be much flatter, with less pronounced night-side maxima and more day-side events. Hence it is apparent that the three-year data set considered by Keating and co-authors would have introduced selection effects into the study. Moreover, it was revealed that the type of upflow likely to be detected is dependent on solar cycle; during active solar conditions, the majority of events exceeded the specified flux threshold only, whilst at other only the velocity threshold was exceeded.

Finally, the dependence of upflows at 400-km altitude and enhancements in ion and electron temperatures was considered. It was demonstrated that between 50% and 60% of upflows occurred during intervals of enhanced ion temperature, and perhaps 80% were simultaneous with an elevated ion or electron temperature.

CHAPTER 6

An Investigation of a Simple Model and its Application to a Dayside Ion Upflow Event Observed by EISCAT

6.1 Introduction

An interval of field-aligned ion upflow has been modelled using a simple, steady-state approximation to the field-parallel momentum equation for a single ion. The upflow was detected by the EISCAT radar during a run of Common Programme One on April 3, 1992, an interval previously studied by *Davies et al. (1995)* as an example of prolonged dayside ion-frictional heating. This chapter presents an investigation of the model's ability to account for the observed upflow event. In particular, the relative effects of plasma pressure, gravity, neutral wind, magnetic mirror force and thermal diffusion on the field-aligned ion momentum are investigated. The latter two terms are shown to be insignificant in the present study and the ion velocity profile is dictated by pressure, collisions and gravity. However, the assumption of a single-ion plasma in the analysis of the radar data, and in the model itself, does not allow for agreement between observations and model predictions. It is concluded that accurate modelling of observed velocities requires the true ion composition to be known, in order to minimise errors in the derived parameters and hence supply reliable values to the momentum equation.

6.2 Motivation for Present Study

The preceding two chapters have considered ion upflows in a largely qualitative manner. The initial objective of the current study is a quantitative examination of a typical ion upflow event, in order to better appreciate the relative importance of the various acceleration mechanisms that have thus far been discussed. In addition, the analysis will provide an insight into the applicability and limitations of a simple model, which is similar to that employed in a number of published works.

An additional incentive for the study lies in the upflow event to be modelled. The interval has been previously studied by *Davies et al. (1995)*. Davies and co-authors were interested in the event as an example of extended daytime ion frictional heating. The EISCAT observations were compared with results from the Sheffield University plasmasphere and ionosphere model (SUPIM). It was demonstrated that, when a neutral wind was included in the model, SUPIM generated ion and electron temperature enhancements that were consistent with the observations. However, the model failed to reproduce the large upward field-aligned velocities observed, nor the subsequent downward flows. Indeed, the field-aligned flows predicted by SUPIM were at times opposite in direction to those observed (*Davies, 1996*). It was suggested that the discrepancy between the model results and observations was due, in part, to the modification of the field-aligned velocity by the neutral wind. Neither the ambient meridional neutral wind, nor that resulting from Joule expansion

of the lower thermosphere, were included in the model. In the light of these results, it is of interest to examine whether a very simple, time-independent model, similar to those employed by *Jones et al. (1988)* and *Wahlund et al. (1992)*, could successfully account for the observations.

As discussed in *Chapter 2*, the models employed by *Jones et al. (1988)* and *Wahlund et al. (1992)* were approximations based on the one-dimensional momentum equation for a single ion. Both models primarily considered just pressure gradients, ion-neutral collisions, the magnetic mirror force and gravity, but adequately accounted for the observations. Hence there is evidence that such simple approaches can be effective. The following sections describe a similar modelling study of an ion outflow observed by the EISCAT radar, together with an appraisal of the model employed.

6.3 Observations

Measurements obtained from the EISCAT UHF radar during a run of CP-1 on April 3, 1992 are presented in Figure 6.1. Panels (a) to (d) illustrate the behaviour of the field-parallel ion temperature, electron temperature, electron density and field-parallel ion velocity, respectively, at 300, 450 and 600-km altitude between 0700 and 1500 UT. This interval has been described in detail by *Davies et al. (1995)*. These authors' interest lay in the period of intense F-region ion frictional heating detected between 1200 and 1430 UT (panel a). The heating was caused by an enhanced zonal ion drift velocity that at times exceeded 2 km s^{-1} (not illustrated). The interval was also marked by an increase in the electron temperature above 250-km altitude and a sharp drop in the F-region electron density. In addition, enhanced upward field-parallel ion flows were evident between 1200 and 1300 UT. Upward ion velocities, indicated by positive values in panel (d), were detected above about 350 km (not shown in the figure), increasing with altitude and exceeding 100 m s^{-1} at around 1230 UT. Subsequently, return flows of greater magnitude were observed. Davies and co-authors attributed the flows to enhanced diffusion resulting from modified ion and electron temperature gradients. However, simulations performed by the SUPIM model were unable to account for the observed flows. It is therefore of interest to examine the upflow in more detail, using a simple model to provide an insight into the acceleration mechanisms involved, and to examine the limitations of the model itself.

It is noted that some authors (eg. *Liu et al., 1995; Caton et al., 1996; Blnelly et al., 1996*) have included the effects of electron precipitation in their upflow models. However, *Davies et al. (1995)* indicated that there was no evidence of particle precipitation during this interval. Therefore, it should be possible to simulate the observed velocities with an approximation similar to that employed by *Jones et al. (1988)*, that is, primarily by considering ambipolar diffusion and ion-neutral collisions. The event is also of interest because it occurred during the day; the study presented in the preceding chapter demonstrated that day-side upflows are infrequently observed by the EISCAT radar.

6.4 The Model

CP-1-J 3 April 1992 Tromso

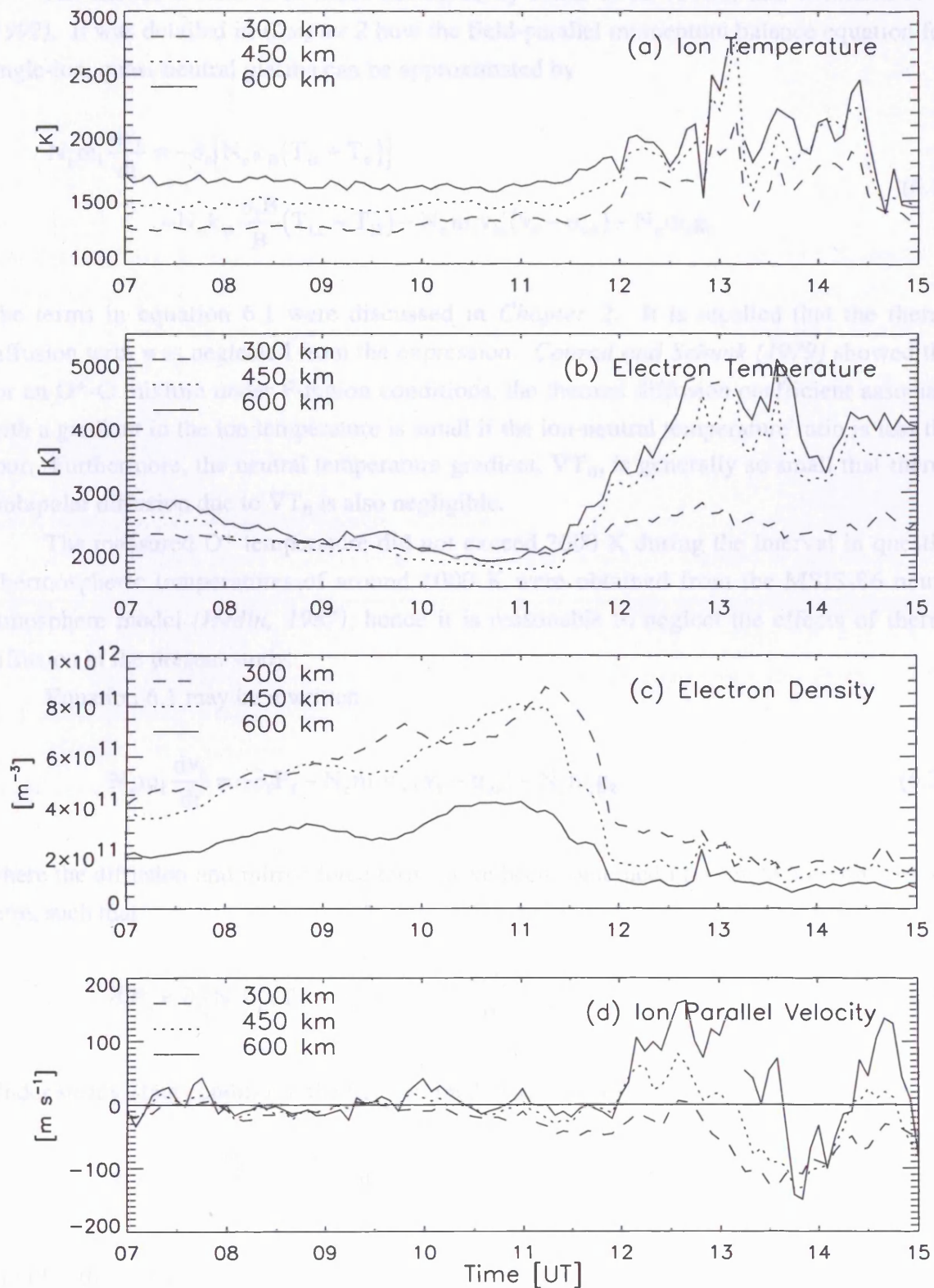


Figure 6.1 EISCAT CP-1-J long-pulse measurements of (a) ion temperature, (b) electron temperature, (c) electron density and (d) ion parallel velocity at 300, 450 and 600-km altitude from 3 April, 1992.

6.4 The Model

The model is similar to those described by *Jones et al. (1988)* and *Wahlund et al., (1992)*. It was detailed in *Chapter 2* how the field-parallel momentum balance equation for a single-ion, quasi-neutral plasma can be approximated by

$$N_e m_i \frac{dv_{\parallel}}{dt} = -\partial_{\parallel} [N_e k_B (T_{i\parallel} + T_e)] - N_e k_B \frac{\partial_{\parallel} B}{B} (T_{i\perp} - T_{i\parallel}) - N_e m_i v_{in} (v_{\parallel} - \mathbf{u}_{n\parallel}) - N_e m_i \mathbf{g}_{\parallel} \quad (6.1)$$

The terms in equation 6.1 were discussed in *Chapter 2*. It is recalled that the thermal diffusion term was neglected from the expression. *Conrad and Schunk (1979)* showed that, for an O⁺-O mixture under F-region conditions, the thermal diffusion coefficient associated with a gradient in the ion temperature is small if the ion-neutral temperature ratio is less than four. Furthermore, the neutral temperature gradient, ∇T_n , is generally so small that thermal ambipolar diffusion due to ∇T_n is also negligible.

The measured O⁺ temperature did not exceed 3000 K during the interval in question. Thermospheric temperatures of around 1000 K were obtained from the MSIS-86 neutral atmosphere model (*Hedin, 1987*), hence it is reasonable to neglect the effects of thermal diffusion in the present study.

Equation 6.1 may be rewritten

$$N_e m_i \frac{dv_{\parallel}}{dt} = -\partial_{\parallel} \mathbf{P}_{\parallel} - N_e m_i v_{in} (v_{\parallel} - \mathbf{u}_{n\parallel}) - N_e m_i \mathbf{g}_{\parallel} \quad (6.2)$$

where the diffusion and mirror-force terms have been combined in a single pressure gradient term, such that

$$\partial_{\parallel} \mathbf{P}_{\parallel} = \partial_{\parallel} [N_e k_B (T_{i\parallel} + T_e)] + N_e k_B \frac{\partial_{\parallel} B}{B} (T_{i\perp} - T_{i\parallel}) \quad (6.3)$$

Under steady-state conditions, the field-aligned velocity may therefore be approximated by

$$v_{\parallel} = -\frac{\partial_{\parallel} \mathbf{P}_{\parallel}}{N_e m_i v_{in}} - \frac{\mathbf{g}_{\parallel}}{v_{in}} + \mathbf{u}_{n\parallel} \quad (6.4)$$

Finally, the ion-neutral collision frequency for a single-ion plasma of O⁺ and a neutral atmosphere consisting of O, O₂ and N₂ is given by (*Bailey and Sellek, 1990*)

$$v_{in} = v_{O^+-O} + v_{O^+-O_2} + v_{O^+-N_2} \quad (6.5)$$

where

$$\begin{aligned} v_{O^+-O} &= 4.45 \times 10^{-11} [O] T_r^{\frac{1}{2}} (1.04 - 0.067 \log_{10} T_r)^2 \\ v_{O^+-O_2} &= 6.64 \times 10^{-10} [O_2] \\ v_{O^+-N_2} &= 6.82 \times 10^{-10} [N_2] \end{aligned} \quad (6.6)$$

and

$$T_r = \frac{1}{2} (T_i + T_n) \quad (6.7)$$

The expressions in square brackets symbolize neutral densities per cubic centimetre. T_n represents the thermospheric temperature and T_i the three-dimensional ion temperature. The former, along with the neutral densities, were obtained from the MSIS-86 neutral atmosphere model (*Hedin, 1987*).

6.5 Method and Results

6.5.1. Modelling of Observed Velocity Profiles

The data from April 3, 1992 were integrated at 5-minute resolution and analysed as described in *Chapter 3*, using the standard EISCAT plasma composition model, illustrated in Figure 3.9. For each height profile, comprising 21 range gates between 140 and 600-km altitude, the plasma pressure gradient in the field-parallel direction was calculated. Hence, theoretical velocity profiles were derived via equation 6.4.

Initially, the velocity profile was modelled during an interval for which flow magnitudes were small at all altitudes, indicating little altitudinal acceleration, and when the field-parallel velocity was relatively constant in time, representing steady-state conditions. The observed profile at 0915 UT satisfied these criteria. Figure 6.2(a) illustrates the gravitational (dashed line) and pressure (dotted line) terms from equation 6.4. Positive velocity values represent upward field-aligned flow. Isotropic ion temperatures were assumed, hence the hydrodynamic mirror force was neglected. The modelled velocity profile above 300-km altitude is represented by the full line. The measured velocity at 300 km was taken as a lower boundary condition for the modelled velocity. In effect, this merely provides an estimate of the neutral wind term, \mathbf{u}_{\parallel} , in equation 6.4. The value obtained was approximately 16 m s^{-1} . The 300-km range gate was selected as the lower boundary primarily because the plasma composition model adopted in the analysis assumes that O^+ is the only ion present above that altitude. The assumptions made in the model therefore limit its validity to heights above 300 km. Furthermore, the field-parallel component of neutral wind is estimated at the lower range and assumed to be constant with increasing altitude, implying a horizontal neutral wind that is invariant with altitude. *Baron and Wand (1983)* argued that the neutral wind is constant with altitude above about 300 km, viscosity reducing variations above that height, although other authors (eg. *Rishbeth 1972; Wharton et al., 1984*)

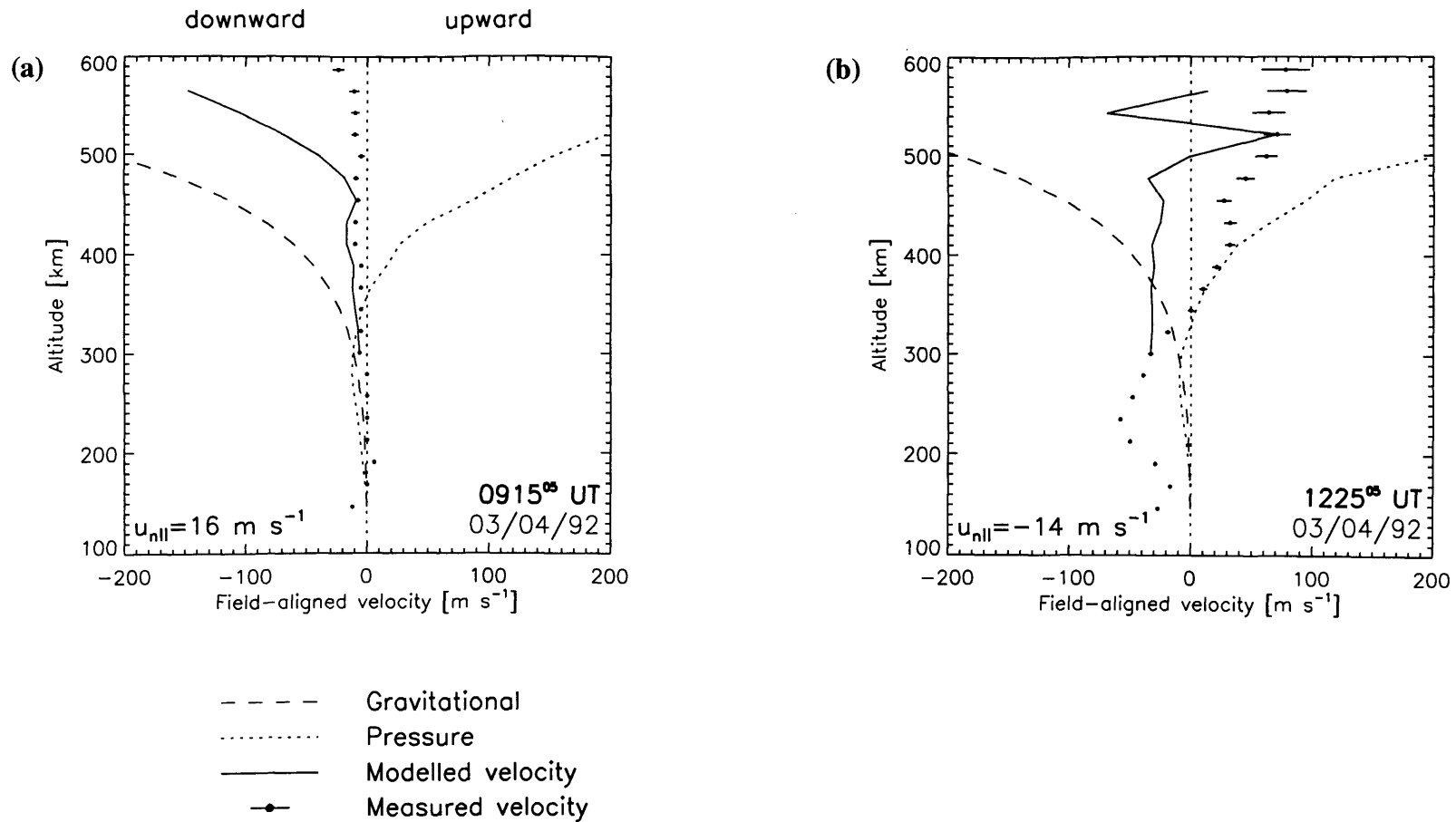


Figure 6.2 Velocity profiles resulting from the gravitational (dashed line) and pressure (dotted line) terms of equation 6.4 for (a) 0915 UT and (b) 1225 UT on 3 April, 1992. The full line in each panel represents the resultant modelled velocity profile derived from equation 6.4. The field-parallel component of the neutral wind velocity is indicated in each frame. Measured velocities are represented by points with error bars.

have suggested that the neutral wind is invariant with height above about 200 km.

The modelled velocity profile was compared with the observed velocity, the latter illustrated in the figure as points with error bars. It is clear that there is no similarity whatsoever between the velocity profiles beyond about 450-km altitude. Even below that height, the magnitude of the modelled velocity profile exceeds the observed value by approximately 10 m s^{-1} . Although the error is not great, it is significant in comparison with the observed velocities of only a few m s^{-1} . Notably, the observed and modelled velocity profiles do not agree even within experimental uncertainty.

Figure 6.2(b) presents the same parameters for 1225 UT, approximately the time when maximum upward velocities were detected. The deviation between the modelled and observed velocity profiles is more pronounced in this case. Theoretical velocity estimates are, in the main, opposite in direction to measured values, indicating that the gravitational term is dominant over the pressure term in the model. Notably, the sudden fluctuation of the velocity profile between negative and positive values near 500-km altitude illustrates the sensitivity of the theoretical velocity to the pressure gradient.

These examples demonstrate that the simple model cannot account for the observed upflows. Some doubt exists as to the value of the O^+ -O collision frequency (eg. *Winser et al., 1988a; Burnside et al., 1987*). However, modified values do not improve the agreement between model and observations, since both the pressure and gravitational terms of equation 6.4 are a function of v_{in} .

Several factors may account for the failure of the simple model. During intervals of ion frictional heating, temperature anisotropies arise, and, in the presence of a magnetic field gradient, the magnetic mirror force will come into play (*Suvanto et al., 1989*). However, the mirror force is unlikely to be of influence during undisturbed conditions such as were prevalent at 0915 UT. A more probable source of error lies in the assumption of the ion composition profile. Analysis of the data employed the standard plasma composition model (Figure 3.9). It was detailed in *Chapter 3* how the relative proportion of molecular ions can become enhanced during intervals of ion frictional heating, through increased reaction rates and neutral atmosphere upwelling (*St.-Maurice and Torr, 1978; Raitt et al., 1975*). Underestimation of the proportion of molecular ions leads to underestimations of both ion and electron temperatures (*Lockwood et al., 1993*), whilst velocity measurements are unaffected. Such an error would clearly affect the derived plasma pressure profile. Furthermore, any change in either the neutral atmosphere or plasma constituents at a given altitude would modify the collision frequency, thus affecting the modelled velocity. These effects are likely present to some degree during the interval of ion heating and upflow, but probably not during the quieter period. Then, the standard ion composition model and the MSIS-86 neutral atmosphere model should be representative of the real conditions. The failure of the model might question the validity of the MSIS model or the standard ion composition model adopted in the analysis. However, it seems more likely that the simple model is itself at fault.

6.5.2. A Comparison of Force Terms

It was intimated in the preceding discussion that the modelled velocity profile was largely influenced by the plasma pressure gradient. A comparison of the relative importance of the force terms of equation 6.2 is illustrated in Figure 6.3. The field-parallel ion velocity is again assumed constant with time, but now altitudinal acceleration is included, such that

$$\frac{dv_{\parallel}}{dt} = v_{\parallel} \partial_{\parallel} v_{\parallel} \quad (6.8)$$

Neglecting the neutral wind term, equation 6.2 may be expressed

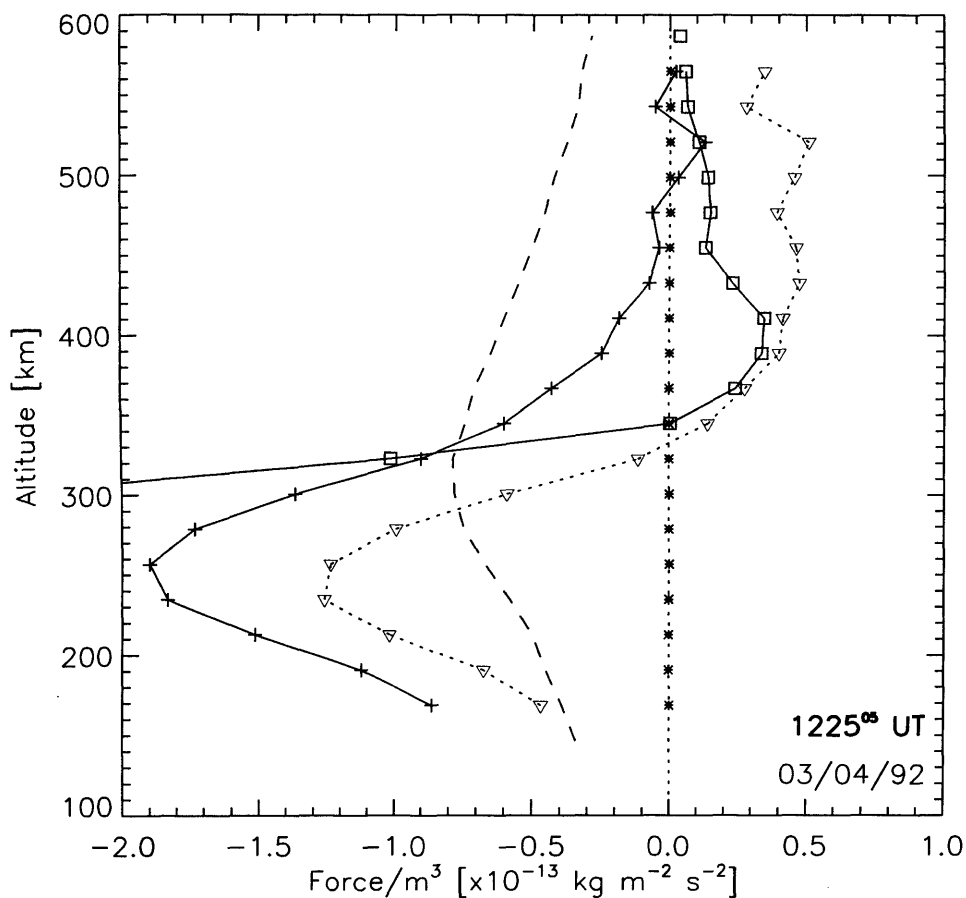
$$N_e m_i v_{in} v_{\parallel} + N_e m_i v_{\parallel} \partial_{\parallel} v_{\parallel} = -\partial_{\parallel} P_{\parallel} - N_e m_i g_{\parallel} \quad (6.9)$$

Figure 6.3 illustrates the four terms above, derived from measurements at 1225 UT. In addition, the sum of the terms on the left-hand side of the equation (a and b in the figure) are compared with those on the right (c and d in the figure). As discussed by *Wahlund et al. (1992)*, the LHS of equation 6.9 (a+b) represents the force (per m³) needed to produce the observed velocity profile, and the RHS the force available from pressure and gravitational sources (c+d). Again, isotropic ion temperatures were assumed, hence the mirror force is not considered. The figure demonstrates that, above about 300-km altitude, diffusion alone is unable to account for the observed velocity profile. Below that height, the collisional term, $N_e m_i v_{\parallel} v_{in}$, ceases to be meaningful since the assumption of a single-ion plasma is no longer valid. Analysis of the 0915 UT profile (not illustrated) resulted in a similar conclusion.

However, Figure 6.3 is informative in that it indicates the relative insignificance of the altitudinal acceleration term, $N_e m_i v_{\parallel} \partial_{\parallel} v_{\parallel}$. In fact, this term is of the order of 1000 times smaller than the others in equation 6.9. Finally, the pressure gradient, $\partial_{\parallel} P_{\parallel}$, is compared with the observed velocity profile illustrated in Figure 6.2(b). It is apparent that the velocity is positive where the pressure gradient is negative, and vice versa, indicating that the pressure profile is a controlling factor in determining the velocity. However, there is still a clear deficiency in the available force above 300-km altitude.

6.5.3 Consideration of the Magnetic Mirror Force

In view of the inability of simple plasma diffusion to account for the observed upflow, the magnetic mirror force might be considered as a source term. Anisotropic ion temperatures, coupled with the inhomogeneous geomagnetic field, lead to modulation of the field-parallel ion velocity through the hydrodynamic mirror force (*Suvanto et al., 1989*). Temperature anisotropies were indeed evident during the interval of ion frictional heating between 1200 and 1500 UT. *Davies (1996)* reported that the perpendicular ion temperature exceeded the parallel value by up to 1000 K at 278-km altitude. However, assuming a dipolar



- (a) $\square \square \square N_e m_i v_{\parallel} \nu_{in}$ (collisional)
- (b) $* * * N_e m_i v_{\parallel} \partial_{\parallel} v_{\parallel}$ (alt. accⁿ)
- (c) $\dots \nabla \dots -\partial_{\parallel} P_{\parallel}$ (pressure)
- (d) $- - - N_e m_i g_{\parallel}$ (gravitational)
- (a)+(b) (needed)
- + + + (c)+(d) (available)

Figure 6.3 Comparison of the force terms of equation 6.2 for the upflow at 1225 UT. The “needed” term (full line) is the sum of the collisional and altitudinal acceleration forces. The crossed full line represents the combined plasma pressure and gravitational forces. Above 300-km altitude, pressure driven diffusion is insufficient to account for the observed upflow.

geomagnetic field, such a temperature difference equates to a force the order of 10^{-27} N, some 100 times smaller than the gravitational force. Even at the highest observed altitude of 600 km, the mirror force is of the same order of magnitude. Therefore, the hydrodynamic mirror force may be reasonably neglected from further consideration.

6.6 Assessment of the Model

6.6.1 Errors Arising from an Incorrect Ion Composition Model

It has been ascertained that the simple model (equation 6.4) is unable to replicate the ion parallel velocities observed by EISCAT during the interval in question, even for undisturbed conditions. Discrepancies between model and observations arise largely because the theoretical velocity is extremely sensitive to changes in the pressure gradient, particularly at high altitudes, where ion-neutral collisions are comparatively rare. Thus, small errors in the calculated pressure gradient, of perhaps a few per cent, can result in velocity deviations of tens or hundreds of m s^{-1} at the highest altitudes. Given the errors inherent in the derived ion and electron temperatures and electron density, the modelling technique adopted thus far is unlikely to achieve agreement with observed velocity profiles.

This section describes an analysis intended to establish the validity of the model. From an assumption that the approximation is indeed valid, the model was used to derive pressure gradient profiles consistent with the observed ion velocities. These calculated pressure gradients were then compared with measured values; agreement between derived and measured $\partial_{\parallel} \mathbf{P}_{\parallel}$ profiles would indicate that the observed velocities were *consistent* with the measured pressure profile and that the model was valid.

Illustrated in Figure 6.4 are altitude profiles from 0800 and 0915 UT, these being intervals characteristic of undisturbed conditions prior to the upflow event. Within each panel, the measured ion velocities and associated uncertainties are represented by the blue points, and are scaled according to the upper axis. The measured plasma pressure profile is indicated by the dotted green line and is scaled according to the lower axis. As in Figure 6.3, the pressure gradient, $-\partial_{\parallel} \mathbf{P}_{\parallel}$, is represented by the black dotted line. Finally, superimposed in red is the *theoretical* pressure gradient, that is, the gradient required to produce the *observed* ion velocity above 300-km altitude.

This theoretical profile was derived from equation 6.4, simply by introducing observed velocity values into the left-hand side of the expression and adopting the measured pressure gradient at 300-km altitude as a boundary condition in order to derive an estimate of the neutral wind term, $\mathbf{u}_{n\parallel}$. The latter is also indicated in each panel.

Figure 6.4 demonstrates that, within uncertainty estimates, the measured and theoretical pressure gradients are largely in agreement. Thus it is surmised that the model is both applicable and largely representative of the conditions during the quieter intervals. It follows that the standard plasma composition model employed in the analysis is also valid for this

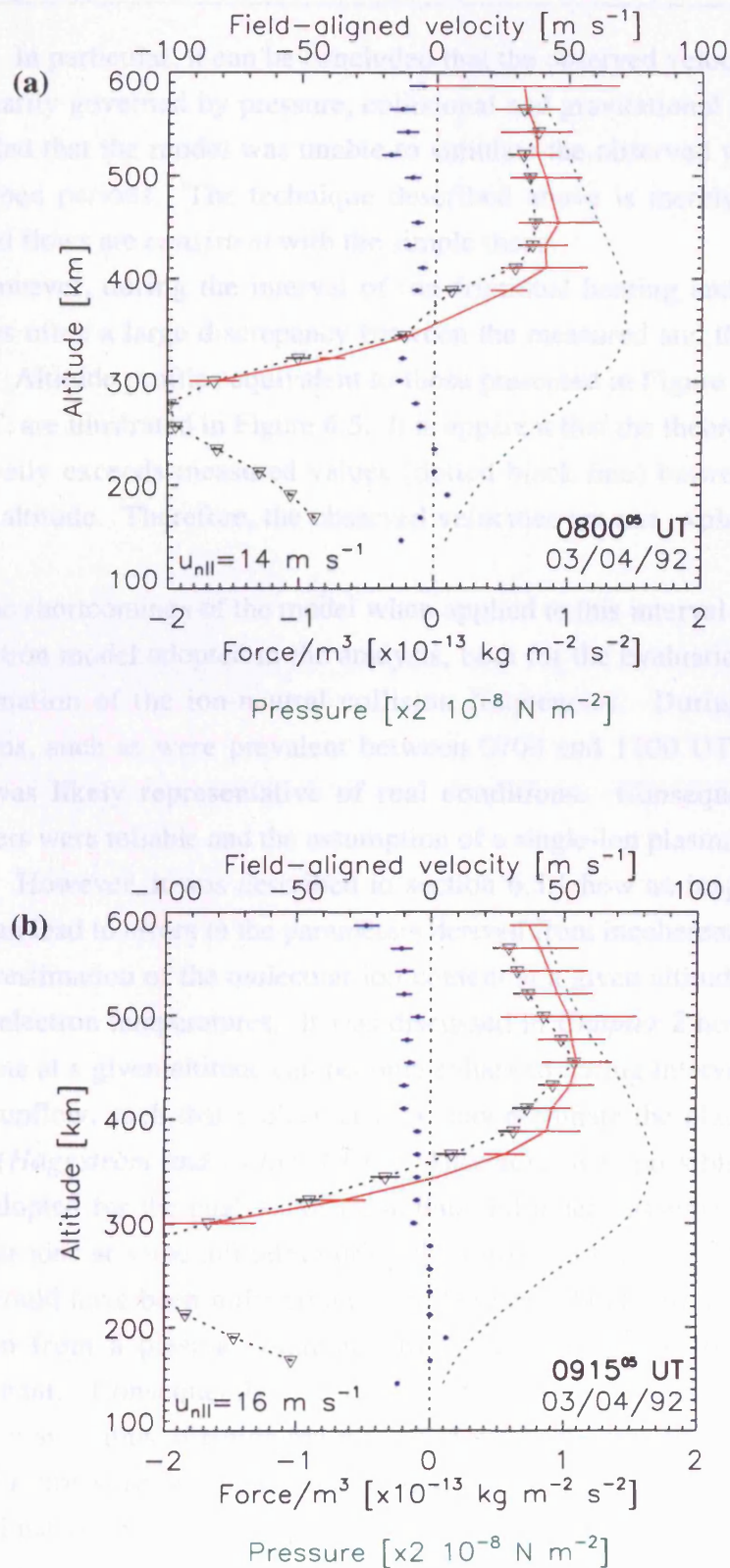


Figure 6.4 Profiles of the measured pressure gradient (dotted black line) and the pressure gradient derived from equation 6.4 (red line with error bars). In effect, the red line represents the pressure gradient profile that is consistent with the observed velocity profile (blue points). (The pressure gradient profiles are scaled according the lower axis and have dimensions of $\text{kg m}^{-2} \text{ s}^{-2}$). The green dotted lines illustrate the pressure profile. These intervals (0800 UT and 0915 UT) are representative of undisturbed conditions prior to the upflow. The figure indicates that the model is applicable at such times.

interval. In particular, it can be concluded that the observed velocities above 300-km altitude are primarily governed by pressure, collisional and gravitational forces. However, it should be recalled that the model was unable to simulate the observed velocities even during these undisturbed periods. The technique described above is merely able to establish that the measured flows are *consistent* with the simple theory.

However, during the interval of ion frictional heating and large field-aligned flows, there was often a large discrepancy between the measured and theoretical pressure gradient profiles. Altitude profiles equivalent to those presented in Figure 6.4, but for 1225, 1230 and 1235 UT, are illustrated in Figure 6.5. It is apparent that the theoretical pressure gradient (red line) greatly exceeds measured values (dotted black line) between approximately 300 and 450-km altitude. Therefore, the observed velocities are *not* explained by the model at these times.

The shortcomings of the model when applied to this interval probably stem from the ion composition model adopted in the analysis, both for the evaluation of the radar data and for the estimation of the ion-neutral collision frequencies. During undisturbed ionospheric conditions, such as were prevalent between 0700 and 1100 UT, the adopted composition model was likely representative of real conditions. Consequently, the derived plasma parameters were reliable and the assumption of a single-ion plasma appropriate above 300-km altitude. However, it was described in section 6.5.1 how an inappropriate ion composition model can lead to errors in the parameters derived from incoherent scatter data. In particular, an underestimation of the molecular ion content at a given altitude results in underestimated ion and electron temperatures. It was discussed in *Chapter 2* how the molecular content of the plasma at a given altitude can become enhanced during intervals of ion frictional heating and ion upflow, such that molecular ions may dominate the plasma up to perhaps 400-km altitude (*Hägström and Collis, 1990*). Therefore, it is possible that the ion composition model adopted for the analysis of these data did indeed assume insufficient proportions of molecular ions at some altitudes during the disturbed period. The error in the composition model would have been most pronounced between about 150 and 300 km, in the region of transition from a plasma dominated by molecular ions to one where atomic ions are predominant. Consequently, the measured pressure at such altitudes would have been underestimated, thus affecting the measured pressure gradient at *all* altitudes. In short, the measured pressure gradient (the dotted black line in Figure 6.5) may have been underestimated due to the adoption of the standard composition model. Furthermore, the assumption of a single ion species above 300-km altitude would not be appropriate, and the present model no longer applicable.

It is noted that other difficulties arise in the analysis of incoherent scatter during disturbed conditions. The ion temperature is derived by assuming that the ion velocity distribution function along the radar line-of-sight is Maxwellian. If the distribution is actually non-Maxwellian then the ion temperature is overestimated and the electron temperature

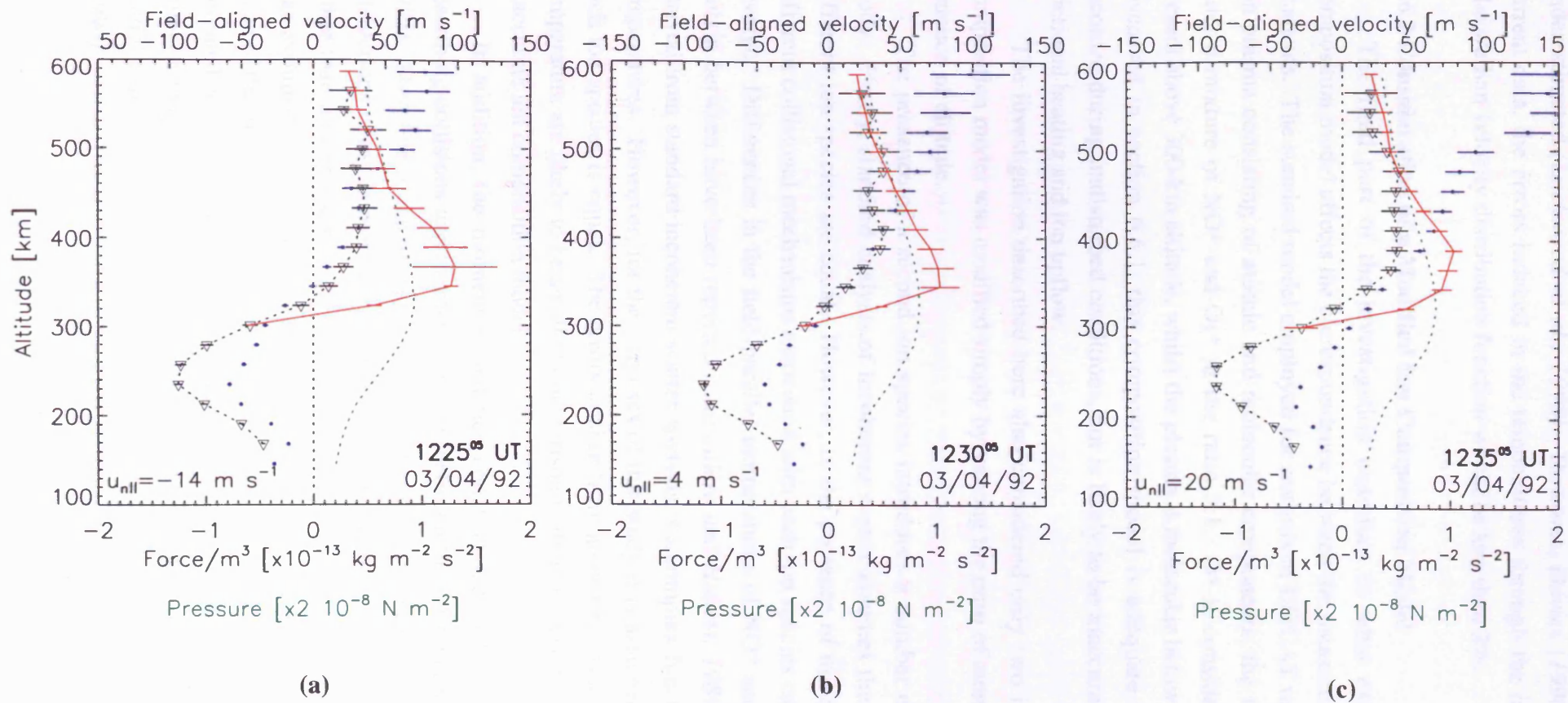


Figure 6.5 Same as Figure 6.4 but for 1225, 1230 and 1235 UT, during the upflow event. Here, measured pressure gradients (black dotted line) are significantly less than required values between 300 and 450-km altitude, indicating that the model is not applicable during this interval.

underestimated (*Lockwood et al., 1993*). However, *Davies (1996)* indicated that, for the current data, the errors induced in the temperatures through the incorrect assumption of a Maxwellian velocity distribution function would be less than 2%.

6.6.2 Consideration of a Modified Ion Composition Model

The final part of the investigation examines to what extent a modified plasma composition model affects the correspondence between the measured and theoretical pressure gradients. The standard model employed for analysis of EISCAT radar data considers a two-ion plasma consisting of atomic and molecular components, the former being O^+ and the latter a mixture of NO^+ and O_2^+ in the ratio 3:1. O^+ is considered the only ion species present above 300-km altitude, whilst the plasma is molecular below 150 km (Figure 3.9). As discussed in section 6.6.1, this composition model is adequate for the analysis of data recorded during undisturbed conditions, but is likely to be inaccurate during intervals of ion frictional heating and ion upflow.

The investigation described here also considered only two ion species. The plasma composition model was modified simply by varying the ratio of atomic to molecular ions as a function of altitude.

The presence of a second ion species introduces a number of complications into the study. Firstly, standard analysis of incoherent scatter assumes that the temperatures of the different ion species are equal. However, in the presence of ion-neutral relative flow, the different collisional mechanisms associated with each ion species cause their temperatures to diverge. Differences in the field-parallel temperatures of NO^+ and O^+ of several hundred Kelvin between have been reported (*Lathuillère and Hubert, 1989*). The ion temperature derived from standard incoherent scatter analysis is a complex function of the individual ion temperatures. However, for the purposes of this study it is assumed that the temperature of each ion species is equal. The errors arising from an erroneous assumption of a single ion temperature are likely to be small in comparison with those resulting from the adoption of an inaccurate ion composition model.

In addition, the momentum balance equation for each ion species contains terms describing collisions and thermal diffusion between the different species (eg. *Moffett et al., 1993*). Therefore, if the ion velocity were to be accurately modelled then each species, and its interactions with the other ions and neutrals, should be considered individually. However, rather than attempting to solve the momentum equation for each species, a single equation was assumed to describe the plasma, where the adopted ion mass was simply a weighted mean of the masses of the constituent ions. Similarly, the ion-neutral collision frequency was weighted according to the relative proportions of atomic and molecular ions; the O^+ -neutral collision frequency was derived from equations 6.5 and 6.6, whilst NO^+ -neutral and O_2^+ -neutral collision frequencies were obtained via expressions presented by *Bailey and Sellek (1990)*.

It is appreciated that this is an extremely simplistic approach. If the intention were to replicate the observations then this method would not be appropriate, since in reality the each ion population exhibits different temperatures and velocities, and experiences interactions with the other ion species. However, the purpose here is not to accurately reproduce the observations, but rather to investigate the effects on both the observations and the model of changes in plasma composition which are likely during the upflow event.

6.6.3 The Effect of a Modified Ion Composition Model

The composition model adopted in the analysis of incoherent scatter influences the derived ion and electron temperatures, and hence the measured plasma pressure gradient. In addition, the modelled pressure gradient is influenced by the ion mass and ion-neutral collisions, both of which are affected by the composition model. To simulate the effects of an increased concentration of molecular ions in the F-region, such as might occur through plasma upwelling and increased reaction rates, the analysis described in section 6.6 was repeated with a modified ion composition model.

Initially, a “worst case” composition model was adopted, in which the ion content was entirely molecular up to 350-km altitude and purely atomic above that height. Obviously, such a sudden transition is not realistic, but the profile was employed to assess whether or not a change in composition could have a significant enough effect to allow agreement between the observations and model. The full line in Figure 6.6(b) illustrates the modified altitude profile of ion composition in terms of molecular ion content. For comparison, the standard composition model is illustrated by the dotted line.

The EISCAT radar data were re-analysed using the modified plasma composition model. The measured and theoretical pressure gradients were then calculated as before. These parameters, together with the measured velocity and pressure profiles, are illustrated in Figure 6.6(a) for 1225 UT. At this time, the correspondence between observations and model was poorest (Figure 6.5).

Comparing the measured pressure profiles (dotted green lines) depicted in Figures 6.5 and 6.6(a), the pressure is clearly enhanced below 350-km altitude in the latter, resulting from the expected increase in the ion and electron temperatures. Beyond that altitude, the profiles are similar for each. The sudden step in the pressure profile in Figure 6.6(a) is a consequence of the transition in the composition model. This step, although unrealistic, does illustrate the influence that the composition model has on the derived plasma parameters.

The magnitude of the measured pressure gradient (dotted black lines) is dramatically increased at 350-km altitude because of the discontinuity in pressure. More interesting is the change in the theoretical pressure gradient. It is noted that, since the velocity profile is independent of the adopted composition model, the change in the theoretical pressure gradient must be a consequence of the modified collision frequency and ion mass. Hence, it has been shown that an increase in the molecular content of the plasma at F-region altitudes can

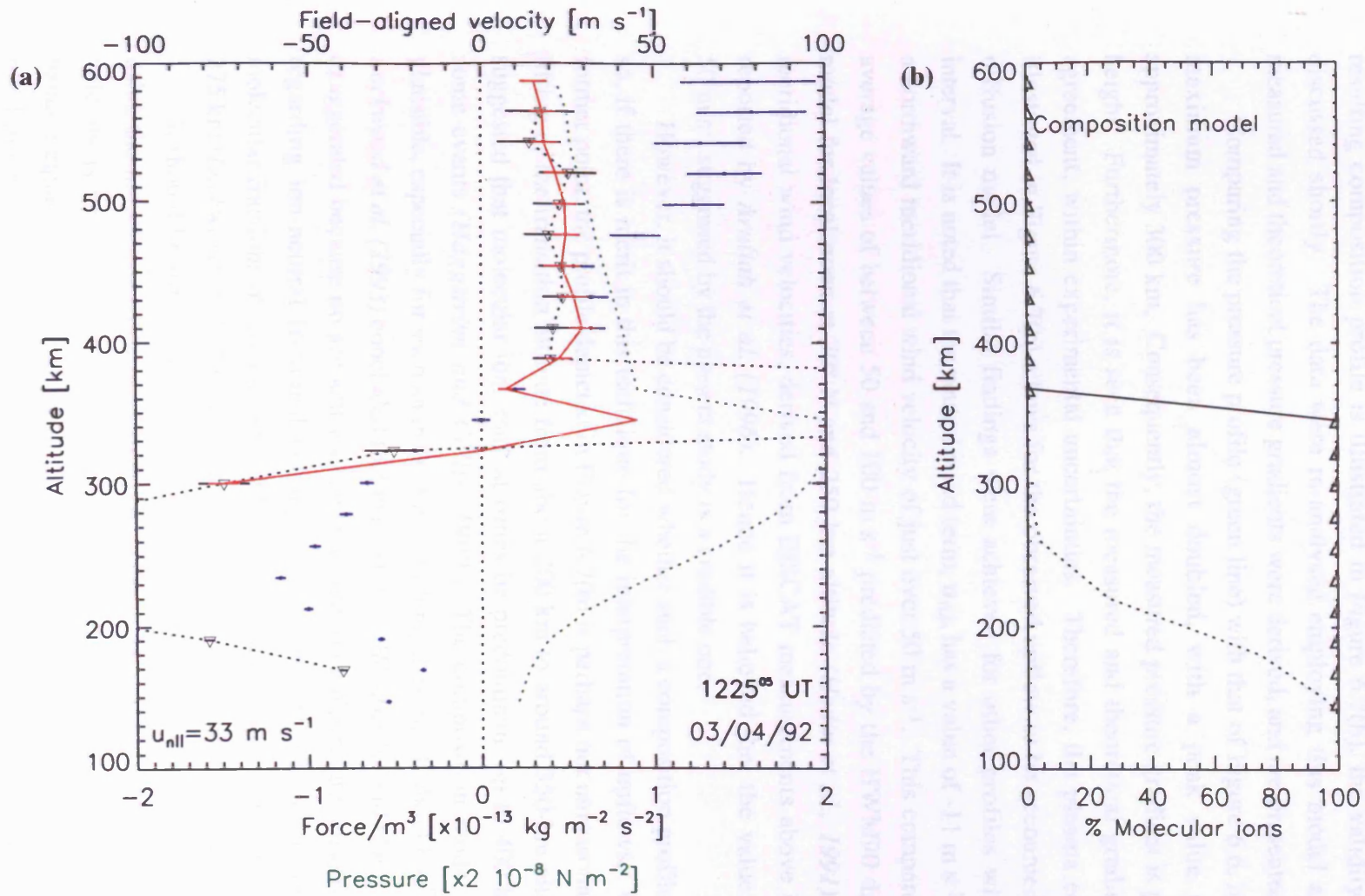


Figure 6.6 Same as panel (a) of Figure 6.5 but here the data were analysed using the ion composition model illustrated in panel (b). The step-like form of the composition profile introduces distortions into the derived pressure and pressure gradient profiles. The “required” pressure gradient (red line) is also affected by changes in the ion mass and ion-neutral collision frequency induced by the composition change.

substantially modify both the observations and the predictions of the modelled values.

Finally, an iterative method was used to derive a plasma composition model that would allow for agreement between the measured and modelled pressure gradient profiles. The resulting composition profile is illustrated in Figure 6.7(b), the validity of which will be discussed shortly. The data were re-analysed employing this model and, as before, the measured and theoretical pressure gradients were derived, and are presented in Figure 6.7(a).

Comparing the pressure profile (green line) with that of Figure 6.6, it is evident that the maximum pressure has been almost doubled, with a peak value at an altitude of approximately 300 km. Consequently, the measured pressure gradient is positive above that height. Furthermore, it is seen that the measured and theoretical gradients are largely in agreement, within experimental uncertainties. Therefore, the plasma composition model illustrated in Figure 6.7(b) allows for the observed upflow to be accounted for by the simple diffusion model. Similar findings were achieved for other profiles within the disturbed interval. It is noted that the neutral wind term, \mathbf{u}_{nl} , has a value of -11 m s^{-1} , corresponding to a northward meridional wind velocity of just over 50 m s^{-1} . This compares favourably with average values of between 50 and 100 m s^{-1} predicted by the HWM90 thermospheric wind model for local noon at 70° N and 250-km altitude (*Hedin et al., 1991*). Similar average meridional wind velocities, derived from EISCAT measurements above Kiruna, have been reported by *Aruliah et al. (1996)*. Hence it is believed that the value of approximately 50 m s^{-1} suggested by the present study is a credible one.

However, it should be considered whether such a composition profile is realistic and, if so, if there is merit in this technique for the interpretation of upflows. With regard to the former point, the profile depicted in Figure 6.7(b) is perhaps not unreasonable; it represents a lifting of the transition altitude from about 200 km to around 350-km altitude. It has been suggested that molecular ions may at times be predominant up to 400-km altitude during some events (*Hägström and Collis, 1990*). The composition model may therefore be plausible, especially for such an intense and prolonged event. It should be noted, though, that *Lockwood et al. (1993)* concluded that the results of *Hägström and Collis (1990)* were likely exaggerated because no account was taken of the ion temperature anisotropy. Other studies regarding ion-neutral frictional heating and ion temperature anisotropy have predicted molecular fractions of, for example, 50% at 265-km altitude (*McCrea et al., 1995*), 90% at 275 km (*Lockwood et al., 1993*) and 20% at 350 km (*Jenkins et al., 1996*).

It should be stressed that it is certainly not possible to replicate the observed velocities using the model described in section 6.4. The analysis has demonstrated that the modelled velocity is very sensitive to the pressure gradient in the simplified 1-D ion momentum balance equation. Experimental errors in the derived plasma parameters, in particular those resulting from the adoption of an inappropriate composition model, result in large discrepancies between the observed and modelled ion parallel velocities. However, the analysis was able to indicate that the observed upflows were consistent with diffusion driven

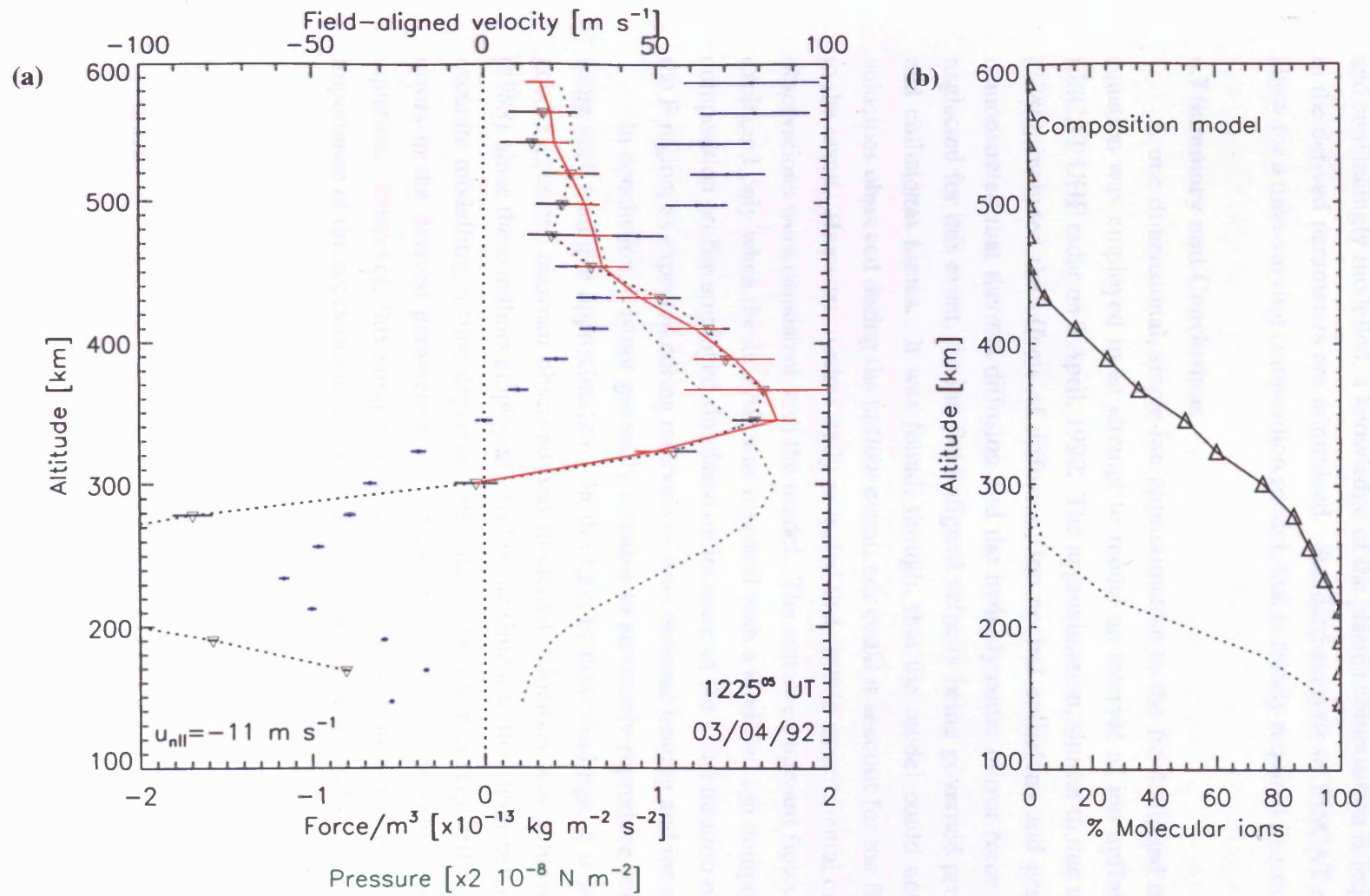


Figure 6.7 Same as Figure 6.6 but for data analysed using the plasma composition profile illustrated in panel (b).

by pressure gradients and neutral winds.

One of the purposes of the study was to investigate the applicability and limitations of such a simple model. This final study demonstrates that, if a specific event is to be accurately and convincingly modelled, a knowledge of the plasma composition is required so that errors in the derived parameters are minimised. Standard analysis of EISCAT radar data does not allow for a time-varying composition model; that is clearly required in a study such as this.

6.7 Summary and Conclusions

A one-dimensional, single-ion approximation to the field-aligned momentum balance equation was employed in an attempt to model an interval of ion upflow observed by the EISCAT UHF radar on 3 April, 1992. The approximation, similar to that used by *Jones et al. (1988)*, included the effects of diffusion, ion-neutral collisions and gravity. It has been demonstrated that thermal diffusion and the hydrodynamic mirror force can be reasonably neglected for this event, the ion field-aligned velocity being governed primarily by pressure and collisional forces. It was found, though, that the model could not replicate the ion velocities observed during the upflow event, nor could it account for the flows detected prior to the event. However, further study revealed that, within experimental error, the quiet-time observations were consistent with the model. The enhanced upward flows could be similarly explained only when the analysis was repeated with a modified ion composition model. The composition profile employed simulated an increase of the concentration of molecular ions in the F-region, as expected during intervals of ion-frictional heating and ion upflow.

In conclusion, it is not generally possible to accurately reproduce velocity observations using such a simple approximation. In the light of these findings, it is surprising that such good agreement between observed and modelled velocities was achieved by *Jones et al. (1988)*, since these authors employed a technique similar to that described in this chapter. For accurate modelling, a time-dependent plasma composition is required in order to minimise errors in the derived parameters and hence introduce correct values into the momentum equation. However, this simple approach has provided an initial estimate of the relative importance of the acceleration mechanisms responsible for the upflow.

CHAPTER 7

Summary

7.1 Introduction

Ion flow along geomagnetic field lines is an important mechanism in the coupling of the magnetosphere-ionosphere system. A wealth of radar and satellite observations has revealed that the high-latitude ionosphere is a steady and significant source of magnetospheric ions. In particular, ion upflows are a common occurrence in the auroral ionosphere. Field-aligned upflows of O^+ are often detected, and fluxes exceeding $10^{13} \text{ m}^{-2} \text{ s}^{-1}$ and velocities of up to a few km s^{-1} have been reported. A number of acceleration mechanisms, primarily associated with disturbed auroral conditions, have been proposed to account for events of transient ion upflow. The present thesis has documented a study of ion upflows observed in the high-latitude F-region and topside ionosphere. The work was based almost entirely upon incoherent scatter measurements from the EISCAT radar, as described in *Chapter 3*. A review of previous observations and analyses of ion upflows was presented in *Chapter 2*, focusing on the physical mechanisms that can generate large field-aligned ion upflows. This final chapter summarizes the studies presented in the preceding three chapters, in which the general characteristics of upflows were investigated and statistical and numerical studies documented.

7.2 Summary of Chapter 4

A case study of three events of ion upflow observed during a run of the EISCAT UK Special Programme UFIS was presented in *Chapter 4*. The UFIS programme employs the UHF and VHF radars, both of which operate at 90° elevation, thus yielding simultaneous observations along a continuous line-of-sight between approximately 150 and 1000-km altitude. In addition, observations from the remote UHF receivers allow for tristatic measurement of the ion velocity at a height of 312 km. Three events of ion upflow were observed during a six-hour run of UFIS on January 17, 1990. At 2200 UT, an upflow was detected in which the vertical ion velocity approached 300 m s^{-1} at 800-km altitude, whilst fluxes of order $10^{13} \text{ m}^{-2} \text{ s}^{-1}$ were measured at 500 km. At F-region altitudes the upflow was simultaneous with an interval of ion frictional heating, the result of an enhanced convection electric field adjacent to an auroral arc. The upflow exhibited characteristics reminiscent of both the type 1 and type 2 events described by *Wahlund et al. (1992)*, demonstrating some of the features that can exist within the structure of an auroral arc and which can induce upward plasma flow.

A later event exhibited larger vertical ion velocities and fluxes, simultaneous with a greatly enhanced electron temperature. Little ion heating was detected, consistent with the moderate observed field-perpendicular ion velocity. These features are characteristic of a type 2 ion upflow, where upward plasma acceleration is induced by thermal diffusion and

enhanced field-parallel electric fields in the presence of an elevated electron temperature.

The third event exhibited lesser vertical velocities of perhaps 200 m s^{-1} at 800-km altitude. The upflow was detected only by the VHF radar above 600 km, and was apparently uncorrelated with any features at lower altitudes. The lack of temperature measurements above 500-km altitude inhibited the interpretation of this event, although it was likely associated with topside plasma heating.

The operation of both the UHF and VHF radars in the UFIS experiment allowed for simultaneous measurements from E-region heights up to the topside ionosphere, thus allowing the nature of the upflows to be investigated within several altitude regimes. However, the study also highlighted the problems inherent in interpreting vertical observations in terms of field-aligned features, especially when studying transient events such as field-parallel upflows. It was also indicated that single pointing direction experiments such as UFIS, although achieving excellent temporal resolution, can suffer as a result of limited spatial coverage. It is suggested that, in future, collaborative experiments with the Superdarn CUTLASS radar may aid in the interpretation of single point observations.

7.3 Summary of Chapter 5

Chapter 5 presented a synoptic study of F-region upflows observed by the EISCAT radar. More than 12 years' EISCAT field-parallel observations, obtained between 1984 and 1996 from Common Programmes One and Two, were employed. In addition, 5 years' CP-7 data provided vertical observations up to 800-km altitude. Thus the study extended that of *Keating et al. (1990)* in terms of both time and altitude range covered. Significantly, the large data set enabled the relationship between upflow occurrence and solar cycle to be examined.

An upflow "event" was considered to have occurred if the measured field-aligned ion velocity exceeded 100 m s^{-1} and/or the flux was greater than $10^{13} \text{ m}^{-2} \text{ s}^{-1}$ for any given observation. These threshold values are greater than might be expected due to neutral winds and plasma pressure gradients under quiet conditions, and are identical to the selection criteria adopted by *Keating et al. (1990)*. An initial investigation of the diurnal variation of upflows between 200 and 600-km altitude revealed distributions similar to those of Keating and co-authors, with a higher occurrence frequency of upflows observed in the evening sector, maximizing at 2200 UT (local magnetic midnight). It was suggested that the diurnal variation is partially attributable to the ambient field-aligned flow being directed upward in the evening sector, a consequence of typically southward neutral wind flow on the night-side. However, when the ambient flow was accounted for, it was found that there was also a real increase in the number of upflows observed by EISCAT in the evening sector. It was also shown that the frequency of upflows increased steadily with height up to the highest measured altitude. The larger data set also revealed a more pronounced dependence of upflow occurrence on season than was reported by *Keating et al. (1990)*, with a typically higher frequency of events during the winter months. The relationship between upflow occurrence and geomagnetic activity, as

measured by the K_p index, was also examined. It was found that, in general, upflows occurred more frequently during intervals of greater geomagnetic activity. Notably, it was established that upflows were detected with greater frequency during solar maximum. Furthermore, the form of the diurnal upflow distributions varied markedly with solar cycle; during solar minimum, the night-side maxima were less pronounced and more day-side events were evident. In addition, during active solar conditions the majority of upflow events exceeded the flux threshold only, whilst at other times only the velocity threshold was exceeded. Finally, a quantitative investigation of upflows associated with enhanced ion and electron temperatures revealed that between 50% and 60% of events occurred during intervals of enhanced ion temperature, and perhaps 80% were simultaneous with an elevated ion and/or electron temperature.

The study also highlighted the limitations imposed by the selection criteria, in particular the problem of classifying transient enhancements in ion and electron temperature. The analysis would be improved by a reliable method of identifying such events. In addition, it would be instructive to examine the relationship of topside upflows with heating at lower altitudes, and perhaps extend the study to investigate the distributions of downward field-aligned flows. Further work is also required to account for the seasonal variation in upflow occurrence above 350-km altitude, which might be facilitated by examining distributions of plasma heating events as a function of season. The increased number of dayside *vertical* upflows should also be examined in more detail. Finally, it would also be informative to consider these results in conjunction with studies of satellite observations of high-altitude ion outflows with the aim of quantifying the relationship between ionospheric upflows and outflows.

7.4 Summary of Chapter 6

Chapter 6 presented a modelling study of an ion upflow event. The model employed was a simple one-dimensional approximation to the ion momentum balance equation, similar to that used by *Jones et al. (1988)* and *Wahlund et al. (1992)*. The study was carried out to investigate the relative significance of the acceleration mechanisms most commonly thought to drive F-region upflows. In addition, the analysis highlighted some of the limitations of the simple model.

The event studied was observed by the EISCAT UHF radar between 1200 and 1300 UT on April 3, 1992. This interval has been previously scrutinized by *Davies et al. (1995)* in an investigation of dayside ion frictional heating. These authors compared the observations with the results from the Sheffield ionosphere and plasmasphere model which, although successfully described the observed behaviour of the ion and electron temperature, did not reproduce the large field-aligned ion flows. Hence it was of interest to examine whether or not a simple, time-independent model could account for the observations. It was first demonstrated that the effects of thermal diffusion and the hydrodynamic mirror force could

be neglected. However, it was found that the model could not reproduce the observed field-parallel velocities either prior to or during the upflow. In order to validate the model, it was employed to derive pressure profiles consistent with the measured velocities. Agreement between the calculated and measured pressure gradients, for the undisturbed interval, demonstrated that the model was indeed valid. However, accordance between model and observations for the interval of ion upflow was only achieved when the data were re-analysed with a modified ion composition model. The revised composition profile simulated an increase in the concentration of molecular ions at F-region altitudes.

In summary, the analysis demonstrated that the field-aligned ion velocity is a sensitive function of the plasma pressure gradient. Hence, uncertainties of only a few per cent in the measured pressure gradient may cultivate errors of several hundred m s^{-1} in the derived ion velocity. It is, therefore, difficult to model accurately ion velocities using this technique. However, it was demonstrated that the model was consistent with observations of an upflow event observed on April 3, 1992 when an appropriate ion composition model was employed in the analysis. It was clear from the study that the adopted ion composition model had a significant effect on the analysis and interpretation of the data. It would be an interesting exercise to derive ion composition models for the entire interval between 0700 and 1500 UT on April 3, 1992, in order to examine how the composition varies throughout the event. Ultimately, the model should be extended to incorporate time-dependent effects.

REFERENCES

- Abe T., B. A. Whalen, A. W. Yau, R. E. Horita, S. Watanabe and E. Sagawa**, EXOS D (Akebono) suprathermal mass spectrometer observations of the polar wind, *J. Geophys. Res.*, **98**, 11191, 1993.
- Aikio A. T., H. J. Opgenoorth, M. A. L. Persson and K. U. Kaila**, Ground-based measurements of an arc-associated electric field, *J. Atmos. Terr. Phys.*, **55**, 797, 1993.
- Arnoldy R. L., K. A. Lynch, P. M. Kintner, J. Vago, S. Chesney, T. E. Moore and C. J. Pollock**, Bursts of transverse ion acceleration at rocket altitudes, *Geophys. Res. Lett.*, **19**, 413, 1992.
- Aruliah A. L., A. D. Farmer, D. Rees and U. Brändström**, The seasonal behaviour of high-latitude thermospheric winds and ion velocities observed over one solar cycle, *J. Geophys. Res.*, **101**, 15701, 1996.
- Axford W. I.**, The polar wind and the terrestrial helium budget, *J. Geophys. Res.*, **73**, 6855, 1968.
- Axford W. I. and C. O. Hines**, A unifying theory of high-latitude geophysical phenomena and geomagnetic storms, *Can. J. Phys.*, **39**, 1433, 1961.
- Bailey G. J. and R. Selleck**, A mathematical model of the Earth's plasmasphere and its application in a study of He⁺ and L=3, *Ann. Geophys.*, **8**, 171, 1990.
- Banks P. M. and T. E. Holzer**, The polar wind, *J. Geophys. Res.*, **73**, 6846, 1968.
- Banks P. M. and T. E. Holzer**, Features of plasma transport in the upper atmosphere, *J. Geophys. Res.*, **74**, 6304, 1969a.
- Banks P. M. and T. E. Holzer**, High-latitude plasma transport: The polar wind, *J. Geophys. Res.*, **74**, 6317, 1969b.
- Barker R. H.**, *Communication Theory*, (p. 273), Academic Press, London, 1958
- Baron M. J. and R. H. Wand**, F-region ion temperature enhancements resulting from Joule heating, *J. Geophys. Res.*, **88**, 4114, 1983.
- Bartels J.**, The standardised index, K_s, and the planetary index, K_p, *Int. Union Geod. Geophys., IATME Bull.*, **97**, 1949.
- Bates H. F.**, Atmospheric expansion through Joule heating by horizontal electric fields, *Planet. Space Sci.*, **21**, 2073, 1973.
- Bates H. F.**, Atmospheric expansion from Joule heating, *Planet. Space Sci.*, **22**, 925, 1974.
- Beynon W. J. G. and P. J. S. Williams**, Incoherent scatter of radio waves from the ionosphere, *Rep. Prog. Phys.*, **41**, 909, 1978.
- Blelly P.-L. and D. Alcaydé**, Electron heat flow in the auroral ionosphere inferred from EISCAT-VHF observations, *J. Geophys. Res.*, **99**, 13181, 1994.
- Blelly P.-L., A. Robineau and D. Alcaydé**, Numerical modelling of intermittent ion outflow events above EISCAT, *J. Atmos. Terr. Phys.*, **58**, 273, 1996.

- Block L. P. and C.-G. Fälthammar**, Effects of field-aligned currents on the structure of the ionosphere, *J. Geophys. Res.*, **73**, 4807, 1968.
- Bowles K. L.**, Observation of vertical incidence scattering from the ionosphere at 41 Mc/sec, *Phys. Res. Lett.*, **1**, 454, 1958.
- Buneman O.**, Excitation of field-aligned sound waves by electron streams, *Phys. Rev. Lett.*, **10**, 285, 1963.
- Burnside R. G., C. A. Tepley and V. B. Wickwar**, the O⁺-O collision cross-section - can it be inferred from aeronomical measurements?, *Ann. Geophys.*, **5A**, 343, 1987.
- Calvert W.**, The auroral plasma cavity, *Geophys. Res. Lett.*, **8**, 919, 1981.
- Caton R., J. L. Horwitz, P. G. Richards and C. Liu**, Modelling of F-region ionospheric upflows observed by EISCAT, *Geophys. Res. Lett.*, **23**, 1537, 1996.
- Chandler M. O.**, Observations of downward moving O⁺ in the polar topside ionosphere, *J. Geophys. Res.*, **100**, 5795, 1995.
- Chandler M. O., J. H. Waite Jr. and T. E. Moore**, Observations of polar ion outflows, *J. Geophys. Res.*, **96**, 1421, 1991.
- Chang T. and B. Coppi**, Lower hybrid acceleration and ion evolution in the supraauroral region, *Geophys. Res. Lett.*, **8**, 1253, 1981.
- Chappell C. R.**, The terrestrial plasma source: A new perspective in solar-terrestrial processes from Dynamics Explorer, *Rev. Geophys.*, **26**, 229, 1988.
- Chappell C. R., T. E. Moore and J. H. Waite Jr.**, The ionosphere as a fully adequate source of plasma for the Earth's magnetosphere, *J. Geophys. Res.*, **92**, 5896, 1987.
- Chappell C. R., R. C. Olsen, J. L. Green, J. F. E. Johnson and J. H. Waite Jr.**, The discovery of nitrogen ions in the Earth's magnetosphere, *Geophys. Res. Lett.*, **9**, 937, 1982.
- Cole K. D.**, Joule heating of the upper atmosphere, *Aust. J. Phys.*, **15**, 223, 1962.
- Cole K. D.**, Atmospheric excitation and ionization by ions in strong auroral and man-made electric fields, *J. Atmos. Terr. Phys.*, **33**, 1241, 1971.
- Conrad J. R. and R. W. Schunk**, Diffusion and heat flow equations with allowance for large temperature differences between interacting species, *J. Geophys. Res.*, **84**, 811, 1979.
- Cowley S. W. H.**, Plasma populations in a simple open magnetosphere, *Space Sci. Rev.*, **26**, 217, 1980.
- Craven P. D., R. C. Olsen, C. R. Chappell and L. Kakani**, Observations of molecular ions in the Earth's magnetosphere, *J. Geophys. Res.*, **90**, 7599, 1985.
- Crew G. B., T. Chang, J. M. Retterer, W. K. Peterson, D. A. Gurnett and R. L. Huff**, Ion cyclotron resonance heated conics: Theory and observations, *J. Geophys. Res.*, **95**, 3959, 1990.
- Crowley G., N. M. Wade, J. A. Waldock, T. R. Robinson and T. B. Jones**, High time-resolution observations of periodic frictional heating associated with a Pc5 micropulsation, *Nature*, **316**, 528, 1985.

- Davies J. A.**, Ion frictional heating in the high-latitude ionosphere, PhD Thesis, University of Leicester, UK, 1996.
- Davies J. A., M. Lester, B. Jenkins and R. J. Moffet**, Dayside ion frictional heating: EISCAT observations and comparison with model results, *J. Atmos. Terr. Phys.*, **57**, 775, 1995.
- Davies J. A., M. Lester and I. W. McCrea**, A statistical study of ion frictional heating observed by EISCAT, *Ann. Geophys.*, In Press, 1997.
- Davies K.**, Ionospheric Radio, Peter Peregrinus Ltd., London, 1990.
- De La Beaujardière O., R. Vondrak and M. Baron**, Radar observations of electric fields and currents associated with auroral arcs, *J. Geophys. Res.*, **82**, 5051, 1977.
- Delcourt D. C., B. L. Giles, C. R. Chappell and T. E. Moore**, Low-energy bouncing ions in the magnetosphere: A three-dimensional numerical study of Dynamics Explorer 1 data, *J. Geophys. Res.*, **93**, 1859, 1988.
- Dougherty J. P. and D. T. Farley**, A theory of incoherent scattering of radio waves by a plasma, *Proc. R. Soc.*, **A259**, 79, 1960.
- Du Castel F. and G. Vasseur**, Evaluation des performances d'un sondeur ionosphérique a diffusion incohérent, *Ann. Telecommun.*, **27**, 239, 1972.
- Dungey J. W.**, Interplanetary magnetic field and the auroral zones, *Phys. Rev. Lett.*, **6**, 47, 1961.
- Eastman T. E., B. Popielawska and L. A. Frank**, Three-dimensional plasma populations near the magnetosphere boundary, *J. Geophys. Res.*, **90**, 9519, 1985.
- Evans J. V.**, Theory and practice of ionosphere study by Thomson scatter radar, *Proc. IEEE*, **57**, 496, 1969.
- Fabry C.**, C. r. hebd. Séance Acad. Sci., Paris, **187**, 777, 1928.
- Farley D. T.**, A plasma instability resulting in field-aligned irregularities, *J. Geophys. Res.*, **68**, 6083, 1963.
- Farley D. T.**, Multiple pulse incoherent scatter correlation function measurements, *Radio Sci.*, **7**, 661, 1972.
- Farmer A. D., T. J. Fuller-Rowell and S. Quegan**, Comparing numerical simulations of the high-latitude ionosphere to an empirical mean model based on EISCAT data, *Adv. Space Res.*, **10**, 143, 1990.
- Fejer J. A.**, Scattering of radio waves by an ionised gas in thermal equilibrium in the presence of a uniform magnetic field, *Can. J. Phys.*, **38**, 1114, 1960
- Feldstein Y. I. and Y. I. Galperin**, The auroral luminosity structure in the high-latitude upper atmosphere: Its dynamics and relationship to large-scale structure of the Earth's magnetosphere, *Rev. Geophys.*, **23**, 217, 1985.
- Folkestad K., T. Hagfors and S. Westerlund**, EISCAT: An updated description of technical characteristics and operational capabilities, *Radio Sci.*, **6**, 867, 1983.

- Forme F. R. E., J.-E. Wahlund, H. J. Opgenoorth, M. A. L. Persson and E. V. Mishin,** Effects of current driven instabilities on the ion and electron temperatures in the topside ionosphere, *J. Atmos. Terr. Phys.*, **55**, 647, 1993.
- Foster J. C., C. Del Pozo and K. Groves,** Radar observations of the onset of current-driven instabilities in the topside ionosphere, *Geophys. Res. Lett.*, **15**, 160, 1988.
- Fuller-Rowell T. J.,** A two-dimensional, high-resolution, nested-grid model of the thermosphere 1: Neutral response to an electric field spike, *J. Geophys. Res.*, **89**, 2971, 1984.
- Fuller-Rowell T. J.,** A two-dimensional, high-resolution, nested-grid model of the thermosphere 2: Response of the thermosphere to narrow and broad electrodynamic features, *J. Geophys. Res.*, **90**, 6567, 1985.
- Ganguli G., M. J. Keskinen, H. Romero, R. Heelis, T. Moore and C. Pollock,** Coupling of microprocesses and macroprocesses due to velocity shear: An application to the low-altitude ionosphere, *J. Geophys. Res.*, **99**, 8873, 1994.
- Ganguli S. B.,** The polar wind, *Revs. Geophys.*, **34**, 311, 1996.
- Ghielmetti A. G., R. G. Johnson, R. D. Sharp and E. G. Bailey,** The latitudinal, diurnal and altitudinal distributions of upward flowing energetic ions of ionospheric origin, *Geophys. Res. Lett.*, **5**, 59, 1978.
- Giles B. L., C. R. Chappell, T. E. Moore, R. H. Comfort and J. H. Waite Jr.,** Statistical survey of pitch angle distributions in core (0-50 eV) ions from Dynamics Explorer 1: Outflow in the auroral zone, polar cap and cusp, *J. Geophys. Res.*, **99**, 17483, 1994.
- Gombosi T. I, T. E. Cravens and A. F. Nagy,** A time-dependent theoretical model of the polar wind: Preliminary results, *Geophys. Res. Lett.*, **12**, 167, 1985.
- Gombosi T. I. and T. L. Killeen,** Effects of thermospheric motions on the polar wind: A time-dependent numerical study, *J. Geophys. Res.*, **92**, 4725, 1987.
- Gombosi T. I. and A. F. Nagy,** Time-dependent modelling of field-aligned current-generated ion transients in the polar wind, *J. Geophys. Res.*, **94**, 359, 1989.
- Gordon W. E.,** Incoherent scattering of radio waves by free electrons with applications to space exploration by radar, *Proc. IRE*, **46**, 1824, 1958.
- Gorney D., J. A. Clarke, D. Croley, J. F. Fennell, J. Luhmann and P. Mizera,** The distribution of ion beams and conics below 8000 km, *J. Geophys. Res.*, **86**, 83, 1981.
- Greenwald R. A., K. B. Baker, J. R. Dudeney, M. Pinnock, T. B. Jones, E. C. Thomas, J.-P. Villain, J.-C. Cerisier, C. Senior, C. Hanuise, R. D. Hunsucker, G. Sofko, J. Koehler, E. Nielsen, R. Pellinen, A. D. M. Walker, N. Sato and H. Yamagishi,** DARN/SUPERDARN: A Global View of the Dynamics of High-Latitude Convection, *Space Sci. Rev.*, **71**, 761, 1995.
- Hagfors T.,** Density fluctuations in a plasma in a magnetic field with applications to the ionosphere, *J. Geophys. Res.*, **66**, 1699, 1961.

- Hagfors T., P. S. Kildal, H. J. Karcher, B. Leisenkotter and G. Schroer**, VHF parabolic cylinder antenna for incoherent scatter radar research, *Radio Sci.*, **17**, 1607, 1982.
- Häggström I. and P. N. Collis**, Ion composition changes during F-region density depletions in the presence of electric fields at auroral latitudes, *J. Atmos. Terr. Phys.*, **52**, 519, 1990.
- Hays P. B., R. A. Jones and M. H. Rees**, Auroral heating and the composition of the neutral atmosphere, *Planet. Space Sci.*, **21**, 559, 1973.
- Hedin A. E.**, MSIS-86 thermospheric model, *J. Geophys. Res.*, **92**, 4649, 1987.
- Hedin A. E., M. A. Biondi, R. G. Burnside, G. Hernandez, R. M. Johnson, T. L. Killeen, C. Mazaudier, J. W. Meriwether, J. E. Salah, R. J. Sica, R. W. Smith, N. W. Spencer, V. B. Wickwar and T. S. Viridi**, Revised global model of thermosphere winds using satellite and ground-based observations, *J. Geophys. Res.*, **96**, 7657, 1991.
- Heelis R. A., G. J. Bailey, R. Sellek, R. J. Moffett and B. Jenkins**, Field-aligned drifts in subauroral ion drift events, *J. Geophys. Res.*, **98**, 21493, 1993.
- Heelis R. A., J. D. Winningham, M. Sugiura and N. C. Maynard**, Particle acceleration parallel and perpendicular to the magnetic field observed by DE-2, *J. Geophys. Res.*, **89**, 3893, 1984.
- Ho C. W., J. L. Horwitz and G. R. Wilson**, Effects of a sudden impulse in electron temperature on the polar wind: A time-dependent, semi-kinetic model, *Modelling Magnetospheric Plasma Processes Geophys. Monog. Ser.*, **62**, 105, 1991.
- Hoffman J. H.**, Studies of the composition of the ionosphere with a magnetic deflection mass spectrometer, *Int. J. Mass Spectrom. Ion. Phys.*, **4**, 315, 1970.
- Horwitz J. L.**, The ionosphere as a source for magnetospheric ions, *Rev. Geophys. Space Phys.*, **20**, 929, 1982.
- Horwitz J. L.**, Features of ion trajectories in the polar magnetosphere, *Geophys. Res. Lett.*, **11**, 1111, 1984.
- Horwitz J. L. and M. Lockwood**, The cleft ion fountain: A two-dimensional kinetic model, *J. Geophys. Res.*, **90**, 9749, 1985.
- Hubert D. and E. Kinzelin**, Atomic and molecular ion temperatures and ion temperature anisotropy in the auroral F-region in the presence of large electric fields, *J. Geophys. Res.*, **97**, 4053, 1992.
- Hubert D. and C. Lathuillère**, Incoherent scattering of radar waves in the auroral ionosphere in the presence of high electric fields and measurement problems with the EISCAT facility, *J. Geophys. Res.*, **94**, 3635, 1989.
- Hultqvist B.**, Review paper: Extraction of ionospheric plasma by magnetospheric processes, *J. Atmos. Terr. Phys.*, **53**, 3, 1991.
- Hultqvist B., R. Lundin, K. Stasiewicz, L. Block, P.-A. Lindqvist, G. Gustafsson, H. Koskinen, A. Bahnsen, T. A. Potemra and L. J. Zanetti**, Simultaneous observation of upward moving field-aligned energetic electrons and ions on auroral zone field lines, *J. Geophys. Res.*, **93**, 9765, 1988.

- Jenkins B., R. J. Moffett, J. A. Davies and M. Lester**, A nightside ion-neutral frictional heating event: ion composition and O⁺ and NO⁺ temperature anisotropy, *Adv. Space Res.*, **18**, 57, 1996.
- Johnson R. G., R. D. Sharp and E. G. Shelley**, The discovery of energetic He⁺ ions in the magnetosphere, *J. Geophys. Res.*, **79**, 3135, 1974.
- Jones G. O. L., P. J. S. Williams and K. J. Winser**, Large ionospheric plasma flows along magnetic field lines: EISCAT observations and their interpretation, *Adv. Space Res.*, **12**, 157, 1992.
- Jones G. O. L., P. J. S. Williams, K. J. Winser, M. Lockwood and K. Suvanto**, Large plasma velocities along the magnetic field line in the auroral zone, *Nature*, **336**, 231, 1988.
- Jones G. O. L., K. J. Winser and P. J. S. Williams**, Measurements of plasma velocity at different heights along a magnetic field line, *J. Atmos. Terr. Phys.*, **48**, 887, 1986.
- Keating J. G., F. J. Mulligan, D. B. Doyle, K. J. Winser, M. Lockwood**, A statistical study of large field-aligned flows of thermal ions at high latitudes, *Planet. Space Sci.*, **9**, 1187, 1990.
- Kindel J. M. and C. R. Kennel**, Topside current instabilities, *J. Geophys. Res.*, **76**, 3055, 1971.
- Kintner P. M., J. LaBelle, W. Scales, A. W. Yau, B. A. Whalen and C. Pollock**, Observations of plasma waves with regions of perpendicular acceleration, *Geophys. Res. Lett.*, **13**, 1113, 1986.
- Kivelson M. G.**, "Physics of Space Plasmas" in *Introduction to Space Physics*, Cambridge University Press, 1995, ISBN 0-521-45714-9.
- Klumpar D. M.**, Transversely accelerated ions: An ionospheric source of hot magnetospheric ions, *J. Geophys. Res.*, **84**, 4229, 1979.
- Körösmezey A., C. E. Rasmussen, T. I. Gombosi and G. V. Khazanov**, Anisotropic ion heating and parallel O⁺ acceleration in regions of rapid ExB convection, *Geophys. Res. Lett.*, **19**, 2289, 1992.
- La Hoz C.**, EISCAT meetings 82/7, 1982.
- Lathuillère C.**, Ion composition response to auroral energy inputs in the lower F-region, *Ann. Geophys.*, **5**, 450, 1987.
- Lathuillère C. and D. Hubert**, Ion composition and ion temperature anisotropy in periods of high electric fields from incoherent scatter observations, *Ann. Geophys.*, **7**, 285, 1989.
- Lathuillère C., G. Legeune and W. Kofman**, Direct measurements of ion composition with EISCAT in the high-latitude F1-region, *Radio Sci.*, **18**, 887, 1983.
- Lee N. C. and G. K. Parks**, Ponderomotive acceleration of ions by circularly polarized electromagnetic waves, *Geophys. Res. Lett.*, **23**, 327, 1996.
- Lehtinen M. S. and I. Häggstrom**, A new modulation principle for incoherent scatter measurements, *Radio Sci.*, **22**, 625, 1987.

- Lewis R. V., P. J. S. Williams, G. O. L. Jones, H. J. Opgenoorth and M. A. L. Persson**, The Electrodynamics of a Drifting Auroral Arc, *Ann. Geophys.*, **12**, 478, 1994.
- Li X. and M. Temerin**, Ponderomotive effects on ion acceleration in the auroral zone, *Geophys. Res. Lett.*, **20**, 13, 1993.
- Liu C., J. L. Horwitz and P. J. Richards**, Effects of frictional ion heating and soft-electron precipitation on high-latitude F-region upflows, *Geophys. Res. Lett.*, **22**, 2713, 1995.
- Lockwood M.**, Thermal ion flows in the topside auroral ionosphere and the effects of low-altitude, transverse acceleration, *Planet. Space Sci.*, **30**, 595, 1982.
- Lockwood M., B. J. I. Bromage, R. B. Horne, J. P. St.-Maurice, D. M. Willis and S. W. H. Cowley**, Non-Maxwellian ion velocity distributions observed using EISCAT, *Geophys. Res. Lett.*, **14**, 111, 1987.
- Lockwood M., M. O. Chandler, J. L. Horwitz, J. H. Waite Jr., T. E. Moore and C. R. Chappell**, The cleft ion fountain, *J. Geophys. Res.*, **90**, 9736, 1985a.
- Lockwood M., I. W. McCrea, G. H. Millward, R. J. Moffet and H. Rishbeth**, EISCAT observations of ion composition and temperature anisotropy in the high-latitude F-region, *J. Atmos. Terr. Phys.*, **55**, 895, 1993.
- Lockwood M., T. E. Moore, J. H. Waite Jr., C. R. Chappell, J. L. Horwitz and R. A. Heelis**, The geomagnetic mass spectrometer - mass and energy dispersions of ionospheric ion flows into the magnetosphere, *Nature*, **316**, 612, 1985b.
- Lockwood M., K. Suvanto, J. P. St.-Maurice, K. Kikuchi, B. J. I. Bromage, D. M. Willis, S. R. Crothers, H. Todd and S. W. H. Cowley**, Scattered power from non-thermal F-region plasma observed by EISCAT: Evidence for coherent echoes ?, *J. Atmos. Terr. Phys.*, **50**, 467, 1988.
- Lockwood M., J. H. Waite Jr., T. E. Moore, J. F. E. Johnson and C. R. Chappell**, A new source of suprathermal O^+ ions near the dayside polar cap boundary, *J. Geophys. Res.*, **90**, 4099, 1985c.
- Loranc M., W. B. Hanson, R. A. Heelis and J.-P. St.-Maurice**, A morphological study of vertical ionospheric flows in the high-latitude F-region, *J. Geophys. Res.*, **96**, 3627, 1991.
- Loranc M. and J.-P. St.-Maurice**, A time dependent gyrokinetic model of thermal ion upflows in the high-latitude F-region, *J. Geophys. Res.*, **99**, 17429, 1994.
- Lu G., P. H. Reiff, T. E. Moore and R. A. Heelis**, Upflowing ionospheric ions in the auroral region, *J. Geophys. Res.*, **97**, 16855, 1992.
- Maehlum B. N., T. L. Hansen, A. Brekke, K. Folkestad and O. Holt**, Preliminary results from a study of the F-region heating during an intense aurora observed by EISCAT, *J. Atmos. Terr. Phys.*, **46**, 619, 1984.
- Marklund G.**, Auroral arc classification scheme based on the observed arc-associated electric field pattern, *Planet. Space Sci.*, **32**, 193, 1984.
- McCrea I. W.**, Radar observations of energy deposition and dissipation in the high-latitude ionosphere, PhD Thesis, University of Leicester, UK, 1989.

- McCrea I. W., G. O. L. Jones and M. Lester**, The BEAN experiment - an EISCAT study of ion temperature anisotropies, *Ann. Geophys.*, **13**, 177, 1995.
- McCrea I. W., M. Lester, T. R. Robinson, N. M. Wade and T. B. Jones**, On the identification and occurrence of ion frictional heating events in the high-latitude ionosphere, *J. Atmos. Terr. Phys.*, **53**, 587, 1991.
- Moffett R. J., B. Jenkins and G. J. Bailey**, A modelling study of anisotropic ion temperatures generated in the F-layer by subauroral ion drifts, *Ann. Geophys.*, **11**, 1051, 1993.
- Moorcroft D. R.**, On the determination of temperature and ionic composition by electron backscattering from the ionosphere and magnetosphere, *J. Geophys. Res.*, **69**, 955, 1964.
- Moorcroft D. R. and K. Schlegel**, Evidence for non-Maxwellian ion velocity distributions in the F-region, *J. Atmos. Terr. Phys.*, **50**, 455, 1989.
- Moore T. E., M. O. Chandler, C. J. Pollock, D. L. Reasoner, R. L. Arnoldy, B. Austin, P. M. Kintner and J. Bonnell**, Plasma heating and flow in an auroral arc, *J. Geophys. Res.*, **101**, 5279, 1996.
- Mozer F. S., C. W. Carlson, M. K. Hudson, R. B. Torbert, B. Parady and J. Yatteau**, Observations of paired electrostatic shocks in the polar magnetosphere, *Phys. Rev. Lett.*, **38**, 292, 1977.
- Murdin J.**, Errors in incoherent scatter radar measurements, EISCAT technical note 79/16, 1979.
- Nagai T., J. H. Waite Jr., J. L. Green, C. R. Chappell, R. C. Olsen and R. H. Comfort**, First measurements of supersonic polar wind in the polar magnetosphere, *Geophys. Res. Lett.*, **11**, 669, 1984.
- Newman A. L.**, Thermal energization of ions during impulsive field events, *Geophys. Res. Lett.*, **17**, 1061, 1990.
- Norqvist P., M. André, L. Eliasson, A. I. Eriksson, L. Blomberg, H. Lühr and J. H. Clemmons**, Ion cyclotron heating in the dayside magnetosphere, *J. Geophys. Res.*, **101**, 13179, 1996.
- Opgenoorth H. J., I. Häggström, P. J. S. Williams and G. O. L. Jones**, Regions of strongly enhanced perpendicular electric fields adjacent to auroral arcs, *J. Atmos. Terr. Phys.*, **52**, 449, 1990.
- Papadopoulos K.**, A review of anomalous resistivity for the ionosphere, *Rev. Geophys. Space Phys.*, **15**, 113, 1977.
- Persoon A. M., D. A. Gurnett, W. K. Peterson, J. H. Waite, J. L. Burch and J. L. Green**, Electron density depletions in the nightside auroral zone, *J. Geophys. Res.*, **93**, 1871, 1988.
- Pollock C. J., M. O. Chandler, T. E. Moore, J. H. Waite Jr., C. R. Chappell and D. A. Gurnett**, A survey of upwelling ion event characteristics, *J. Geophys. Res.*, **95**, 18969, 1990.

- Raitt W. J., U. von Zahn and P. Christopherson**, A comparison of thermospheric neutral gas heating and related energetic plasma phenomena at high latitudes during geomagnetic disturbances, *J. Geophys. Res.*, **80**, 2277, 1975.
- Raman R. S. V., J. P. St.-Maurice and R. S. B. Ong**, Incoherent scattering of radar waves in the auroral ionosphere, *J. Geophys. Res.*, **86**, 4751, 1981.
- Rees D., A. H. Greenaway, R. Gordon, I. McWhirter, P. J. Charleton and Å. Steen**, The Doppler imaging system - initial observations of the auroral thermosphere, *Planet. Space Sci.*, **32**, 273, 1984(a).
- Rees D., R. W. Smith, P. J. Charleton, F. G. McCormac, N. Lloyd and Å. Steen**, The generation of vertical thermospheric winds and gravity-waves at auroral latitudes. 1. Observations of vertical winds, *Planet. Space Sci.*, **32**, 667, 1984(b).
- Rees D., M. F. Smith and R. Gordon**, The generation of vertical thermospheric winds and gravity-waves at auroral latitudes. 2. Theory and numerical modelling of vertical winds, *Planet. Space Sci.*, **32**, 685, 1984(c).
- Rees M. H. and J. C. G. Walker**, Ion and electron heating by auroral electric fields, *Ann. Geophys.*, **24**, 293, 1968.
- Retterer J. M., T. Chang and J. R. Jaspere**, Transversely accelerated ions in the topside ionosphere, *J. Geophys. Res.*, **99**, 13189, 1994.
- Richmond A. D.**, "Thermospheric Dynamics and Electrodynamics" in *Solar Terrestrial Physics - Principles and Theoretical Foundations*, D. Reidel Publishing Company, Dordrecht, Holland, 1983, ISBN 90-277-1632-3.
- Rietveld M. T., P. N. Collis and J.-P. St.-Maurice**, Naturally enhanced ion-acoustic waves in the auroral ionosphere observed with the EISCAT 933 MHz radar, *J. Geophys. Res.*, **96**, 19291, 1991.
- Rishbeth H.**, Thermospheric winds and the F-region: a review, *J. Atmos. Terr. Phys.*, **34**, 1, 1972.
- Rishbeth H. and A. P. Van Eyken**, EISCAT: early history and the first ten years of operation, *J. Atmos. Terr. Phys.*, **55**, 525, 1993
- Rishbeth H. and P. J. S. Williams**, The EISCAT ionospheric radar: the system and its early results, *Q. J. Astr. Soc.*, **26**, 478, 1985.
- Robineau A., P.-L. Blelly and J. Fontanari**, Time dependent models of the auroral ionosphere above EISCAT, *J. Atmos. Terr. Phys.*, **58**, 257, 1996.
- Robinson T. R.**, The effects of the resonance broadening of Farley-Buneman waves on electrodynamic and heating in the auroral E-region, *J. Atmos. Terr. Phys.*, **54**, 749, 1992.
- Rodger A. S., R. J. Moffet and S. Quegan**, Review paper: The role of ion drift in the formation of ionization troughs in the mid- and high-latitude ionosphere - a review, *J. Atmos. Terr. Phys.*, **54**, 1, 1992.

- Sagawa E., I. Iwamoto, S. Watanabe, B. A. Whalen, A. W. Yau and H. Fukunishi, Low energy upflowing ion events observed by EXOS-D: Initial results, *Geophys. Res. Lett.*, **18**, 337, 1991.
- St.-Maurice J.-P. and W. B. Hanson, Ion frictional heating at high latitudes and its possible use for *in situ* determination of neutral thermospheric winds, *J. Geophys. Res.*, **87**, 7580, 1982.
- St.-Maurice J.-P. and R. W. Schunk, Auroral ion velocity distributions using a relaxation model, *Planet. Space. Sci.*, **22**, 1115, 1973.
- St.-Maurice J.-P. and R. W. Schunk, Behaviour of ion velocity distributions for a simple collisional model, *Planet. Space. Sci.*, **22**, 1, 1974.
- St.-Maurice J.-P. and R. W. Schunk, Ion velocity distributions in the high-latitude ionosphere, *Rev. Geophys. Space Phys.*, **17**, 243, 1979.
- St.-Maurice J.-P. and D. G. Torr, Nonthermal rate coefficients in the ionosphere: The reactions of O⁺ with N₂, O₂ and NO, *J. Geophys. Res.*, **83**, 969, 1978.
- Schlegel K. and J.-P. St.-Maurice, Anomalous heating of the polar ionosphere by unstable plasma waves: 1. Observations, *J. Geophys. Res.*, **86**, 1447, 1981.
- Schunk R. W. and A. F. Nagy, Electron temperatures in the F-region of the ionosphere: theory and observations, *Rev. Geophys. Space Phys.*, **16**, 355, 1978.
- Schunk R. W. and J. C. G. Walker, Ion velocity distributions in the auroral ionosphere, *Planet. Space. Sci.*, **20**, 2175, 1972.
- Schunk R. W. and J. J. Sojka, Ion temperature variation in the daytime high-latitude F-region, *J. Geophys. Res.*, **87**, 5169, 1982.
- Schunk R. W. and J. J. Sojka, A three-dimensional, time-dependent model of the polar wind, *J. Geophys. Res.*, **94**, 8973, 1989.
- Sellek R., G. J. Bailey, R. J. Moffett, R. A. Heelis and P. C. Anderson, Effects of large zonal plasma drifts on the subauroral ionosphere, *J. Atmos. Terr. Phys.*, **53**, 557, 1991.
- Shannon C. E., A mathematical theory of communication, *Bell Systems Technical Journal*, p.379, 1948.
- Sharp R. D., R. G. Johnson and E. G. Shelley, Energetic O⁺ ions in the magnetosphere, *J. Geophys. Res.*, **79**, 1844, 1974.
- Sharp R. D., R. G. Johnson and E. G. Shelley, Observations of an ionospheric acceleration mechanism producing energetic (keV) ions primarily normal to the geomagnetic field direction, *J. Geophys. Res.*, **82**, 3324, 1977.
- Shelley E. G., R. G. Johnson and R. D. Sharp, Satellite observations of energetic heavy ions during a geomagnetic storm, *J. Geophys. Res.*, **77**, 6104, 1972.
- Shelley E. G., W. K. Peterson, A. G. Ghielmetti and J. Geiss, The polar ionosphere as a source of energetic magnetospheric plasma, *Geophys. Res. Lett.*, **9**, 941, 1982.
- Shelley E. G., R. D. Sharp and R. G. Johnson, Satellite observations of an ionospheric acceleration process, *Geophys. Res. Lett.*, **3**, 654, 1976.

- Singh N., K. S. Hwang, D. G. Torr and P. Richards**, Temporal features of the outflow of heavy ionospheric ions in response to a high altitude plasma cavity, *Geophys. Res. Lett.*, **16**, 29, 1989.
- Suvanto K., M. Lockwood and T. J. Fuller-Rowell**, The influence of anisotropic F-region ion velocity distributions on ionospheric ion outflows into the magnetosphere, *J. Geophys. Res.*, **94**, 1347, 1989.
- Swift D. W.**, A mechanism for energizing electrons in the magnetosphere, *J. Geophys. Res.*, **70**, 3061, 1965.
- Torr M. R., D. G. Torr, P. G. Richards and S. P. Yung**, Mid- and low-latitude model of thermospheric emissions, 1, $O^+(^2P)$ 7300 Å and $N_2(^2P)$ 3371 Å, *J. Geophys. Res.*, **95**, 21147, 1990.
- Tsunoda R. T., R. C. Livingston, J. F. Vickrey, R. A. Heelis, W. B. Hanson, F. J. Rich and P. F. Bythrow**, Dayside observations of thermal-ion upwellings at 800-km altitude: An ionospheric signature of the cleft ion fountain, *J. Geophys. Res.*, **94**, 15277, 1989.
- Turunen T.**, GEN-SYSTEM - A new experimental philosophy for EISCAT radars, *J. Atmos. Terr. Phys.*, **48**, 777, 1986.
- Ungstrup E., D. M. Klumpar and W. J. Heikkila**, Heating of Ions to Superthermal Energies in the Topside Ionosphere by Electrostatic Ion Cyclotron Waves, *J. Geophys. Res.*, **84**, 4289, 1979.
- Villante U.**, Some remarks on the structure of the distant neutral sheet, *Planet. Space Sci.*, **23**, 723, 1975.
- Wahlund J.-E. and H. Opgenoorth**, EISCAT observations of strong ion outflows from the F-region ionosphere during auroral activity: Preliminary results, *Geophys. Res. Lett.*, **16**, 727, 1989.
- Wahlund J.-E., H. J. Opgenoorth, F. R. E. Forme, M. A. L. Persson, I. Häggström and J. Lilén**, Electron energization in the topside auroral ionosphere: on the importance of ion-acoustic turbulence, *J. Atmos. Terr. Phys.*, **55**, 623, 1993.
- Wahlund J.-E., H. J. Opgenoorth, I. Häggström, K. J. Winser and G. O. L. Jones**, EISCAT Observations of Topside Ionospheric Ion Outflows During Auroral Activity: Revisited, *J. Geophys. Res.*, **97**, 3019, 1992.
- Waite J. H. Jr., T. Nagai, J. F. E. Johnson, C. R. Chappell, J. L. Burch, T. L. Killeen, P. B. Hays, G. R. Carignan, W. K. Peterson and E. G. Shelley**, Escape of suprathermal O^+ ions in the polar cap, *J. Geophys. Res.*, **90**, 1619, 1985.
- Walker J. C. and M. H. Rees**, Ionospheric electron temperatures and densities in aurorae, *Planet. Space Sci.*, **16**, 459, 1968.
- Whalen B. A., W. Bernstein and P. W. Daly**, Low altitude acceleration of ionospheric ions, *Geophys. Res. Lett.*, **5**, 55, 1978.
- Whalen B. A., S. Watanabe and A. W. Yau**, Thermal and suprathermal ion observations in the low altitude transverse ion energization region, *Geophys. Res. Lett.*, **18**, 725, 1991.

- Wharton L. E., N. W. Spencer and H. G. Mayr**, The Earth's thermospheric superrotation from Dynamics Explorer 2, *Geophys. Res. Lett.*, **11**, 531, 1984.
- Whittaker J. H.**, The transient response of the topside ionosphere to precipitation, *Planet. Space Sci.*, **25**, 773, 1977.
- Williams P. J. S. and A. R. Jain**, Observations of the high-latitude trough using EISCAT, *J. Atmos. Terr. Phys.*, **48**, 423, 1986.
- Williams P. J. S., G. O. L. Jones and A. R. Jain**, Methods of measuring plasma velocity with EISCAT, *J. Atmos. Terr. Phys.*, **46**, 521, 1984.
- Wilson G. R.**, Kinetic modelling of O⁺ upflows resulting from ExB convection heating in the high-latitude F-region ionosphere, *J. Geophys. Res.*, **99**, 17453, 1994.
- Winser K. J., A. Farmer, D. Rees and A. Aruliah**, Ion neutral dynamics in the high-latitude ionosphere - 1st results from the INDI experiment, *J. Atmos. Terr. Phys.*, **50**, 369, 1988a.
- Winser K. J., G. O. L. Jones and P. J. S. Williams**, A quantitative study of the high latitude ionospheric trough using EISCAT's common programmes, *J. Atmos. Terr. Phys.*, **48**, 893, 1986.
- Winser K. J., G. O. L. Jones and P. J. S. Williams**, Large field-aligned velocities observed by EISCAT, *J. Atmos. Terr. Phys.*, **50**, 379, 1988b.
- Winser K. J., G. O. L. Jones and P. J. S. Williams**, Variations in Field-Aligned Plasma Velocity with Altitude and Latitude in the Auroral Zone; EISCAT Observations and the Physical Interpretation, *Physica Scripta*, **37**, 640, 1988c.
- Winser K. J., G. O. L. Jones, P. J. S. Williams and M. Lockwood**, Observations of large field-aligned flows of thermal plasma in the auroral ionosphere, *Adv. Space. Res.*, **9**, 57, 1989.
- Winser K. J., M. Lockwood and G. O. L. Jones**, Non-thermal plasma observations using EISCAT: Aspect angle dependence, *Geophys. Res. Lett.*, **14**, 957, 1987.
- Yau A. W., E. G. Shelley, W. K. Peterson and L. Lenchyshyn**, Energetic auroral and polar ion outflow at DE-1 altitudes: Magnitude, composition, magnetic activity dependence and long-term variations, *J. Geophys. Res.*, **90**, 8417, 1985.
- Yau A. W., B. A. Whalen, W. K. Petersen and E. G. Shelley**, Distribution of upflowing ionospheric ions in the high-latitude polar cap and auroral ionosphere, *J. Geophys. Res.*, **89**, 5507, 1984.
- Yeh H.-C. and J. C. Foster**, Storm time heavy ion outflow at mid-latitude, *J. Geophys. Res.*, **95**, 7881, 1990.
- Young D. T., J. Geiss, H. Balsinger, P. Eberhardt, A. Ghilemetti and H. Rosenbauer**, Discovery of He²⁺ and O²⁺ ions of terrestrial origin in the outer magnetosphere, *Geophys. Res. Lett.*, **4**, 551, 1977.